



**THE IMPACT OF HEAT RELEASE IN TURBINE
FILM COOLING**

THESIS

Dave S. Evans, Lieutenant, USN

AFIT/GAE/ENY/08-J02

**DEPARTMENT OF THE AIR FORCE
AIR UNIVERSITY**

AIR FORCE INSTITUTE OF TECHNOLOGY

Wright-Patterson Air Force Base, Ohio

APPROVED FOR PUBLIC RELEASE; DISTRIBUTION UNLIMITED

The views expressed in this thesis are those of the author and do not reflect the official policy or position of the United States Air Force, United States Navy, Department of Defense, or the United States Government.

AFIT/GAE/ENY/08-J02

THE IMPACT OF HEAT RELEASE IN TURBINE FILM COOLING

THESIS

Presented to the Faculty

Department of Aeronautics and Astronautics

Graduate School of Engineering and Management

Air Force Institute of Technology

Air University

Air Education and Training Command

In Partial Fulfillment of the Requirements for the
Degree of Master of Science in Aeronautical Engineering

Dave S. Evans, BME

Lieutenant, USN

June 2008

APPROVED FOR PUBLIC RELEASE; DISTRIBUTION UNLIMITED

THE IMPACT OF HEAT RELEASE IN TURBINE FILM COOLING

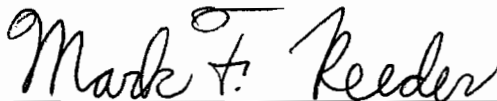
Dave S. Evans, BME
Lieutenant, USN

Approved:



Paul King (Chairman)

28 May 08
date



Mark Reeder (Member)

27 May 08
date



Marc Polanka (Member)

27 MAY 08
date

Abstract

The Ultra Compact Combustor is a design that integrates a turbine vane into the combustor flow path. Because of the high fuel-to-air ratio and short combustor flow path, a significant potential exists for unburned fuel to enter the turbine. Using contemporary turbine cooling vane designs, the injection of oxygen-rich turbine cooling air into a combustor flow containing unburned fuel could result in heat release in the turbine and a large decrease in cooling effectiveness. The current study explores the interaction of cooling flow from typical cooling holes with the exhaust of a fuel-rich well-stirred-reactor operating at high temperatures over a flat plate. Surface temperatures, heat flux, and heat transfer coefficients are calculated for a variety of reactor fuel-to-air ratios, cooling hole geometries, and blowing ratios. Results demonstrate that reactions in the turbine cooling film can result in increased heat transfer to the surface. The amount of this increase depends on hole geometry and blowing ratio and fuel content of the combustor flow. Failure to design for this effect could result in augmented heat transfer caused by the cooling scheme, and turbine life could be degraded substantially.

Acknowledgements

There are many people who spent a tremendous amount of time and energy in assisting me with my part of this project. I would like to thank Dr. Joe Zelina and Dr. Marc Polanka for bringing me in on this project and giving me the opportunity to play with fire. Thank you for the many hours of conversation and guidance, and for reviewing the many drafts of this thesis. I would also like to thank my advisor, Dr. Paul King, for allowing me to undertake such an ambitious project and for all of the guidance throughout this process. To Dr. Scott Stouffer, your commitment to this research and to my education and success is truly humbling. Thank you for all of your time, energy, and advice.

To Wes Anderson, thank you for spending so many hours of aggravation and boredom with me, even though they were highlighted by moments of sheer terror. Thanks also to Mike Arstingstall, one of the greatest problem solvers I have ever met. To Jon McCall and Jay Rutledge, thanks for the suggestions, comments, and for helping me knock off a decade of academic rust.

Finally, I would like to thank my wife and my children. Without your patience, understanding, and support, I would not have reached this milestone. Thank you.

Dave S. Evans

Table of Contents

Abstract	iv
Acknowledgements	v
Table of Contents	vi
List of Figures	viii
List of Tables	xv
List of Symbols	xvi
I. Introduction	1
1.1 Turbine Film Cooling	1
1.2 Potential for Heat Release in Film Cooling	2
1.3 Ultra-Compact Combustor	4
1.4 Objectives	6
II. Background	7
2.1 Film Cooling	7
2.2 Calculation of Stoichiometric Fuel-to-Air and Equivalence Ratios	12
2.3 Calculation of Heat Transfer and Surface Temperatures	13
2.4 Previous Research in Turbine Film Heat Release	16
2.5 Estimation of Flow Conditions for Design	20
2.6 Estimation of Heat Transfer for Design	22
III. Experimental Setup	26
3.1 Well Stirred Reactor	26
3.2 Test Rig	31
Transition Section	32
Test Section	36
Cooling Air Assembly	40
Heat Transfer Gauge Assembly	44
Window Assembly	46
Aft Plate	47
3.3 Facility Fuel, Air, and Nitrogen Supply and Control	48
3.4 Chemical Sampling	53
3.5 Instrumentation and Data Acquisition	54
IV. Results	56
4.1 Test Plan and Procedure	56
4.2 Visible Boundary Layer Reactions	59
4.3 WSR Exhaust Temperature Measurements and Modeling	65
4.4 Temperature Data and Calculations	68
4.5 Overall Effectiveness	75
4.6 Heat Flux and the Heat Transfer Coefficient	82
4.7 Comparison of Heat Transfer Coefficient –Geometry	87
4.8 Comparison of Heat Transfer Coefficient –Test Condition	90
4.9 Local Temperature Rise	93

V.	Conclusion	94
5.1	Overview	94
5.2	Major Findings	94
5.3	Recommendations for Further Research	95
Appendix A	Temperature Data	97
Appendix B	Overall Effectiveness Results	115
Appendix C	Heat Flux and Heat Transfer Coefficient Results	123
Appendix D	Thin Film Gauge Design and Operation.....	139
References	144

List of Figures

Figure 1. Comparison between turbine inlet temperature and blade material limits highlighting the importance of cooling technology	1
Figure 2. Secondary combustion phenomena in a traditional combustor	3
Figure 3. Conventional axial combustor (left) and Ultra-Compact combustor (right) ⁴	4
Figure 4. Local film cooling effectiveness at varying blowing ratios	10
Figure 5. Effect of injection angle on local film cooling effectiveness ¹⁰	11
Figure 6. Effect of M on cylindrical and fanshaped laidback holes (data from Ref. 13)	12
Figure 7. Least square line fit for thermal conductivity of Hastelloy-X [®]	14
Figure 8. Potential for local temperature increase due to reaction in the turbine	17
Figure 9. Heat flux for $M = 0.6$ and $M = 2.0$ for reacting and nonreacting cooling jets ¹⁷	18
Figure 10. Numerical results of temperature profile of a reacting jet ¹⁷ , $M = 0.5$, 2.0 , $Da = 0.3$, 25	19
Figure 11. Simplified flat plate heat transfer model	22
Figure 12. WSR schematic, modified from Ref.	27
Figure 13. Lower toroidal half section of WSR in housing	27
Figure 14. WSR Jet Ring and lower half section	28
Figure 15. Flames caused by the leakage of gases through WSR cracks	29
Figure 16. Reactor upper half-section mounted onto jet ring	30
Figure 17. Exterior of WSR, showing upper and lower reactor housing.....	31
Figure 18. Photograph of Test Rig with sections and assemblies identified	32
Figure 19. Views of transition geometry from reactor exhaust (left), and test section inlet (right)	33
Figure 20. Components of transition section	34
Figure 21. Assembled transition section	34
Figure 22. Mounting Plate	35
Figure 23. Hardware Connections between mounting plate and WSR upper housing	36
Figure 24. Instrument Block	37
Figure 25. Forward facing step at connection of instrument block and flat plate	38
Figure 26. Flat plate design.....	39

Figure 27. Cooling water connections and flow direction	40
Figure 28. Plena and cooling air insert, with thermocouples installed	41
Figure 29. Cooling Air Assembly inserted into flat plate	41
Figure 30. Cooling insert geometries	42
Figure 31. Drawing detail of fan-shaped laidback cooling hole geometry (inches)	43
Figure 32. Heat Transfer Gauge Block	45
Figure 33. Heat transfer gauge block mounting and thermocouple installation	45
Figure 34. Heat transfer gauge numbering convention	46
Figure 35. Test rig view highlighting elements of the window assembly	47
Figure 36. Flow of fuel-rich exhaust leaving the test rig	48
Figure 37. Fuel, air, and nitrogen supply system schematic	49
Figure 38. Propane tank, heaters, and regulator	51
Figure 39. Control panel for fuel, air, and nitrogen supply system	52
Figure 40. Mass flow controller for cooling hole air/N ₂ flow	52
Figure 41. Sampling train for gaseous emissions measurements, modified from Ref. 22	53
Figure 42. Labview screenshot	54
Figure 43. WSR operation in the fuel-rich regime	57
Figure 44. Field of view for boundary layer combustion photographs	60
Figure 45. Visible combustion in cooling film, normal holes, $M = 2.0$	61
Figure 46. Visible combustion in cooling film, normal holes, $M = 1.75$	61
Figure 47. Visible combustion in cooling film, normal holes, $M = 1.25$	61
Figure 48. Visible combustion in cooling film, normal holes, $M = 1.0$	61
Figure 49. Visible combustion in cooling film, normal holes, $M = 0.75$	62
Figure 50. Visible combustion in cooling film, normal holes, $M = 0.5$	62
Figure 51. Nitrogen cooling film, angled holes, $M = 2.0$	63
Figure 52. Visible combustion in cooling film, angled holes, $M = 2.0$	63
Figure 53. Visible combustion in cooling film, angled holes, $M = 1.0$	63
Figure 54. Visible combustion in cooling film, angled holes, $M = 0.5$	63
Figure 55. Variation in T_∞ with Φ at constant m_{air}	66
Figure 56. Gauge data, normal holes, $\Phi = 0.6$, $m_{air} = 1020$ g/min, upstream gauges	70

Figure 57. Gauge data, normal holes, $\Phi = 0.6$, $m_{air} = 1020$ g/min, downstream gauges.....	70
Figure 58. Gauge data, fanshaped holes, $\Phi = 1.5$, $m_{air} = 1020$ g/min, upstream gauges.....	71
Figure 59. Gauge data, fanshaped holes, $\Phi = 1.5$, $m_{air} = 1020$ g/min, downstream gauges.....	72
Figure 60. Dependence of T_c on M , normal holes, $\Phi = 0.6$, $m_{air} = 1020$ g/min.....	73
Figure 61. Measured T_c at varying locations in the plenum, $\Phi = 1.7$, $M = 0.5$, $m_{air} = 1020$ g/min	74
Figure 62. T_∞ , $\Phi = 0.6$, $m_{air} = 1020$ g/min, taken during normal holes data collection	75
Figure 63. Dependence of φ on M , fanshaped holes, $\Phi = 0.6$, $m_{air} = 1020$ g/min	76
Figure 64. Dependence of φ on M , fanshaped holes, $\Phi = 1.5$, $m_{air} = 1020$ g/min.....	77
Figure 65. Dependence of $\Delta\varphi$ on M , upstream normal holes, at different test conditions	78
Figure 66. Dependence of $\Delta\varphi$ on M , downstream normal holes, at different test conditions	79
Figure 67. Dependence of $\Delta\varphi$ on M , upstream angled holes, at different test conditions	79
Figure 68. Dependence of $\Delta\varphi$ on M , downstream angled holes, at different WSR test conditions	80
Figure 69. Dependence of $\Delta\varphi$ on M , upstream fanshaped holes, at different test conditions	80
Figure 70. Dependence of $\Delta\varphi$ on M , downstream fanshaped holes, at different test conditions	81
Figure 71. Dependence of $\Delta\varphi$ on M , all geometries, $\Phi = 1.5$, $m_{air} = 1020$ g/min	82
Figure 72. Dependence of q'' on M , normal holes, $\Phi = 0.6$, $m_{air} = 1020$ g/min.....	83
Figure 73. Dependence of h_{eff} on M , normal holes, $\Phi = 0.6$, $m_{air} = 1020$ g/min	84
Figure 74. Dependence of q'' on M , fanshaped holes, $\Phi = 1.5$, $m_{air} = 1020$ g/min.....	84
Figure 75. Dependence of h_{eff} on M , fanshaped holes, $\Phi = 1.5$, $m_{air} = 1020$ g/min.....	85
Figure 76. Modeled temperature profile in flat plate ²⁵	86
Figure 77. Comparison of cooling hole geometries: Dependence of h_{eff} on M , $\Phi = 0.6$	88
Figure 78. Comparison of cooling hole geometries: Dependence of h_{eff} on M , $\Phi = 0.95$	89

Figure 79. Comparison of cooling hole geometries: Dependence of h_{eff} on M , $\Phi = 1.5$	90
Figure 80. Increase in h_{eff} due to reactions, normal holes.....	91
Figure 81. Increase in h_{eff} due to reactions, angled holes	92
Figure 82. Increase in h_{eff} due to reactions, fanshaped holes.....	92
Figure 83. Local temperature increase, all geometries, $\Phi = 1.5$, $m_{air} = 1020$ g/min	93
Figure 84. Temperature data, normal holes, $\Phi = 0.6$, $m_{air} = 1020$ g/min, upstream gauges.....	97
Figure 85. Temperature data, normal holes, $\Phi = 0.6$, $m_{air} = 1020$ g/min, downstream gauges	97
Figure 86. Temperature data, normal holes, $\Phi = 0.8$, $m_{air} = 1020$ g/min, upstream gauges.....	98
Figure 87. Temperature data, normal holes, $\Phi = 0.8$, $m_{air} = 1020$ g/min, downstream gauges	98
Figure 88. Temperature data, normal holes, $\Phi = 0.95$, $m_{air} = 720$ g/min, upstream gauges.....	99
Figure 89. Temperature data, normal holes, $\Phi = 0.95$, $m_{air} = 720$ g/min, downstream gauges	99
Figure 90. Temperature data, normal holes, $\Phi = 1.5$, $m_{air} = 1020$ g/min, upstream gauges.....	100
Figure 91. Temperature data, normal holes, $\Phi = 1.5$, $m_{air} = 1020$ g/min, downstream gauges	100
Figure 92. Temperature data, normal holes, $\Phi = 1.6$, $m_{air} = 1020$ g/min, upstream gauges.....	101
Figure 93. Temperature data, normal holes, $\Phi = 1.6$, $m_{air} = 1020$ g/min, downstream gauges	101
Figure 94. Temperature data, normal holes, $\Phi = 1.7$, $m_{air} = 1020$ g/min, upstream gauges.....	102
Figure 95. Temperature data, normal holes, $\Phi = 1.7$, $m_{air} = 1020$ g/min, downstream gauges	102
Figure 96. Temperature data, angled holes, $\Phi = 0.6$, $m_{air} = 1020$ g/min, upstream gauges.....	103
Figure 97. Temperature data, angled holes, $\Phi = 0.6$, $m_{air} = 1020$ g/min, downstream gauges	103
Figure 98. Temperature data, angled holes, $\Phi = 0.8$, $m_{air} = 1020$ g/min, upstream gauges.....	104

Figure 99. Temperature data, angled holes, $\Phi = 0.8$, $m_{air} = 1020$ g/min, downstream gauges	104
Figure 100. Temperature data, angled holes, $\Phi = 0.95$, $m_{air} = 720$ g/min, upstream gauges	105
Figure 101. Temperature data, angled holes, $\Phi = 0.95$, $m_{air} = 720$ g/min, downstream gauges	105
Figure 102. Temperature data, angled holes, $\Phi = 1.5$, $m_{air} = 1020$ g/min, upstream gauges	106
Figure 103. Temperature data, angled holes, $\Phi = 1.5$, $m_{air} = 1020$ g/min, downstream gauges	106
Figure 104. Temperature data, angled holes, $\Phi = 1.6$, $m_{air} = 1020$ g/min, upstream gauges	107
Figure 105. Temperature data, angled holes, $\Phi = 1.6$, $m_{air} = 1020$ g/min, downstream gauges	107
Figure 106. Temperature data, angled holes, $\Phi = 1.7$, $m_{air} = 1020$ g/min, upstream gauges	108
Figure 107. Temperature data, angled holes, $\Phi = 1.7$, $m_{air} = 1020$ g/min, downstream gauges	108
Figure 108. Temperature data, fanshaped holes, $\Phi = 0.6$, $m_{air} = 1020$ g/min, upstream gauges	109
Figure 109. Temperature data, fanshaped holes, $\Phi = 0.6$, $m_{air} = 1020$ g/min, downstream gauges	109
Figure 110. Temperature data, fanshaped holes, $\Phi = 0.8$, $m_{air} = 1020$ g/min, upstream gauges	110
Figure 111. Temperature data, fanshaped holes, $\Phi = 0.8$, $m_{air} = 1020$ g/min, downstream gauges	110
Figure 112. Temperature data, fanshaped holes, $\Phi = 0.95$, $m_{air} = 720$ g/min, upstream gauges	111
Figure 113. Temperature data, fanshaped holes, $\Phi = 0.95$, $m_{air} = 720$ g/min, downstream gauges	111
Figure 114. Temperature data, fanshaped holes, $\Phi = 1.5$, $m_{air} = 1020$ g/min, upstream gauges	112
Figure 115. Temperature data, fanshaped holes, $\Phi = 1.5$, $m_{air} = 1020$ g/min, downstream gauges	112
Figure 116. Temperature data, fanshaped holes, $\Phi = 1.6$, $m_{air} = 1020$ g/min, upstream gauges	113

Figure 117. Temperature data, fanshaped holes, $\Phi = 1.6$, $m_{air} = 1020$ g/min, downstream gauges	113
Figure 118. Temperature data, fanshaped holes, $\Phi = 1.7$, $m_{air} = 1020$ g/min, upstream gauges	114
Figure 119. Temperature data, fanshaped holes, $\Phi = 1.7$, $m_{air} = 1020$ g/min, downstream gauges	114
Figure 120. Dependence of φ on M , normal holes, $\Phi = 0.6$, $m_{air} = 1020$ g/min.....	115
Figure 121. Dependence of φ on M , normal holes, $\Phi = 0.8$, $m_{air} = 1020$ g/min.....	115
Figure 122. Dependence of φ on M , normal holes, $\Phi = 0.95$, $m_{air} = 720$ g/min.....	116
Figure 123. Dependence of φ on M , normal holes, $\Phi = 1.5$, $m_{air} = 1020$ g/min.....	116
Figure 124. Dependence of φ on M , normal holes, $\Phi = 1.6$, $m_{air} = 1020$ g/min.....	117
Figure 125. Dependence of φ on M , normal holes, $\Phi = 1.7$, $m_{air} = 1020$ g/min.....	117
Figure 126. Dependence of φ on M , angled holes, $\Phi = 0.6$, $m_{air} = 1020$ g/min	118
Figure 127. Dependence of φ on M , angled holes, $\Phi = 0.8$, $m_{air} = 1020$ g/min	118
Figure 128. Dependence of φ on M , angled holes, $\Phi = 0.95$, $m_{air} = 720$ g/min	119
Figure 129. Dependence of φ on M , angled holes, $\Phi = 1.5$, $m_{air} = 1020$ g/min	119
Figure 130. Dependence of φ on M , angled holes, $\Phi = 1.6$, $m_{air} = 1020$ g/min	120
Figure 131. Dependence of φ on M , angled holes, $\Phi = 1.7$, $m_{air} = 1020$ g/min	120
Figure 132. Dependence of φ on M , fanshaped holes, $\Phi = 0.8$, $m_{air} = 1020$ g/min.....	121
Figure 133. Dependence of φ on M , fanshaped holes, $\Phi = 0.95$, $m_{air} = 720$ g/min.....	121
Figure 134. Dependence of φ on M , fanshaped holes, $\Phi = 1.6$, $m_{air} = 1020$ g/min.....	122
Figure 135. Dependence of φ on M , fanshaped holes, $\Phi = 1.7$, $m_{air} = 1020$ g/min.....	122
Figure 136. Dependence of q'' on M , normal holes, $\Phi = 0.8$, $m_{air} = 1020$ g/min.....	123
Figure 137. Dependence of h_{eff} on M , normal holes, $\Phi = 0.8$, $m_{air} = 1020$ g/min	123
Figure 138. Dependence of q'' on M , normal holes, $\Phi = 0.95$, $m_{air} = 720$ g/min.....	124
Figure 139. Dependence of h_{eff} on M , normal holes, $\Phi = 0.95$, $m_{air} = 720$ g/min	124
Figure 140. Dependence of q'' on M , normal holes, $\Phi = 1.5$, $m_{air} = 1020$ g/min.....	125
Figure 141. Dependence of h_{eff} on M , normal holes, $\Phi = 1.5$, $m_{air} = 1020$ g/min	125
Figure 142. Dependence of q'' on M , normal holes, $\Phi = 1.6$, $m_{air} = 1020$ g/min.....	126
Figure 143. Dependence of h_{eff} on M , normal holes, $\Phi = 1.6$, $m_{air} = 1020$ g/min	126
Figure 144. Dependence of q'' on M , normal holes, $\Phi = 1.7$, $m_{air} = 1020$ g/min.....	127
Figure 145. Dependence of h_{eff} on M , normal holes, $\Phi = 1.7$, $m_{air} = 1020$ g/min	127

Figure 146. Dependence of q'' on M , angled holes, $\Phi = 0.6$, $m_{air} = 1020$ g/min.....	128
Figure 147. Dependence of h_{eff} on M , angled holes, $\Phi = 0.6$, $m_{air} = 1020$ g/min	128
Figure 148. Dependence of q'' on M , angled holes, $\Phi = 0.8$, $m_{air} = 1020$ g/min.....	129
Figure 149. Dependence of h_{eff} on M , angled holes, $\Phi = 0.8$, $m_{air} = 1020$ g/min	129
Figure 150. Dependence of q'' on M , angled holes, $\Phi = 0.95$, $m_{air} = 720$ g/min.....	130
Figure 151. Dependence of h_{eff} on M , angled holes, $\Phi = 0.95$, $m_{air} = 720$ g/min	130
Figure 152. Dependence of q'' on M , angled holes, $\Phi = 1.5$, $m_{air} = 1020$ g/min.....	131
Figure 153. Dependence of h_{eff} on M , angled holes, $\Phi = 1.5$, $m_{air} = 1020$ g/min	131
Figure 154. Dependence of q'' on M , angled holes, $\Phi = 1.6$, $m_{air} = 1020$ g/min.....	132
Figure 155. Dependence of h_{eff} on M , angled holes, $\Phi = 1.6$, $m_{air} = 1020$ g/min	132
Figure 156. Dependence of q'' on M , angled holes, $\Phi = 1.7$, $m_{air} = 1020$ g/min.....	133
Figure 157. Dependence of h_{eff} on M , angled holes, $\Phi = 1.7$, $m_{air} = 1020$ g/min	133
Figure 158. Dependence of q'' on M , fanshaped holes, $\Phi = 0.6$, $m_{air} = 1020$ g/min	134
Figure 159. Dependence of h_{eff} on M , fanshaped holes, $\Phi = 0.6$, $m_{air} = 1020$ g/min	134
Figure 160. Dependence of q'' on M , fanshaped holes, $\Phi = 0.8$, $m_{air} = 1020$ g/min	135
Figure 161. Dependence of h_{eff} on M , fanshaped holes, $\Phi = 0.8$, $m_{air} = 1020$ g/min	135
Figure 162. Dependence of q'' on M , fanshaped holes, $\Phi = 0.95$, $m_{air} = 720$ g/min	136
Figure 163. Dependence of h_{eff} on M , fanshaped holes, $\Phi = 0.95$, $m_{air} = 720$ g/min	136
Figure 164. Dependence of q'' on M , fanshaped holes, $\Phi = 1.6$, $m_{air} = 1020$ g/min	137
Figure 165. Dependence of h_{eff} on M , fanshaped holes, $\Phi = 1.6$, $m_{air} = 1020$ g/min	137
Figure 166. Dependence of q'' on M , fanshaped holes, $\Phi = 1.7$, $m_{air} = 1020$ g/min	138
Figure 167. Dependence of h_{eff} on M , fanshaped holes, $\Phi = 1.7$, $m_{air} = 1020$ g/min	138
Figure 168. Single serpentine-shaped Thin Film Gauge designed for the current study	140
Figure 169. Schematic of High Density Thin Film Gauge array ²⁶	141
Figure 170. High Density Thin Film Gauge array	141
Figure 171. Design of TFG and HDTFG heat transfer gauge block	143

List of Tables

Table 1. Thermal Conductivity of Hastelloy-X [®]	14
Table 2. Temperature and <i>MW</i> results of equilibrium calculation.....	20
Table 3. Estimated Reynolds number, trip height, and transition distance.....	21
Table 4. Pressure transducers and locations	54
Table 5. Thermocouple locations and types	55
Table 6. Cooling hole geometry and WSR test conditions	58
Table 7. Test plan and data acquisition sheet for WSR test condition $\Phi = 0.6$, <i>mair</i> = 1020 g/min	59
Table 8. Penetration and plume lengths of cooling jets	65
Table 9. Modeled concentration, velocity, and density information prior to cooling holes	67
Table 10. Chemical times and the Damkohler number for modeled test conditions	68
Table 11. Comparison of measured heat transfer coefficient to empirical correlation ¹⁵	87
Table 12. Comparison of surface temperature measurement designs.....	142

List of Symbols

English symbols

A	=	area (m^2)
a_0, a_1	=	curve fit parameter
C	=	constant of integration
c_f	=	friction coefficient
c_p	=	specific heat at constant pressure ($\text{J/kg}\cdot\text{K}$)
D	=	diameter (m)
Da	=	Damkohler number
g	=	acceleration of gravity (m/s^2)
Gr	=	Grashof number
h	=	heat transfer coefficient ($\text{W/m}^2\cdot\text{K}$)
H^*	=	heat release potential
H_T	=	total enthalpy (J)
I_s	=	current (A)
k	=	thermal conductivity ($\text{W/m}^2\cdot\text{K}$); trip height (m)
L	=	total length (M)
M	=	blowing ratio
\dot{m}	=	mass flow rate (g/min; g/s)
MW	=	molecular weight (g/mol)
Nu	=	Nusselt number
P	=	pressure (N/m^2)
Pr	=	Prandtl number
q	=	heat transfer rate (W)
q''	=	heat flux (W/m^2)
R	=	universal gas constant ($\text{J/mol}\cdot\text{K}$)
Re	=	Reynolds number
St	=	Stanton number
t	=	thickness (m)
T	=	temperature (K)
U	=	velocity (m/s)
V	=	voltage (V)
v_f	=	film voltage (V)
x	=	location; distance (m)

Greek symbols

α	=	injection angle ($^\circ$)
α_R	=	temperature coefficient of resistance (1/K)
β	=	coefficient of thermal expansion (1/K)
ε	=	emissivity
η	=	film effectiveness
μ	=	viscosity ($\text{kg/m}\cdot\text{s}$)

ρ	=	density (kg/m ³)
σ	=	Boltzmann constant (J/K)
τ_{chem}	=	characteristic chemical time (s)
τ_{flow}	=	characteristic flow time (s)
Φ	=	equivalence ratio
φ	=	overall effectiveness

Subscripts

0	=	reference
1	=	near-surface thermocouple location
2	=	deep thermocouple location
4	=	turbine inlet condition
∞	=	freestream; reactor exhaust stream
aw	=	adiabatic wall
c	=	coolant; convection
D	=	diameter
f	=	film
k	=	trip location; conduction
L	=	body length
r	=	radiation
ref	=	reference
s	=	surface
tr	=	transition
x	=	specific location

Abbreviations

AFRL	=	Air Force Research Laboratories
FID	=	Flame Ionization Detector
HC	=	Hydrocarbons
HDTFG	=	High Density Thin Film Gauge
ITB	=	Inter-Turbine Burner
PFR	=	Plug Flow Reactor
PSR	=	Perfectly Stirred Reactor
SLPM	=	Standard Liters Per Minute
TFG	=	Thin Film Gauge
UCC	=	Ultra-Compact Combustor
WSR	=	Well Stirred Reactor

THE IMPACT OF HEAT RELEASE IN TURBINE FILM COOLING

I. Introduction

1.1 Turbine Film Cooling

The thermal efficiency and specific thrust of gas turbine engines increase with increasing turbine inlet temperature (T_4). The maximum allowable T_4 ($T_{4\max}$) in practical engines is limited to those temperatures below which material failure or unacceptable reductions in service life are likely to occur. As shown in Figure 1, gas turbine designs have shown a continued increase in $T_{4\max}$ since the invention of the gas turbine engine. Because of the requirements to increase fuel efficiency and performance of aeronautical engines, designers will continue to push towards higher $T_{4\max}$.

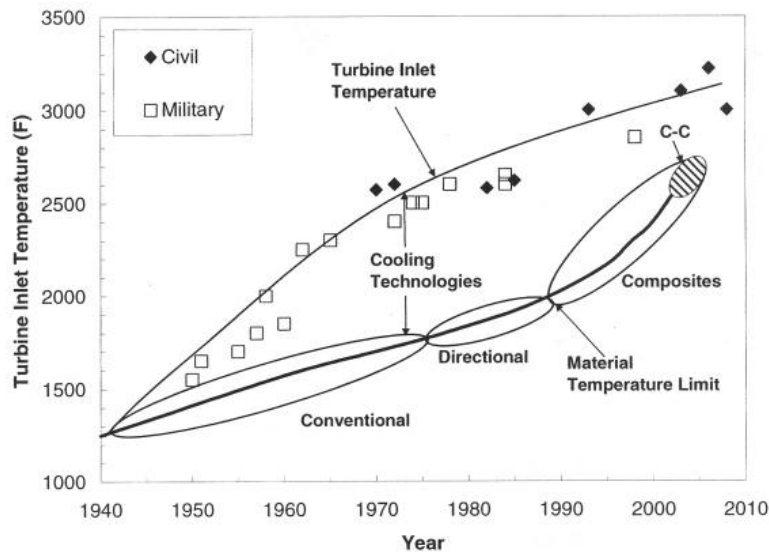


Figure 1. Comparison between turbine inlet temperature and blade material limits highlighting the importance of cooling technology¹

For decades, $T_{4\max}$ has exceeded the temperatures that would cause material failure of the turbine components². To keep these components from failing and to extend their life, they have been cooled with air bled from the compressor. Initially, these components were cooled from the inside, by a flow of bleed air through passages cut in the turbine blades. Later, turbines were designed to allow bleed air to be forced out through the turbine surfaces, forming a cooling film along the surface. Though this bleed air may locally increase the heat transfer coefficient, the film serves to decrease the high temperatures that turbine surfaces contact, and if correctly designed, decreases the heat transfer to the surfaces from the flow. The introduction of high temperature materials for turbine components has increased in recent years; however, the necessity of continuing to incorporate cooling technologies cannot be overstated¹.

1.2 Potential for Heat Release in Film Cooling

Historically, the combustion sections of gas turbine engines have operated at overall fuel to air ratios much less than stoichiometric³. Additionally, a relatively long flow path within the combustor, on the order of 25-50 cm, compared to chemical and mixing times ensured that reactions were complete before leaving the combustor. Therefore, the impact of reactions occurring in the turbine cooling film has been largely insignificant. However, the desire to increase efficiency has led to the development of combustion sections that operate at an overall fuel to air ratio much closer to stoichiometric conditions. At the same time, advanced combustors are becoming more compact in order to increase the thrust to weight ratio⁴. The possibility of unburned fuel

entering the turbine is no longer insignificant. When the unburned fuel mixes with oxygen rich compressor bleed air in the turbine cooling film, the conditions become right for burning in the turbine. Figure 2 illustrates this effect.

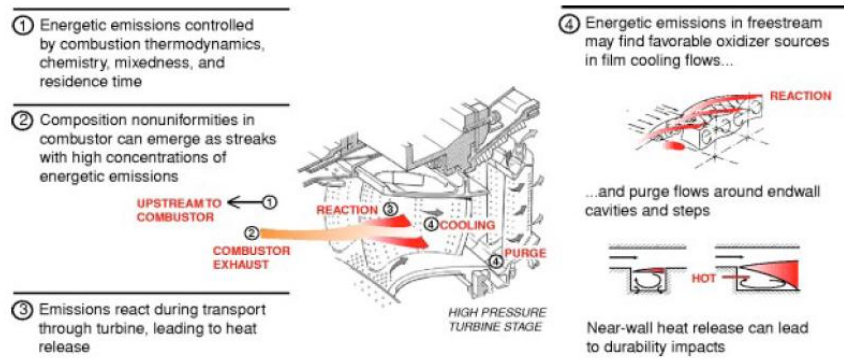


Figure 2. Secondary combustion phenomena in a traditional combustor⁵

Even in the absence of fuel streaks, the high fuel to air ratios and high temperatures of future engine concepts introduce new challenges for turbine cooling. As combustor temperatures increase, an increasing amount of energy released from the fuel will be stored in the flow not as increased temperature, but in the form of dissociated highly energetic species, such as carbon monoxide. This energy has the potential to be released in the relatively cool conditions of the turbine section, because cooling temperatures promote the recombination of dissociated species. Recombination would be particularly favored in the turbine cooling film, where it has the potential to augment the heat transfer and reduce the cooling effectiveness of the turbine cooling design. Heat release in the cooling film, whether from recombination of dissociated species or from the combustion of unburned fuel, would drastically reduce the cooling effectiveness of the turbine cooling scheme, with potentially severe effects on engine component durability.

1.3 *Ultra-Compact Combustor*

The Ultra-Compact Combustor/Inter-Turbine Burner (UCC/ITB) is a revolutionary combustion system currently being developed at the Air Force Research Laboratories (AFRL)^{4,6}. The basis of the concept is to direct the flow of combustion air in the circumferential direction in order to reach sufficient residence times while at the same time reducing the axial length of the component. Figure 3 shows images of a conventional annular combustor (on the left) and the UCC (on the right).

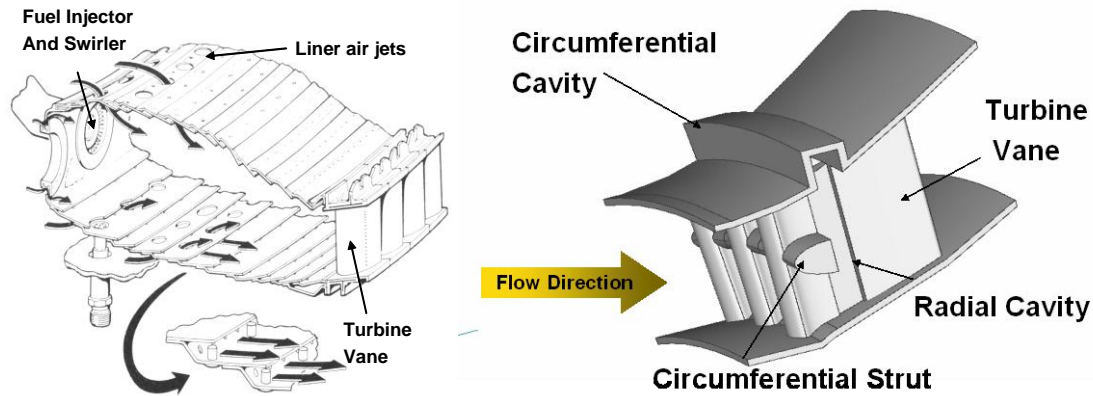


Figure 3. Conventional axial combustor (left) and Ultra-Compact combustor (right)⁴

In a conventional combustor, air flows through the combustor in the axial direction. The amount of time the air remains in the combustor is simply a function of the flow speed and the length of the combustor. The combustor must be long enough to allow time for mixing, ignition, and complete combustion of the fuel and air.

In the UCC, a circumferential cavity is placed around the outside of the turbine inlet guide vanes. The air flow is allowed to pass directly from compressor to the extended turbine inlet guide vanes. The guide vanes have radial vane cavities which are

aligned with the circumferential cavity, allowing the airflow to become entrained along the cavity. Fuel is injected into this cavity, where combustion occurs in a fuel rich regime⁴. The circumferential flow in the cavity benefits the combustion process because the axial length of the combustor no longer limits residence time. Also, the circumferential flow causes a high g-loading, which increases burning rates⁷. Intermediate combustion products flow into the radial vane cavities, where they complete combustion.

The UCC shortens the axial length of the combustor, and reduces the need for other gas turbine engine components such as the compressor exit guide vane and the turbine inlet guide vane. The design is estimated to shorten the combustion system by at least 66%⁴, with significant weight saving accompanying the reduction in length. The design is sufficiently compressed that the concept is being investigated for use as a second stage combustor, located between the low-pressure and high-pressure turbines. This concept is known as the Inter-Turbine Burner. High levels of energy can be extracted from the low-pressure turbine, which could be used for a wide range of applications⁸.

The UCC/ITB presents significant challenges in vane cooling because the turbine blades are incorporated into the combustor design, and the design fuel to air ratio is very high. The potential for unburned fuel to mix with oxygen rich compressor bleed air in the turbine cooling film is greatly increased. The challenges presented by this design require a fuller understanding of the interaction between turbine cooling films and incomplete combustion products, and the relationship between boundary layer reactions and turbine durability.

1.4 Objectives

The objective of this research is to explore the effect of reactions on turbine film cooling. Specifically, the impact of blowing ratio, equivalence ratio, and cooling hole shape on the occurrence of heat release on a flat plate geometry are quantified, using a Well Stirred Reactor (WSR) to provide a well characterized source of combustion products. This research will serve as an incremental step towards the understanding of the physics of reacting boundary layers as they relate to compact combustion systems such as the UCC, in which the turbine vane is integrated into the combustor design. The goal of the research program is to establish a sufficient understanding for the development of turbine cooling schemes that enable the application of the UCC/ITB to future systems.

II. Background

2.1 Film Cooling

For a simple case of a fluid flowing over a surface, the heat transfer to the surface per unit area (q'') can be modeled by a convective heat transfer equation²:

$$q'' = h(T_{ref} - T_s) \quad (1)$$

Where h is a convective heat transfer coefficient, T_{ref} is the appropriate driving temperature of the fluid, and T_s is the temperature of the surface. Many relationships exist for the prediction of heat transfer coefficients in a wide variety of uniform flow fields. In a film cooling layer, the heat transfer coefficient and the fluid temperature are not uniform and are far more difficult to quantify.

Film cooling operates by protecting from the freestream temperature (T_∞) by a flow of coolant at a coolant temperature, T_c . The temperature now driving heat transfer is the temperature (T_f) of the film located adjacent to the surface. Ideally, the coolant ejected from the cooling holes would remain attached to the surface. In this case, T_f would be very close to T_c . This does not in fact occur. The coolant air mixes with the mainstream flow quickly, resulting in a T_f somewhere between T_c and T_∞ .

If the film temperature and flow condition are known, the adiabatic temperature, T_{aw} , can be determined. T_{aw} is the temperature that the surface would reach if there was no heat transfer from the surface. A nondimensional film effectiveness can then be defined to describe the success of a particular cooling scheme in bringing T_{aw} close to T_c , where T_c is measured at the exit of the cooling hole:

$$\eta = \frac{(T_\infty - T_{aw})}{(T_\infty - T_{c,exit})} \quad (2)$$

In the current study, the film temperature is not directly measured and the wall cannot be treated as adiabatic, so T_{aw} is unknown. As such, the parameter of interest is the overall effectiveness (φ) defined below, where T_c is the temperature of the coolant entering the cooling holes:

$$\varphi = \frac{(T_\infty - T_s)}{(T_\infty - T_c)} \quad (3)$$

There are limitations in the use of this parameter, as it is dependent on the geometry and conditions being reported. The geometry used in this study is actively cooled with water to intentionally lower T_s (see Section 3.2). Therefore, φ is significantly higher than reported in other test conditions⁹, and is used only to compare the overall effectiveness of conditions within this report.

It is important to note that h in Eq. (1) is highly dependent on flow conditions. In fact, the presence of a cooling hole generally increases h . It is possible under the right conditions for a cooling hole to actually augment the heat transfer to the surface with a constant T_f due to the increase in heat transfer coefficient². To allow for this difference, Eq. (1) is rewritten as follows, where h_f is the convective heat transfer coefficient with the cooling film.

$$q'' = h_f(T_f - T_s) \quad (4)$$

Since T_f is not measured in this experiment, Eq. (4) is modified with T_∞ as the reference temperature, and h_f is replaced with the effective heat transfer coefficient, h_{eff} . Eq. (5) is the form of the convective heat transfer equation used in the analysis of the results of this study.

$$q'' = h_{eff}(T_\infty - T_s) \quad (5)$$

There are many fluid mechanical factors that influence the film cooling behavior. The current study explores a number of them, in addition to the chemistry of the flow: Blowing ratio, injection angle, and hole shape. The most important for the current study is the mass flux ratio, M , also referred to as the blowing ratio.

$$M = \frac{\rho_c U_c}{\rho_\infty U_\infty} \quad (6)$$

The calculation of M from Eq. (6) directly requires precise knowledge of the density of the gases. The determination of this property in reacting systems is imprecise. Therefore, M will be calculated in this experiment using the conservation of mass. The statement of conservation of mass for a constant area flow in an incompressible fluid is given in Eq. (7):

$$\frac{\dot{m}}{A} = \rho U \quad (7)$$

Substitution of Eq. (7) into Eq. (6) for both coolant flow and reactor exhaust flow yields the following:

$$M = \frac{\dot{m}_{c,total} A_\infty}{\dot{m}_\infty A_{c,total}} \quad (8)$$

Here, $\dot{m}_{c,total}$ is the total mass flow of the coolant through all cooling holes, $A_{c,total}$ is the area of all cooling holes, A_∞ is the cross-sectional area of the test rig, and \dot{m}_∞ is the mass flow of the reactor exhaust, equaling the sum of \dot{m}_{fuel} and \dot{m}_{air} .

The effect of M on η downstream of a cooling hole with an incidence angle of 30° was examined in Ref. 10, and is shown in Figure 4. The location of the maximum value of η is indicated with a white triangle. For low values of M , peak η occurs immediately downstream of the cooling hole, and shows a consistent decay with downstream distance. Higher blowing ratios have a greater effect downstream, largely due to the higher mass flow of coolant. However, η immediately downstream of the hole is lower. This can be attributed to the tendency of high mass ratio film cooling jets to separate from the surface immediately after the hole, and reattaching further downstream. Higher blowing ratio jets also tend to have reduced area averaged effectiveness due to the separation.

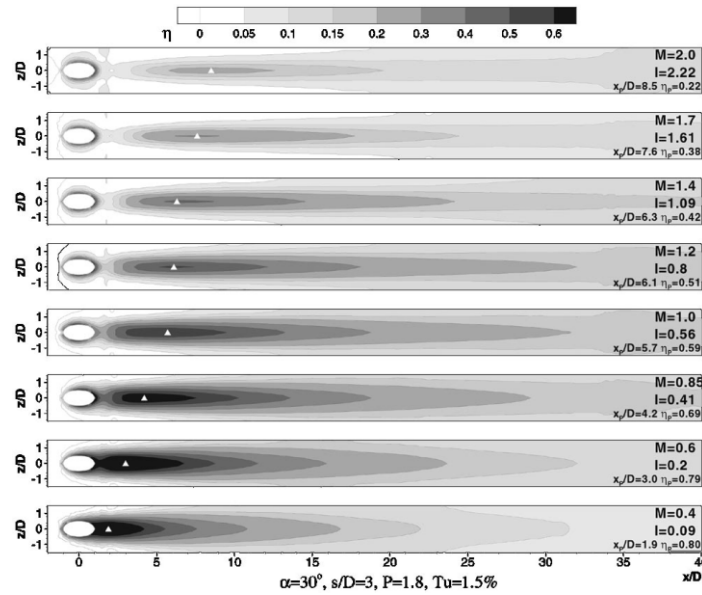


Figure 4. Local film cooling effectiveness at varying blowing ratios¹⁰

The effect of injection angle, α , was also examined in Ref. 10. Figure 5 below compares η at 30° and 90° over a range of M . Previous studies^{11,12} have suggested that at

low M , the angled holes are more effective. However, at very high M there is an increase in film efficiency for normal jets. This effect can be seen in Figure 5 by comparing η far downstream of the cooling hole for the M cases.

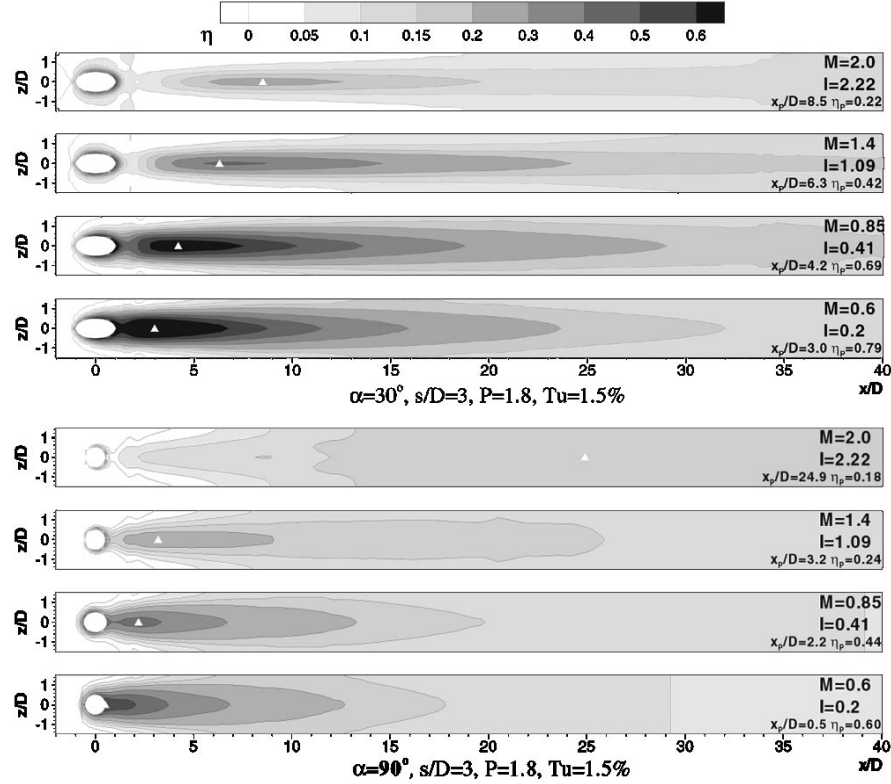


Figure 5. Effect of injection angle on local film cooling effectiveness¹⁰

The relative benefits of cylindrical, fanshaped, and laidback fanshaped holes were studied in Ref. 13. The laidback fanshaped hole has the advantages of ejecting more coolant flow at a lower blowing ratio, thus achieving higher effectiveness. It accomplishes this because of the increasing area of the hole near the exit, thus reducing

the tendency of the jet to separate. The benefit of shaping is dramatic, as shown in Figure 6, particularly at high blowing ratios.

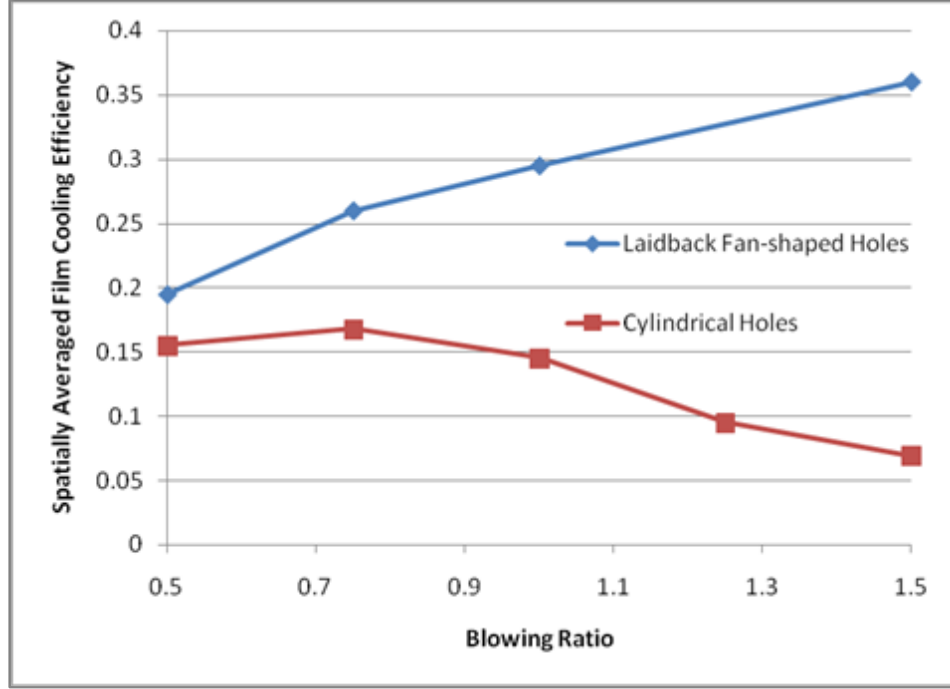
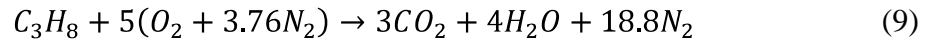


Figure 6. Effect of M on cylindrical and fanshaped laidback holes (data from Ref. 13)

2.2 Calculation of Stoichiometric Fuel-to-Air and Equivalence Ratios

The fuel used in the current study is propane (C_3H_8). The global reaction for the combustion of propane in air is given in Eq. (9) below¹⁴:



The fuel-to-air ratio at stoichiometric conditions can be determined from the moles of fuel and oxidizer from the global reaction:

$$\frac{\dot{m}_{fuel}}{\dot{m}_{air}} = \frac{1 \times MW_{C_3H_8}}{5 \times (4.76 \times MW_{air})} = 0.06395 \quad (10)$$

In the above equation, \dot{m}_{fuel} is the mass flow rate of propane, \dot{m}_{air} is the mass flow rate of combustion air, and MW is the molecular weight. The equivalence ratio (Φ) is defined as the ratio of the fuel-to-ratio of a specific condition to the fuel-to-air ratio at stoichiometric conditions:

$$\Phi = \frac{\left(\frac{\dot{m}_{fuel}}{\dot{m}_{air}}\right)}{\left(\frac{\dot{m}_{fuel}}{\dot{m}_{air}}\right)_{stoich}} \quad (11)$$

Thus, $\Phi > 1$ is fuel rich, $\Phi < 1$ is fuel lean, and $\Phi = 1$ is stoichiometric.

2.3 Calculation of Heat Transfer and Surface Temperatures

In the current study, the surface temperature of the metal and the heat flux are determined by measuring the temperature using thermocouples at two depths within the flat plate. Assuming one-dimensional heat transfer, the heat transfer between two thermocouples is calculated for Fourier's law of conduction, as follows¹⁵:

$$q''_x = -k \frac{dT}{dx} \quad (12)$$

Where q''_x is the heat transfer per unit area, k is the thermal conductivity of the material, T is the temperature in the material, and x is the distance of the thermocouples from the surface. Assuming steady state conditions, q''_x is constant, and Eq. (12) may be rearranged and integrated as follows:

$$\int q''_x dx = - \int k dT \quad (13)$$

The gauges are constructed of Hastelloy-X[®]. The temperatures in the gauges vary from as high as 850K on the hot surface to as low as 450K at the deep thermocouple location (1.9 cm from the surface). Over this range, the thermal conductivity varies greatly. The values reported by the manufacture, Haynes International, are summarized in Table 1. A plot of these data, Figure 7, reveals that over the range of interest, thermal conductivity varies in a nearly linear manner.

Table 1. Thermal Conductivity of Hastelloy-X[®] ¹⁶

Temperature (K)	k (W/m-K)
366.5	11.0
533.2	14.1
866.5	20.8
977.6	22.9

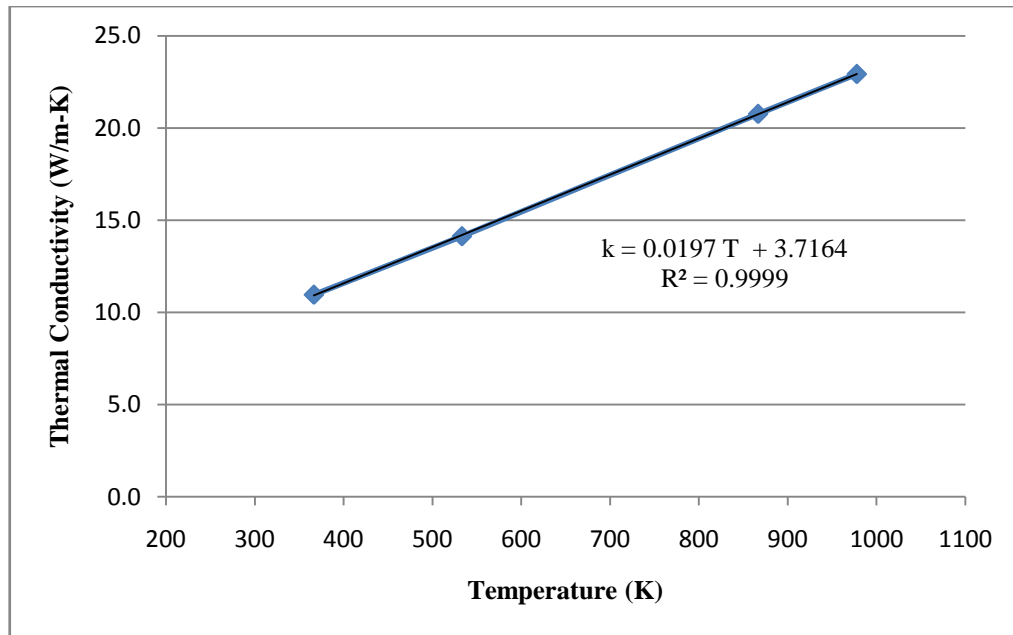


Figure 7. Least square line fit for thermal conductivity of Hastelloy-X[®]

Thermal conductivity can therefore be expressed in the form $k(T) = a_0 + a_1T$, which can be substituted into Eq. (13) and integrated.

$$\int q_x'' dx = - \int (a_0 + a_1T) dT \quad (14)$$

$$q_x''x - C = - \left(a_0T + a_1 \frac{T^2}{2} \right) \quad (15)$$

$$\frac{a_1}{2}T^2 + a_0T + q_x''x - C = 0 \quad (16)$$

Here, C is a constant of integration. The heat transfer gauges provide two thermocouple temperatures, giving two equations that can be used to find q_x'' and C :

$$\frac{a_1}{2}T_1^2 + a_0T_1 + q_x''x_1 - C = 0 \quad (17)$$

$$\frac{a_1}{2}T_2^2 + a_0T_2 + q_x''x_2 - C = 0 \quad (18)$$

Setting Eq. (17) equal to Eq. (18) and solving for q_x'' gives the equation used to determine the heat flux per unit area:

$$q_x'' = \frac{\frac{a_1}{2}(T_1^2 - T_2^2) + a_0(T_1 - T_2)}{(x_2 - x_1)} \quad (19)$$

Substitution of this value back into Eq. (17) gives the value of the constant of integration.

Once q_x'' and C have been found, T_s can be determined from Eq. (16) by setting $x = 0$ and solving the equation for T .

2.4 *Previous Research in Turbine Film Heat Release*

The potential effect of heat release in the turbine was studied in Ref. 5. It was found that the potential local rise depends largely on the amount of chemical energy remaining in the flow. Three compositions were defined in the study, defined by the concentration of CO-equivalent present in the flow downstream of the combustor. CO-equivalent is a measure of the total energy available to cause local temperature rise, determined by the sum of energy content in CO, OH, H₂, O, and HC emissions.

In Figure 8 below, the potential local temperature rise is shown as a function of initial mixture temperature and pressure for each of the compositions. Composition 1 represents a fuel streak of $\Phi = 0.5$ in a current era high efficiency combustor. Composition 2 represents the same combustor operating at a lower efficiency. Composition 3 is intended to represent a fuel streak of $\Phi = 1.2$ in a future combustor operating at a stoichiometric fuel to air ratio at a low combustor efficiency. Figure 8 shows that the temperature rise could become large and potentially catastrophic at the high levels of CO-equivalent corresponding to the high fuel-to-air ratio conditions of future combustion systems.

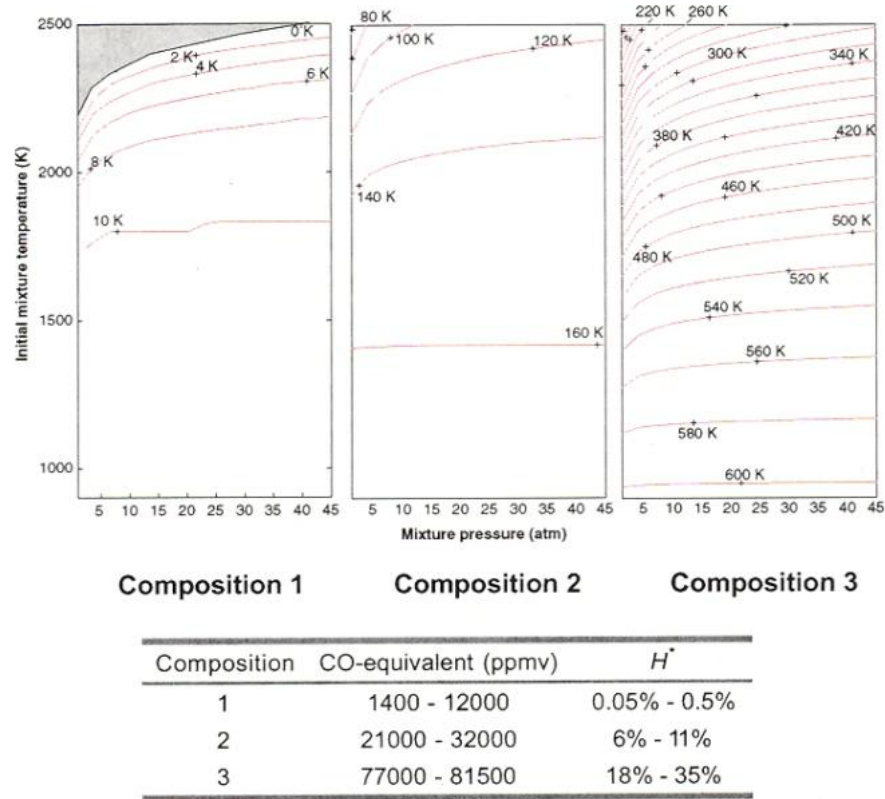


Figure 8. Potential for local temperature increase due to reaction in the turbine

In Ref. 17, a series of shock tube experiments were conducted that examined the impact of near wall reactions in a cooling film. Their experimental setup allowed concurrent heat flux measurements for a reacting (air) coolant flow and nonreacting (N_2) coolant flow through a 35° injection angle into a freestream mixture of ethylene and argon. Blowing ratios in the test ranged from 0.5 to 2.0, for CO-equivalent concentrations ranging from 2000-80000 ppm. Results indicate that at high concentrations of CO-equivalent, as much as 30% increase in heat flux may occur. At moderate CO concentrations, the increase reaches approximately 10%. At low concentrations, the difference between reacting and nonreacting flows is insignificant.

The amount of heat rise that was seen within the scale examined depended on the Damkohler number (Da) of the flow. This nondimensional parameter is defined as the ratio of a characteristic flow time to a characteristic chemical time. As defined in Ref. 17, Da is the amount of time required for the flow to travel a distance of 10 hole diameters, divided by the time for the reaction to reach 95% completion:

$$Da = \frac{\tau_{flow}}{\tau_{chem}} = \frac{10D}{U_{\infty}\tau_{chem95}} \quad (20)$$

The impact of blowing ratio on the heat flux augmentation was significant in their study. In Figure 9, the heat flux is compared for reacting and nonreacting flows at $M = 0.5$, representing an attached jet, and $M = 2.0$, representing a lifted jet. The figure shows the dramatic increase in heat flux caused by the reacting cooling film. Note the peak heat flux augmentation occurs at approximately 10-15 hole diameters downstream of the cooling hole.

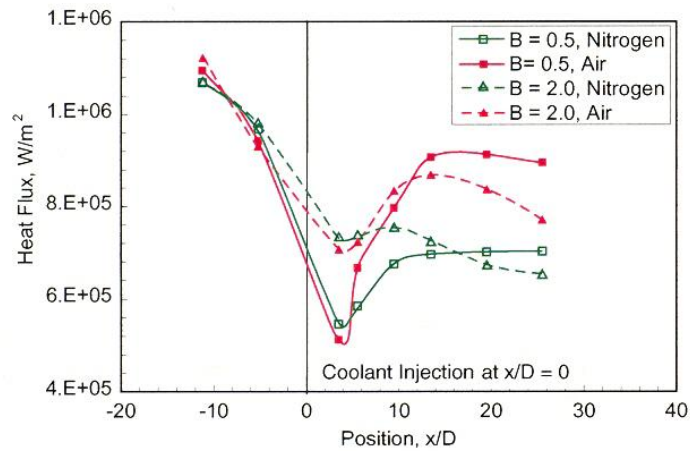


Figure 9. Heat flux for $M = 0.6$ and $M = 2.0$ for reacting and nonreacting cooling jets¹⁷

In Ref. 17, a numerical simulation of the cooling flow was performed that assists in a qualitative understanding of the nature of reacting coolant flows. Figure 10 demonstrates the strong impact of the reaction rate on heat release in the jet. It also shows the difference in the effect of an attached jet ($M = 0.5$) and a lifted jet ($M = 2.0$). H^* is defined as $\Delta H_T/H_T$, where ΔH_T is the potential rise in total enthalpy due to reactions, and H_T is the total enthalpy of the freestream. In Figure 10, the value of H^* indicates that there is a high concentration of energetic species in the freestream.

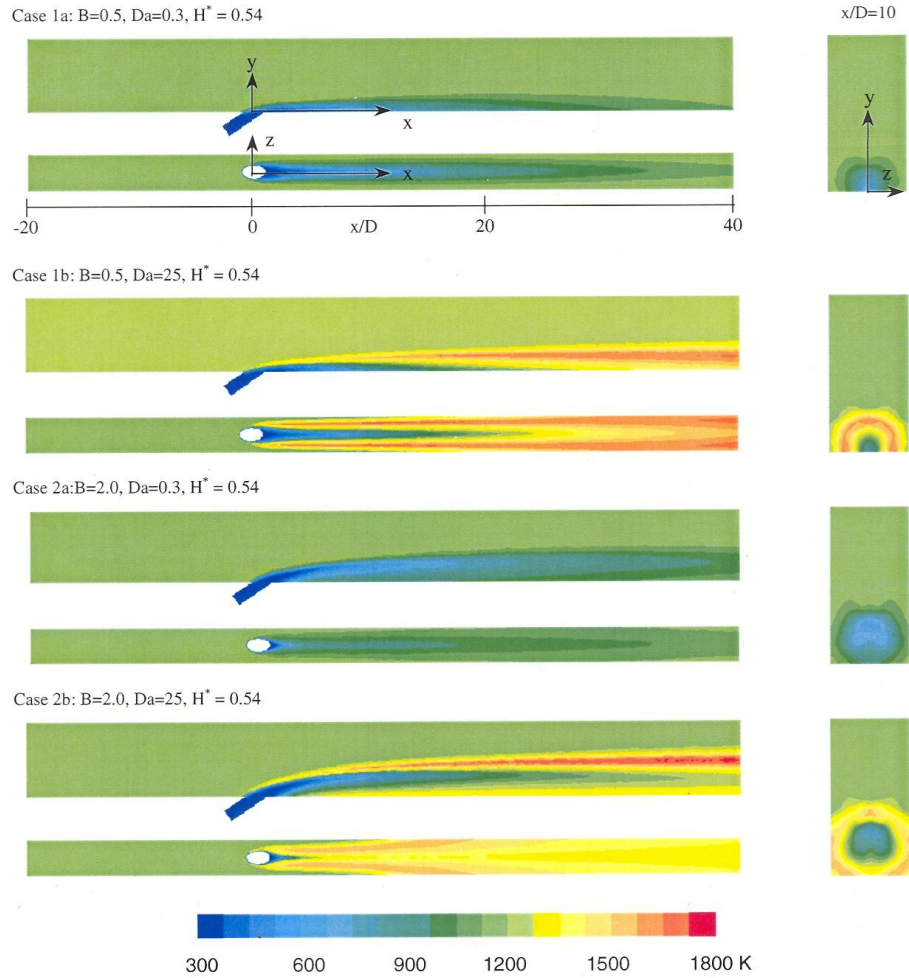


Figure 10. Numerical results of temperature profile of a reacting jet¹⁷, $M = 0.5, 2.0$, $Da = 0.3, 25$

2.5 Estimation of Flow Conditions for Design

Estimates of flow conditions and temperatures of the WSR exhaust flow through the rig were conducted during the design phase. These estimates were used to determine the sufficient trip height and transition distance necessary to ensure a turbulent boundary layer before the flow reaches the cooling holes. The required parameters for the estimation of these parameters are the temperature (T_∞), density (ρ_∞), and viscosity (μ_∞) of the WSR exhaust flow.

The WSR reactor exhaust T_∞ and molecular weight (MW) were calculated for a range of stoichiometric to fuel rich conditions using an equilibrium model¹⁸. The results are given in Table 2.

Table 2. Temperature and MW results of equilibrium calculation

Φ	1.0	1.5	1.6	1.7
T_∞ (K)	2269.2	1977.1	1904.8	1834.7
MW (g/mol)	28.17	25.79	25.33	24.90

The calculation of ρ_∞ follows from the ideal gas law, where R is the universal gas constant, and P_∞ is the pressure of the rig, taken to be a typical value of 0.98 atmospheres.

$$P_\infty = \rho_\infty \frac{R}{MW} T_\infty \quad (21)$$

The value of μ_∞ is taken to be close to air at elevated temperatures, and is estimated using Sutherland's formula, where the subscript 0 represents a reference temperature, and the value 110 K is a constant for air:

$$\frac{\mu}{\mu_0} = \left(\frac{T}{T_0}\right)^{\frac{3}{2}} \left(\frac{T_0 + 110}{T + 110}\right) \quad (22)$$

The Reynolds number is now calculated, where $U_\infty = 100$ m/s, the design velocity of the flow in the test rig.

$$Re_x = \frac{\rho_\infty U_\infty}{\mu_\infty} x \quad (23)$$

The required trip height is estimated from Eq. (24), where k is the trip height:

$$\frac{\rho_\infty U_\infty}{\mu_\infty} k \geq 900 \quad (24)$$

The distance between the trip and the transition point is given by Eq. (25), where x_{tr} is location of the transition point and x_k is the trip location.

$$\frac{\rho_\infty U_\infty}{\mu_\infty} (x_{tr} - x_k) = 2 \times 10^4 \quad (25)$$

The quantities calculated in the preceding equations are summarized in Table 3. From the analysis, the trip size was set as 2.54 mm to be fully effective at all flow conditions. The transition point is upstream of the cooling holes in each case.

Table 3. Estimated Reynolds number, trip height, and transition distance

Φ	1.0	1.5	1.6	1.7
$Re_{x/x} (1/m)$	372000	414000	425000	436000
k (mm)	2.42	2.18	2.12	2.06
$(x_{tr} - x_k)$ (mm)	53.7	48.4	47.1	4.58

2.6 Estimation of Heat Transfer for Design

One design requirement, imposed by the intended use of Thin Film Gauges (TFGs) and High Density Thin Film Gauge arrays (HDTFGs) was maximum allowable T_s of 811 K (see Appendix D for details on TFGs and HDTFG arrays). A one-dimensional steady state heat transfer analysis of the flat plate was performed to determine whether and to what extent active cooling of the plate would be required. Details of the flat plate geometry can be found in Section 3.2.

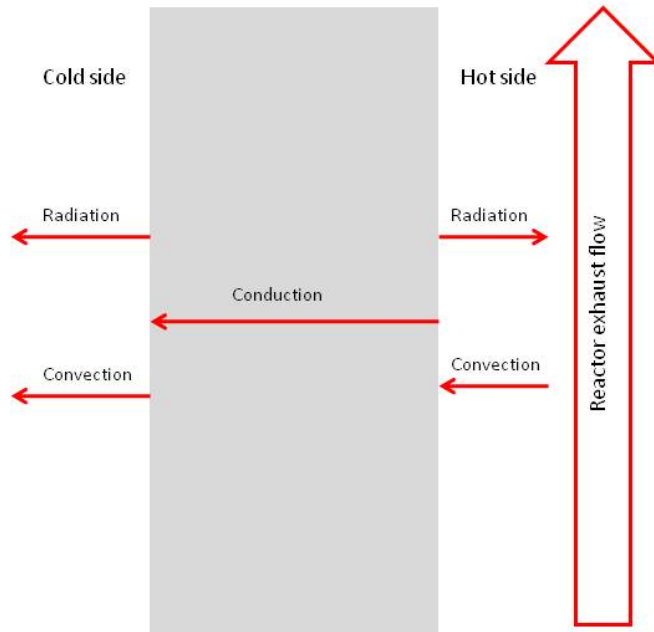


Figure 11. Simplified flat plate heat transfer model

The heat transfer to the plate was assumed to be entirely convective heat transfer for the WSR exhaust flow. Because the flow was intentionally tripped to a turbulent condition, a turbulent heat transfer correlation was used to estimate the convective heat transfer coefficient¹⁵. For a given location, x :

$$Nu_x = 0.0296 Re_x^{\frac{4}{3}} Pr^{\frac{1}{3}} \quad (26)$$

Here, Pr is the Prandtl number and Nu is the Nusselt number:

$$Nu_x = hx/k \quad (27)$$

The correlation for the average Nu over the entire plate is similar:

$$\overline{Nu_L} = 0.037 Re_L^{\frac{4}{3}} Pr^{\frac{1}{3}} \quad (28)$$

The properties used to determine these quantities are interpolated for values given in Ref. 15 at T_f , estimated here as the average of T_∞ and T_s . T_∞ is assumed to be the equilibrium value of at $\Phi = 1.0$. An average h over the entire plate is found from Eqs. (27) and (28), designated $\overline{h_L}$. From this value, the heat flux into the plate is found from Eq. (1). The predicted value of $\overline{h_L}$ is 127 W/m²K for these conditions, which is useful for comparison with experimental results.

Conduction through the plate was estimated assuming a constant thermal conductivity, using Eq. (12) as modified below:

$$q_k'' = \frac{k(T_s - T_c)}{t} \quad (29)$$

In the above equation, T_c is the metal temperature on the cold side of the plate, and t is the thickness of the plate.

The heat lost to radiation is estimated using equation, where ϵ is the emissivity, assumed to be 0.12 based on data for polished nickel in Ref. 15, σ is the Stefan-Boltzmann constant, T is either T_s or T_c , and T_a is the ambient temperature, 298 K.

$$q_r'' = \sigma(T^4 - T_a^4) \quad (30)$$

Heat transfer from the cold side of the flat plate due to convection is treated as free convection. Eq. (1) is used to determine heat flux, after determining h from the following equation¹⁵:

$$\overline{Nu}_L = \frac{\left(\frac{8}{3}\right) Pr^{0.5}}{[336(Pr + 5/9)]^{0.25}} Gr_L^{0.25} \quad (31)$$

The Grashof number, Gr , is an important parameter in free convection, and is defined below¹⁵:

$$Gr_x = g\beta(T_c - T_a)x^3\rho^2/\mu^2 \quad (32)$$

The equations above were balanced and solved using a simple linear solver. The results of this analysis indicated that T_s would be very high, approximately 1600 K, above the melting temperature of Hastelloy-X[®]. Active cooling was therefore included in the design.

Five 6.35mm diameter ducts were machined into the flat plate, at a distance of 3.18 cm from the hot surface of the plate. The number was chosen to provide as nearly uniform heat flux to the plate as possible. The required mass flow of water was found by including the heat transfer per unit length of the cooling water to the energy balance described above, setting T_s equal to the design limit of 810 K, and solving for mass flow. The prediction of heat removed through the cooling water is based on the following equations¹⁵:

$$\overline{Nu_D} = St Re_D Pr \quad (33)$$

In Eq. (33), Nu and Re are based on the diameter of the channels, D . The Stanton number, St , is calculated from the friction coefficient, c_f , in a formula valid for turbulent fully developed pipe flow:

$$St = \frac{c_f/2}{1 + 12.7 (Pr^{2/3} - 1) \sqrt{c_f/2}} \quad (34)$$

Assuming smooth walls, c_f is calculated as follows:

$$(4c_f)^{-\frac{1}{2}} = -1.8 \log_{10} \left(\frac{6.9}{Re_D} \right) \quad (35)$$

Properties for water were taken from Ref. 15. Using the above analysis, it was determined that 0.06 kg/s of water flow would maintain T_c under the design value for all conditions. The facility water supply is able to provide 0.09 kg/s through water cooling channels and associated plumbing, meeting the requirement.

III. Experimental Setup

3.1 *Well Stirred Reactor*

A Well Stirred Reactor (WSR), as developed in Ref. 19 and modified in Ref. 20 and Ref. 21, was used to simulate the turbine entry conditions of a notional combustor. In a WSR, a high rate of mixing of products and incoming reactants is induced. This high rate of mixing results in a very nearly uniform distribution of temperature and species within the reactor and at the exit. Because of the uniformity of the flow at the exit, it is possible to assume a uniform species and temperature distribution at a given distance within the test section.

The reactor is primarily composed of two torroidal half sections of cast zirconia-oxide ceramic, an Inconel[®] jet ring, and a metal housing. A schematic of the WSR is shown in Figure 12. Premixed air and fuel is fed through the fuel-air tubes into the jet ring, into the jet ring manifold, and through 48 fuel air jets into the reactor toroid. The two toroidal half sections fit together on the top and bottom of the jet ring, forming a 250 ml internal volume. Once in the reactor, the fuel-air mixture reacts before exiting through the eight exhaust ports. These ports exhaust into a common exhaust section, which turns the flow upwards into the test section.

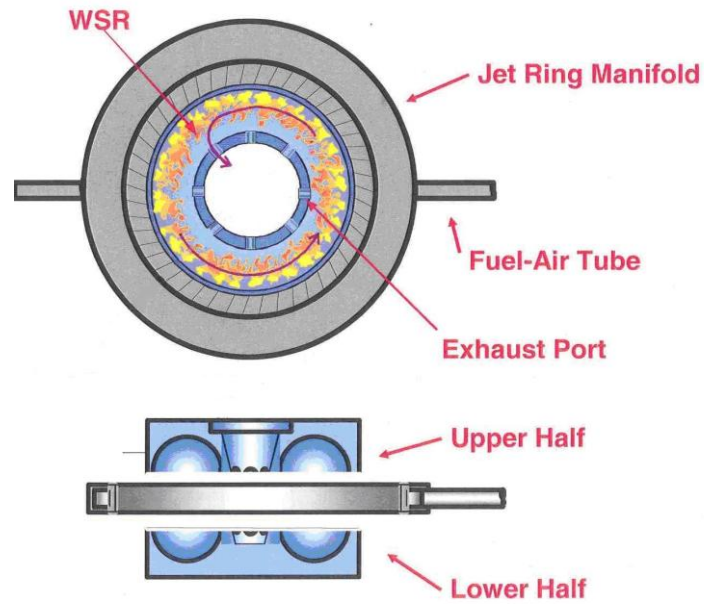


Figure 12. WSR schematic, modified from Ref. 22

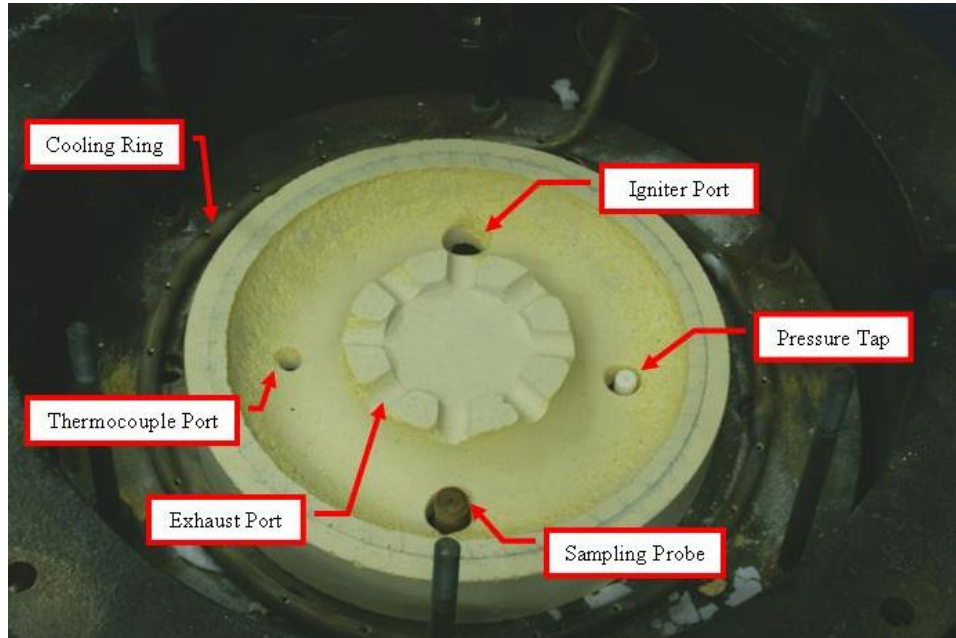


Figure 13. Lower toroidal half section of WSR in housing

The lower half section of the reactor is shown in Figure 13, with additional features highlighted. There are four ports through the bottom of the reactor. A type-B thermocouple is mounted on a stepper motor, allowing the thermocouple to be positioned at a set location within the reactor, or lowered completely out of the reactor. The igniter is mounted on a pneumatic actuator, which allows the igniter to be withdrawn from the reactor once the fuel-air mixture is lit. A ceramic pressure tap and an oil-cooled sampling probe remain in the reactor throughout its operation. A cooling ring surrounds the reactor. Nitrogen flows through the ring and is ejected through a series of holes upward onto the jet ring. This cools the jet ring, and also fills the metal housing with an inert gas.

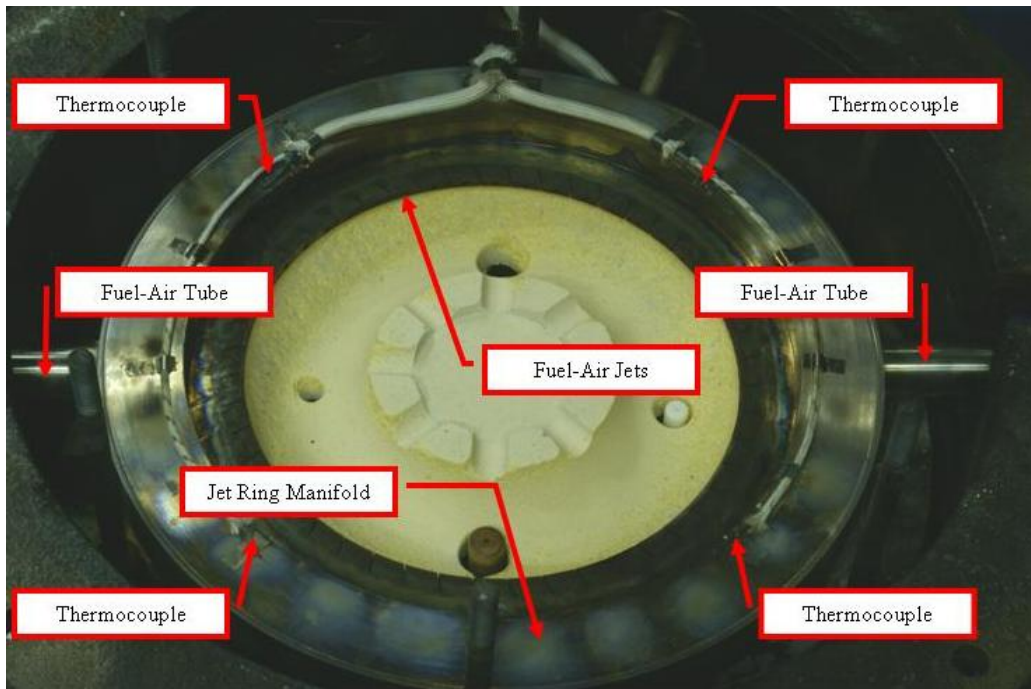


Figure 14. WSR Jet Ring and lower half section

The jet ring fits on top of the lower half-section, as shown in Figure 14. Also shown are the fuel-air tubes, jet ring manifold, and fuel-air jets described earlier. Thermocouples are attached to the jet ring manifold at four locations around the reactor. These serve to monitor the ring for over-temperature, caused by insufficient fuel-air flow through the ring, insufficient nitrogen through the cooling ring, or because of excessive reactor temperature. Rising temperatures on the jet ring manifold, and particularly a wide split between temperatures on different locations on the manifold, could also indicate a crack in the reactor and potential leakage of gases out of the reactor into the reactor housing. In Figure 15, flames are seen originating from reactor cracks, a good indication of WSR failure.

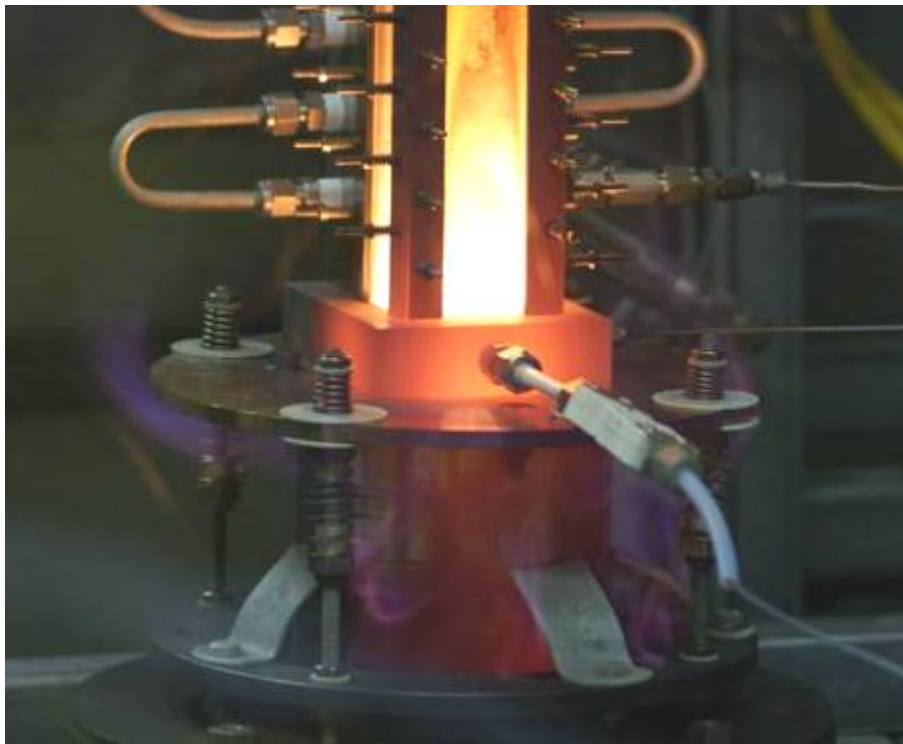


Figure 15. Flames caused by the leakage of gases through WSR cracks

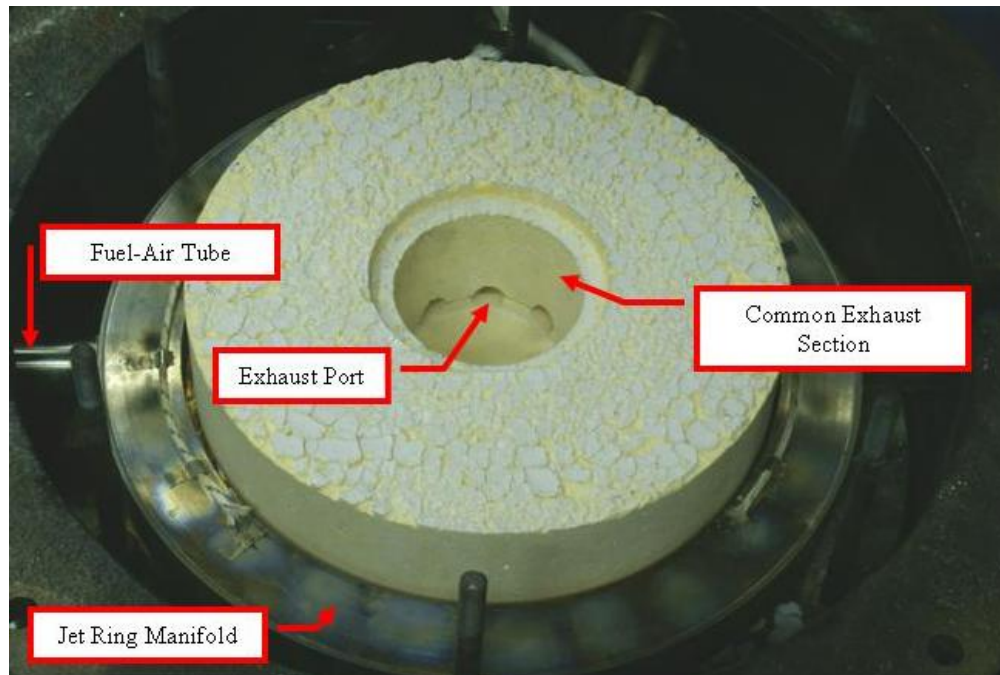


Figure 16. Reactor upper half-section mounted onto jet ring

Figure 16 shows the upper half-section mounted on top of the jet ring and lower half-section. The completed circular exhausts ports and exhaust section are clearly visible. A nitrogen cooling ring, though not shown in Figure 16, is placed over the jet ring, with the holes pointed downwards. Except for the direction of the holes, this ring is identical to the one shown in Figure 13.

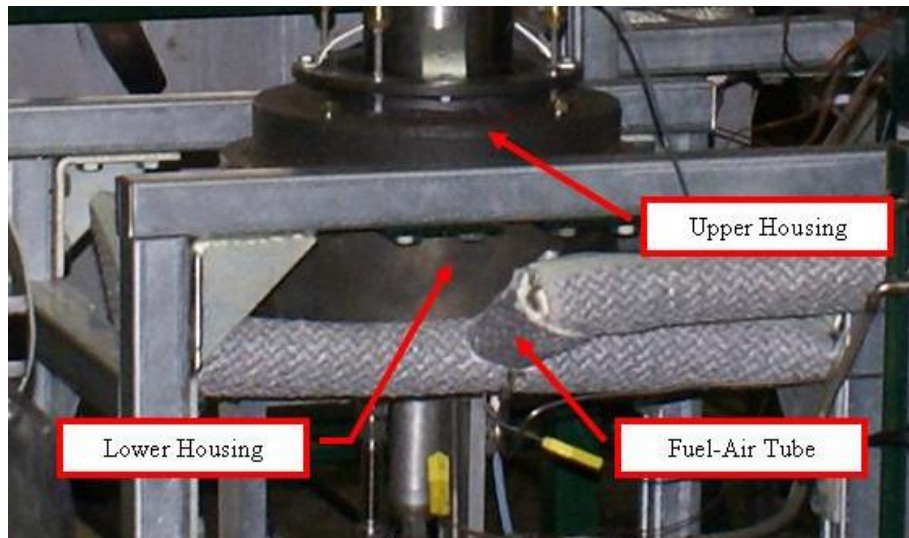


Figure 17. Exterior of WSR, showing upper and lower reactor housing

The exterior of the upper and lower housing is shown in Figure 17. Also visible are the reactor supports and the fuel-air line at the location where it splits to provide the mixture to both sides of the jet ring manifold.

3.2 *Test Rig*

The rig designed for this experiment is a flat plate with necessary modifications to allow cooling air flow, cooling water flow, full laser access to the test section, and temperature and pressure measurements at various locations in the rig. It is made up of a transition section, test section, two cooling air assemblies, four heat transfer gauge assemblies, a window assembly, and an aft plate.

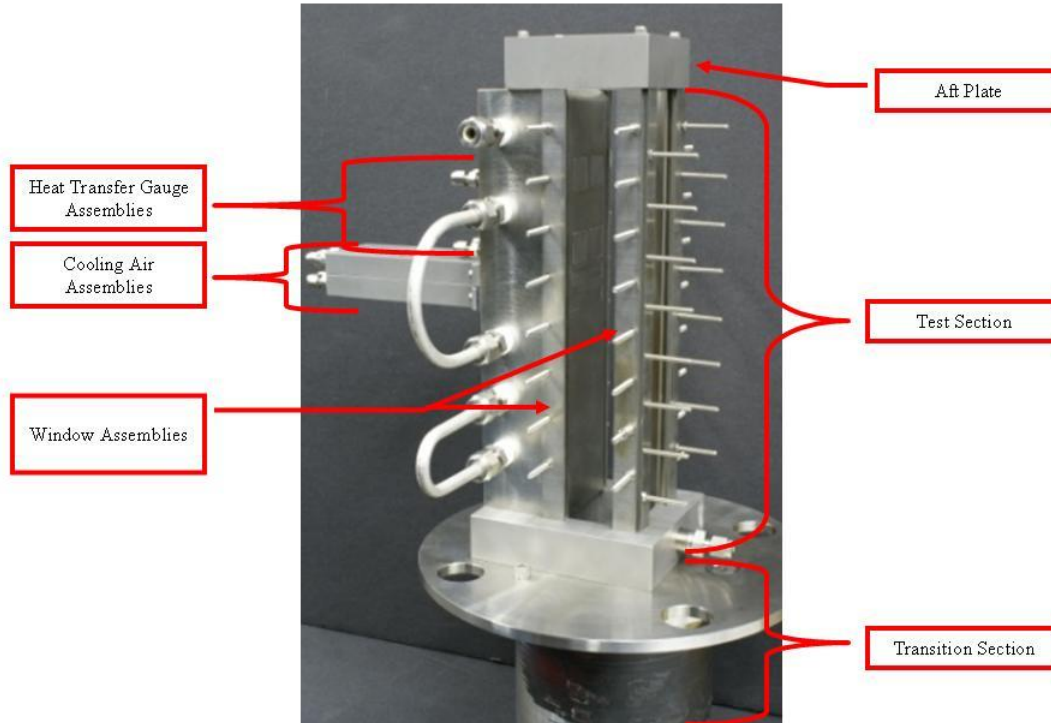


Figure 18. Photograph of Test Rig with sections and assemblies identified

Transition Section

The purpose of the transition section is to smoothly transition the reactor exit flow from a circular exhaust to the geometry of the test section, and to physically support the entire test rig. Even though the exit of the transition section has a smaller area than the inlet, there is an increase in size along some cross sections. Therefore, the transition geometry was designed to prevent the possibility of separation along any cross section. According to the diffuser flow regimes described by Wilson²³, the maximum allowable internal angle in the transition geometry would be 7.5° . To maintain a significant margin above the value at which separation could occur, no internal angle exceeds 4.5° .

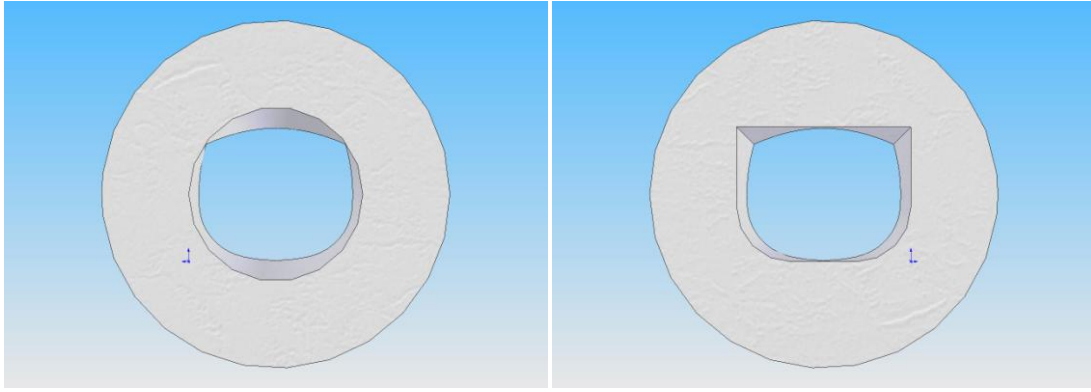


Figure 19. Views of transition geometry from reactor exhaust (left), and test section inlet (right)

The transition geometry was machined into a stack of six 8.9 cm diameter, 2.5 cm thick high density zirconia-oxide discs (Figure 20). Zirconia was chosen because it is easily machined, is an excellent insulator, and can withstand the high temperatures this experiment demands. The stack is aligned using thin zirconia-oxide tubes (metal tubes shown in the picture), then inserted into a 15.2 cm zirconia-oxide cylinder of lower density. The entire assembly is then inserted into a 15.2 cm Hastelloy-X[®] pipe with a 15.2 cm diameter flange to provide structural strength and a means of attaching the chimney to the test section. The assembled transition section is shown in Figure 21.

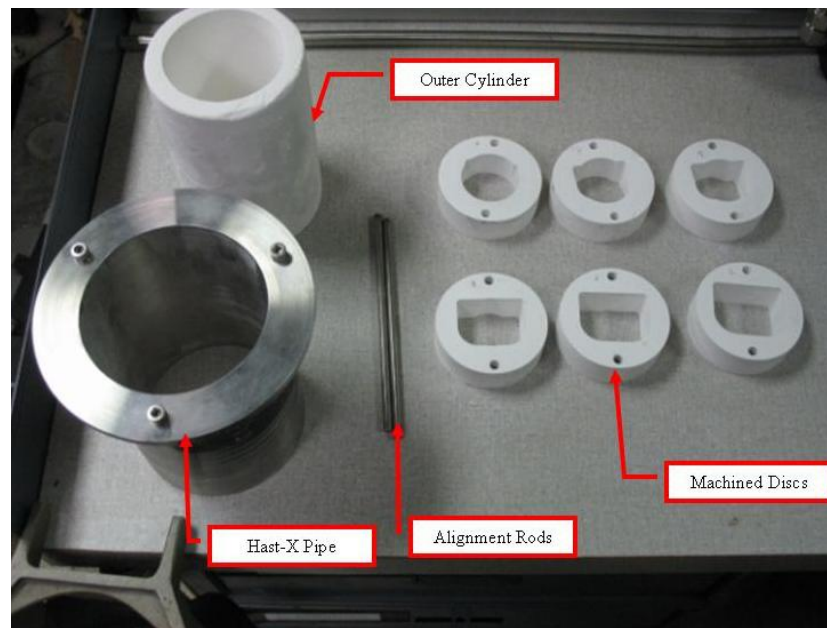


Figure 20. Components of transition section

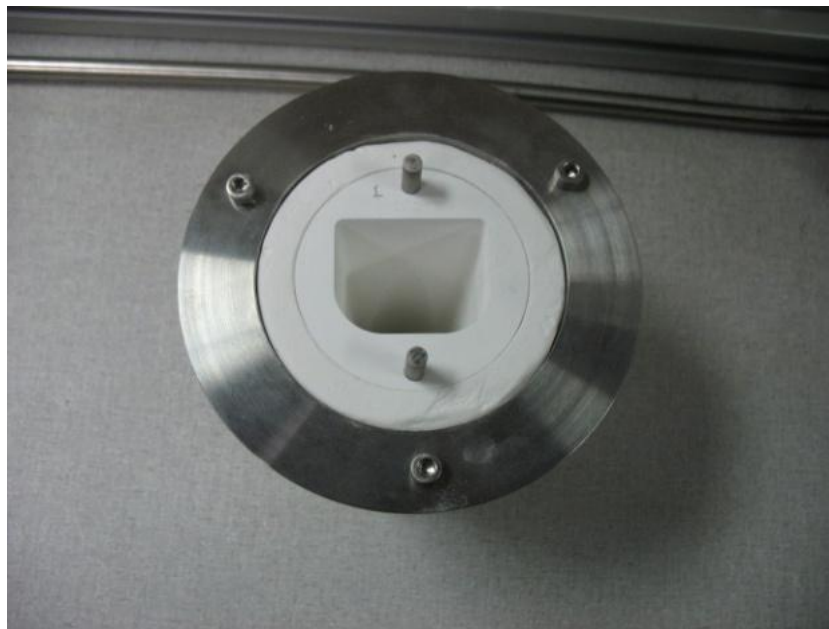


Figure 21. Assembled transition section

The mounting plate is a 30.5 cm diameter Hastelloy-X[®] disk (Figure 22). The shaped hole in the center of the disk matches the geometry of the exit of the transition section. Holes are drilled to provide attachment to the instrument block and flat plate of the test section, and the pipe flange of the transition section.



Figure 22. Mounting Plate

The large holes at the exterior diameter allow the attachment of the mounting plate to the WSR shell using spring-supported rods (Figure 23). The lower springs allow the WSR housing to support most of the test rig weight, while maintaining contact between the WSR exit and the transition section. The upper springs allow for the thermal expansion of the transition section without putting excessive stress on the WSR. Also shown in Figure 23 are the positioning braces, which ensure that the transition section is aligned with the WSR exhaust flow.

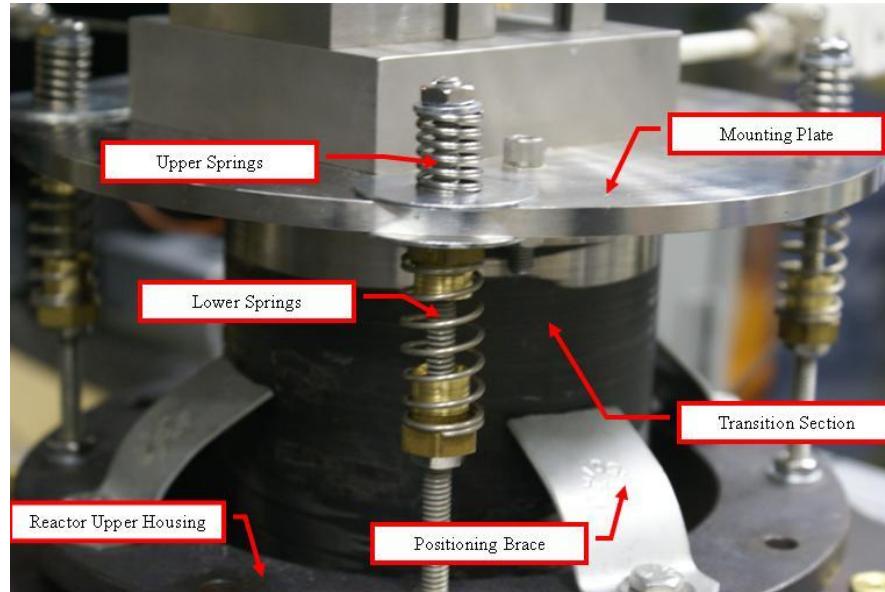


Figure 23. Hardware Connections between mounting plate and WSR upper housing

Test Section

An instrument block (Figure 24) is connected to the mounting plate and is intended to provide instrument access to the reactor flow at the inlet of the test section. It is also constructed of Hastelloy-X[®]. Holes are drilled to accept fittings for static pressure measurements and a type-B thermocouple assembly. The instrument plate also serves to anchor the window rails of the window assembly.

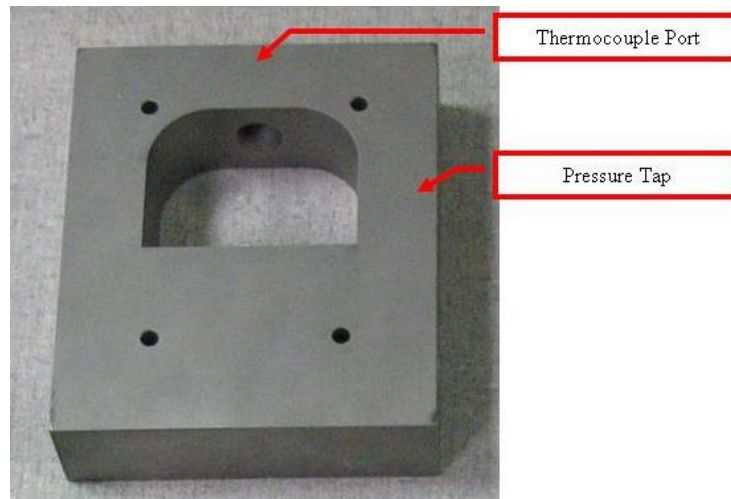


Figure 24. Instrument Block

At the joint between the instrument block and the flat plate, a 2.5 mm forward facing step was allowed. During design, it was intended that the experiment take place over a wide range of Reynolds numbers. Because of this, transition of the boundary layer to a turbulent state was predicted to occur at various locations along the flat plate. To negate the interference of an undetermined boundary layer transition region on the experimental measurements, a trip was implemented that would ensure a turbulent boundary layer state exists at the cooling air inlet at all flow conditions. See Section 2.5 for details on the calculations.

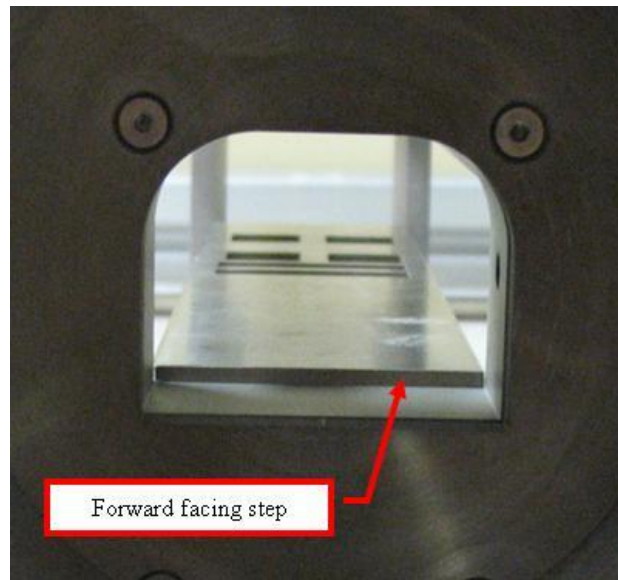


Figure 25. Forward facing step at connection of instrument block and flat plate

The flat plate (Figure 26) was machined from a solid piece of Hastelloy-X[®] of 22.9 cm length, 5.1 cm width, and 5.1 cm depth. Slots have been machined in the piece to allow for the insertion two cooling air assemblies and four heat transfer gauge assemblies. Each of these assemblies is inserted through the back of plate, with their surfaces flush with the surface of the plate. Grooves have been machined along both lengths of the plate and holes have been drilled to allow for windows and window rails. A static pressure tap is located just forward of the first cooling hole assembly slot.

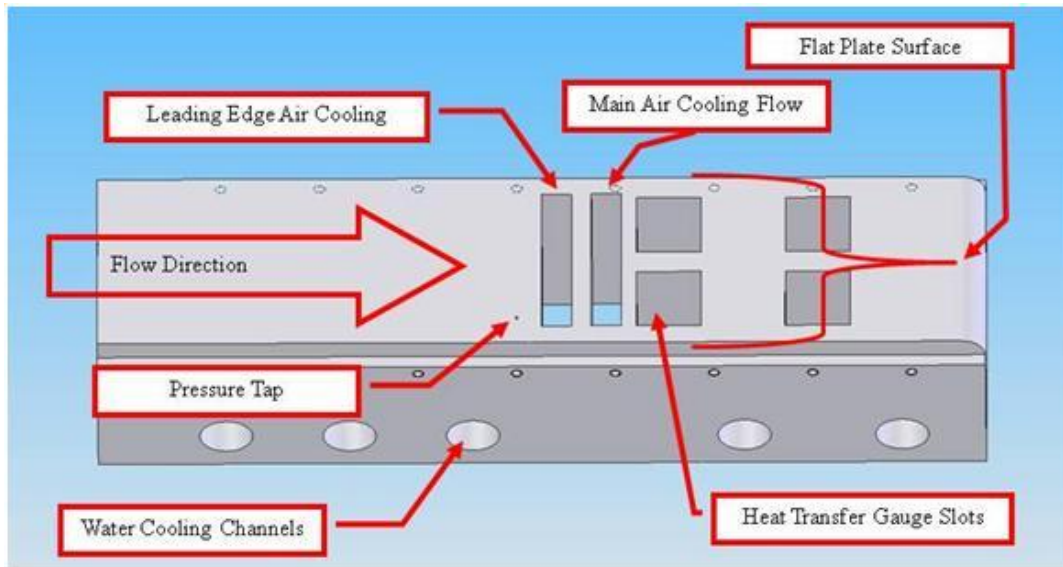


Figure 26. Flat plate design

Water cooling channels were machined in the flat plate. There are five channels, 6.4 mm diameter, located at the positions shown in Figure 26. The channels are connected in series, as shown in Figure 27, to the facility water supply. The flow rate of the water is controlled by a rotometer with a needle valve up to 0.09 kg/s. A type K thermocouple is located in the outlet from the flat plate to monitor the temperature of the water.

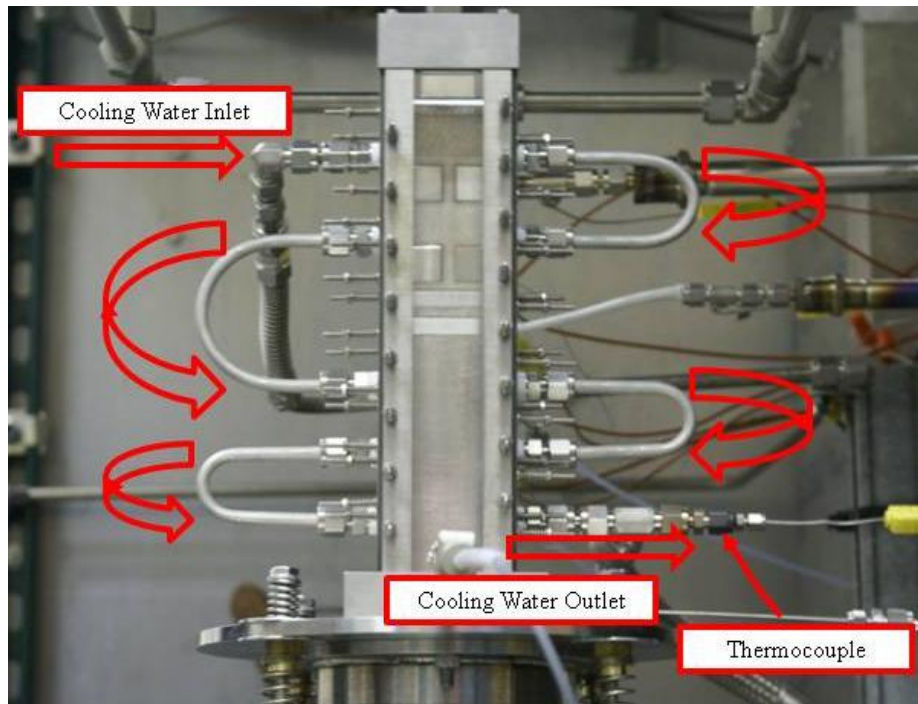


Figure 27. Cooling water connections and flow direction

Cooling Air Assembly

The cooling air assemblies are made up of the cooling hole slot inserts and the plena. Cooling air or nitrogen is fed to the plena from the facility supply. In the plena, the cooling air temperature and pressure are measured. The plena are attached to the cooling hole inserts and sealed with a high temperature adhesive sealant, as shown in Figure 28. Thermocouples were inserted to a location 5.1 mm from the outside surface of the cooling hole inserts. The thermocouples were shielded from contact with the wall of the inserts by a ceramic tube, which was held in place by spot-welded shim stock. In Figure 28, one of the plenum has two thermocouples of different sizes. This setup was used on a single experiment to rule out any effect of radiation on the thermocouple measurement. There was no significant difference in measurements, so the single thermocouple setup was

used. The cooling air assemblies are inserted through the back of the flat plate. A single assembly is shown inserted in the flat plate in Figure 29.

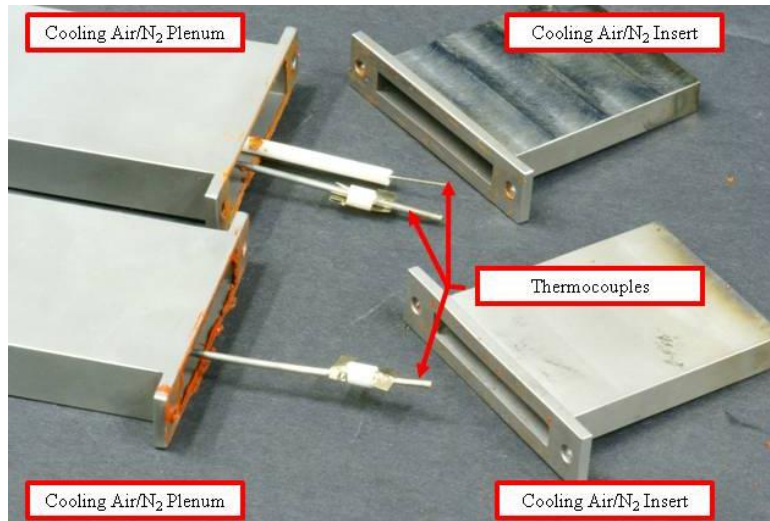


Figure 28. Plena and cooling air insert, with thermocouples installed

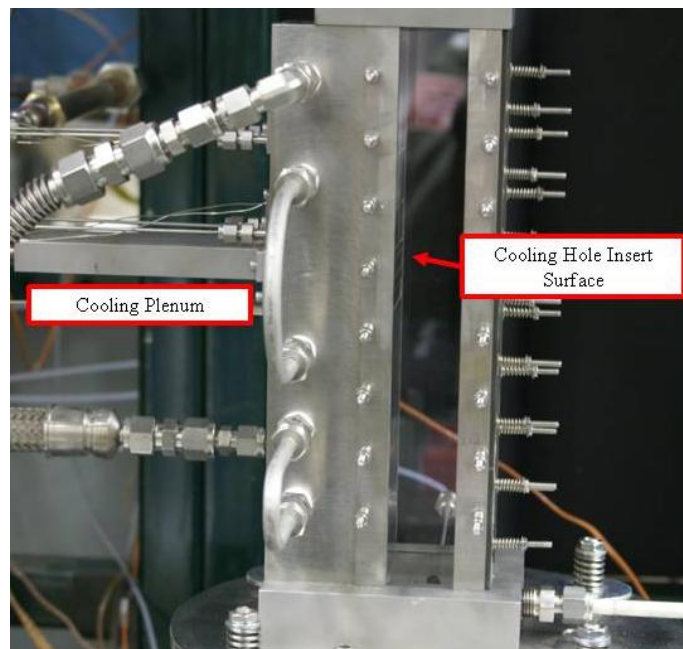


Figure 29. Cooling Air Assembly inserted into flat plate

The cooling hole geometries are machined into the surface of the inserts. There are six different insert geometries that were manufactured: normal holes, two rows of offset normal holes, angled holes, fan-shaped laidback holes, angled slot, and a solid blank (Figure 30).

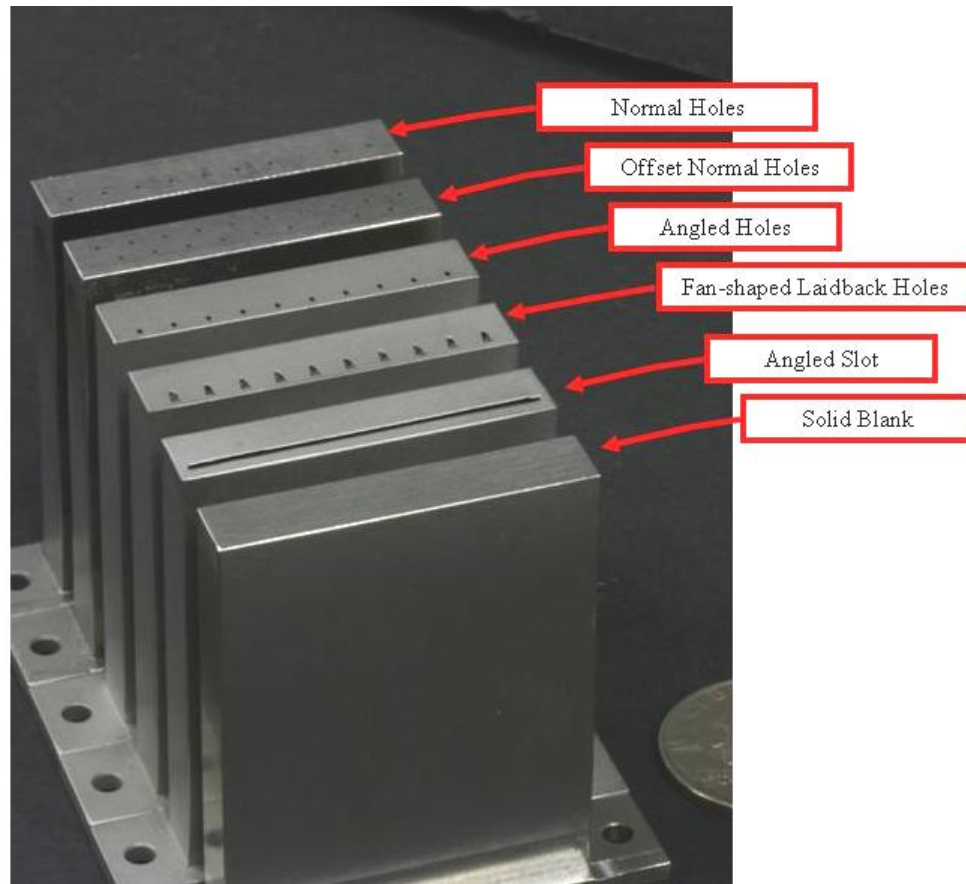


Figure 30. Cooling insert geometries

The normal holes are 0.51 mm diameter machined perpendicularly through a 2.54 mm surface, giving a hole length to diameter ratio (L/D) of 5. The spacing between the holes is 3.81 mm. The offset normal hole geometry is identical to the normal hole geometry, except for the additional row of normal holes, offset from the first row. The

angled holes are also cylindrical holes of 0.51 mm diameter, but are machined at an angle of 30° to the surface. To maintain an L/D of 5, the surface is necessarily thinner, 1.27 mm. The fan-shaped laidback holes are based on the angled hole geometry, being equal in size, angle, and depth. However, at the surface that sees the flow, the sides of the hole flare out 10° . There is also a 10° layback, as pictured in Figure 31.

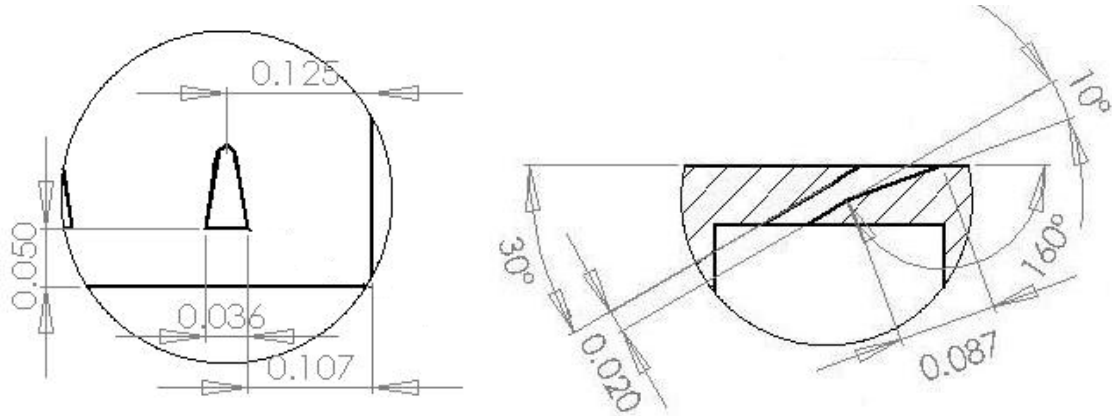


Figure 31. Drawing detail of fan-shaped laidback cooling hole geometry (inches)

The surface of the angled slot geometry is 1.27 mm, to match the angled hole geometry. The insert is intended to be placed into the upstream cooling hole slot of the flat plate. It could either be used to introduce a flow of nitrogen to protect the sensitive downstream Thin-Film Gauges, or be used to simulate the showerhead cooling flow of a notional turbine blade. If the slot flow is not being used, the solid blank insert is used instead. The slot was not used in the current study, but will be used in the follow-on research.

Heat Transfer Gauge Assembly

The heat transfer gauge assemblies are made up of a heat transfer gauge block and mount. The gauges are inserted through the back of the flat plate so that the surface of the heat transfer gauge block is flush with the surface of the flat plate in the test section. The mounting plate attaches the block to the back side of the flat plate, and is designed to allow the block to be instrumented. The assemblies are modular, and are interchangeable in the rig.

The heat transfer gauge block is instrumented with two thermocouples. A near-surface thermocouple passes through the mount and along a channel cut in the side of the block. It is inserted 11.7 mm into a close-fitting hole that is 3.8 mm from the surface of the block (Figure 32). A second thermocouple is inserted through the bottom of the block to a depth of 19.1 mm from the surface. The thermocouples are at different depths, but the same location measured along the surface. For the two upstream gauges, the thermocouples are 10.4 mm downstream of the cooling holes (approximately 20 hole diameters). The downstream gauges are 38.4 mm downstream (approximately 75 diameters). The mounting of the heat transfer gauges on the flat plate and the installation of thermocouples is shown in Figure 33. The surface of the flat plate with all inserts installed is shown in Figure 34. The heat transfer gauge blocks are identified in the Chapter IV as shown in the figure.

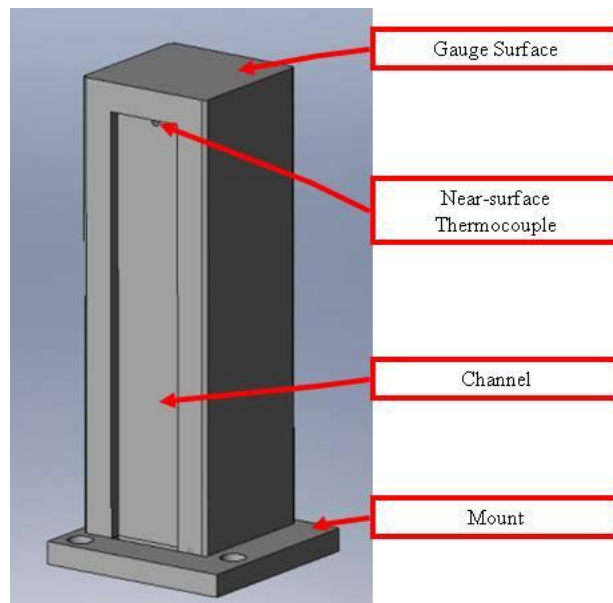


Figure 32. Heat Transfer Gauge Block

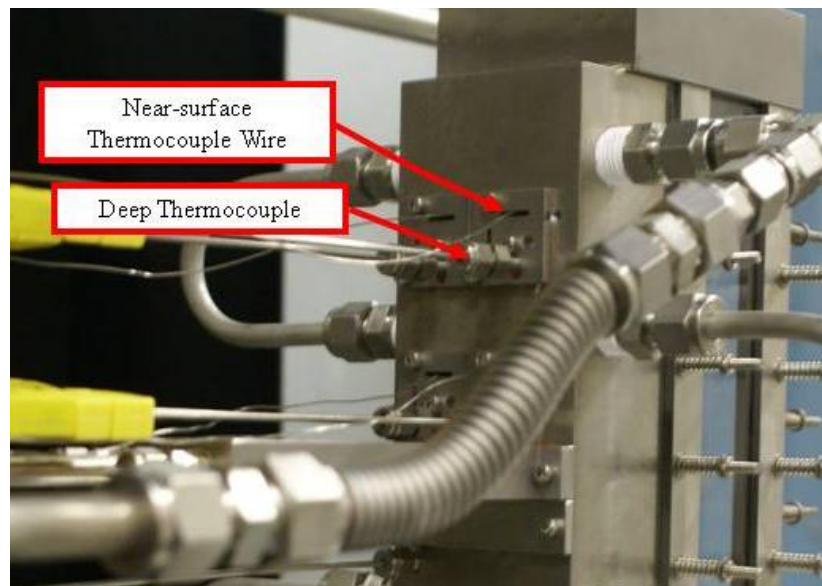


Figure 33. Heat transfer gauge block mounting and thermocouple installation

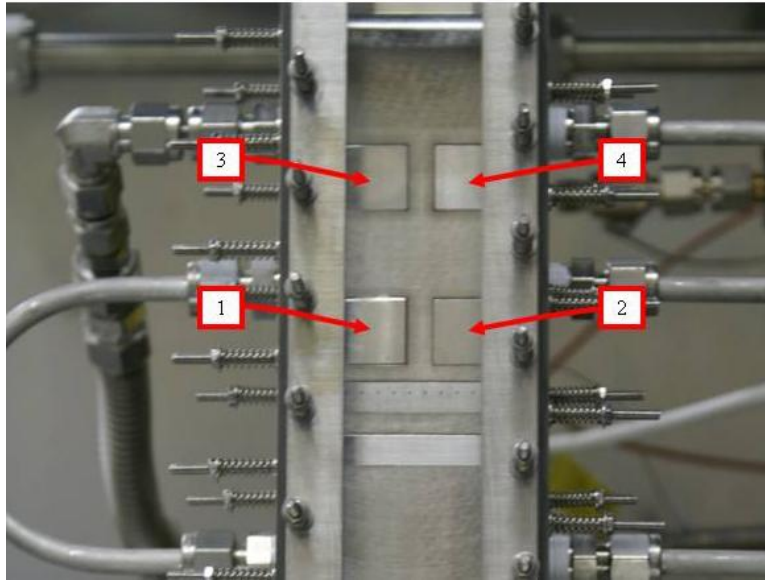


Figure 34. Heat transfer gauge numbering convention

Window Assembly

The window assembly consists of window rails and window frames, machined from Hastelloy-X[®], as well as elements machined into the flat plate, the aft plate, and the instrument block. The rails are held in place by screws attached to the aft plate and instrument block. The screws on the instrument block are spring mounted, to allow for a larger thermal expansion in the rails than the flat plate (Figure 35). The window frames hold the windows in place against the rails or flat plate. The frames are pressed against the windows by spring mounted nuts on threaded rods. These springs allow expansion to occur with excessive stress on the windows. The windows are made of fused quartz. They allow laser and optical access to the test section from three directions.

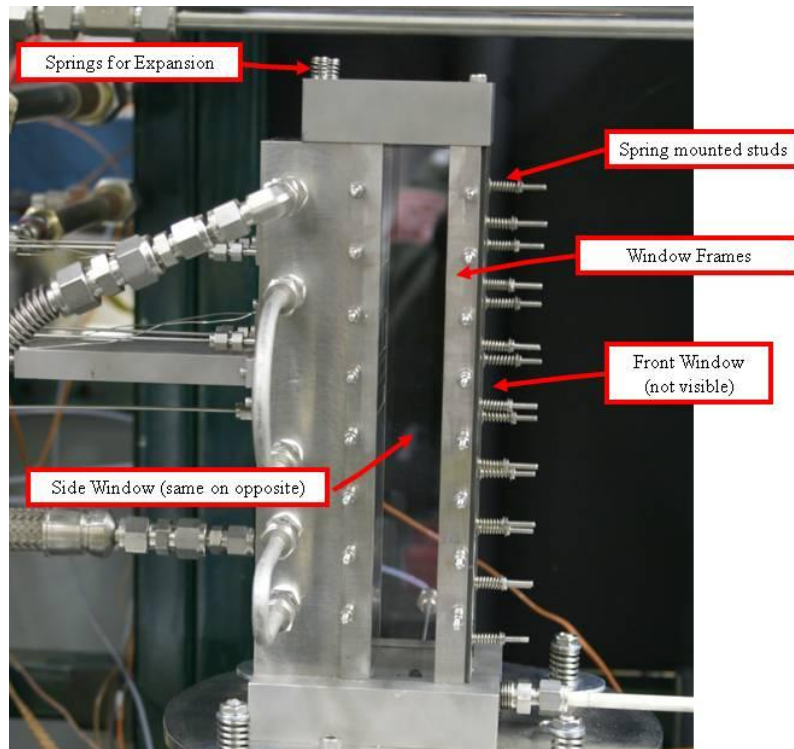


Figure 35. Test rig view highlighting elements of the window assembly

Aft Plate

The aft plate serves to shape the exhaust flow and to anchor the window rails. The area of the passage through the aft plate reduces, causing a slight pressure increase. This prevents the leakage of fresh air into the rig, protects external components, and pushes the exhaust up and away from the exit of the rig. Figure 36 illustrates the flow of fuel-rich reactor exhaust after passing the aft plate.

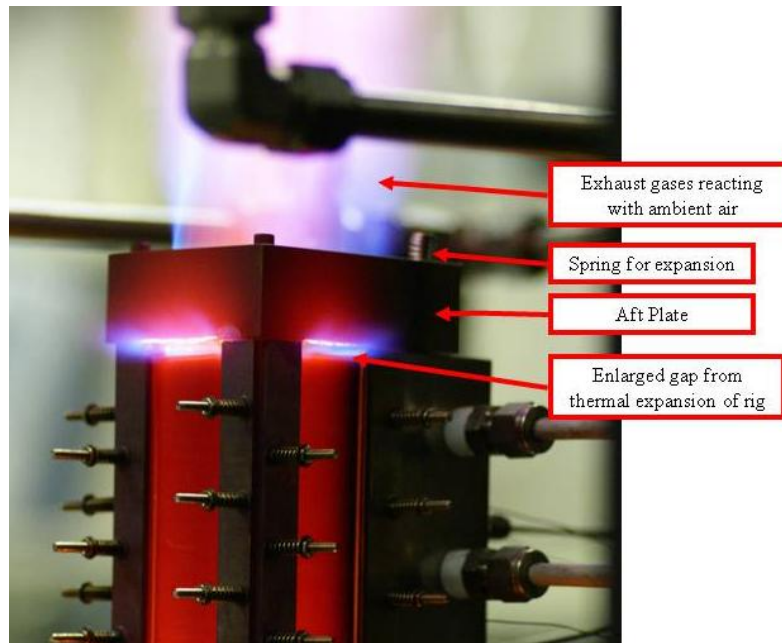


Figure 36. Flow of fuel-rich exhaust leaving the test rig

3.3 *Facility Fuel, Air, and Nitrogen Supply and Control*

The WSR was supplied with propane fuel, air, and nitrogen for the experimentation. The test section was supplied with air and nitrogen. A schematic for the gas supply system is given in Figure 37. Nitrogen is taken from the facility supply, and serves a variety of purposes. It is supplied through a metering valve to the WSR cooling rings (refer to Figure 13) in order to provide cooling to the jet cooling rings, and to flood the WSR housing to protect the reactor in case of a fuel/air leak. Nitrogen is also supplied and controlled through a thermal mass flow controller to the combustion air in order to act as a dilutant. This lowers the WSR temperature, preventing over-temperature when transitioning between fuel-rich and fuel-lean conditions.

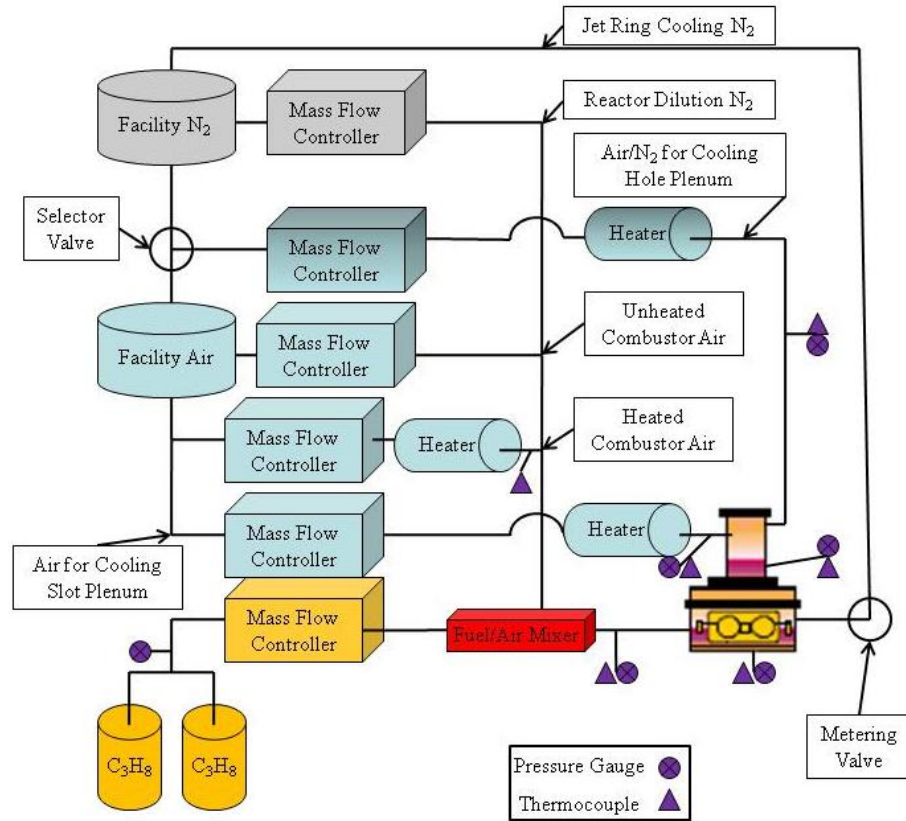


Figure 37. Fuel, air, and nitrogen supply system schematic

Air is provided from the facility compressed air system. The unheated combustion air passes through a thermal mass flow controller, into the fuel-air mixer, and into the WSR. The heated combustion air passes through a thermal mass flow controller then through an electric heater before joining the unheated air just prior to the fuel-air mixer. The heated air is used during startup, aiding light-off in the WSR. Air is also provided to the upstream cooling slot plenum. It passes through a mass flow controller, through an electric heater, then into the cooling slot plenum, where pressure and temperature are measured. From the plenum, air passes through the cooling slot into the test section.

Nitrogen and air are both supplied to the manually operated selector valve that controls the gas source for the cooling hole plenum in the test rig (refer to Figure 29). The selected gas (air or nitrogen) passes through a mass flow controller, a heater, and into the cooling air plenum, where pressure and temperature are measured. From the plenum, the selected gas passes through the cooling holes and into the test section.

The propane fuel is contained in 100-lb (45.4 kg) tanks located outside of the test cell (Figure 38). To ensure the propane boils quickly enough to provide the flow rates required in this experiment, the tank is heated by belt heaters. Gaseous propane flows through the shutoff valve into a manifold, allowing several tanks to supply fuel concurrently. The fuel passes through a regulator, through a shutoff valve at the facility entrance, and to a thermal mass flow controller. Managing the temperature and pressure of the propane at the tank is critical, because of the large pressure drops in the fuel supply system. Condensation of the fuel in the lines resulted in unsteady performance of the mass flow controllers. The propane and combustion air join just upstream of the fuel/air mixer.

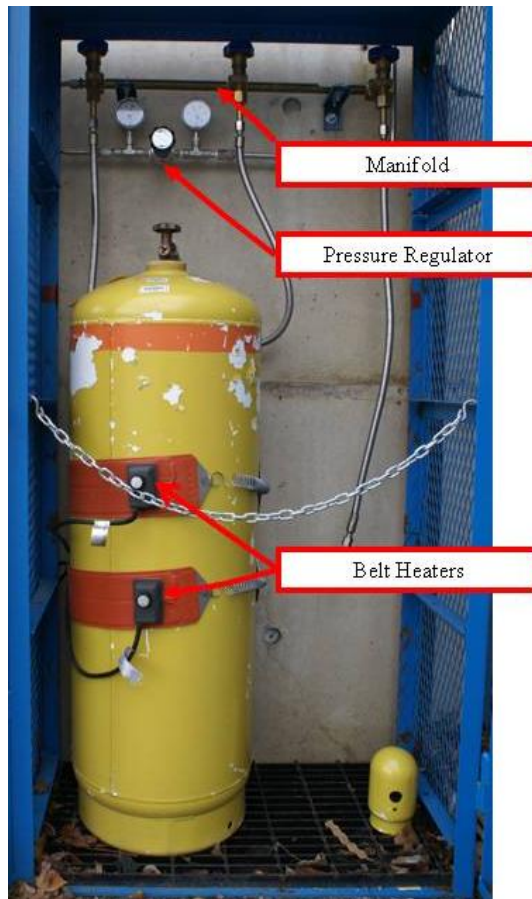


Figure 38. Propane tank, heaters, and regulator

The majority of the controls used in the fuel, air, and nitrogen supply system is managed from the control panel pictured in Figure 39. The measured signals from the mass flow controllers (4-20 mA) are processed by the data acquisition system and displayed in LabView. The mass flow controller for the cooling hole air/nitrogen flow is shown in Figure 40, and is not tied into the data acquisition system.

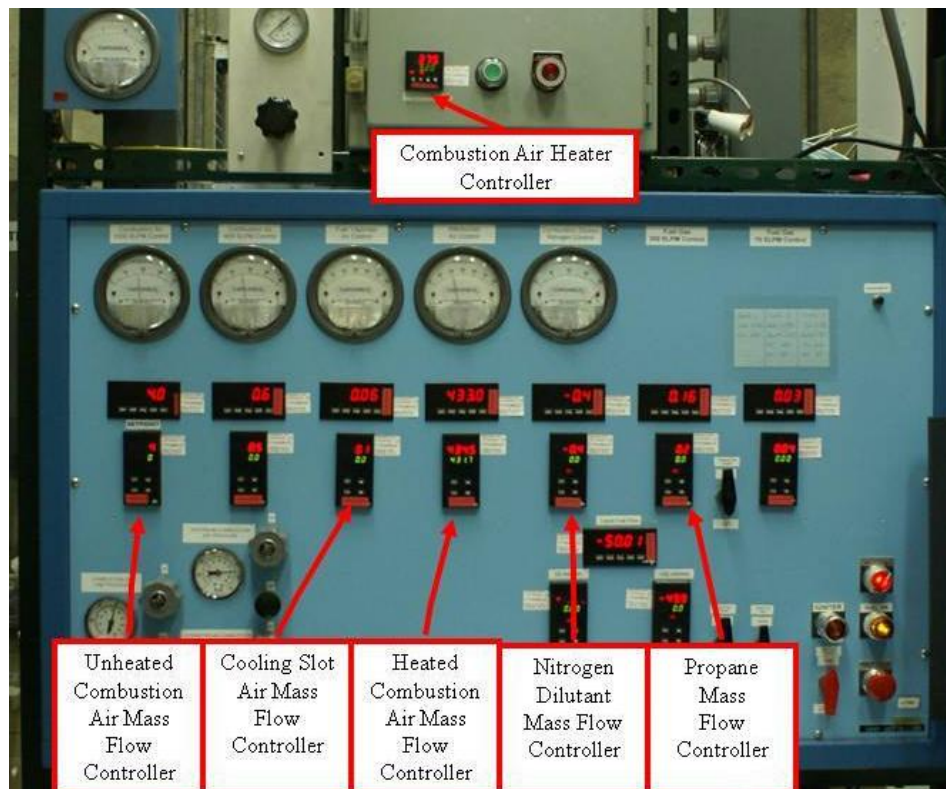


Figure 39. Control panel for fuel, air, and nitrogen supply system



Figure 40. Mass flow controller for cooling hole air/N₂ flow

3.4 Chemical Sampling

To determine the chemical composition of the reactor flow, an emissions sampling probe is installed in the WSR (see Figure 13). The probe is cooled by a circulating oil heater/chiller. The emissions samples are transported to a series of emissions analyzers through heated sampling lines. Total unburned hydrocarbons are measured in a heated Flame Ionization Detector (FID) analyzer. The rest of the sample is then dried and routed to additional analyzers, which determine concentrations of CO, CO₂, NO_x, and O₂.

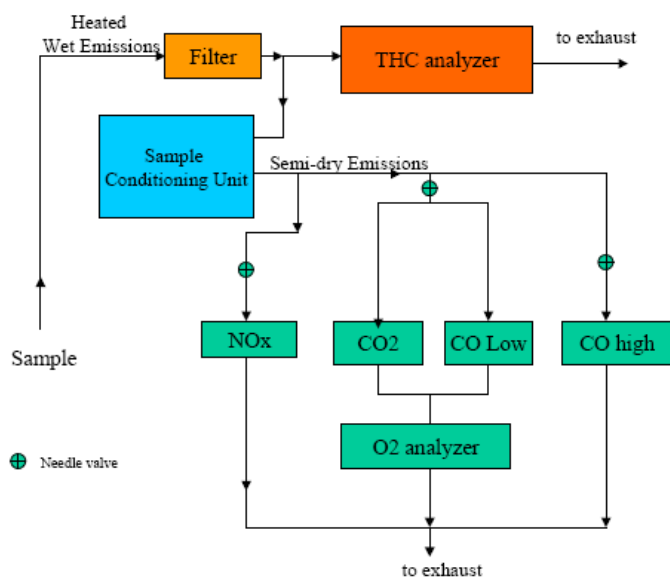


Figure 41. Sampling train for gaseous emissions measurements, modified from Ref. 22

3.5 Instrumentation and Data Acquisition

Data from thermocouples, pressure transducers, mass flow controllers, and chemical sampling equipment are routed to a National Instruments card/chassis and are fed into LabView software. A screenshot of the LabView setup used in this study is presented in Figure 42. Pressure measurements are taken at a number of locations in the rig, as summarized in Table 4. Thermocouple types and locations are listed in Table 5.

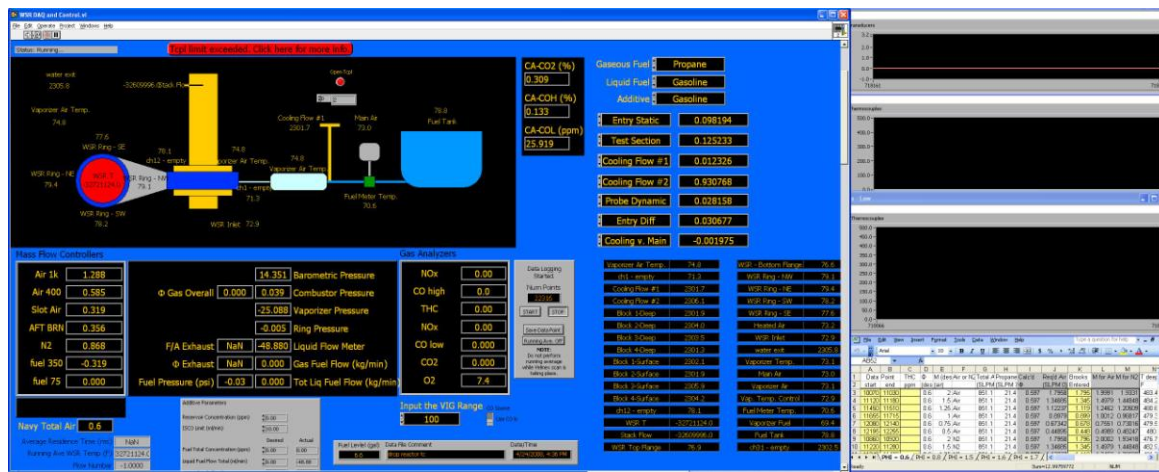


Figure 42. Labview screenshot

Table 4. Pressure transducers and locations

Transducer Name	Transducer Location
Entry Static	Instrument block
Test Section Static	Prior to cooling inserts
Cooling Flow #1	Downstream cooling hole plenum
Cooling Flow #2	Upstream cooling hole plenum

Table 5. Thermocouple locations and types

Thermocouple Name	Thermocouple Location	Thermocouple Type
Stack Temperature	Instrument block	B
Water Exit Temperature	Cooling water outlet	K
Cooling Flow #1	Downstream cooling hole plenum	K
Cooling Flow #2	Upstream cooling hole plenum	K
Block #1 Surface	Near-surface thermocouple in heat transfer gauge block #1	K
Block #2 Surface	Near-surface thermocouple in heat transfer gauge block #2	K
Block #3 Surface	Near-surface thermocouple in heat transfer gauge block #3	K
Block #4 Surface	Near-surface thermocouple in heat transfer gauge block #4	K
Block #1 Deep	Sub-surface thermocouple in heat transfer gauge block #1	K
Block #2 Deep	Sub-surface thermocouple in heat transfer gauge block #2	K
Block #3 Deep	Sub-surface thermocouple in heat transfer gauge block #3	K
Block #4 Deep	Sub-surface thermocouple in heat transfer gauge block #4	K

IV. Results

4.1 Test Plan and Procedure

Prior to light-off for each reactor run, a series of steps are required. Approximately one hour before light-off, a heated airflow is initiated through the reactor. This brings the reactor temperature to 420 K, easing ignition difficulties. The electric belt heaters are applied to the propane tanks until sufficient pressure is available to provide the required flow. Several minutes prior to light-off, the sampling probe oil heater/chiller, test rig water supply, and N₂ flow to the cooling hole plenum are turned on. Instruments and the data acquisition system are initiated and checked, and facility safety checks are completed.

Once the preparatory steps are complete, \dot{m}_{air} is set to 220 g/min and propane flow is initiated to the WSR. The igniter is activated while \dot{m}_{fuel} is being increased. Typically, the WSR lights off at $\Phi = 0.9$. The WSR is allowed to warm up for approximately one half hour before increasing the mass flow.

If the desired test condition is in the fuel-rich regime (Figure 43), N₂ dilution flow is added to the reactor to limit the peak temperature while passing through the stoichiometric condition. Fuel flow is rapidly increased to $\Phi = 1.5$. The WSR is allowed to stabilize in this condition before increasing mass flow. The reason that a dilutant is used to lower peak temperatures is that close to $\Phi = 1$, the temperature of the gases is above the maximum allowable for the thermocouples that monitor conditions in the WSR.

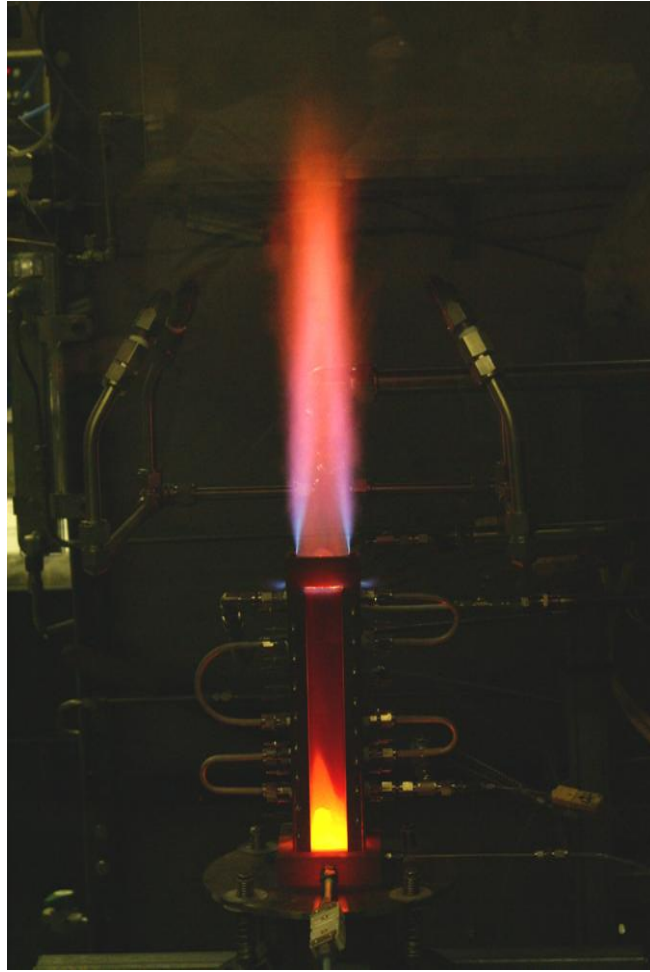


Figure 43. WSR operation in the fuel-rich regime

The WSR test condition is set by slowly raising the mass flow rates of fuel and air concurrently to maintain a steadily increasing reactor temperature. The temperature is limited to 1970 K by the type-B thermocouples in the WSR and test section inlet. A WSR test condition as used in this experiment is a specific combination of the mass flow rate of air and Φ resulting in a desired chemistry and reactor temperature. Each of the cooling hole geometries was tested at several WSR test conditions. These conditions are listed in Table 6. It was discovered during experimentation that the mass flow rate into the reactor

was limited at high temperatures due to an unacceptable rise in WSR pressure. Therefore, the near stoichiometric WSR reactor test condition was set at a reduced \dot{m}_{air} .

Table 6. Cooling hole geometry and WSR test conditions

Hole Geometry	Φ	\dot{m}_{air} (g/min)	\dot{m}_{fuel} (g/min)
Normal	0.6	1020	40.5
Normal	0.8	1020	54.0
Normal	1.5	1020	101.2
Normal	1.6	1020	108.0
Normal	1.7	1020	121.5
Angled	0.6	1020	40.5
Angled	0.8	1020	54.0
Angled	1.5	1020	101.2
Angled	1.6	1020	108.0
Angled	1.7	1020	121.5
Fan-shaped	0.6	1020	40.5
Fan-shaped	0.8	1020	54.0
Fan-shaped	1.5	1020	101.2
Fan-shaped	1.6	1020	108.0
Fan-shaped	1.7	1020	121.5
Normal	0.95	720	45.2
Angled	0.95	720	45.2
Fan-shaped	0.95	720	45.2

Once the WSR test condition is set, a cooling gas (air or N₂) is selected. A value of M is selected, and the required volumetric flow rate of cooling gas is calculated from Eq. (10). The thermocouple readings (test section inlet, WSR, and heat transfer gauge thermocouples) are monitored using a strip chart. Once these readings reached steady state, a sixty second average is taken of all measurements available to the data acquisition system, and the volumetric flow rate of the cooling gas and the data point indices are recorded. A new cooling gas or M value are selected, and the cycle repeats for each combination of cooling gas and M . M values tested were 0.5, 0.75, 1.0, 1.25, 1.5, and 2.0. A representative test condition data acquisition spreadsheet is included as Table 7.

Table 7. Test plan and data acquisition sheet for WSR test condition $\Phi = 0.6$, $\dot{m}_{air} = 1020$ g/min

Data Point		Φ	M (des.)	Air or N2	Total Air	Propane	Calc'd	Req'd Air	Brooks	M for Air	M for N2
start	end	(desired)	(air)		(SLPM 70)	(SLPM 70)	Φ	(SLPM 0)	Entered		
10070	11030	0.6	2	Air	851.1	21.4	0.597	1.7958	1.795	1.9991	1.9331
11120	11180	0.6	1.5	Air	851.1	21.4	0.597	1.34685	1.345	1.4979	1.44848
11450	11510	0.6	1.25	Air	851.1	21.4	0.597	1.12237	1.119	1.2462	1.20509
11655	11715	0.6	1	Air	851.1	21.4	0.597	0.8979	0.899	1.0012	0.96817
12080	12140	0.6	0.75	Air	851.1	21.4	0.597	0.67342	0.678	0.7551	0.73016
12195	12255	0.6	0.5	Air	851.1	21.4	0.597	0.44895	0.448	0.4989	0.48247
10860	10920	0.6	2	N2	851.1	21.4	0.597	1.7958	1.796	2.0002	1.93418
11220	11280	0.6	1.5	N2	851.1	21.4	0.597	1.34685	1.345	1.4979	1.44848
11340	11400	0.6	1.25	N2	851.1	21.4	0.597	1.12237	1.119	1.2462	1.20509
11760	11820	0.6	1	N2	851.1	21.4	0.597	0.8979	0.899	1.0012	0.96817
11905	11965	0.6	0.75	N2	851.1	21.4	0.597	0.67342	0.678	0.7551	0.73016
12325	12385	0.6	0.5	N2	851.1	21.4	0.597	0.44895	0.448	0.4989	0.48247
22-Apr-08											

4.2 Visible Boundary Layer Reactions

A preliminary WSR and systems check was performed prior to initiation of the test matrix. Visible light photographs were taken of the cooling jets using a Sony DSLR-100A digital camera. At a test condition of $\dot{m}_{air} = 1020$ g/min and $\Phi = 1.7$ with the normal hole cooling geometry, cooling jets were not visible with N₂ cooling gas. With the introduction of air as a cooling gas, combustion caused the jet to become visible. Photographs were taken of this condition, and are included as Figure 45 through Figure 50.

Photographs were also taken of the angled hole cooling geometry at a WSR test condition of $\dot{m}_{air} = 1020$ g/min and $\Phi = 1.5$. These photographs are included as Figure 52 through Figure 54. All pictures were taken from the side of the rig, as in Figure 44, with the field of view restricted to the area immediately around the cooling holes.

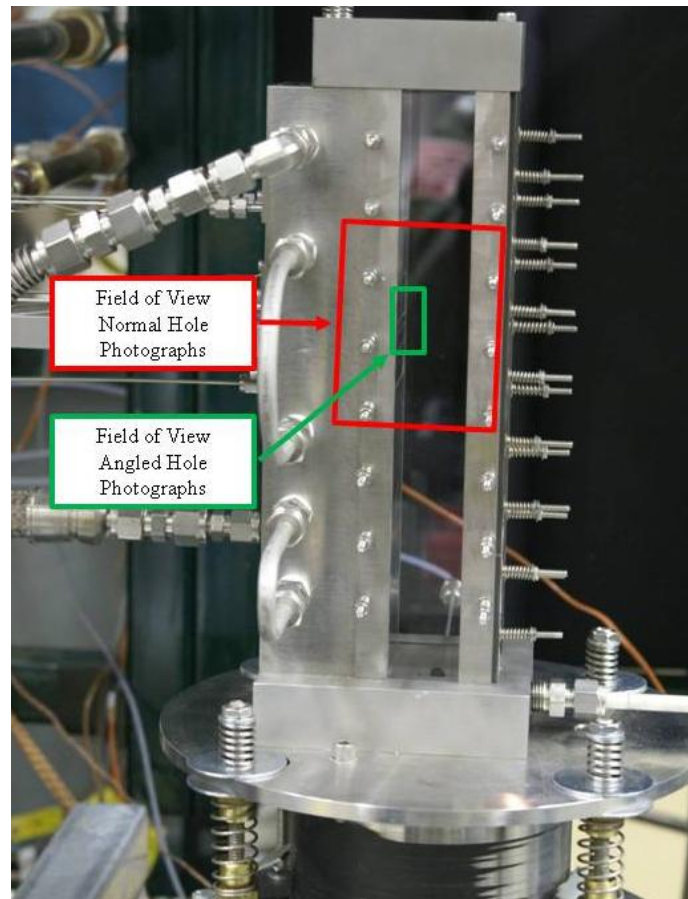


Figure 44. Field of view for boundary layer combustion photographs



Figure 45. Visible combustion in cooling film,
normal holes, $M = 2.0$

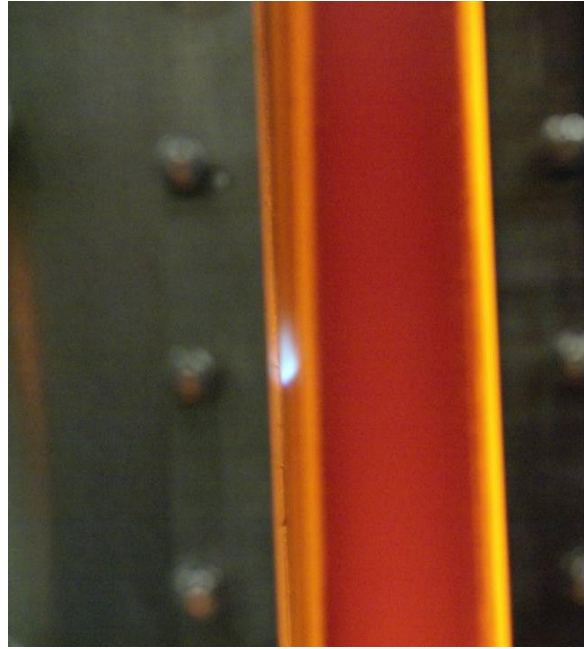


Figure 46. Visible combustion in cooling film,
normal holes, $M = 1.75$

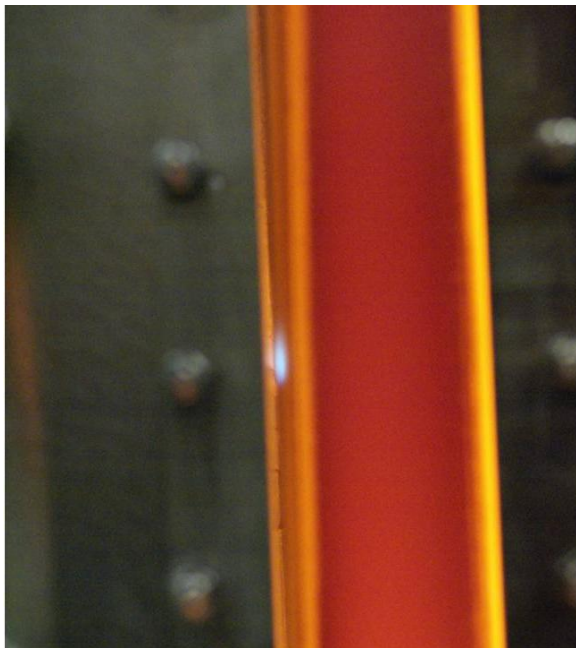


Figure 47. Visible combustion in cooling film,
normal holes, $M = 1.25$

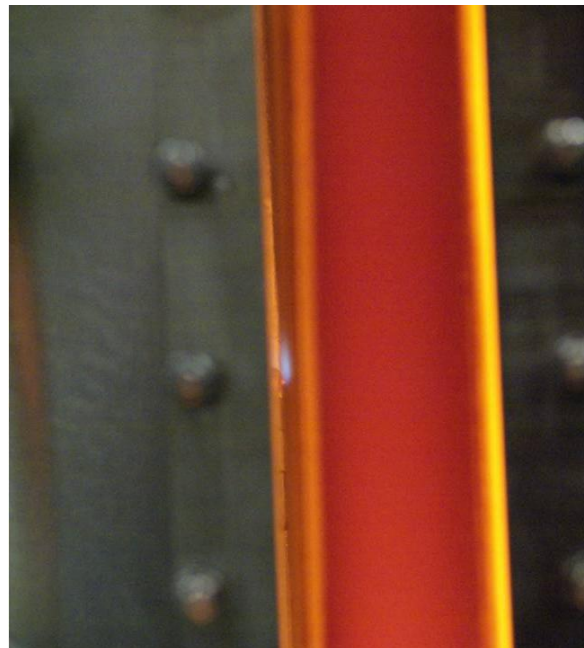


Figure 48. Visible combustion in cooling film,
normal holes, $M = 1.0$



Figure 49. Visible combustion in cooling film,
normal holes, $M = 0.75$

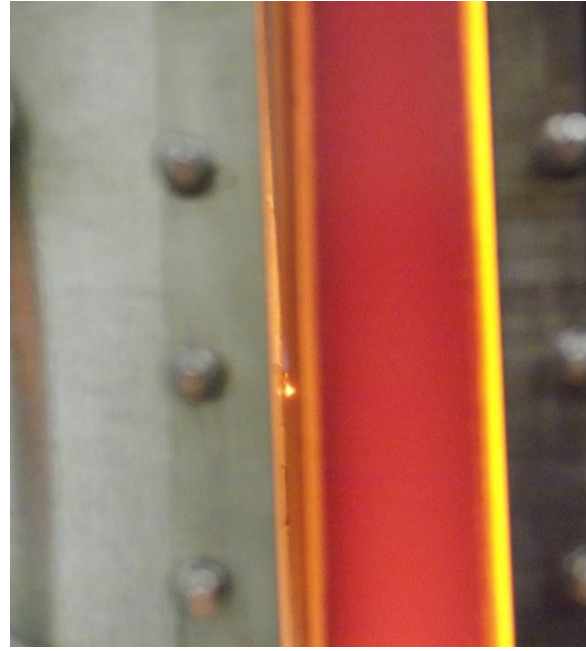


Figure 50. Visible combustion in cooling film,
normal holes, $M = 0.5$

Figure 45 shows the deep penetration of the jet into the freestream. As the jet meets and mixes with the reactor exhaust flow, local combustion occurs. The combustion is visible as a blue-white plume as it is carried downstream. In the above figures, the blowing ratio is sequentially reduced. Because of the reduced momentum of the jet at lower M , they do not penetrate as deeply into the reactor exhaust flow. The burning does not appear as white, possibly due to lower intensity combustion because of the smaller amount of air being provided. At the lower blowing ratios (Figure 47 through Figure 50), the effect of the local reactions on the metal of the cooling hole surface becomes visible as a bright red spot upstream of the visible cooling jet location. The exposure time of the camera was increased in Figure 49 and Figure 50 in order to highlight this effect; it should not be assumed that the location is hotter at lower blowing ratios.



Figure 51. Nitrogen cooling film, angled holes, $M = 2.0$



Figure 52. Visible combustion in cooling film, angled holes, $M = 2.0$



Figure 53. Visible combustion in cooling film, angled holes, $M = 1.0$



Figure 54. Visible combustion in cooling film, angled holes, $M = 0.5$

Figure 51 is a photograph of the area of the angled cooling holes with a nitrogen cooling jet at $M = 2.0$. At these conditions, there is no visible flame. Figure 52 through Figure 54 are photographs of the cooling jets with air as the cooling gas. They exhibit many of the same characteristics as the normal jets. Penetration and plume length were very large for $M = 2.0$, and smaller at $M = 1.0$ and $M = 0.5$. These pictures were taken at different flow conditions, disallowing direct comparison. Qualitatively, it can be seen that the visible combustion in the angled jets stay closer to the surface than the normal jets.

These photographs demonstrate that boundary layer reactions can occur in fuel rich conditions due to the introduction of air from cooling holes. The reactions can occur in close proximity to the surface. These reactions also occur quickly enough to cause significant heat transfer to the surface in the immediate vicinity of the cooling holes. The pictures were taken with external length references, allowing the length of the plume and penetration to be measured. These measurements indicate that all of the visible reactions are occurring within 8 to 16 D downstream of the cooling holes. Overall, the higher blowing ratios penetrated deeper and the plume was longer for both geometries. The length of the plume was longer for the angled hole geometry.

Table 8. Penetration and plume lengths of cooling jets

<i>Geometry</i>	<i>M</i>	Penetration Length (mm)	Plume Length (mm)
Normal	2.0	2.3	7.2
Normal	1.75	2.0	7.1
Normal	1.25	1.2	6.4
Normal	1.0	1.0	4.7
Normal	0.75	0.7	3.8
Normal	0.5	0.5	2.4
Angle	2.0	2.2	9.1
Angle	1.0	1.1	5.0
Angle	0.5	0.5	2.9

4.3 WSR Exhaust Temperature Measurements and Modeling

The temperature of the WSR Exhaust is measured entering the test section with a type-B thermocouple inserted through a fitting in the instrument block. This is the temperature used as T_{∞} in calculating ϕ and h_{eff} (Eqs. (3) and (5)). There is some variation in the temperature measurements over several days, as the reactor changes slightly through its life. The Normal set was run first, followed after several days by the Angle set, then the Fan set. The average temperature at each WSR test condition is given in Figure 55.

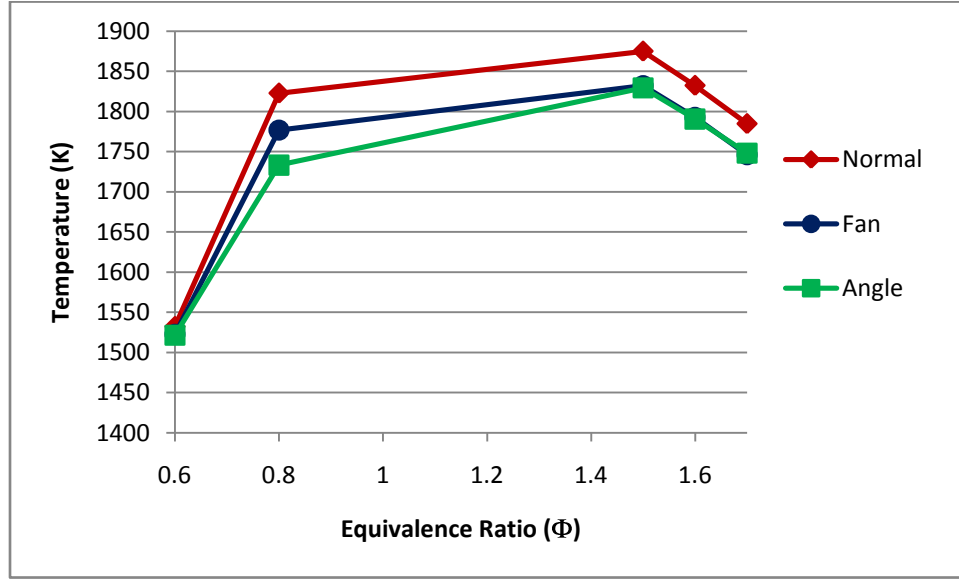


Figure 55. Variation in T_{∞} with Φ at constant \dot{m}_{air}

These temperatures were also used to baseline a computer based chemical kinetics model¹⁸ of the flow. The WSR and rig were modeled as a Perfectly Stirred Reactor (PSR) followed by 2 Plug Flow Reactors (PFRs), a mixer, and a final PFR. The gas inlets of the PSR were the mass flow rates of air and propane to model the $\Phi = 0.6, 0.8, 0.95, 1.5$, and 1.7 conditions. The exhaust flow then moved through a PFR representing the ceramic chimney of the actual rig. The heat loss in this section was set so the temperature in the model matched the actual temperature measured at the instrument block. The next PFR represented the portion of the rig between the stack and the cooling holes, with heat loss based on actual heat flux measurements. Major chemical species (in molar concentration) at the endpoint, as well as velocity and density data, are given in Table 9. According to Ref. 5, the high concentration of CO at the fuel rich conditions exceeds that of Composition 3, while $\Phi = 0.8$ and 0.95 fall into the range of Composition 1. See Section 0 for the discussion of compositions.

Table 9. Modeled concentration, velocity, and density information prior to cooling holes

Φ	<i>0.6</i>	<i>0.8</i>	<i>0.95</i>	<i>1.5</i>	<i>1.7</i>
U_{∞} (m/s)	40.3	50.9	40.8	57.0	55.5
ρ_{∞} (kg/m ³)	0.237	0.189	0.169	0.176	0.183
O_2	0.080517	0.039865	0.012105	9.95E-08	3.44E-05
N_2	0.752017	0.752117	0.739951	0.729436	0.642821
H_2O	0.095477	0.124838	0.144601	0.136648	0.13481
CO_2	0.071667	0.093785	0.106466	0.052183	0.038808
H_2	4.89E-06	9.87E-05	0.00101	0.067178	0.073617
CO	1.69E-05	0.000319	0.003681	0.100724	0.119463
O	8.70E-06	7.11E-05	0.000196	9.86E-08	6.29E-09
OH	0.000191	0.001061	0.002375	3.88E-05	4.54E-06
H	2.89E-07	9.77E-06	0.000129	0.00025	4.25E-05
Total HC (ppm)	3.18E-11	7.00E-08	4.32E-08	8.213862	10128.72

The cooling holes were modeled to estimate the chemical time scales of any reactions that may occur. To model this, the reactions were assumed to be occurring along the outside of cooling jets, essentially as a diffusion flame. With this assumption, the flame front is stoichiometric, so the time scales should be evaluated at this condition. The test rig downstream of the cooling holes is modeled as a PFR. The gas inputs to the PFR are the WSR exhaust flow and a cooling air flow that is equal to the mass flow required to make the entire mixture stoichiometric. This is many times larger than the actual cooling air flow into the rig. The two gas streams are combined in a non-reacting mixer, and then passed into a final PFR, where the entire flow will react as if it were along the flame front.

The temperature begins to rise in the PFR with the residence time, and the chemical time is derived from these two parameters: τ_{chem} is the amount of time required to reach a given percentage of end-state temperature rise. Chemical times and Damkohler numbers, Eq. (20), at the fuel rich conditions are given in Table 1. The denominator in Eq. (20) serves as a characteristic distance, and is included in the chart. Interestingly, the

characteristic distance based on 50% of temperature rise is on the order of the visible flame lengths reported in Section 4.2. The magnitude of Da indicates that for the geometry and conditions in the test rig, a significant portion of any heat rise should be apparent by the location of the heat transfer gauges for each case.

Table 10. Chemical times and the Damkohler number for modeled test conditions

Φ	0.6	0.8	0.95	1.5	1.7
$\tau_{chem,50}$ (s)	0.000685	0.00058	0.000385	8.28E-05	8.18E-05
$\tau_{chem,95}$ (s)	0.00376	0.00307	0.00222	0.00106	0.000957
$U_{\infty}\tau_{chem,50}$ (mm)	27.6	29.5	15.7	4.72	4.54
$U_{\infty}\tau_{chem,95}$ (mm)	152	156	90.5	60.2	53.1
Da_{50}	0.184	0.172	0.324	1.08	1.12
Da_{95}	0.0335	0.0325	0.0561	0.0844	0.0956

4.4 Temperature Data and Calculations

The temperature data figures located in Appendix A, beginning on page 97, show the thermocouple measurements in the test rig for each of the WSR test conditions as a function of blowing ratio (M) and the cooling gas selected (air or nitrogen). Included are the near-surface thermocouple (T_1) and deep thermocouple (T_2) for each of the four heat transfer gauges. The precision error of these temperature measurements is $\pm 0.4\%$. These figures also show the calculated surface temperature (T_s) of each of the four heat transfer gauges. T_s is calculated using the method described in Section 2.3, and an error analysis performed using the method described in Ref. 24 resulted in a precision error of $\pm 3.3\%$. Data is presented for upstream gauges including the coolant temperature (T_c) (precision

error $\pm 0.4\%$) on a single graph, and for the downstream gauges including the freestream temperature (T_∞) (precision error $\pm 0.5\text{K}$) on a second axis.

Heat transfer gauge Block #1 and Block #2, located 20 D downstream of the cooling holes, are designated as upstream gauges, and presented in one figure per test condition. An example of the temperature data from these gauges is given in Figure 56. Block #3 and Block #4, located 75 D downstream of the cooling holes, are designated as downstream gauges and presented in a second figure per test condition. An example of the temperature data from these gauges is given in Figure 57. Several very distinct trends are revealed in these data. The surface temperatures at values of $\Phi < 1$ are not significantly different when using the different cooling gases for the same block. In Figure 56, red and green solid lines represent T_s of Block #1, cooled with an air or nitrogen film, respectively. There is no significant difference between the two lines. The orange and blue solid lines represent T_s of Block #2, and similarly have no significant difference. There is a substantial difference in temperature between the Block #1 and Block #2, even though both are at the same distance downstream. This difference appears in the downstream gauges as well (Figure 57), but not at all flow conditions (see Figure 88, for example), possibly indicating an asymmetry in the flow through the rig.

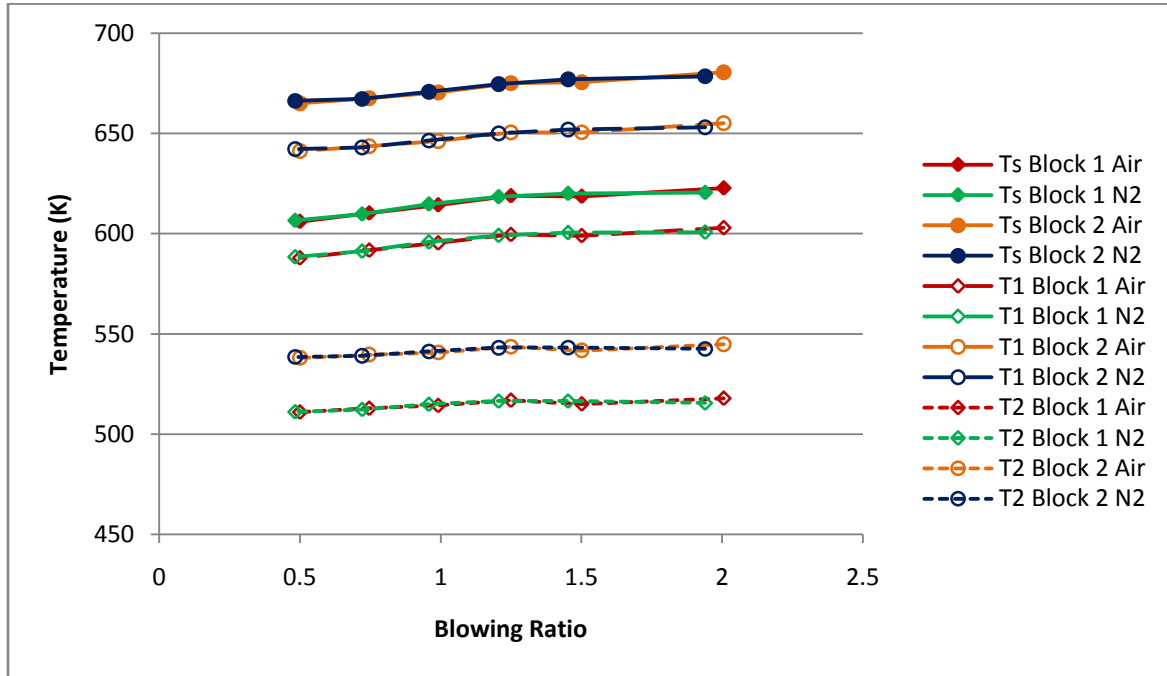


Figure 56. Gauge data, normal holes, $\Phi = 0.6$, $\dot{m}_{air} = 1020$ g/min, upstream gauges

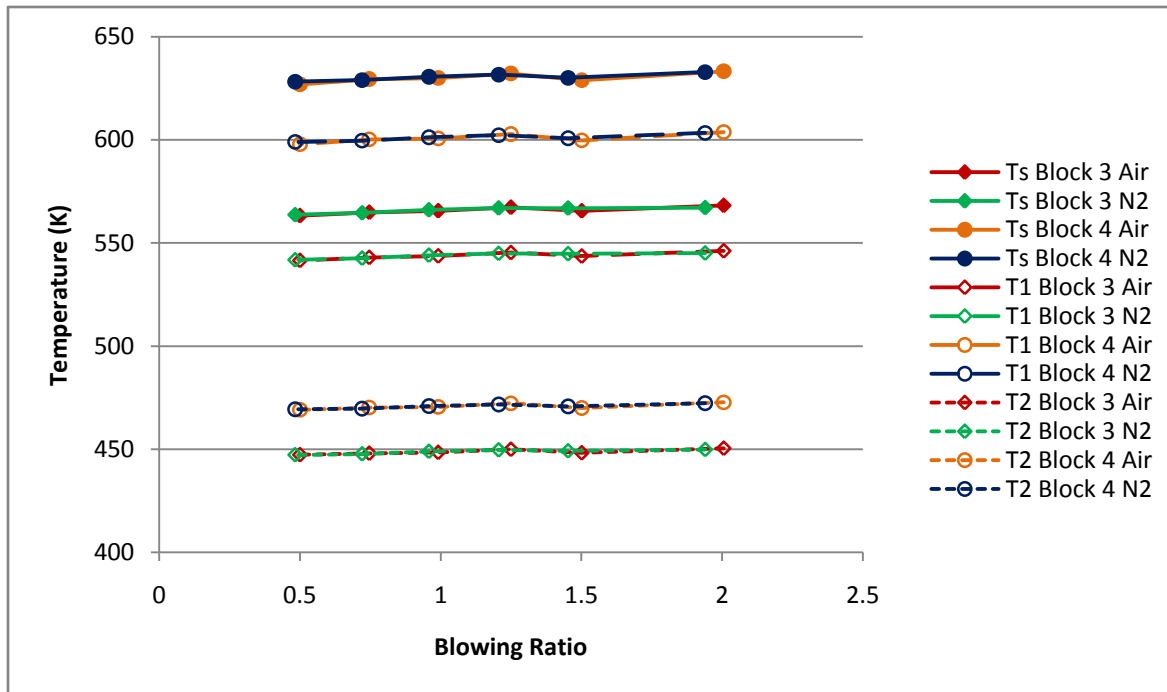


Figure 57. Gauge data, normal holes, $\Phi = 0.6$, $\dot{m}_{air} = 1020$ g/min, downstream gauges

At $\Phi > 1$, there is a higher temperature on the surface for each block when using air vice nitrogen. This effect is easily seen in Figure 58. The temperature data for blocks #1 and #2 for air (red and orange solid lines) are dramatically higher than their respective nitrogen lines (green and blue solid lines, respectively). These data indicate that reactions in the boundary layer increase the surface temperature downstream of the cooling holes. The effect is still present, but to a much smaller degree, further downstream (Figure 59).

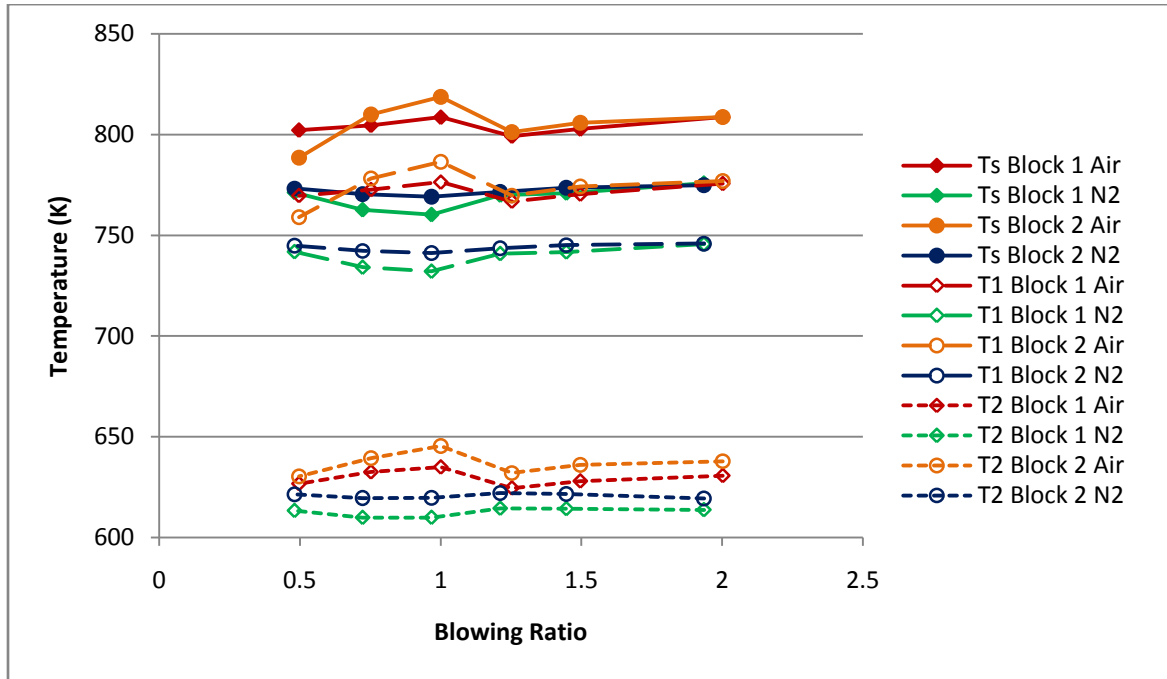


Figure 58. Gauge data, fanshaped holes, $\Phi = 1.5$, $\dot{m}_{air} = 1020$ g/min, upstream gauges

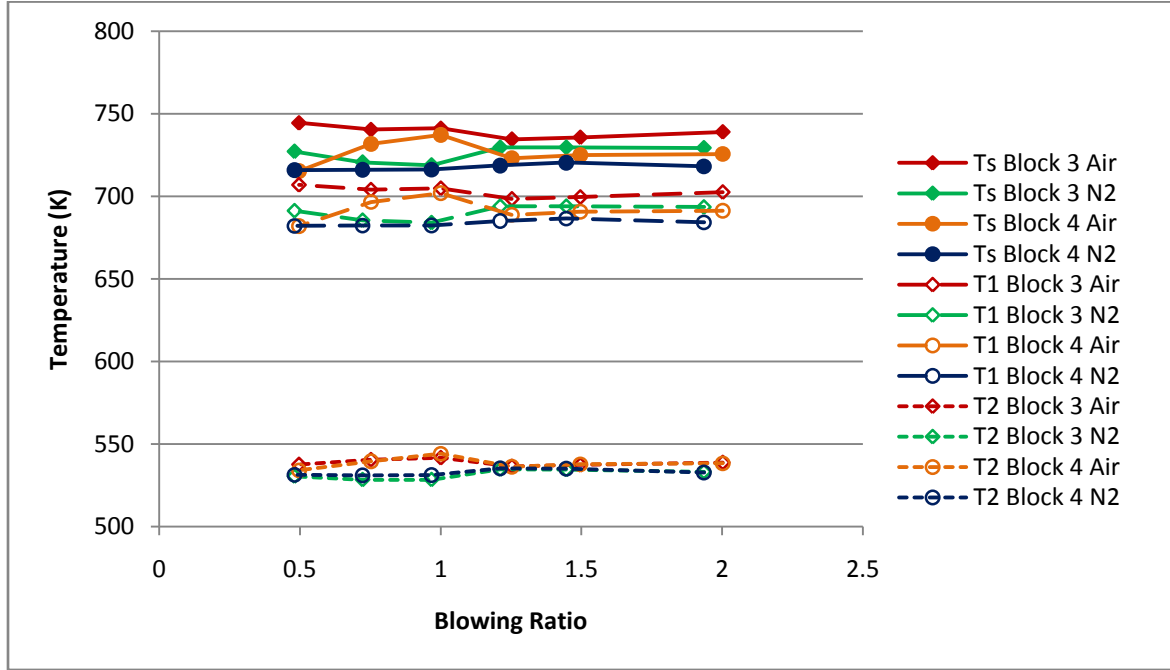


Figure 59. Gauge data, fanshaped holes, $\Phi = 1.5$, $\dot{m}_{air} = 1020$ g/min, downstream gauges

The temperature of the coolant gas, T_c , is measured within the plenum at a location 5.1 mm measured from the outside surface of the cooling hole surface. These data show a dependence of T_c on M . Figure 60 shows a clear trend of decreasing T_c with increasing M . As the cooling flow passes through the plenum and cooling slot insert, heat is transferred from the wall into the gas. The temperature rise of the gas is¹⁵:

$$q = \dot{m}_c c_p (\Delta T_c) \quad (36)$$

In this equation, c_p is the specific heat of the cooling gas, and ΔT_c is the temperature rise in the cooling gas from the entry of the plenum to the exit of the cooling holes. If the heat transfer (q) is assumed to be constant, then a reduction in mass flow must result in an increased ΔT_c .

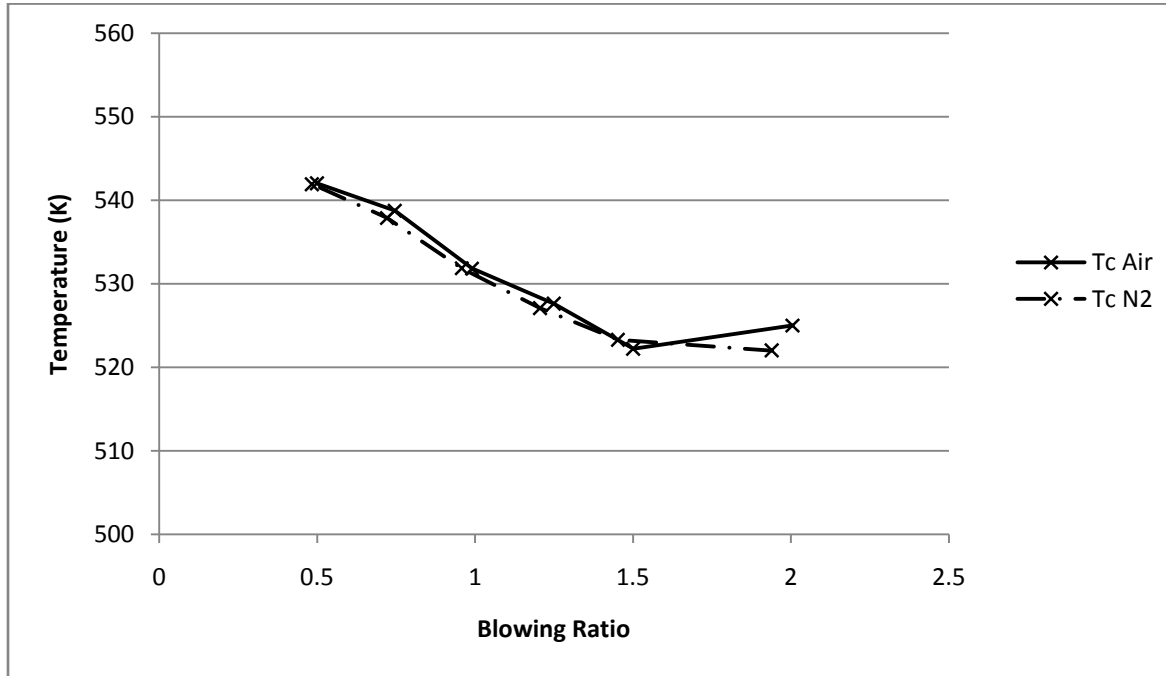


Figure 60. Dependence of T_c on M , normal holes, $\Phi = 0.6$, $\dot{m}_{air} = 1020$ g/min

The location of the T_c measurement has a large impact on the measured value. The low flow rates of the coolant gases and the high wall temperatures create a temperature gradient within the plenum, shown in Figure 61. By the time the cooling gas reaches the exit of the holes, it can be assumed to climb even higher in temperature. A second order curve fit to the data below indicates that the temperature at the exit is approximately 20 K higher than that measured. This introduces a bias error that is discussed further in Section 4.5.

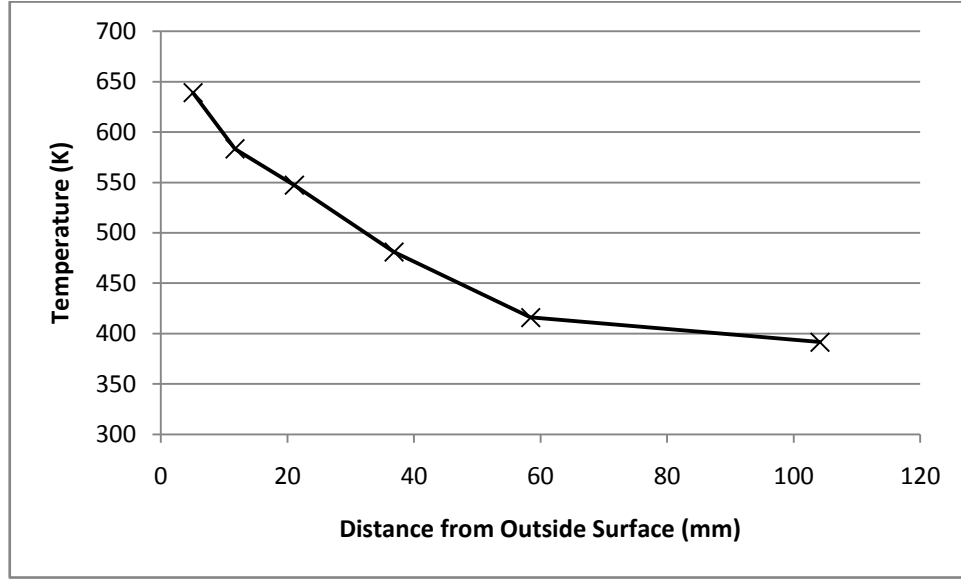


Figure 61. Measured T_c at varying locations in the plenum, $\Phi = 1.7$, $M = 0.5$, $\dot{m}_{air} = 1020$ g/min

There are also variations in T_∞ , though small relative to the magnitude of T_∞ . These variations are caused by small fluctuations in \dot{m}_{air} , \dot{m}_{fuel} , and WSR pressure. These fluctuations are never more than 40 K between the minimum and maximum values during a single WSR test condition. Representative T_∞ data is given in Figure 62. Though presented in a figure with M as the independent variable, T_∞ is not dependent on the cooling gas or M . These measurements reflect the freestream temperature at the time that the particular measurements were taken, and are independent of M . The measurement location is 15.2 cm upstream of the cooling hole location. There is a temperature drop between these locations that is estimated by the computer based chemical kinetic model to be less than 40 K. This introduces a bias error discussed further in the following sections.

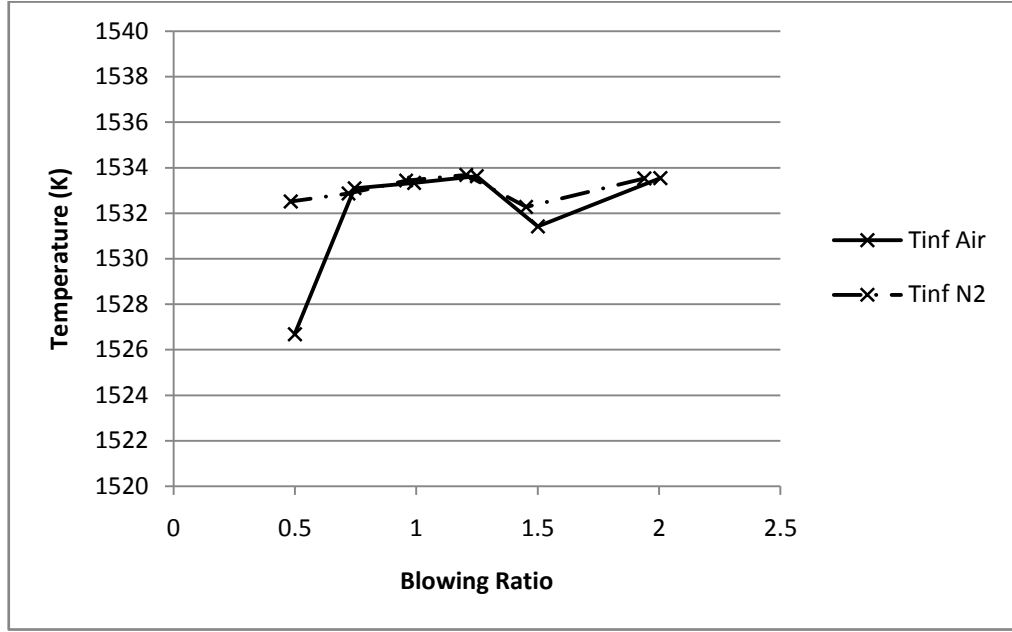


Figure 62. T_{∞} , $\Phi = 0.6$, $\dot{m}_{air} = 1020$ g/min, taken during normal holes data collection

4.5 Overall Effectiveness

The overall effectiveness (ϕ) for each of the WSR test conditions as functions of M is presented in Appendix B, beginning on page 115. Eq. (3) is used to calculate ϕ , based on the average T_s at a given distance downstream of the cooling holes (20 or 75 D). Both upstream (20 D) and downstream (75 D) information is given on the same graph. Because T_c varies with M , T_s does not provide a complete understanding of the relative cooling effect of different values of M . Because ϕ is the ratio of temperature differences, it accounts for these variations in T_c .

The water cooling is very effective at reducing the surface temperature of the heat transfer gauges, so ϕ tends to be very close to unity. In fact, at positions further downstream from the hole, these data suggest that the cooling film becomes *more* effective rather than less, caused by the active cooling. This restricts applicability of this

quantity to comparing a single geometry with different cooling gases and blowing ratios, or different geometries at the same flow conditions. It is a very useful parameter to identify the presence of reactions in the cooling film. Figure 63 shows ϕ as a function of M at the upstream (solid lines) and downstream (broken lines) location for both air and nitrogen at a WSR test condition of $\Phi = 0.6$, $\dot{m}_{air} = 1020$ g/min using fanshaped holes. These data indicate that boundary layer reactions are not significant at this condition, since the nitrogen and air lines are coincident at both locations.

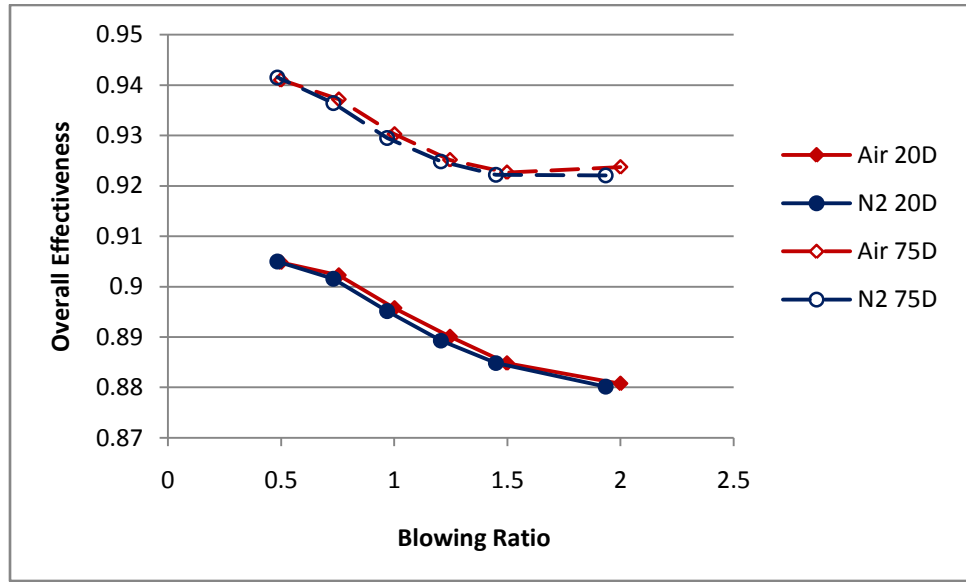


Figure 63. Dependence of ϕ on M , fanshaped holes, $\Phi = 0.6$, $\dot{m}_{air} = 1020$ g/min

Figure 64 shows the same information, but at a WSR test condition of $\Phi = 1.5$, $\dot{m}_{air} = 1020$ g/min, again with fanshaped cooling holes. Here, using nitrogen as a cooling gas is more effective than air. This is due to reactions occurring in the boundary layer and augmenting heat transfer when air is used. The difference between air and nitrogen is

seen to be larger at 20D than 75D, indicating that the strongest impact is closer to the holes.

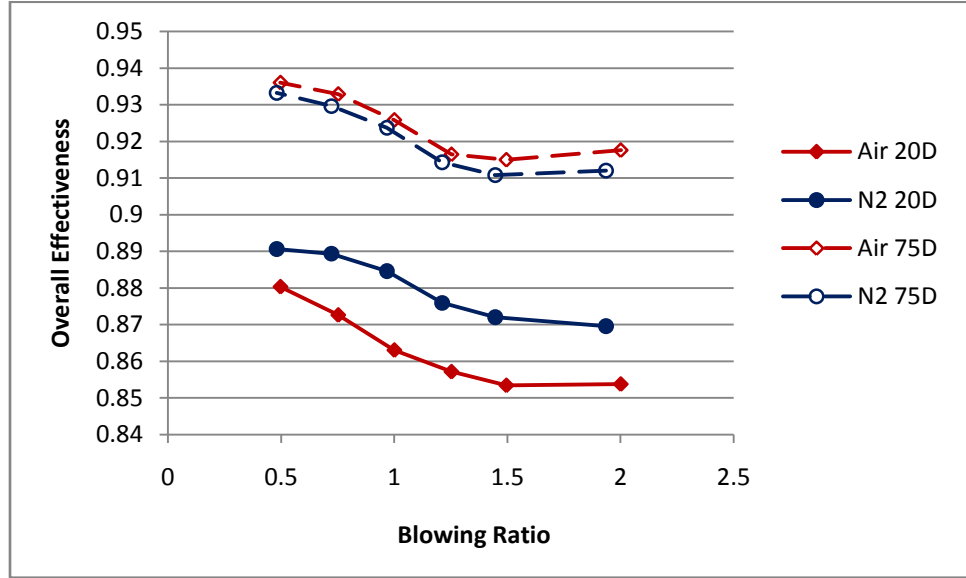


Figure 64. Dependence of ϕ on M , fanshaped holes, $\Phi = 1.5$, $\dot{m}_{air} = 1020$ g/min

Since the change in ϕ ($\Delta\phi$) is more telling in this study than the value itself, the difference between ϕ when using nitrogen (ϕ_{N2}) and when using air (ϕ_{air}) was calculated. This value is plotted in the following figures. Figure 65 and Figure 66 shows $\Delta\phi$ for the normal hole geometry at the upstream and downstream holes, respectively. Figure 67 and Figure 68 show the results for the angled holes, and Figure 69 and Figure 70 show the results for the fan-shaped holes. A positive $\Delta\phi$ indicates that air is less effective than nitrogen, a negative $\Delta\phi$ indicates that nitrogen is less effective than air.

Several trends are common to these graphs. The largest $\Delta\phi$ occurred at $\Phi = 1.5$ at the upstream holes for each geometry. At the downstream holes, At fuel rich conditions, $\Delta\phi$ was relatively small at $M = 0.5$, because of the small amount of air being added to the

flow, and is larger at other values of M . At the downstream holes, $\Delta\phi$ was largest at $\Phi = 1.7$ and $M = 2$. There was little change at $\Phi < 1$, except at high blowing ratios for $\Phi = 0.95$. At $\Phi = 0.95$, there is a consistent and significant negative $\Delta\phi$, indicating that nitrogen is less effective as a cooling gas at this condition. The reason for this is not completely clear, but is likely due to differences in the temperature and specific density of the two gases having a more significant effect at the very low mass flow rates at this WSR test condition. Further study using a more precise method of determining the coolant temperature would be of benefit in attempting to characterize this effect.

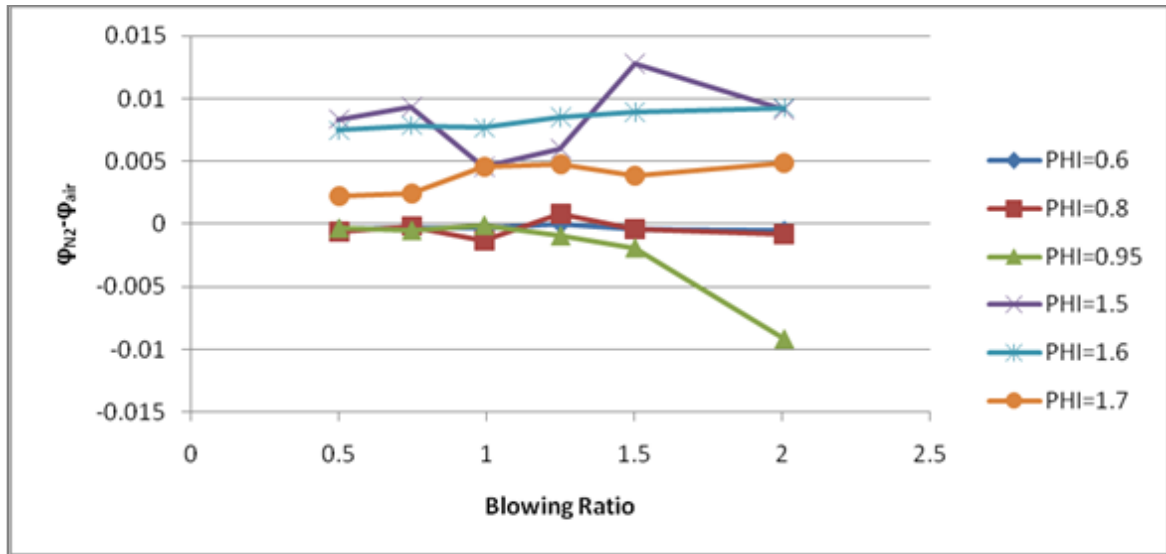


Figure 65. Dependence of $\Delta\phi$ on M , upstream normal holes, at different test conditions

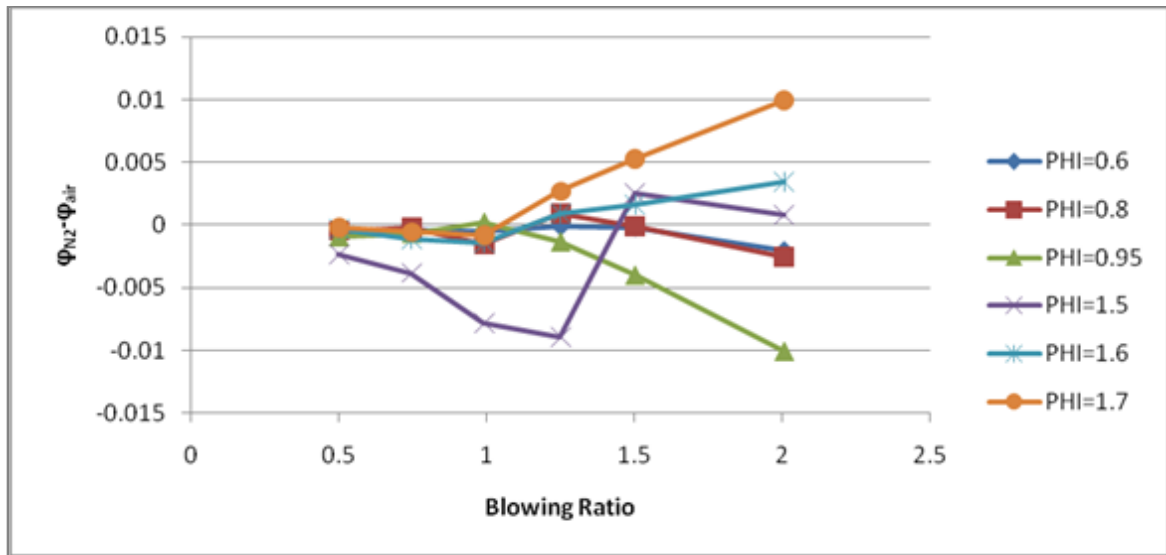


Figure 66. Dependence of $\Delta\phi$ on M , downstream normal holes, at different test conditions

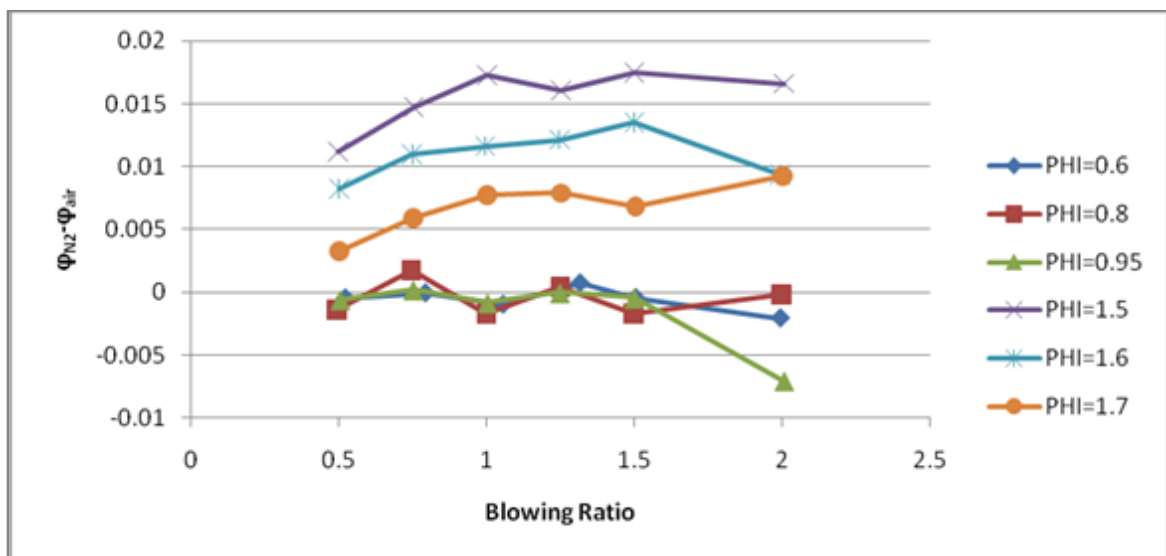


Figure 67. Dependence of $\Delta\phi$ on M , upstream angled holes, at different test conditions

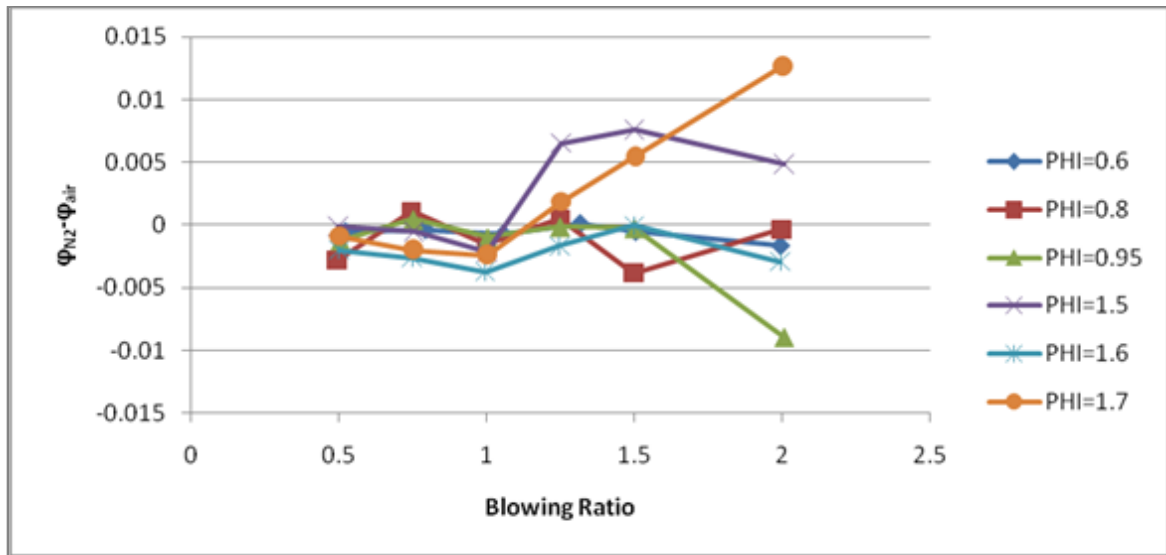


Figure 68. Dependence of $\Delta\phi$ on M , downstream angled holes, at different WSR test conditions

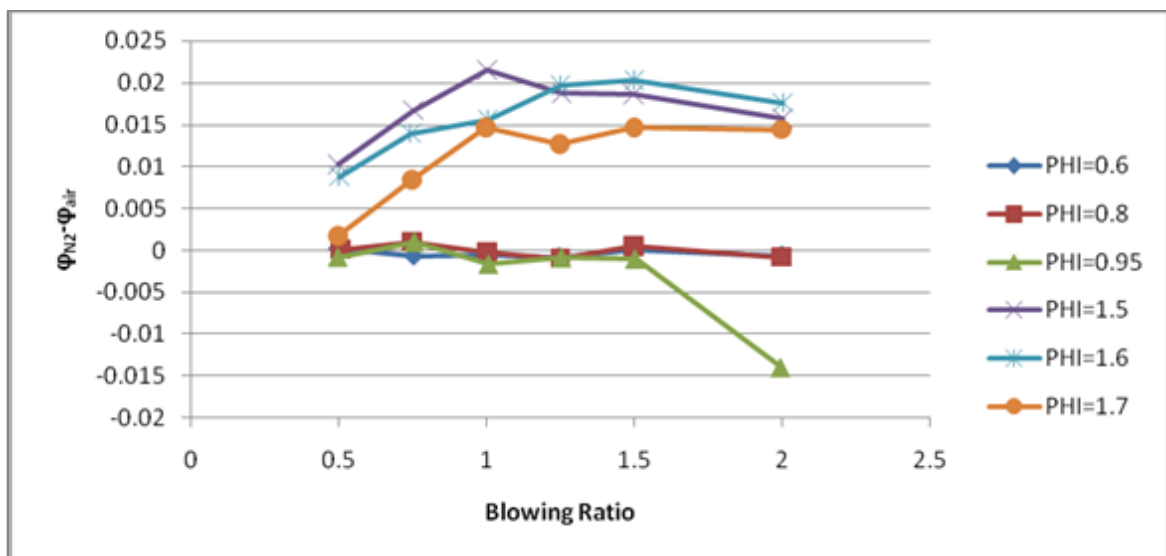


Figure 69. Dependence of $\Delta\phi$ on M , upstream fanshaped holes, at different test conditions

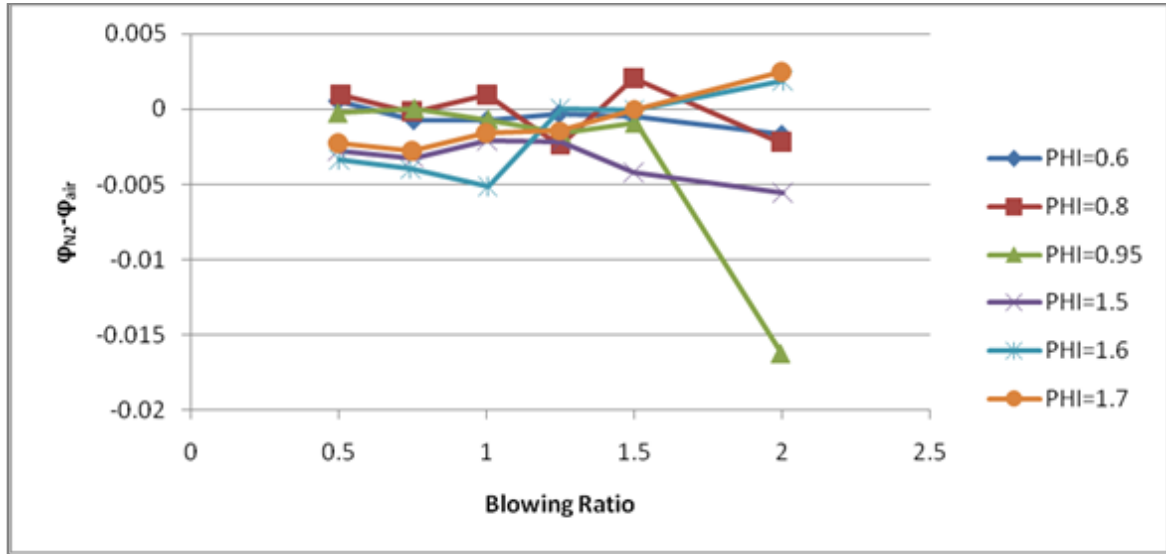


Figure 70. Dependence of $\Delta\phi$ on M , downstream fanshaped holes, at different test conditions

Figure 71 compares $\Delta\phi$ for all three geometries at $\Phi = 1.5$, for both upstream (solid lines) and downstream (broken lines) locations. For the upstream holes, the fanshaped and angled holes show the largest impact from boundary layer reactions. At the downstream locations, the story is not so clear, but it appears that the local temperature rise due to boundary layer reactions was neutralized by this location, due to mixing with the freestream.

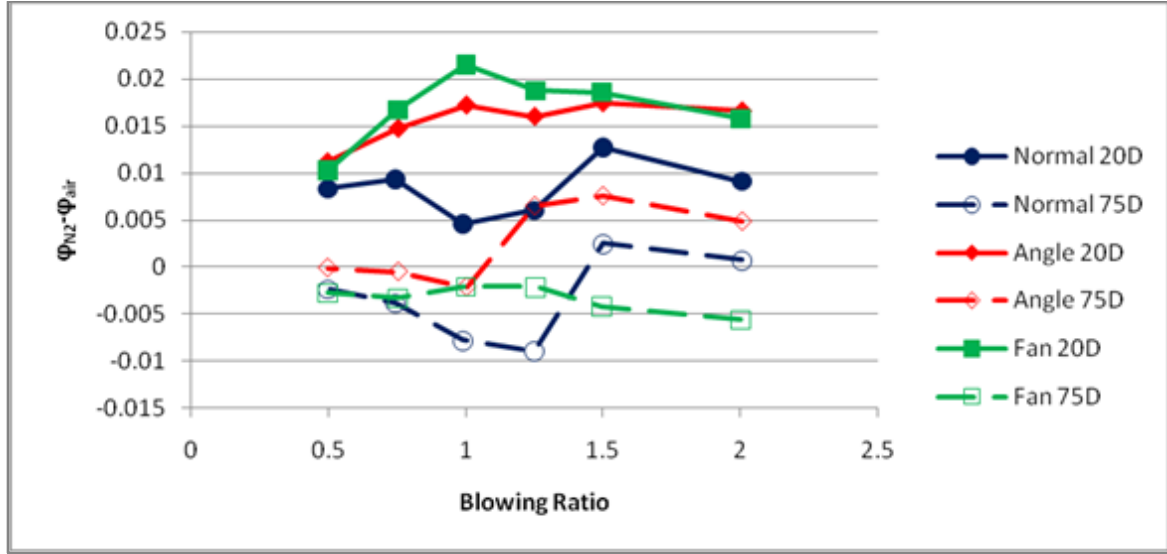


Figure 71. Dependence of $\Delta\phi$ on M , all geometries, $\Phi = 1.5$, $\dot{m}_{air} = 1020$ g/min

An uncertainty analysis was performed that indicated that the error in measurement and calculation of ϕ is 2.5%. There is also a bias error caused by the position of T_c (as much as 20 K low) and T_∞ (as much as 40 K high). These errors bias the result downwards by less than 2%. The precision error was 2.9%, using the method of Ref. 24.

4.6 Heat Flux and the Heat Transfer Coefficient

The heat flux (q'') at 20 or 75 D downstream of the cooling holes is calculated using the method described in Section 2.3, based on the average temperatures for the blocks at the given location. Using the calculated value of q'' , the effective heat transfer coefficient (h_{eff}) is determined by using Eq. (5). These data are presented in Appendix C beginning on page 123.

Heat flux at both 20 D and 75 D downstream are presented in the same figure, 20 D is presented using a solid line, 75 D with a broken line. See Figure 72, for example. In

this case, with $\Phi = 0.6$, the effect of changing gases is negligible, as the data for air and nitrogen are coincident at both locations. The effect of M is stronger closer to the holes, and diminishes at the increased distance.

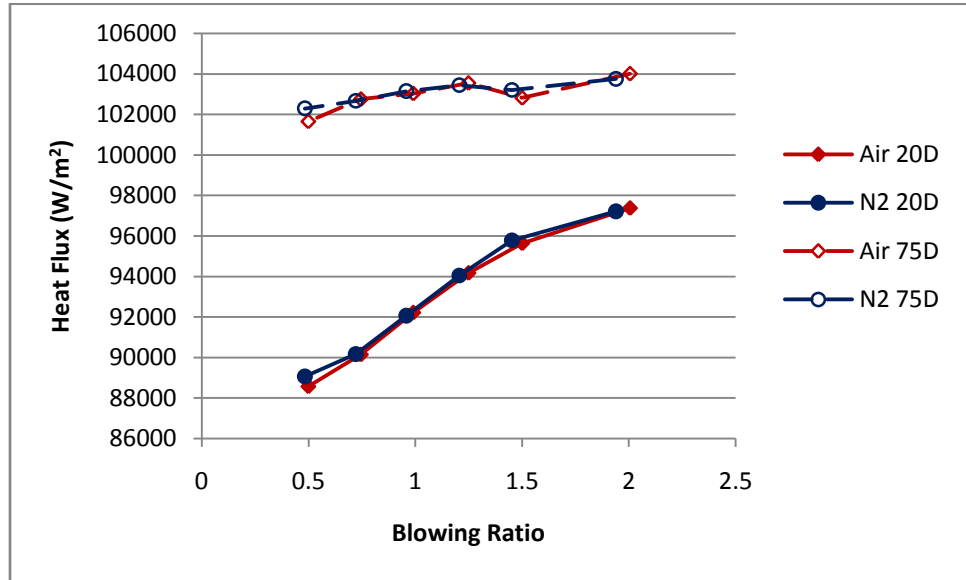


Figure 72. Dependence of q'' on M , normal holes, $\Phi = 0.6$, $\dot{m}_{air} = 1020$ g/min

The figures illustrating h_{eff} show similar trends to q'' (Figure 73). The most notable difference in the h_{eff} and q'' curves is the closer relationship between the values at 20 D to those at 75 D. This is because T_s is lower on Blocks #3 and #4 (75 D) than on #1 and #2 (20 D), resulting in a smaller h_{eff} for a given q'' . The h_{eff} and q'' curves very clearly show the presence and impact of boundary layer reactions on heat transfer. Figure 74 and Figure 75, in particular, demonstrate this effect.

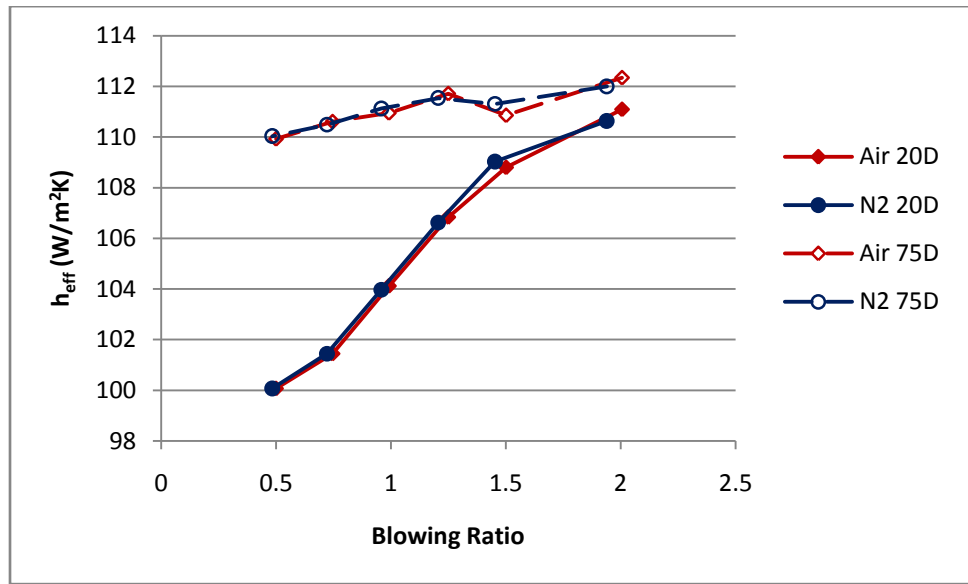


Figure 73. Dependence of h_{eff} on M , normal holes, $\Phi = 0.6$, $\dot{m}_{air} = 1020$ g/min

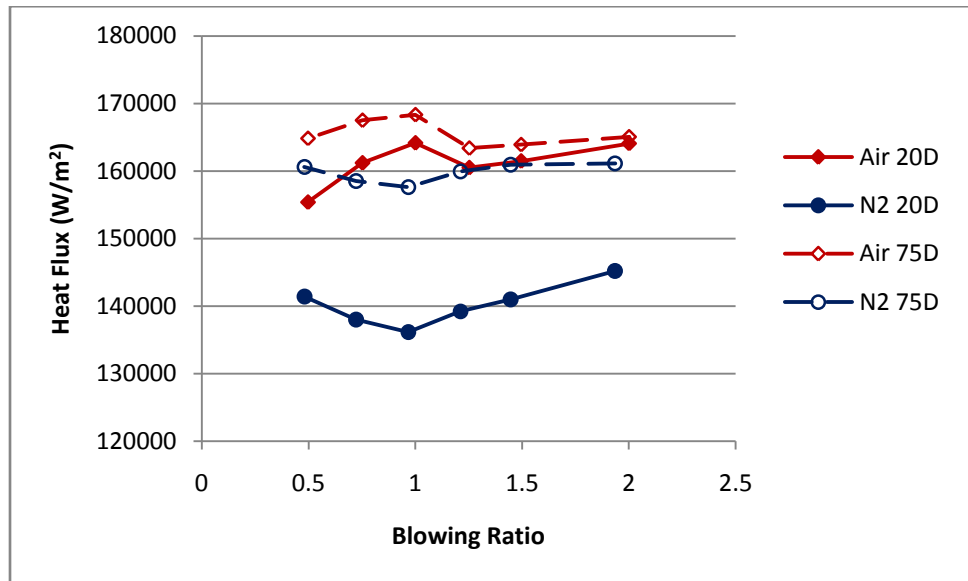


Figure 74. Dependence of q'' on M , fan-shaped holes, $\Phi = 1.5$, $\dot{m}_{air} = 1020$ g/min

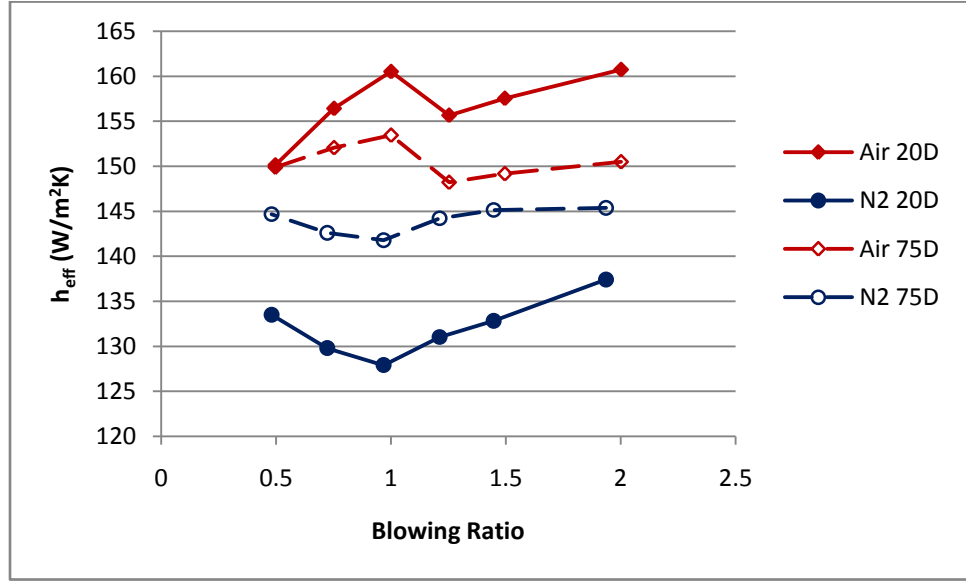


Figure 75. Dependence of h_{eff} on M , fanshaped holes, $\Phi = 1.5$, $\dot{m}_{air} = 1020$ g/min

Because the measurement location used for T_{∞} is upstream of the heat transfer gauge location, there is a bias error in calculated value of h_{eff} . Using the estimated temperature drop, the bias error is less than 4.7%. The precision error calculated according to Ref. 24 was less than 6.2% for q'' , and less than 6.4% for h_{eff} .

The method used to calculate q'' assumes that the heat flux is generally one-dimensional. To examine the legitimacy of this assumption, a finite element model of the flat plate with representative boundary conditions was performed in Ref. 25. The temperature profile within the flat plate is shown in Figure 76. The upstream and downstream heat transfer gauge locations are designated in the figure as PROBE1 and PROBE2. The thermocouple depths are designated as CUT1 and CUT2. It can be seen in this figure that the isotherms are parallel to the surface at PROBE2 between the surface and the deepest thermocouple location. There is a two-dimensional component at the

PROBE1 location, though it is nearly one-dimensional. This may be the cause of q'' being higher at the 75D than at 20D.

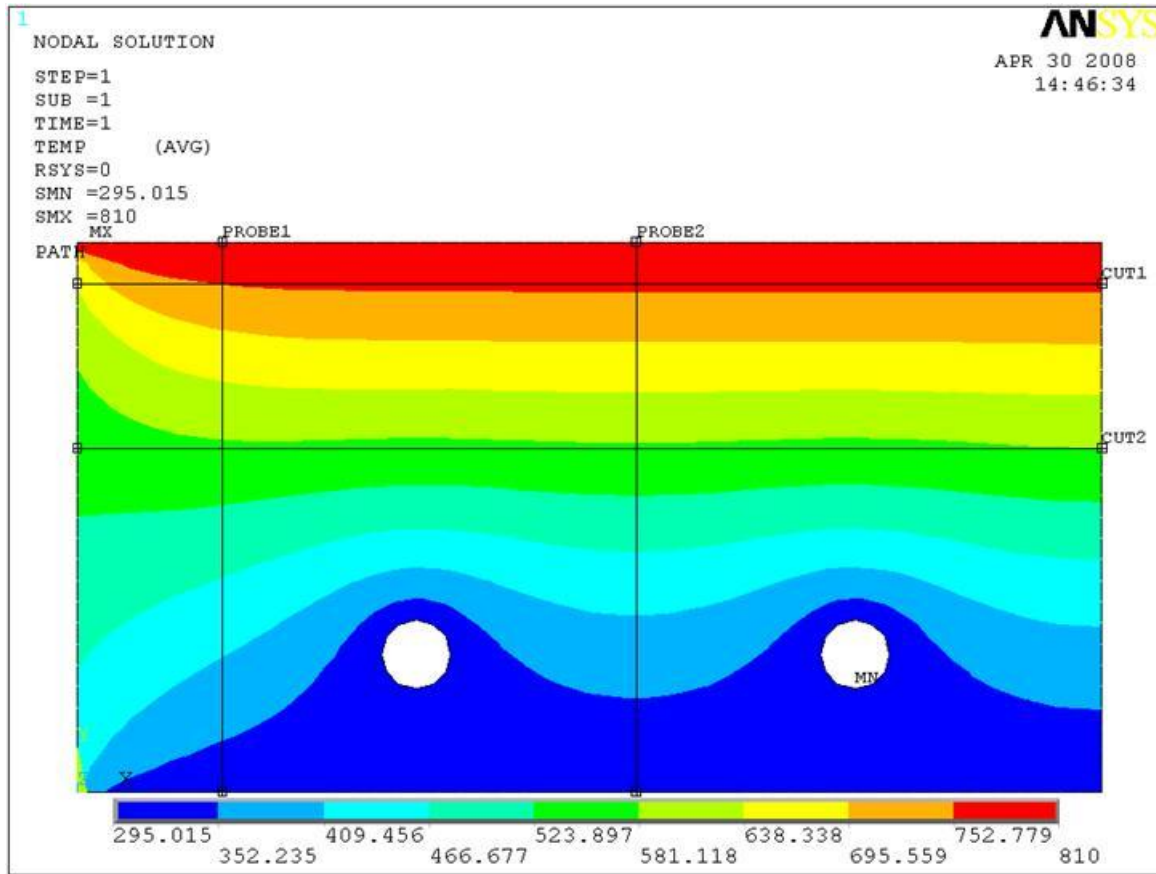


Figure 76. Modeled temperature profile in flat plate²⁵

A baseline case was run at $\Phi = 0.6$, $\dot{m}_{air} = 1020$ g/min with no blowing to determine how well the measured heat transfer coefficient matched empirical correlations for a turbulent boundary layer over a flat plate. The correlations in Section 2.6 (from Ref. 15) were used to calculate predicted heat transfer coefficients at the 20 D and 75 D locations. The predictions for this correlation and experimental data are given in Table 11. An estimate of the radiant heat transfer to and from the plate was performed, based on

the techniques described in Ref. 15. The estimate included the radiation from the plate to the environment, from the window rails to the plate, and from the participating gases in the freestream to the plate (CO_2 and H_2O). The results indicate that the heat flux was approximately 20100 W/m^2 at this WSR test condition, and increased to 40000 W/m^2 at higher temperatures. This correction was applied to h_{eff} , resulting in less than 12% error between measured and predicted values.

Table 11. Comparison of measured heat transfer coefficient to empirical correlation¹⁵

Location	Measured h_{eff} ($\text{W/m}^2 \cdot \text{K}$)	Corrected h_{eff} ($\text{W/m}^2 \cdot \text{K}$)	Predicted h ($\text{W/m}^2 \cdot \text{K}$)
20 D	99.7	76.0	68.0
75 D	96.4	74.1	65.6

4.7 Comparison of Heat Transfer Coefficient –Geometry

The values of h_{eff} for the upstream holes for each of the geometries are compared in the following figures, at representative WSR test conditions. Figure 77 displays the h_{eff} for the angled, fanshaped, and normal holes at $\Phi = 0.6$. The data for cooling air (solid lines) and cooling nitrogen (broken lines) are nearly coincident for each geometry, indicating that boundary layer reactions had no effect on h_{eff} at this Φ . Consistent with the discussion of Section 2.1, the angled holes performed better (maintained a lower h_{eff}) than the cylindrical holes at lower M , but performance degrades at higher M due to separation. The fanshaped hole design provided much lower h_{eff} over the entire range of tested values of M , consistent with the data presented in Figure 5.

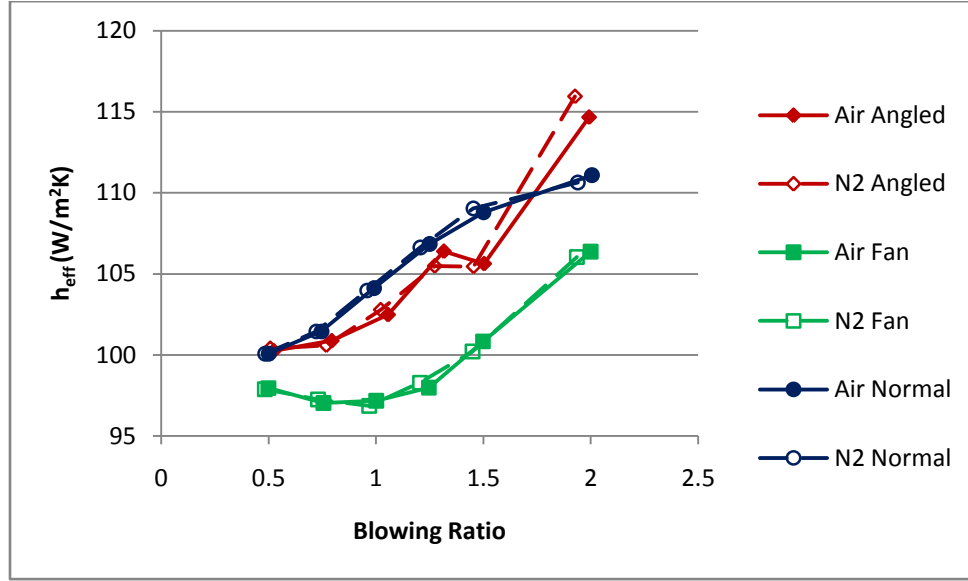


Figure 77. Comparison of cooling hole geometries: Dependence of h_{eff} on M , $\Phi = 0.6$

The h_{eff} data for $\Phi = 0.95$ (Figure 78) shows similar results for the normal holes and fan-shaped holes. The angled holes did not perform as well in this case, though the reason for this has not been determined in this study. One possible cause could be a much lower mass flow rate used at this condition in order to preserve reactor life. This would increase the momentum of the cooling jet relative to the freestream, changing the performance of the cooling stream. More significant for this study is the lack of any noticeable change in h_{eff} due to a change in cooling gas. There is no indication that dissociated combustion products reacting with air in the cooling film results in augmented heat transfer at the surface.

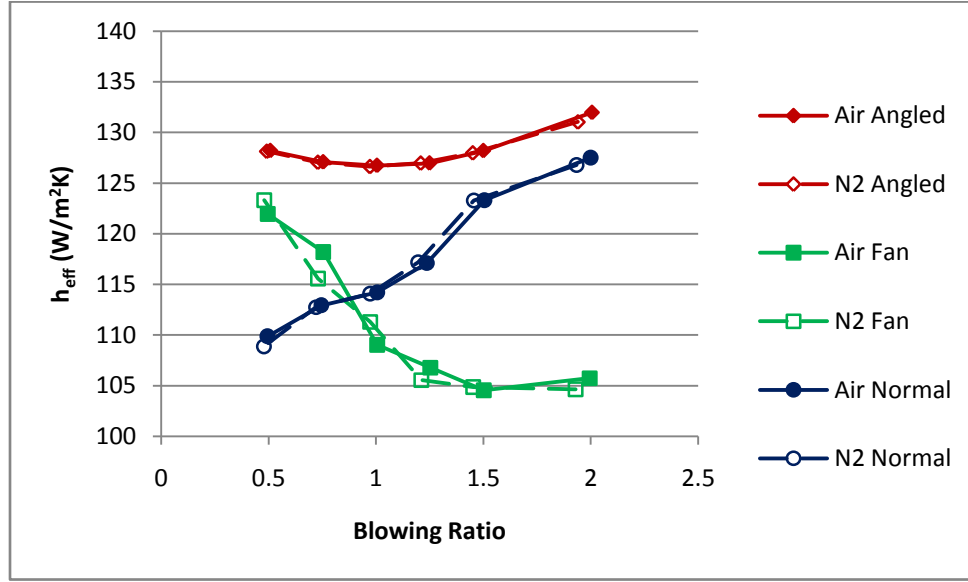


Figure 78. Comparison of cooling hole geometries: Dependence of h_{eff} on M , $\Phi = 0.95$

Figure 79 shows the h_{eff} data for the cooling geometries at $\Phi = 1.5$. The effect of boundary layer reactions is clearly seen by the difference between in the air (solid lines) and nitrogen (broken lines) data. The dependence of the cooling jets on blowing ratio follows similar trends to those of Figure 77. When air is introduced, each geometry indicates a large rise in h_{eff} . The h_{eff} of the normal jets increases by an average of 8% when switching from nitrogen to air. The h_{eff} for angled holes increases by an average of 14%. The fanshaped holes, the most effective in the nonreactive flow conditions, increase h_{eff} by 19%. Notably, the shape of the curve changes for the fanshaped holes. The value of h_{eff} when blowing air peaks at $M = 1$, precisely where it reaches a minimum in a nonreactive case. The increase in h_{eff} from a non-reacting to a reacting cooling flow is 25% at this point. This indicates that the phenomenon which makes the fanshaped holes characteristically so effective, a resistance to separation, may be increasing the effect of heat release in a reacting flow.

This effect is not isolated to this WSR test condition, occurring at $\Phi = 1.6$ and $\Phi = 1.7$ as well (see Figure 165 and Figure 167). There is a similar mirroring effect in the angled hole data, though it is not as large in magnitude, as shown in Figure 153 and Figure 155. It is important to note, that even when reacting, the fanshaped geometry remains effective, especially at high values of M .

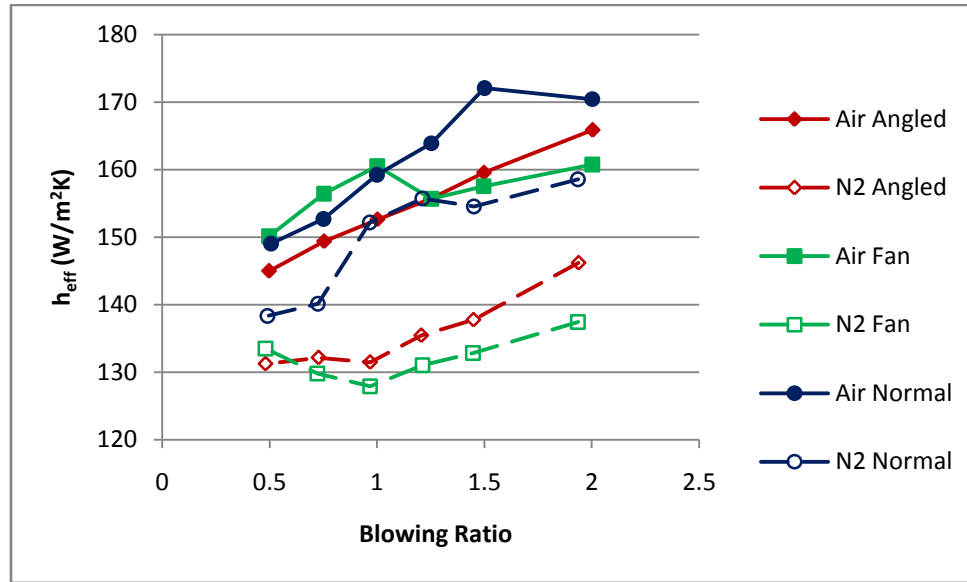


Figure 79. Comparison of cooling hole geometries: Dependence of h_{eff} on M , $\Phi = 1.5$

4.8 Comparison of Heat Transfer Coefficient –Test Condition

The following figures illustrate the ratio of h_{eff} when using air to the value when using nitrogen, for a given hole geometry: $h_{eff,air}/h_{eff,N_2}$. This quantity has a precision error of $\pm 9.8\%$. Figure 80 shows the data for the normal cooling hole geometry. This figure illustrates that there is no significant rise for $\Phi < 1$, since the ratio remains close to unity. For $\Phi > 1$, the effect of boundary layer reactions is shown as an increase in the

ratio. The effect is greatest at $\Phi = 1.5$, decreasing further as Φ increases. These trends occur with the other cooling hole geometries as well. The data for the angled hole geometry is presented in Figure 81, and the fanshaped hole geometry is given in Figure 82. As discussed in Section 0, the fanshaped holes show the largest increase in h_{eff} , followed by the angled holes. The normal holes show the smallest rise. This indicates that the rise in h_{eff} is likely due to near-wall combustion, which would result in a larger effect for the geometries that do a better job of keeping the coolant jet close to the surface.

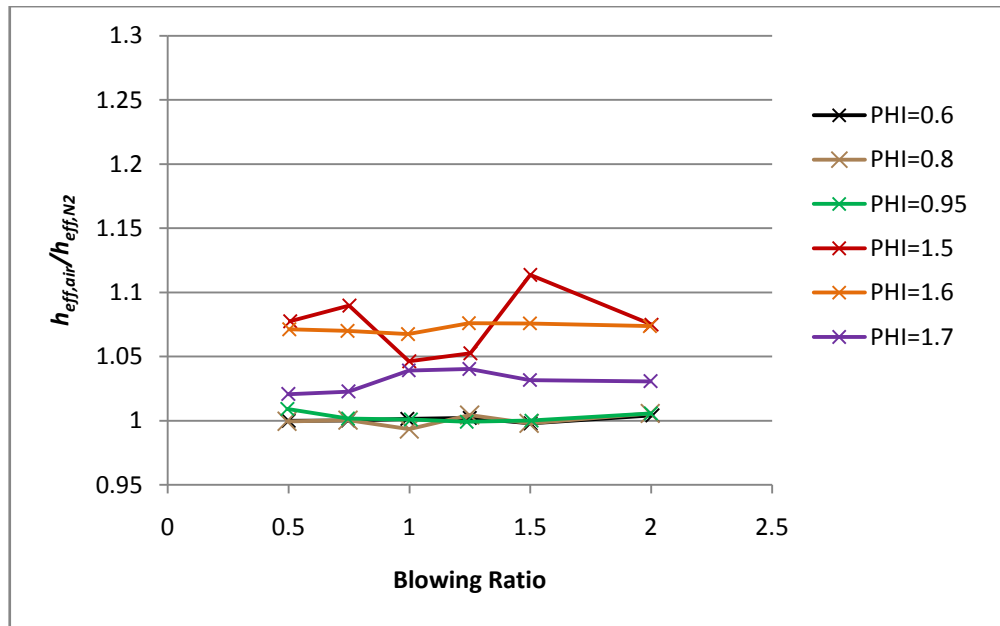


Figure 80. Increase in h_{eff} due to reactions, normal holes

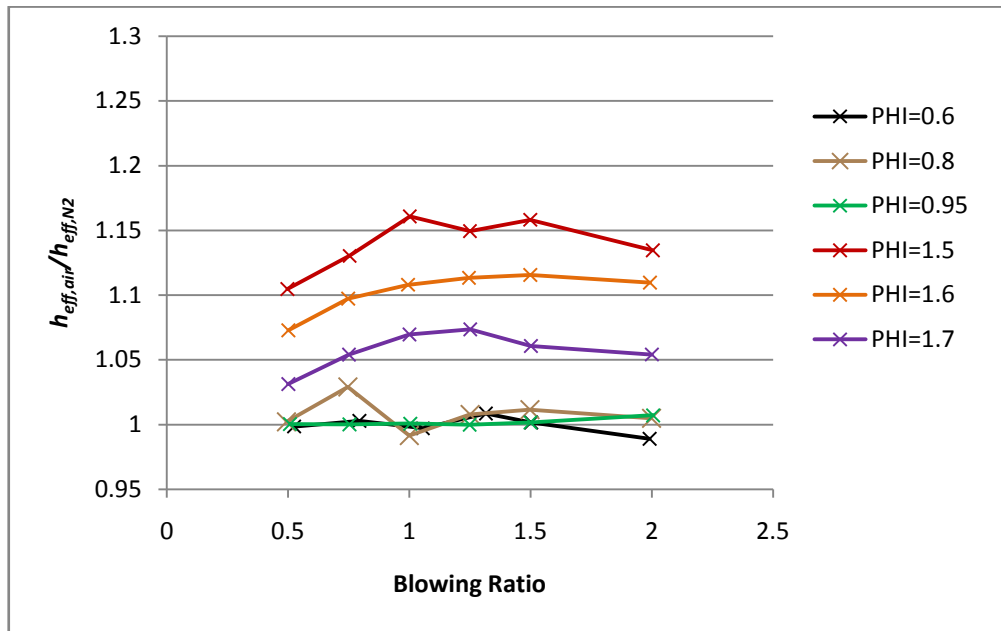


Figure 81. Increase in h_{eff} due to reactions, angled holes

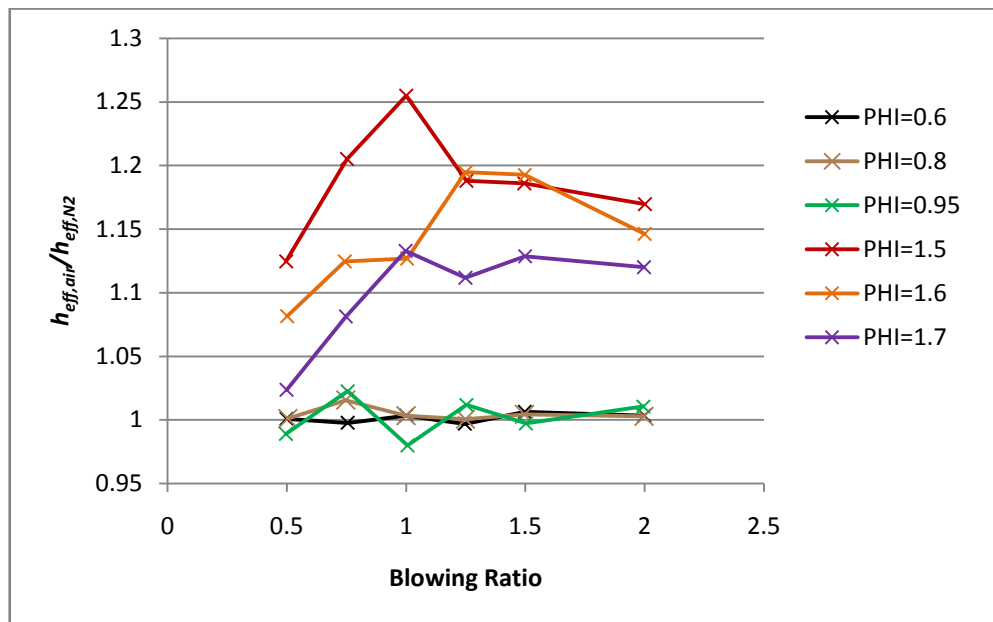


Figure 82. Increase in h_{eff} due to reactions, fan-shaped holes

4.9 Local Temperature Rise

Instead of viewing the increase in q'' as an effective increase in h , it is perhaps better represented as a local increase in T_{ref} . Using the h_{eff} determined for nitrogen at a given WSR test condition and cooling hole geometry, the increase in temperature (ΔT) is calculated using Eqn. (37).

$$\Delta T = \frac{q''}{h_{eff,N2}} - (T_{ref} - T_s) \quad (37)$$

The calculated values of ΔT for each geometry at both upstream (solid lines) and downstream (broken lines) locations are given in Figure 83. These values are from one half to one quarter of the values reported in Figure 8⁵. When comparing these values, it is important to note that Figure 83 reports a temperature rise associated with T_∞ , not T_f , and that the temperature rise is spatially averaged over the area of the heat transfer gauge. With these differences in mind, the results presented here compare well with Ref. 5.

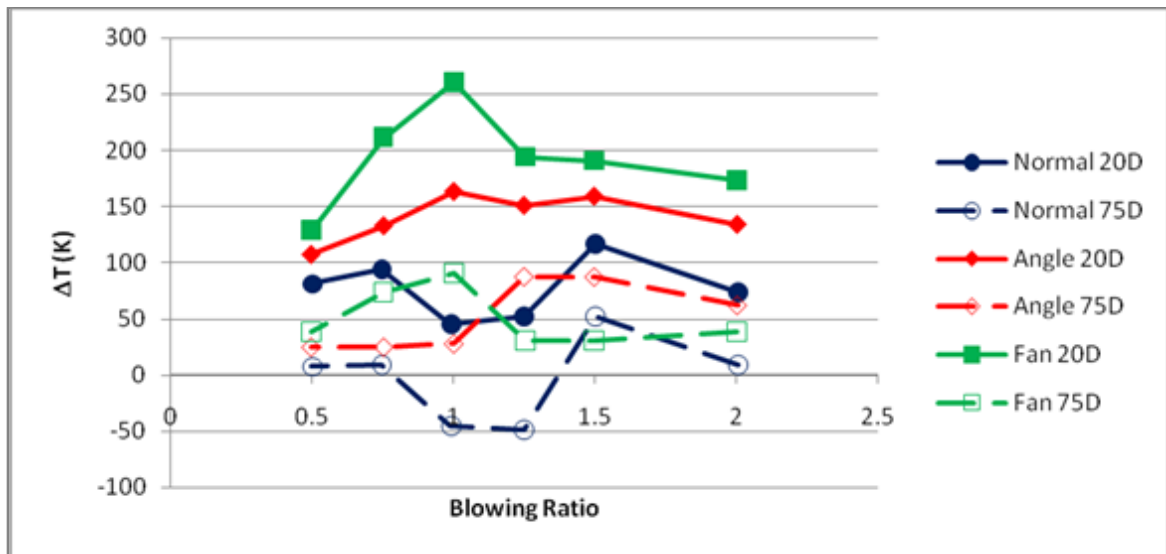


Figure 83. Local temperature increase, all geometries, $\Phi = 1.5$, $\dot{m}_{air} = 1020$ g/min

V. Conclusion

5.1 Overview

In this study, the impact of heat release in turbine film cooling was explored, specifically the interaction of cooling flow with the exhaust of a fuel-rich well-stirred-reactor operating at high temperatures over a flat plate. A test rig was designed and constructed with modular components to allow different cooling hole geometries to be studied. The cooling holes were supplied with either air or nitrogen, allowing the effect of reactions to be isolated. The design of the rig will also support follow-on studies that will use laser diagnostics and high temperature thin film gauge arrays to further explore the impact of heat release. Surface temperatures, heat flux, and heat transfer coefficients were calculated for a variety of reactor fuel-to-air ratios, cooling hole geometries, and blowing ratios. These results were analyzed and compared for different cooling geometries.

5.2 Major Findings

The mixing of oxygen rich turbine cooling air with a combustor exhaust stream containing unburned fuel may result in reactions occurring in the cooling film. These reactions occur close to the surface, and result in augmented heat transfer to the metal. The magnitude of the increase in heat transfer is driven by the fuel content of the combustor exhaust stream, the blowing ratio, and the geometry of the cooling holes. There is no indication in this study that reactions in the boundary layer cause augmented heat transfer at fuel-to-air ratios less than stoichiometric.

The effective heat transfer coefficient was measured for cylindrical normal holes, cylindrical holes with a 30° injection angle, and cylindrical holes with a 30° injection

angle and a laidback, fanshaped exit. The results indicate that the fanshaped holes provide a lower heat transfer coefficient at all reactor test conditions, but that the advantage is seriously degraded by the presence of fuel in the exhaust stream. A turbine cooling scheme designed to take advantage of the improved performance of the fanshaped holes in a nonreactive condition could under-predict the magnitude of augmented heat release due to fuel streaks, potentially resulting in turbine durability degradation.

5.3 *Recommendations for Further Research*

There remains much to be gained from the continuation of current research on a flat plate geometry. Collecting data at higher temperatures, particularly in the fuel-rich regime, would provide more information to illuminate the relationship between chemical reaction rates and heat release in the cooling film. The collection of chemical samples in the test section would assist this effort. Photographs of the burning cooling jets for different geometries at a common WSR test condition would allow a better understanding of the role that penetration depth and plume length play in heat transfer.

The use of Thin Film Gauges and High Density Thin Film Gauge arrays would allow surface temperature measurements that are resolved in the span-wise and stream-wise directions. These gauges could be inserted into the rig while it is running, capturing high frequency transient data that could lead to better measurements of heat transfer and cooling effectiveness. The application of laser diagnostics, particularly Planar Laser Induced Fluorescence, would allow the determination of gas temperatures within the cooling film. This would enable an estimation of film temperature and a determination of actual heat transfer coefficients instead of the effective measurement given in this report.

Laser diagnostics would also allow the determination of a three dimensional gas temperature profile, providing a better physical understanding of the processes that occur in a reacting boundary layer.

The goal of the research program is to lay the experimental groundwork for the design a turbine cooling scheme for use with the Ultra-Compact Combustor/Inter-Turbine Burner. Therefore, it is desirable to conduct similar tests at conditions more representative of an actual combustor. Tests at realistic turbine pressures and flow conditions would eliminate the difficulty of scaling aerodynamic and chemical parameters concurrently. Ultimately, tests on realistic blade shapes in realistic flow conditions would most completely achieve the goals of this research effort.

Appendix A Temperature Data

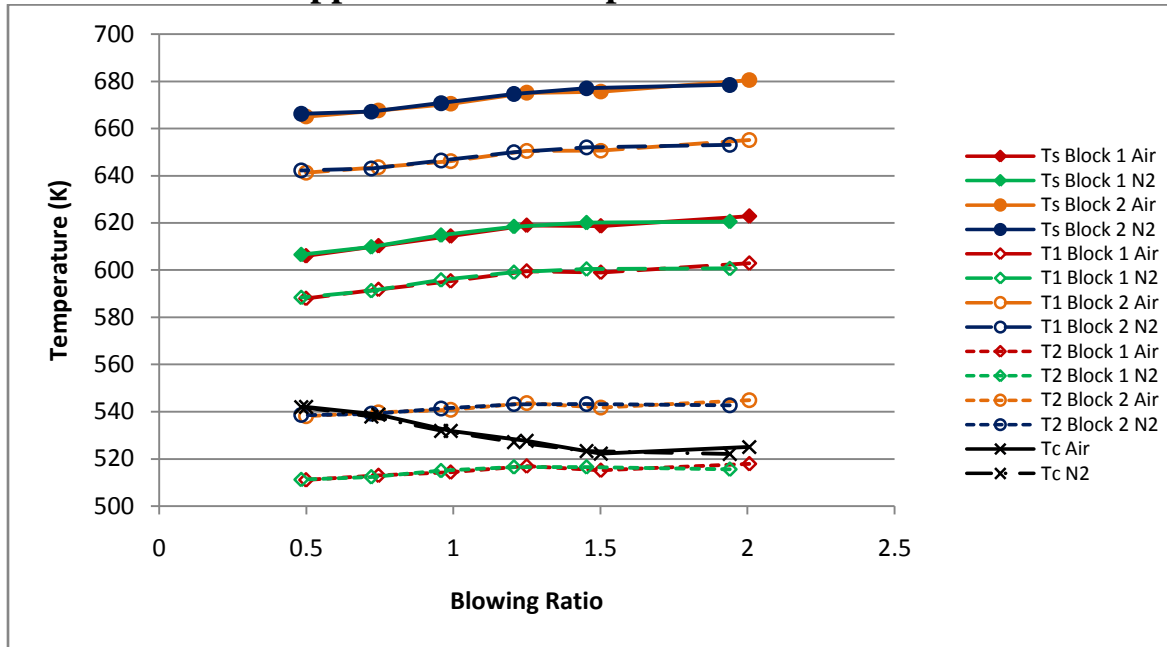


Figure 84. Temperature data, normal holes, $\Phi = 0.6$, $\dot{m}_{air} = 1020$ g/min, upstream gauges

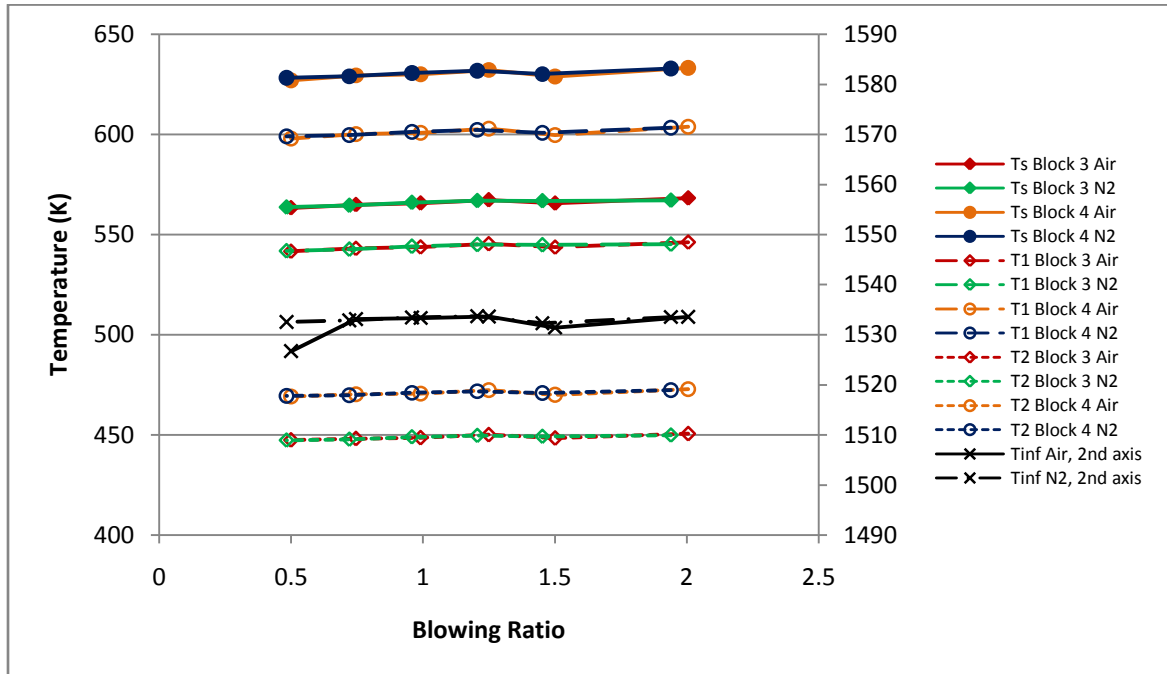


Figure 85. Temperature data, normal holes, $\Phi = 0.6$, $\dot{m}_{air} = 1020$ g/min, downstream gauges

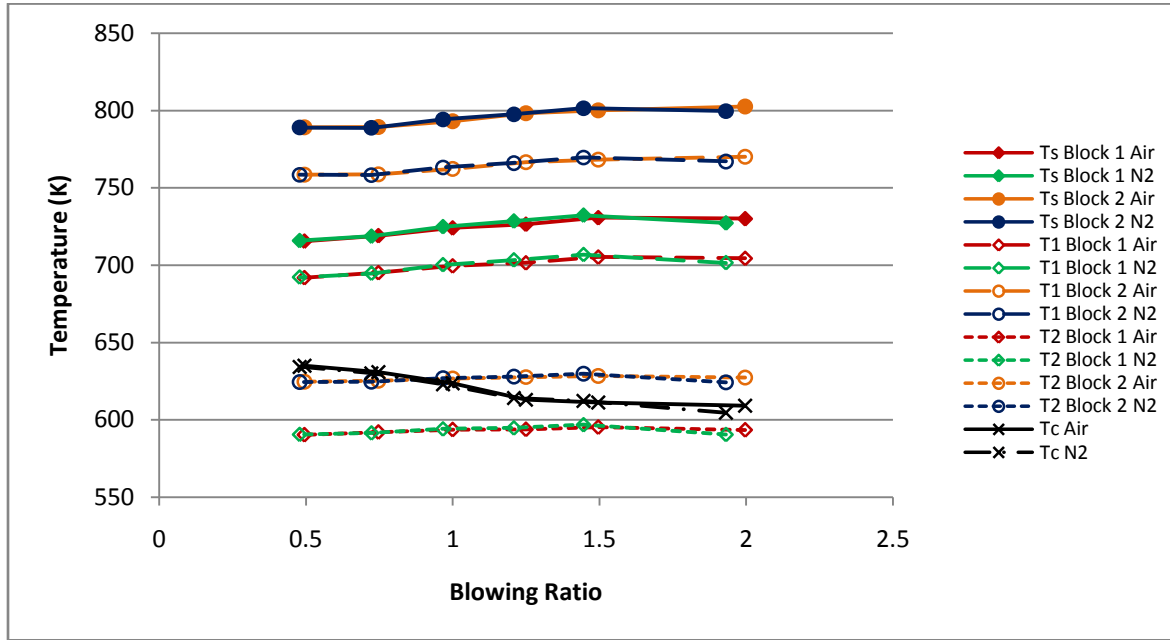


Figure 86. Temperature data, normal holes, $\Phi = 0.8$, $\dot{m}_{air} = 1020$ g/min, upstream gauges

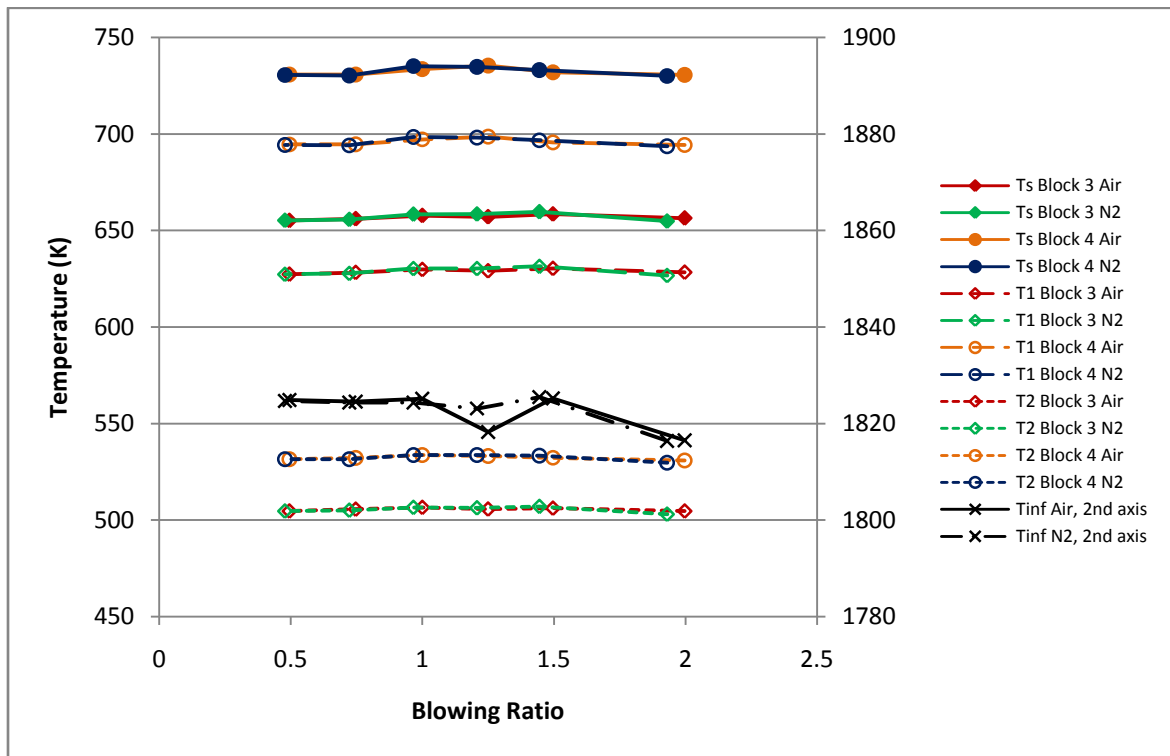


Figure 87. Temperature data, normal holes, $\Phi = 0.8$, $\dot{m}_{air} = 1020$ g/min, downstream gauges

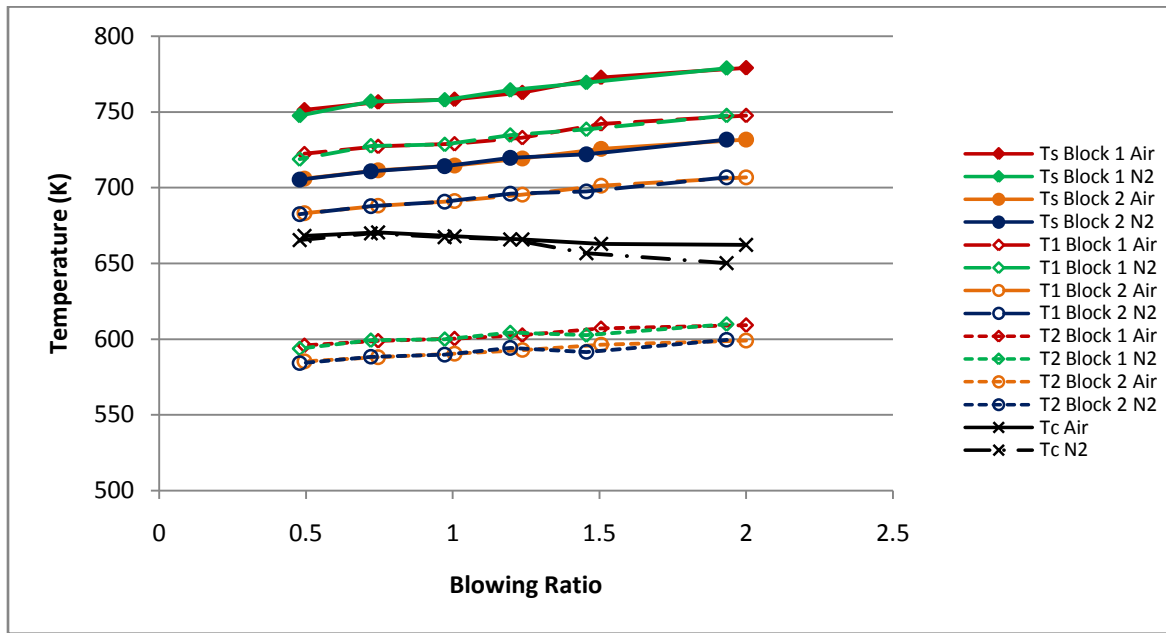


Figure 88. Temperature data, normal holes, $\Phi = 0.95$, $\dot{m}_{air} = 720$ g/min, upstream gauges

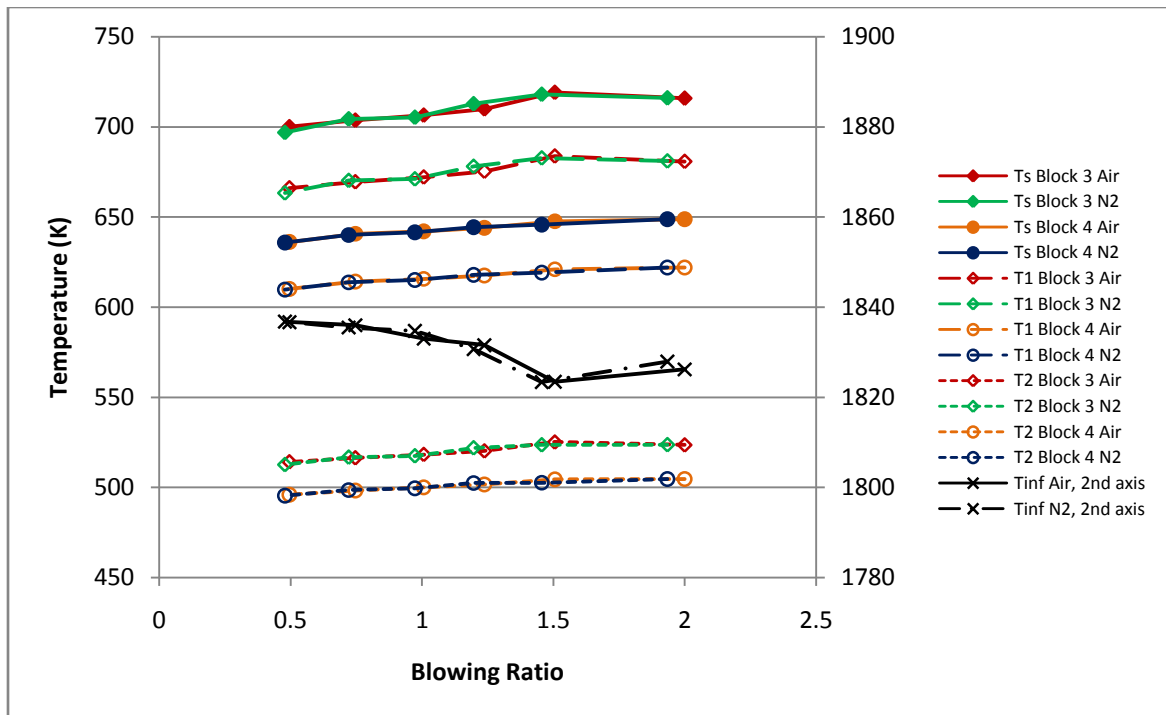


Figure 89. Temperature data, normal holes, $\Phi = 0.95$, $\dot{m}_{air} = 720$ g/min, downstream gauges

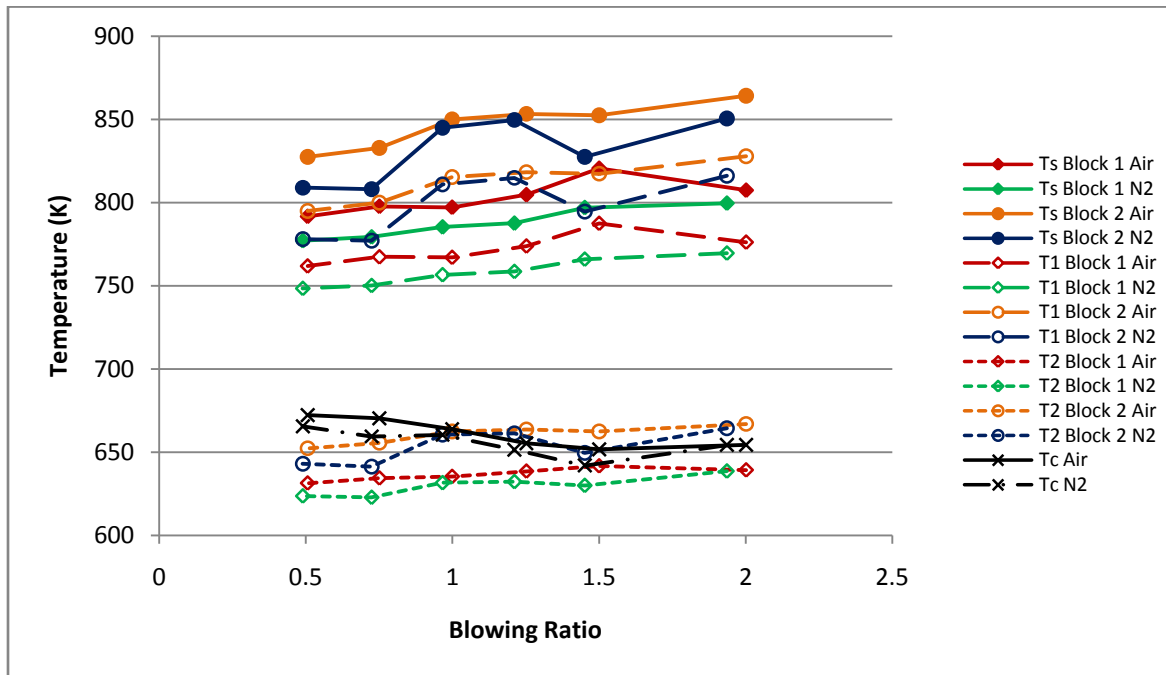


Figure 90. Temperature data, normal holes, $\Phi = 1.5$, $\dot{m}_{air} = 1020$ g/min, upstream gauges

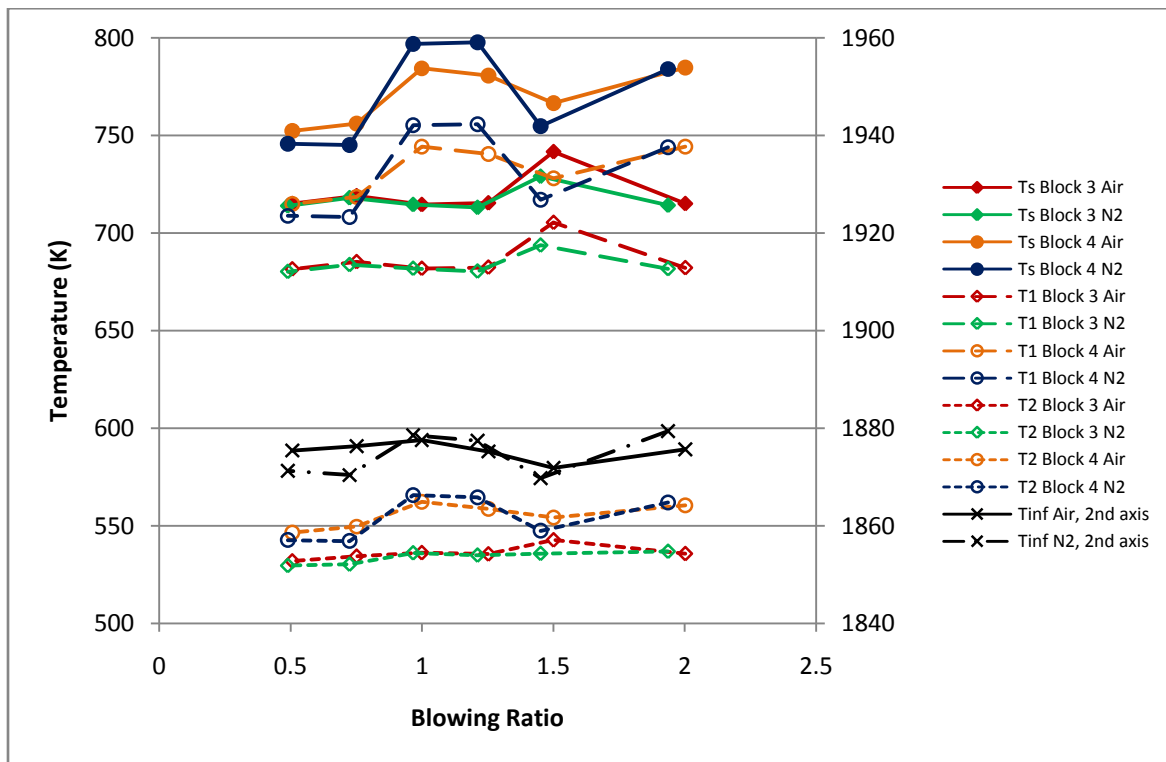


Figure 91. Temperature data, normal holes, $\Phi = 1.5$, $\dot{m}_{air} = 1020$ g/min, downstream gauges

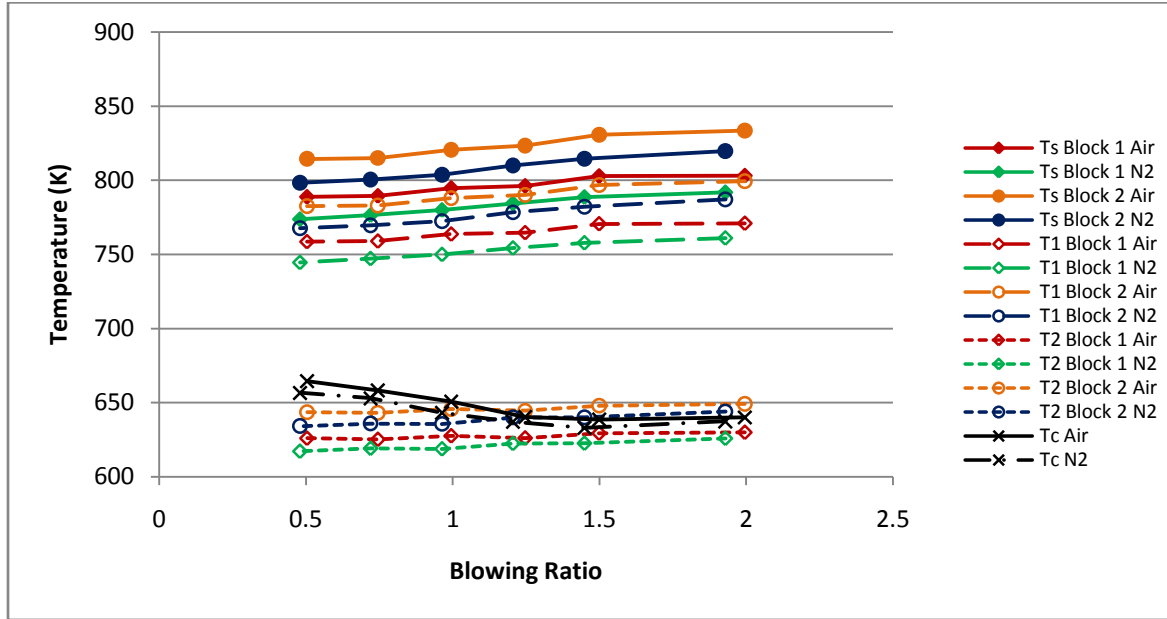


Figure 92. Temperature data, normal holes, $\Phi = 1.6$, $\dot{m}_{air} = 1020$ g/min, upstream gauges

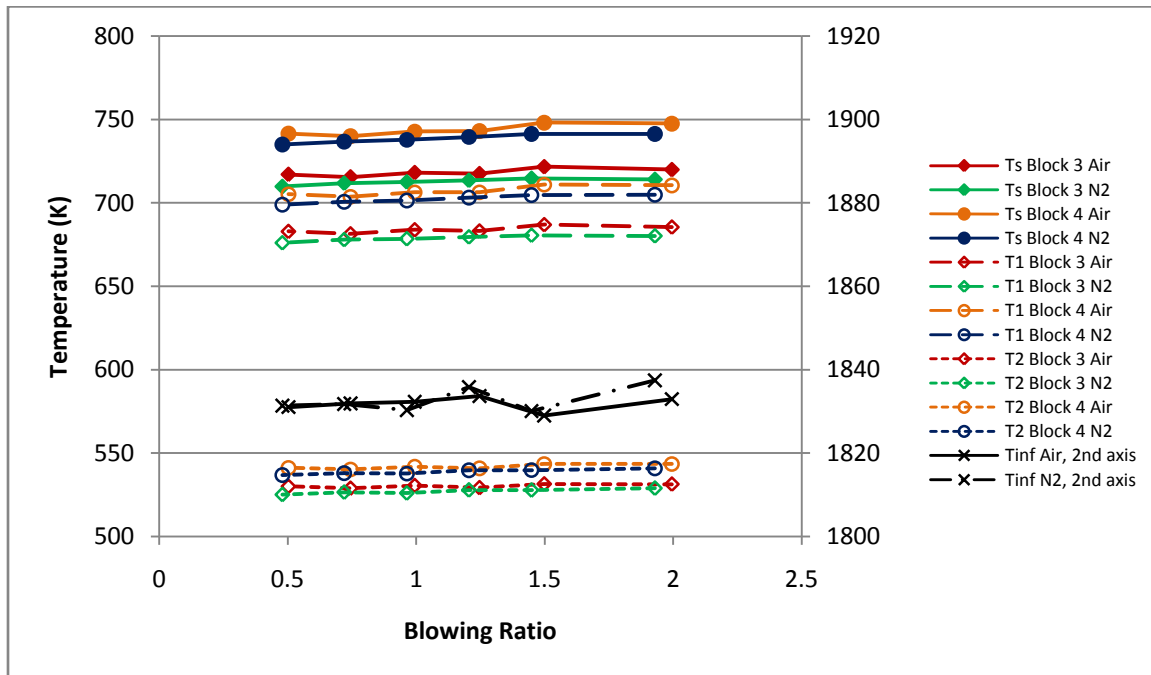


Figure 93. Temperature data, normal holes, $\Phi = 1.6$, $\dot{m}_{air} = 1020$ g/min, downstream gauges

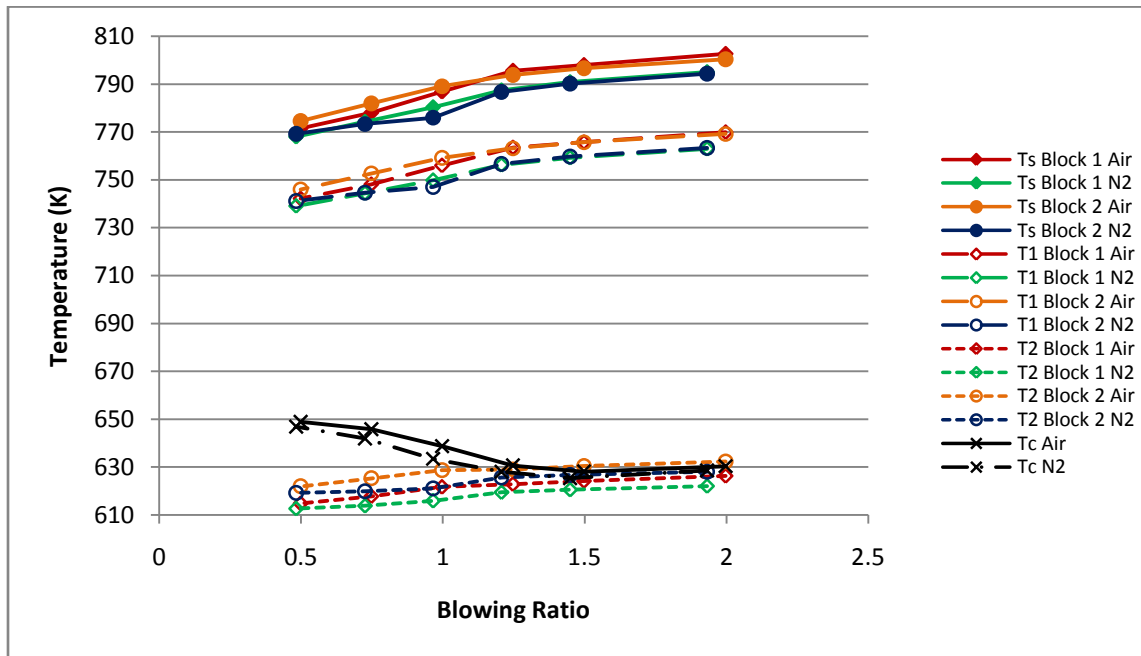


Figure 94. Temperature data, normal holes, $\Phi = 1.7$, $\dot{m}_{air} = 1020$ g/min, upstream gauges

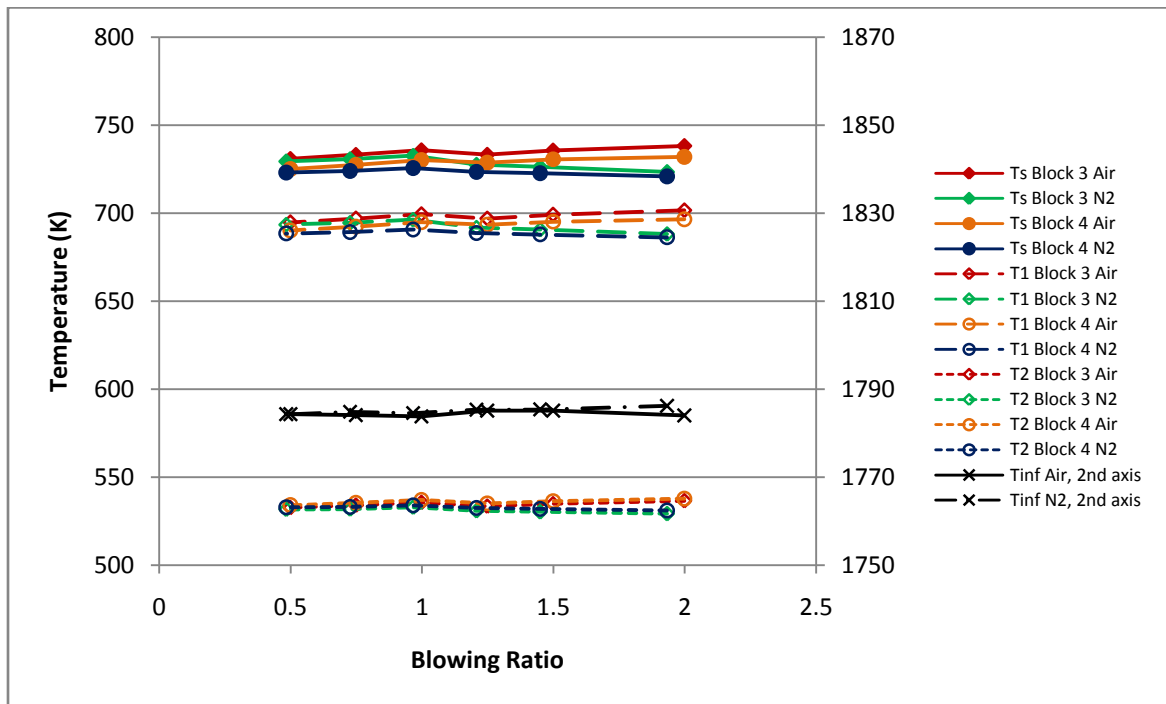


Figure 95. Temperature data, normal holes, $\Phi = 1.7$, $\dot{m}_{air} = 1020$ g/min, downstream gauges

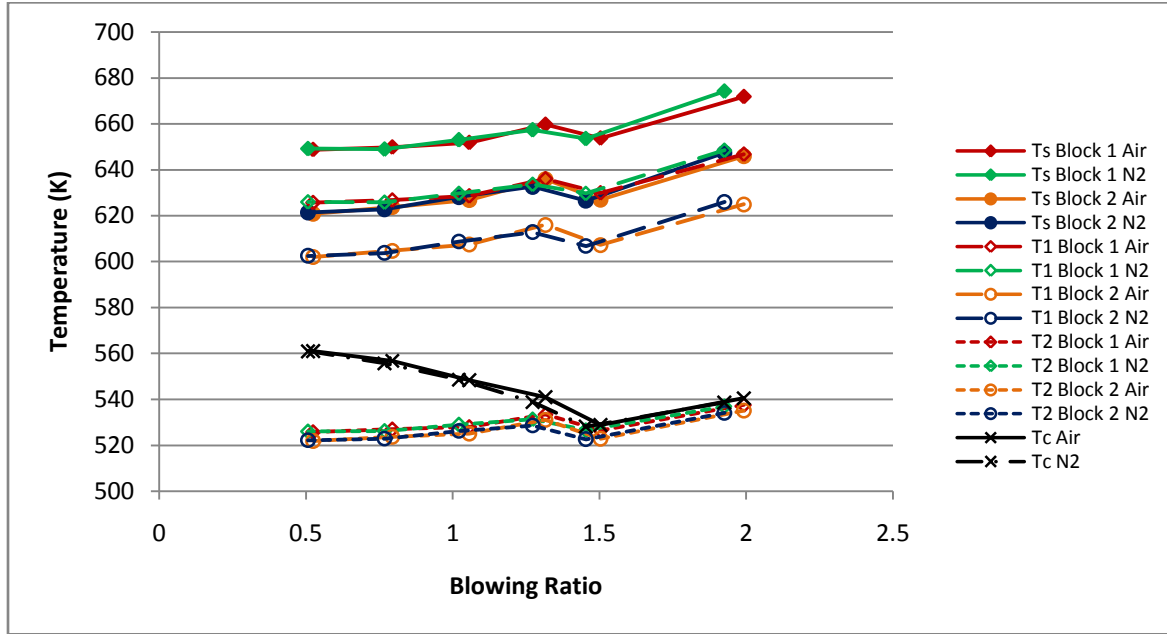


Figure 96. Temperature data, angled holes, $\Phi = 0.6$, $\dot{m}_{air} = 1020$ g/min, upstream gauges

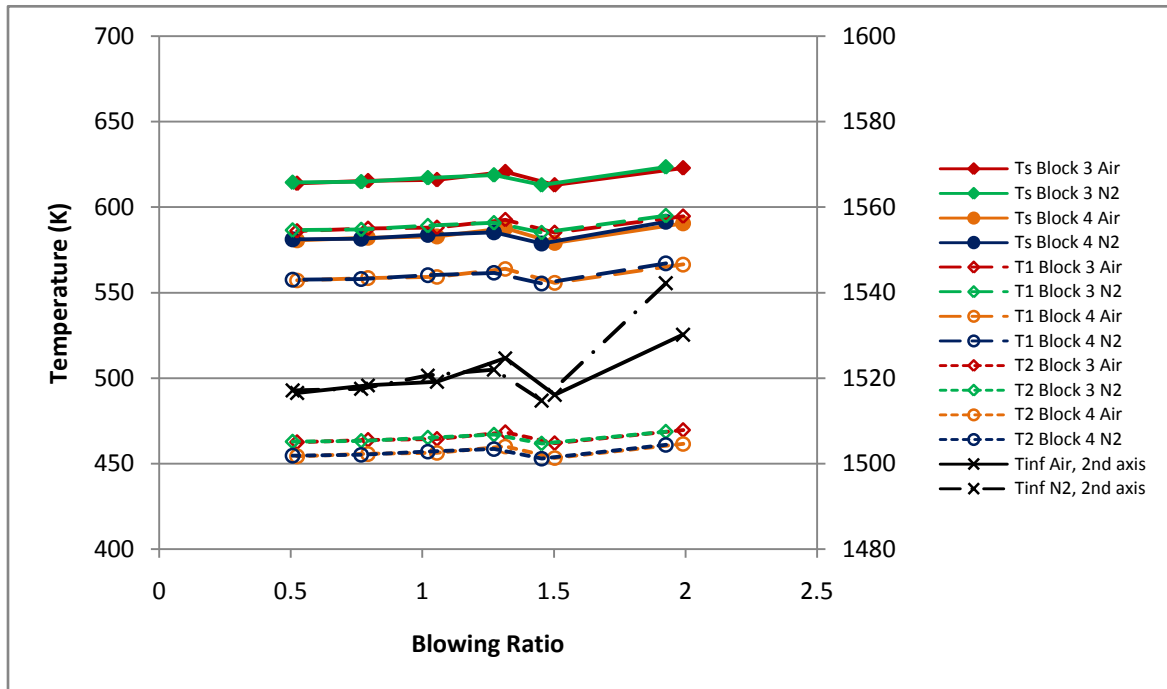


Figure 97. Temperature data, angled holes, $\Phi = 0.6$, $\dot{m}_{air} = 1020$ g/min, downstream gauges

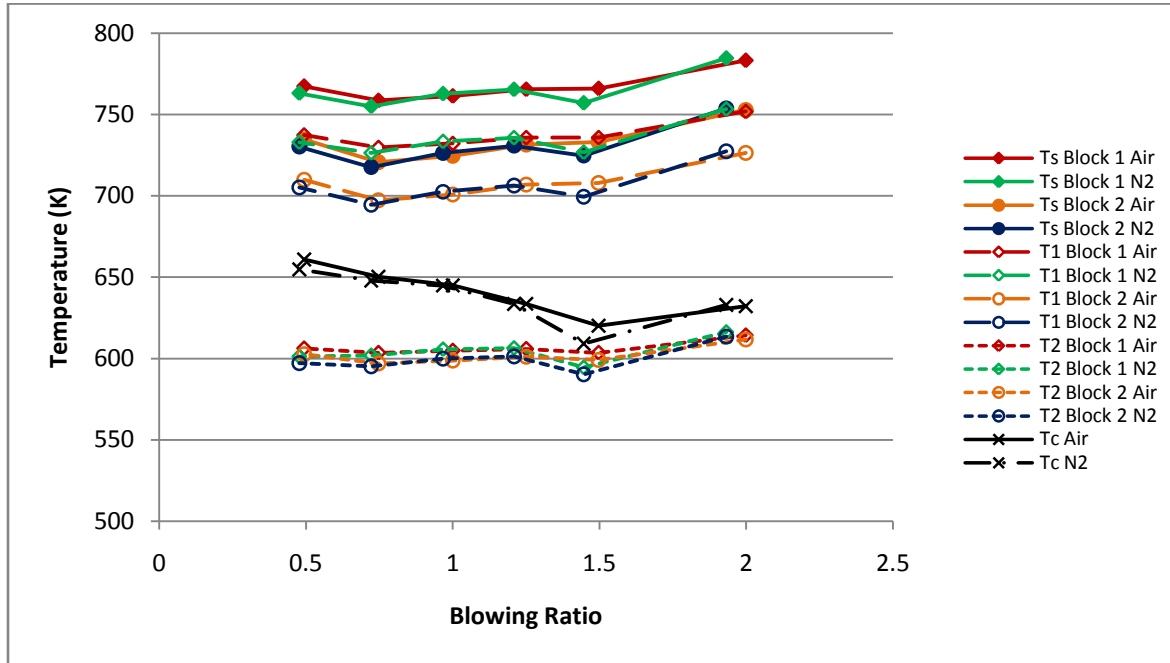


Figure 98. Temperature data, angled holes, $\Phi = 0.8$, $\dot{m}_{air} = 1020$ g/min, upstream gauges

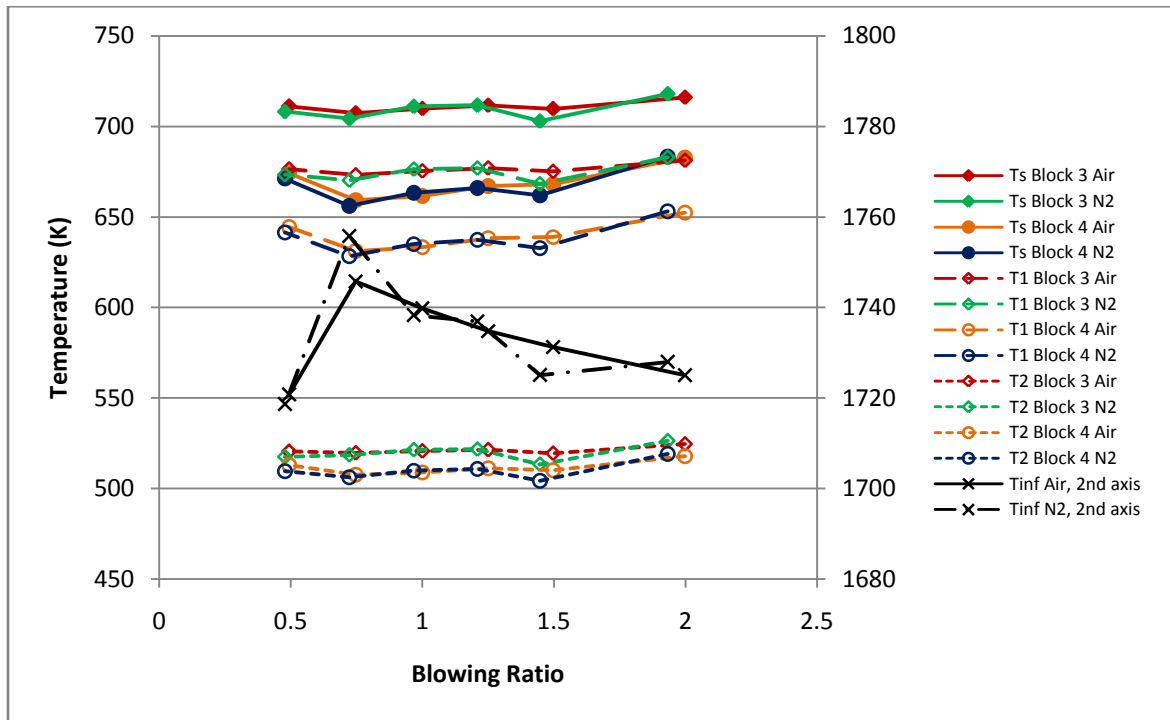


Figure 99. Temperature data, angled holes, $\Phi = 0.8$, $\dot{m}_{air} = 1020$ g/min, downstream gauges

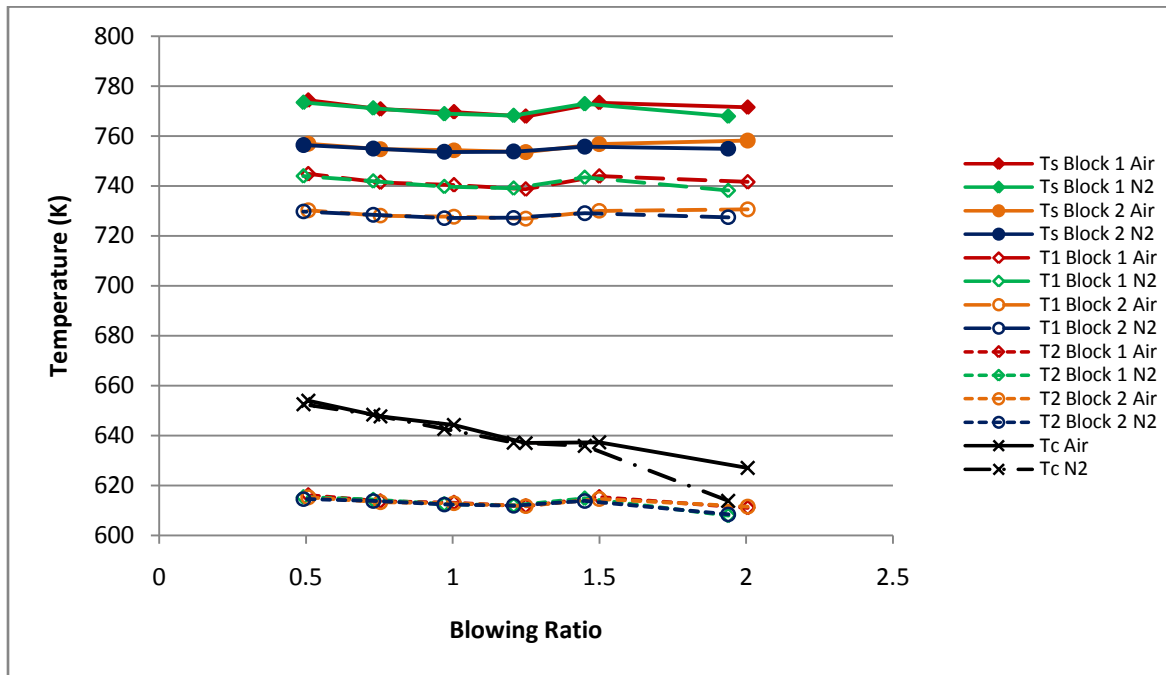


Figure 100. Temperature data, angled holes, $\Phi = 0.95$, $\dot{m}_{air} = 720$ g/min, upstream gauges

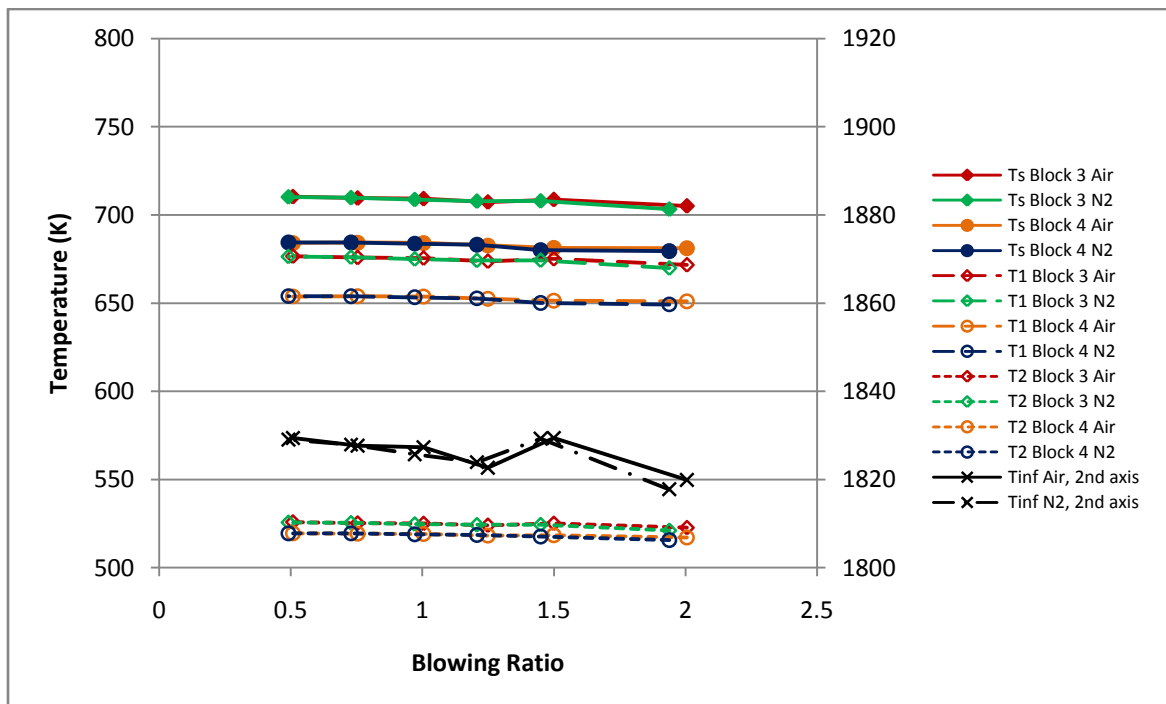


Figure 101. Temperature data, angled holes, $\Phi = 0.95$, $\dot{m}_{air} = 720$ g/min, downstream gauges

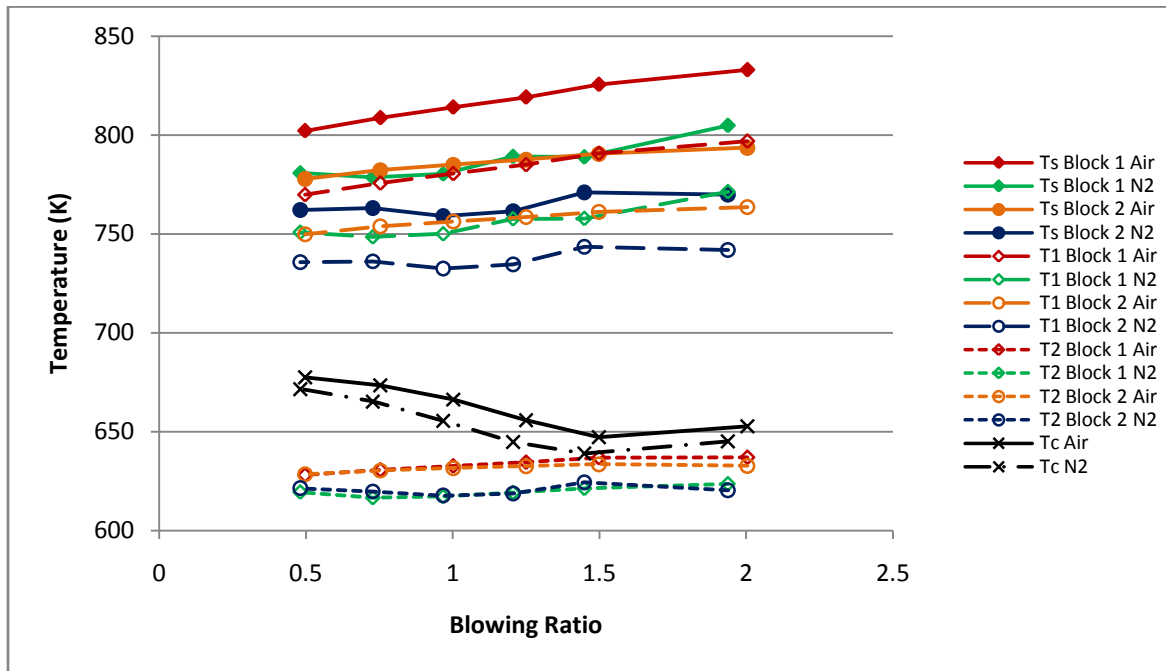


Figure 102. Temperature data, angled holes, $\Phi = 1.5$, $\dot{m}_{air} = 1020$ g/min, upstream gauges

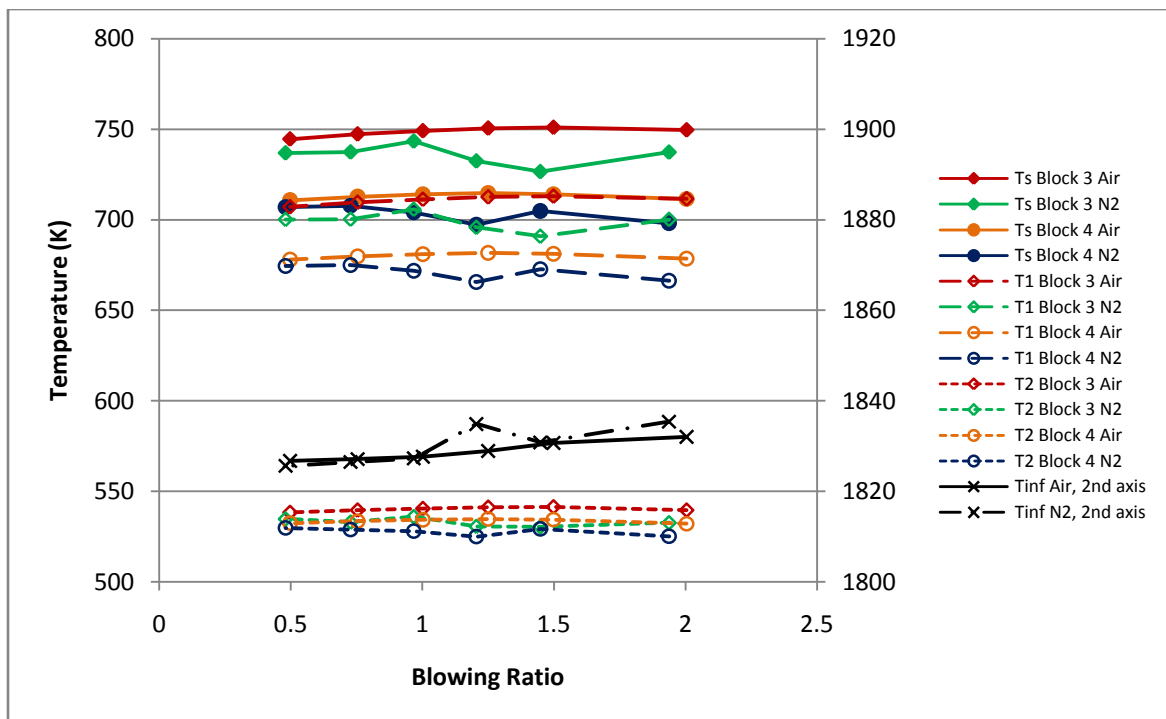


Figure 103. Temperature data, angled holes, $\Phi = 1.5$, $\dot{m}_{air} = 1020$ g/min, downstream gauges

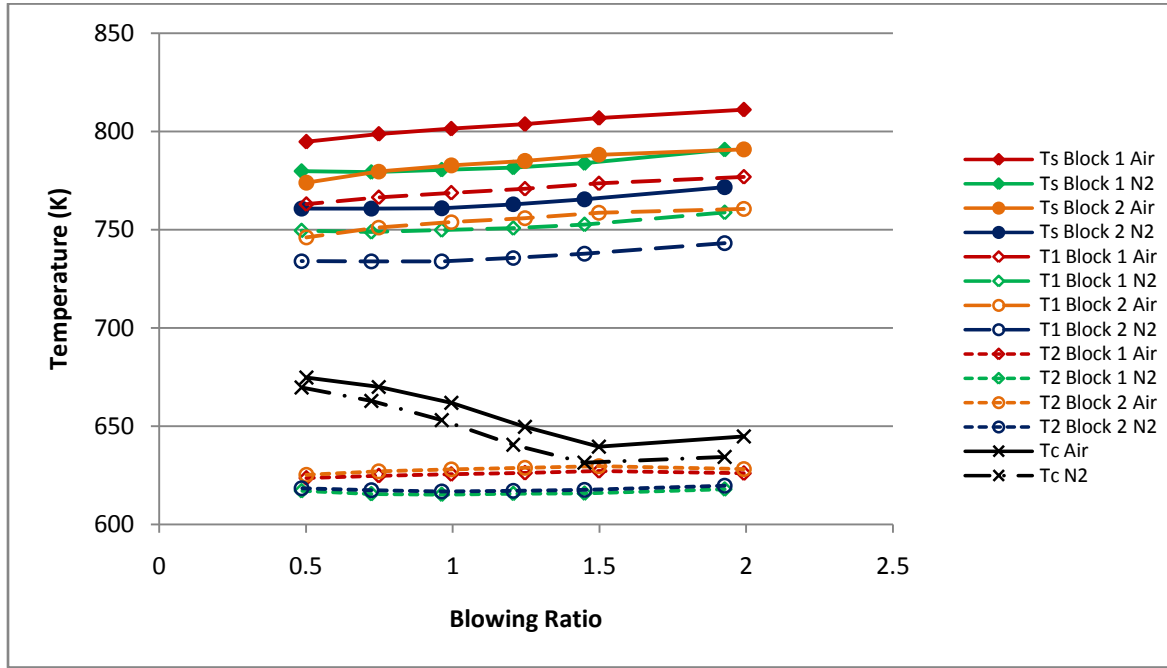


Figure 104. Temperature data, angled holes, $\Phi = 1.6$, $\dot{m}_{air} = 1020$ g/min, upstream gauges

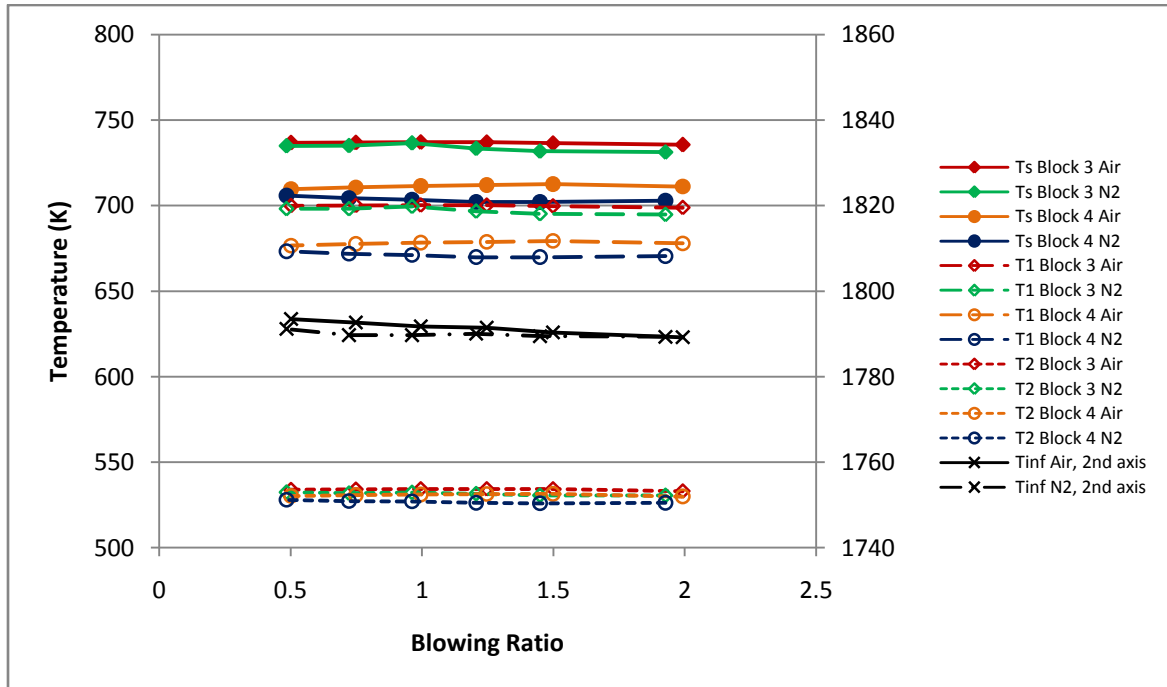


Figure 105. Temperature data, angled holes, $\Phi = 1.6$, $\dot{m}_{air} = 1020$ g/min, downstream gauges

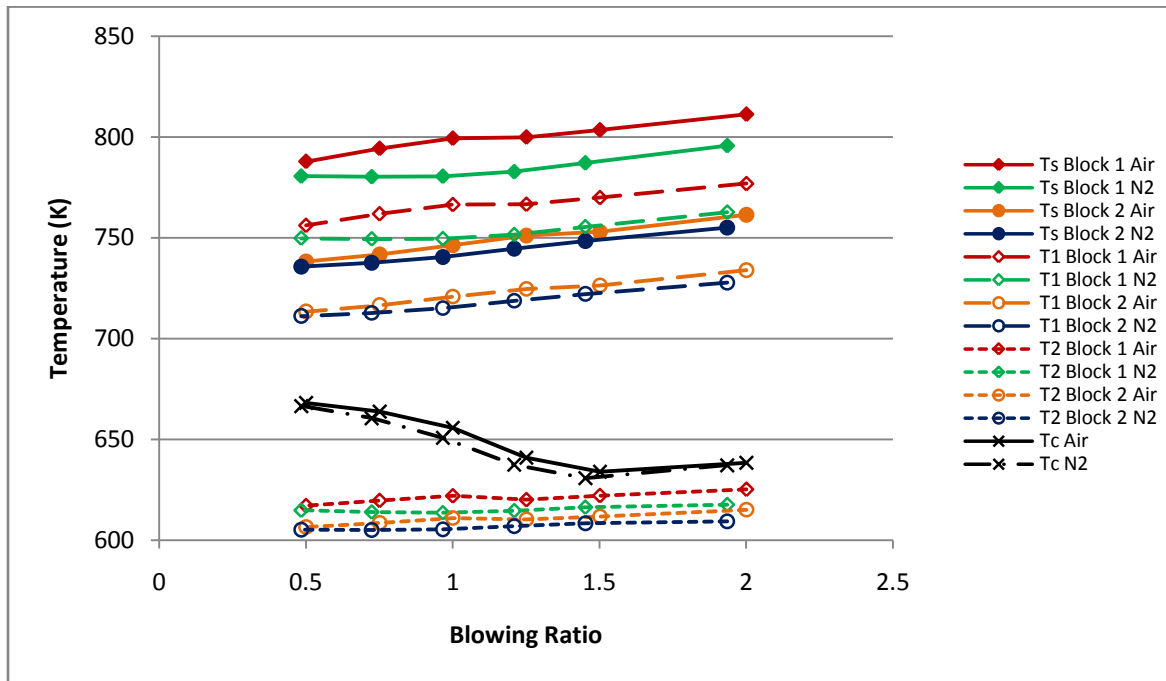


Figure 106. Temperature data, angled holes, $\Phi = 1.7$, $\dot{m}_{air} = 1020$ g/min, upstream gauges

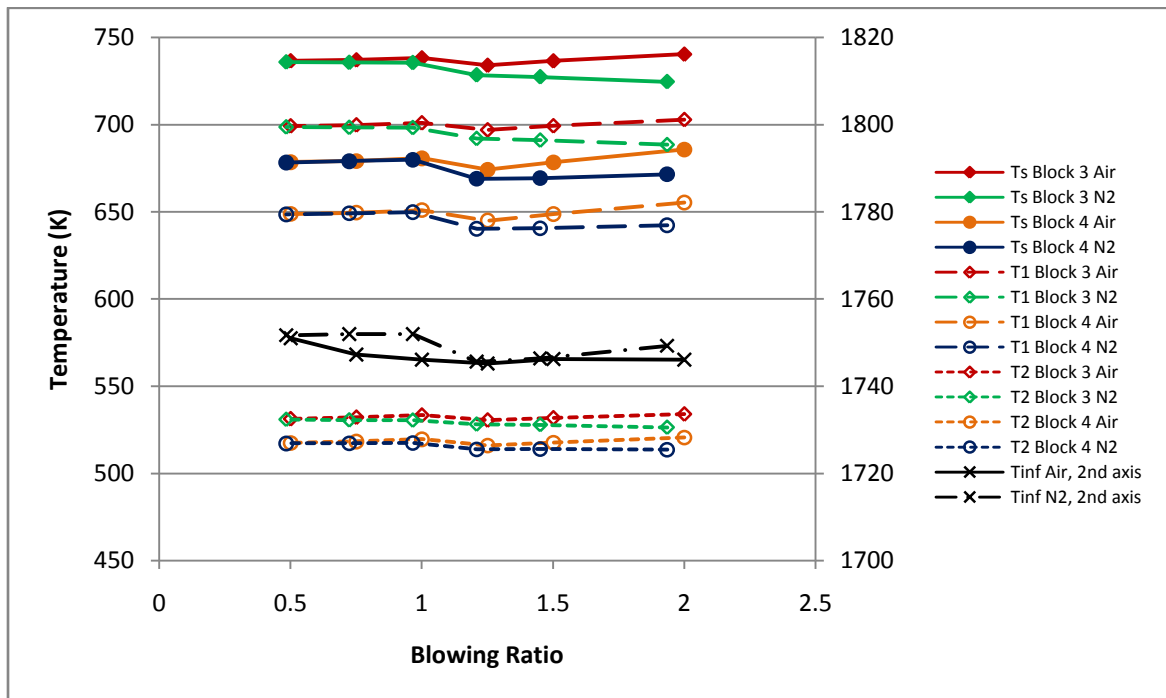


Figure 107. Temperature data, angled holes, $\Phi = 1.7$, $\dot{m}_{air} = 1020$ g/min, downstream gauges

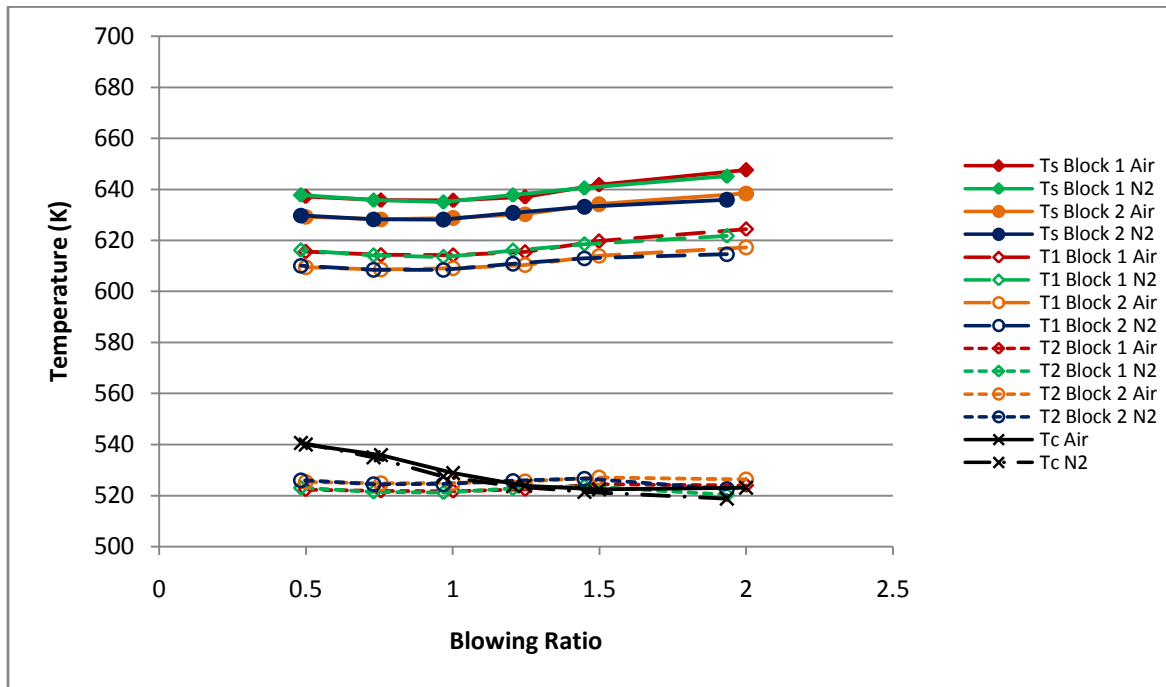


Figure 108. Temperature data, fan-shaped holes, $\Phi = 0.6$, $\dot{m}_{air} = 1020$ g/min, upstream gauges

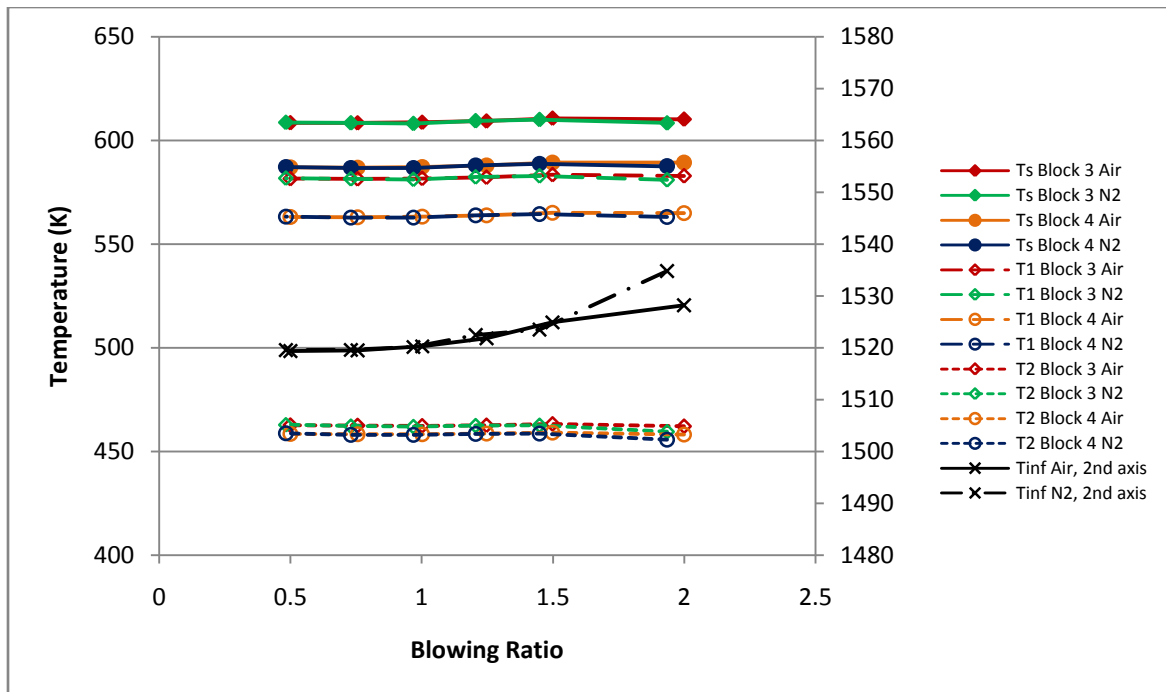


Figure 109. Temperature data, fan-shaped holes, $\Phi = 0.6$, $\dot{m}_{air} = 1020$ g/min, downstream gauges

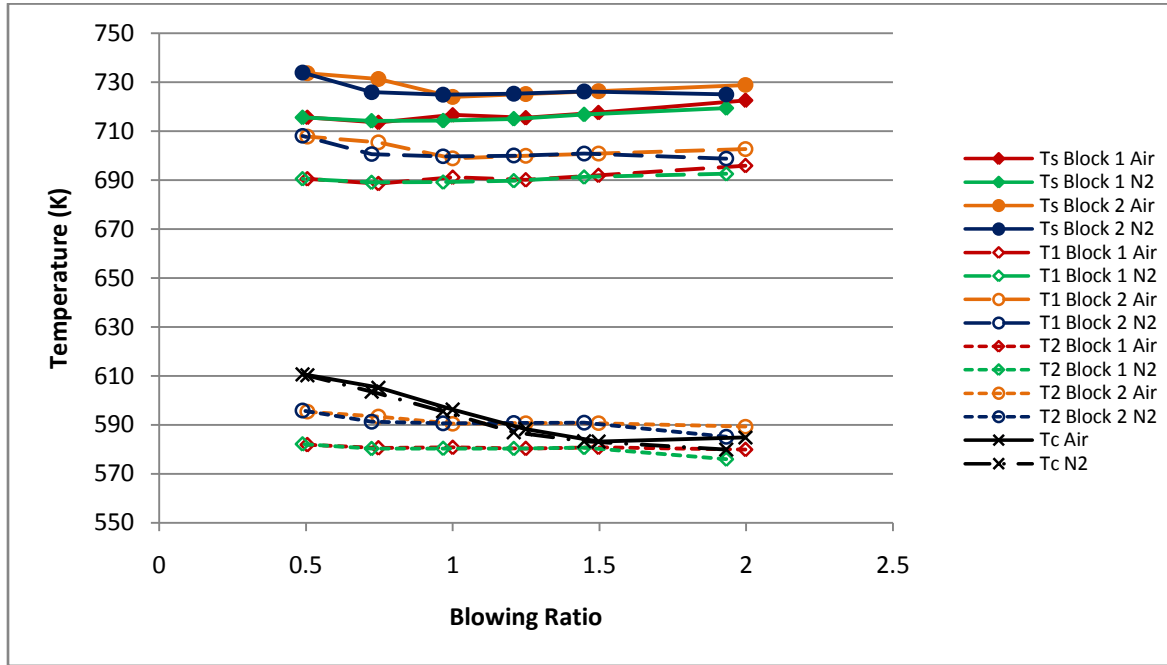


Figure 110. Temperature data, fan-shaped holes, $\Phi = 0.8$, $\dot{m}_{air} = 1020$ g/min, upstream gauges

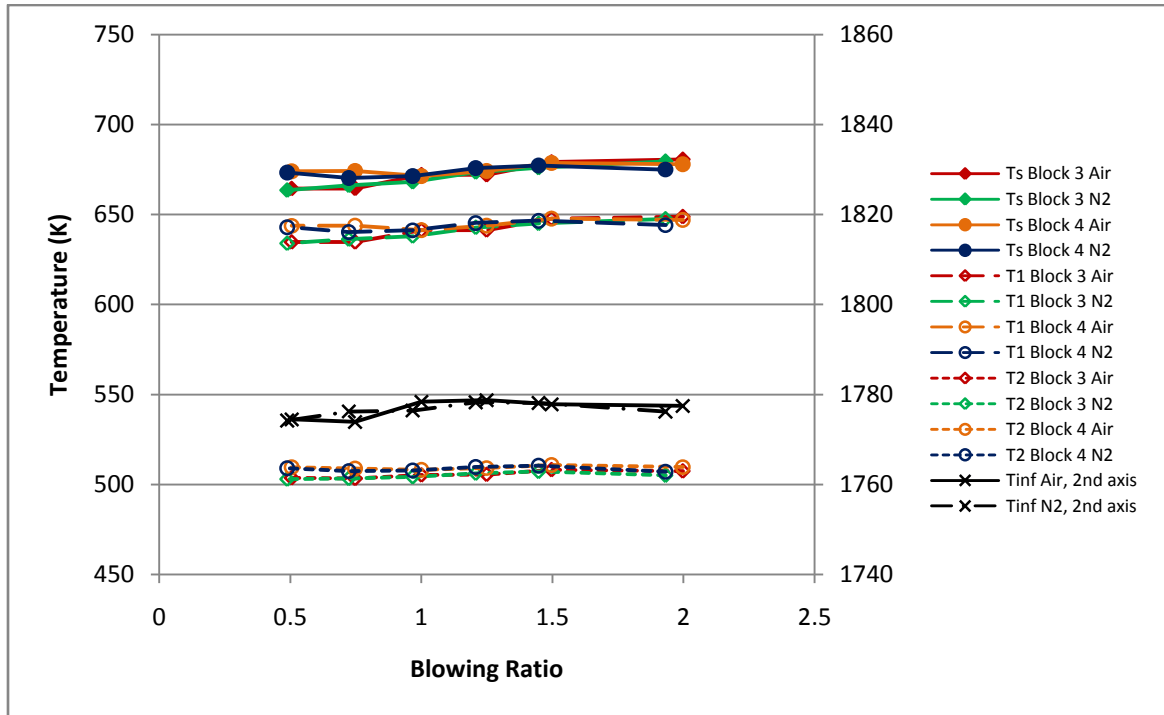


Figure 111. Temperature data, fan-shaped holes, $\Phi = 0.8$, $\dot{m}_{air} = 1020$ g/min, downstream gauges

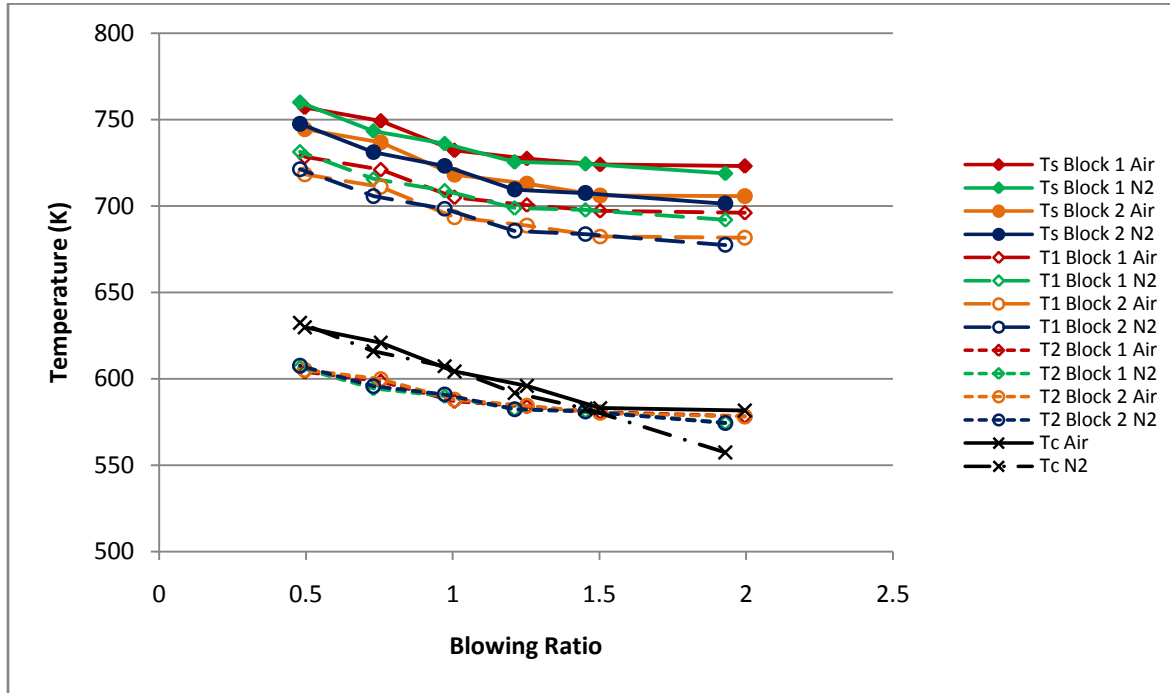


Figure 112. Temperature data, fanshaped holes, $\Phi = 0.95$, $\dot{m}_{air} = 720$ g/min, upstream gauges

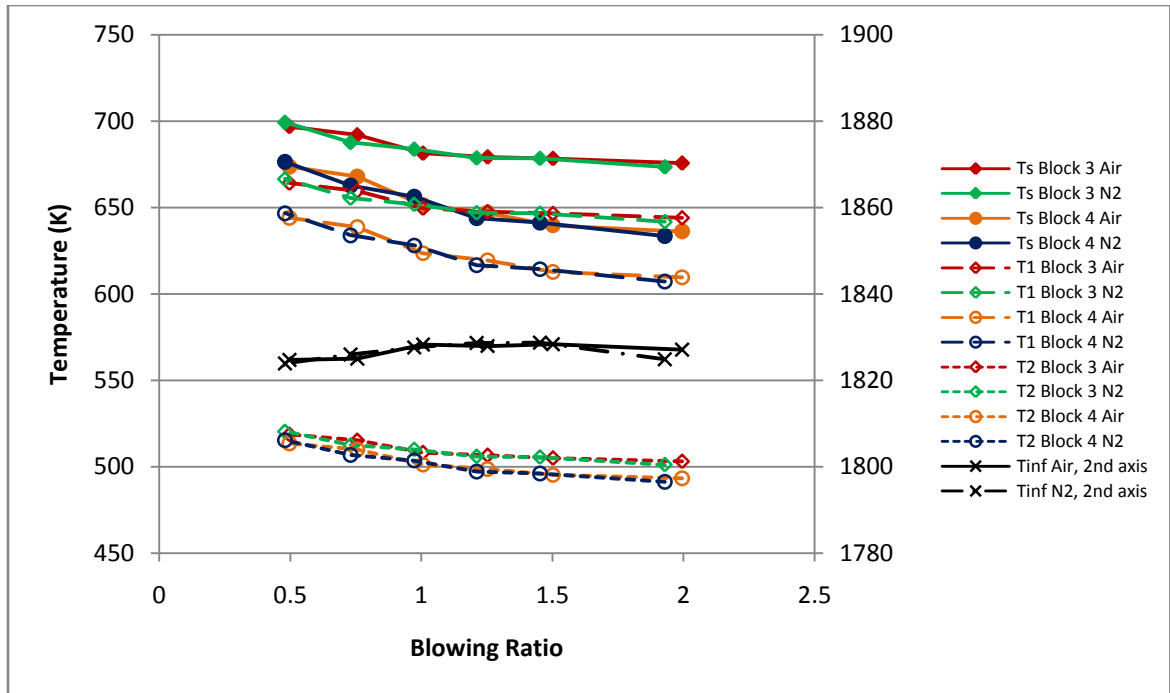


Figure 113. Temperature data, fanshaped holes, $\Phi = 0.95$, $\dot{m}_{air} = 720$ g/min, downstream gauges

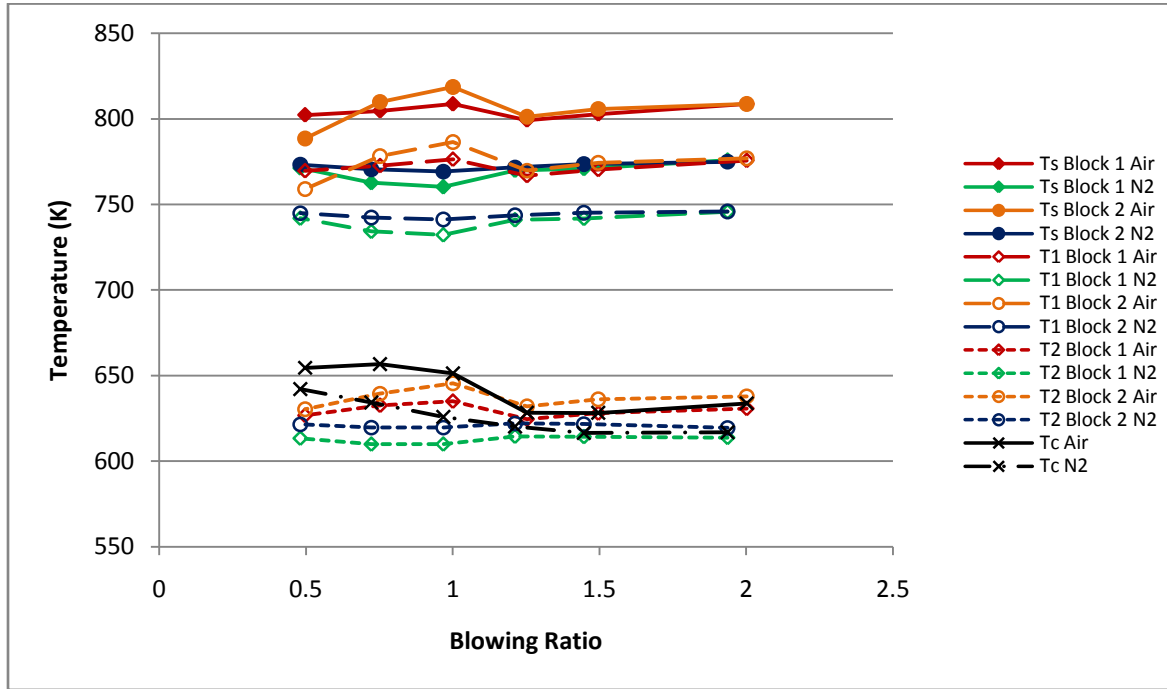


Figure 114. Temperature data, fan-shaped holes, $\Phi = 1.5$, $\dot{m}_{air} = 1020$ g/min, upstream gauges

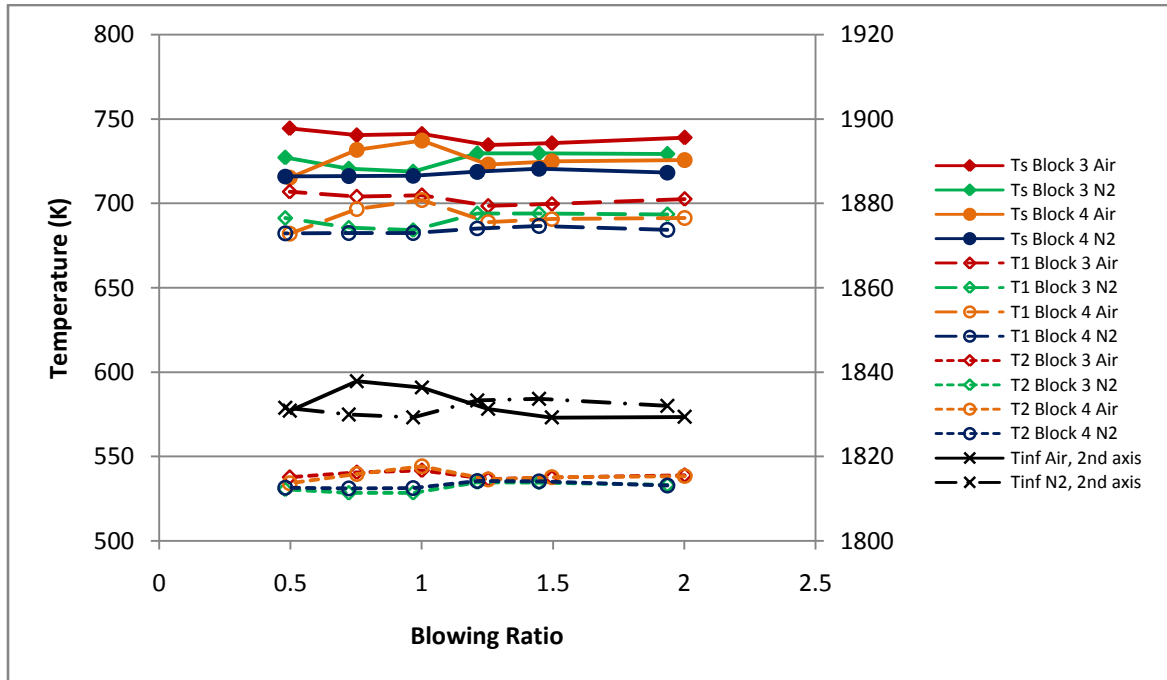


Figure 115. Temperature data, fan-shaped holes, $\Phi = 1.5$, $\dot{m}_{air} = 1020$ g/min, downstream gauges

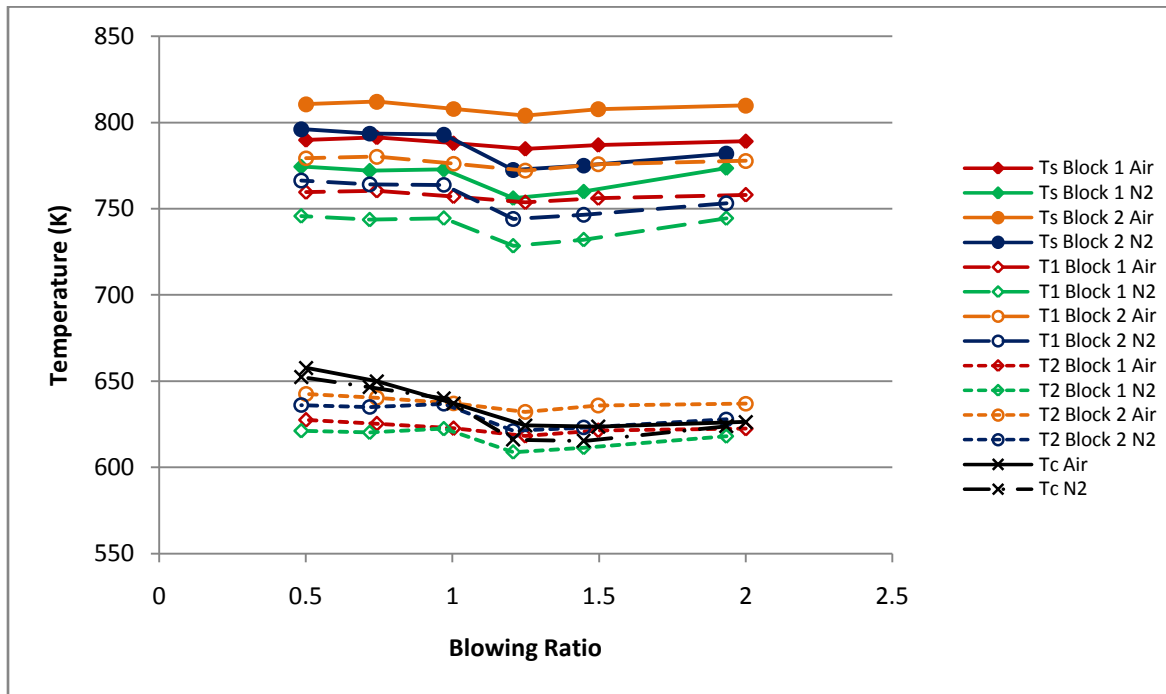


Figure 116. Temperature data, fan-shaped holes, $\Phi = 1.6$, $\dot{m}_{air} = 1020$ g/min, upstream gauges

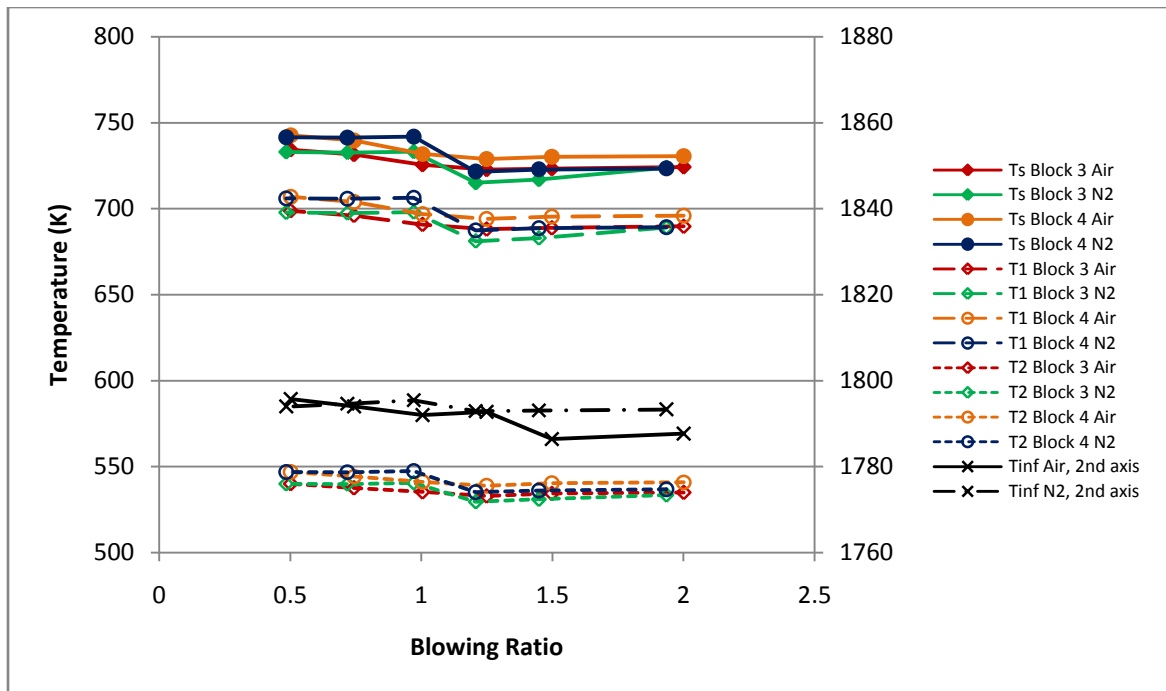


Figure 117. Temperature data, fan-shaped holes, $\Phi = 1.6$, $\dot{m}_{air} = 1020$ g/min, downstream gauges

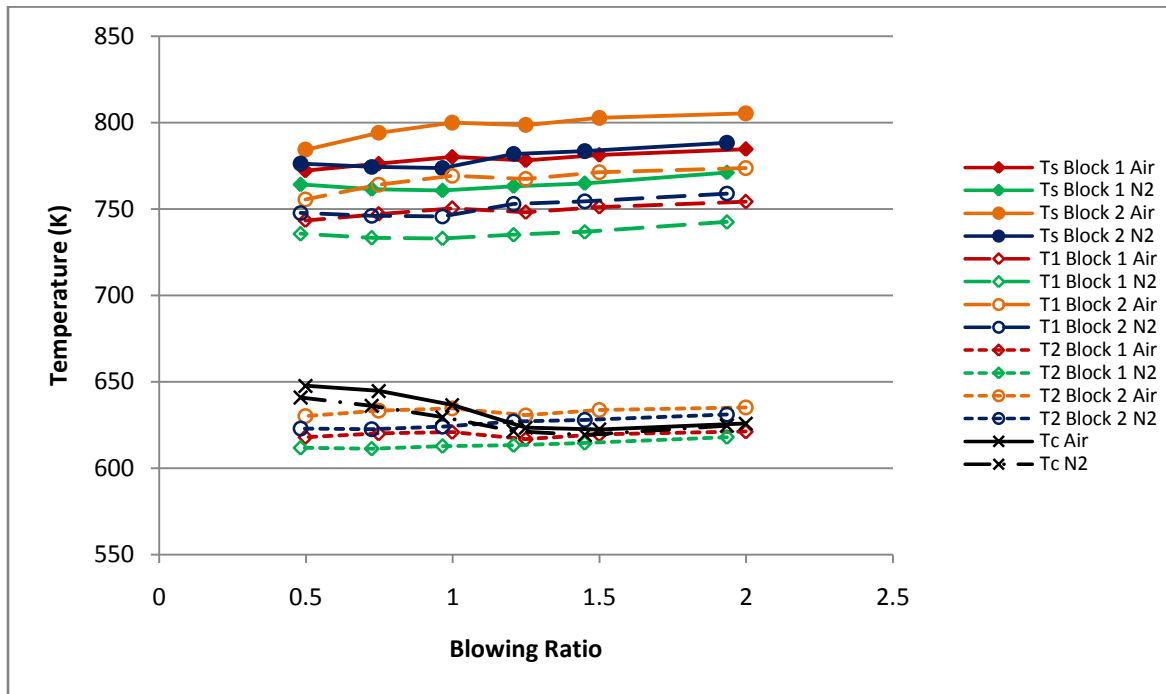


Figure 118. Temperature data, fan-shaped holes, $\Phi = 1.7$, $\dot{m}_{air} = 1020$ g/min, upstream gauges

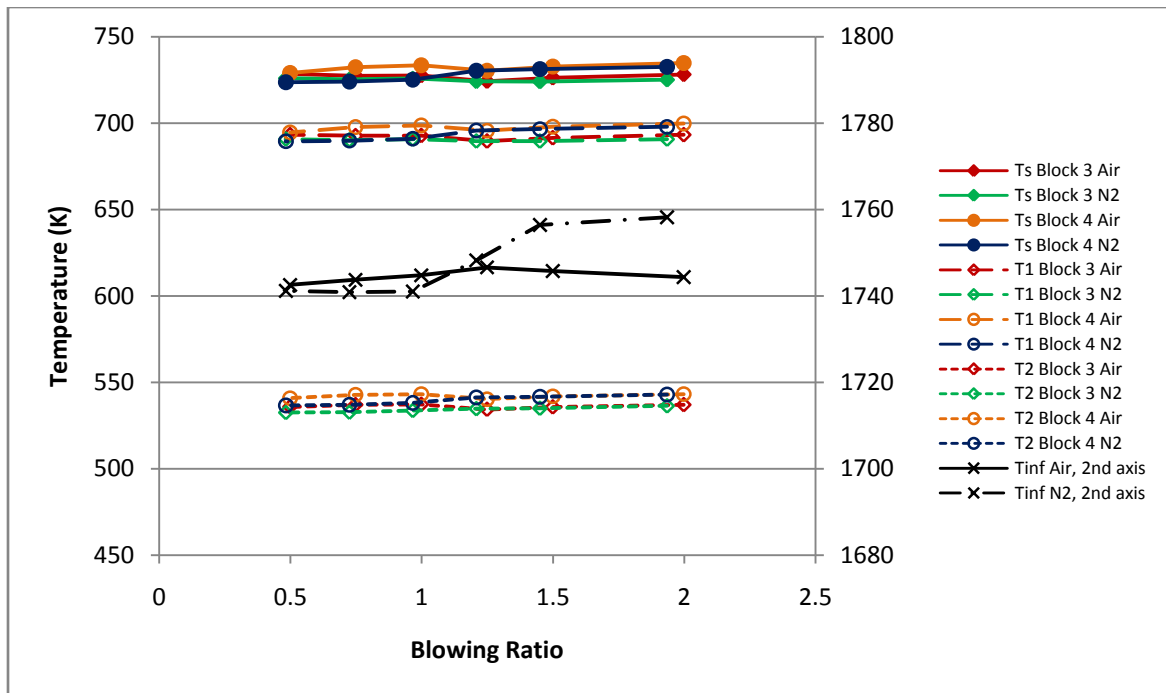


Figure 119. Temperature data, fan-shaped holes, $\Phi = 1.7$, $\dot{m}_{air} = 1020$ g/min, downstream gauges

Appendix B Overall Effectiveness Results

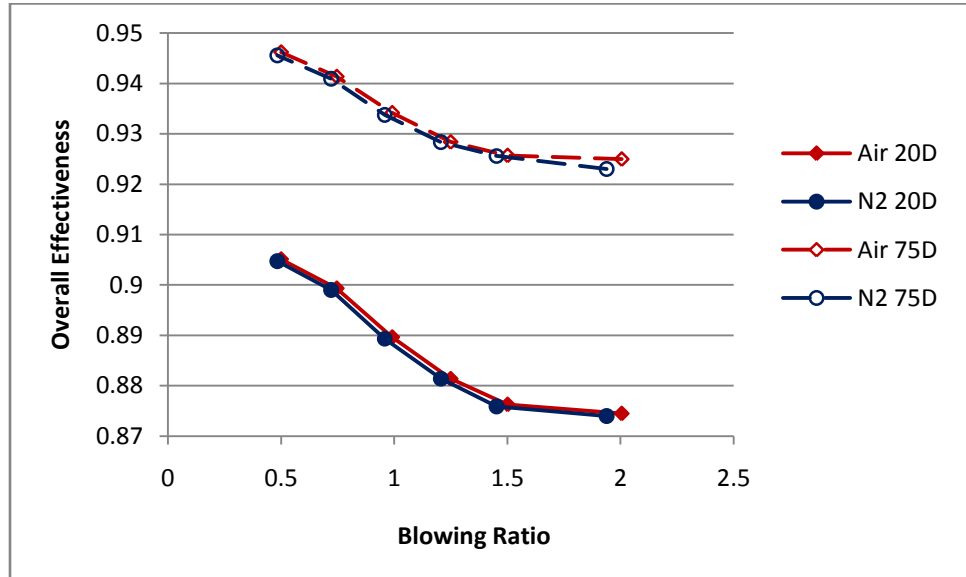


Figure 120. Dependence of φ on M , normal holes, $\Phi = 0.6$, $\dot{m}_{air} = 1020$ g/min

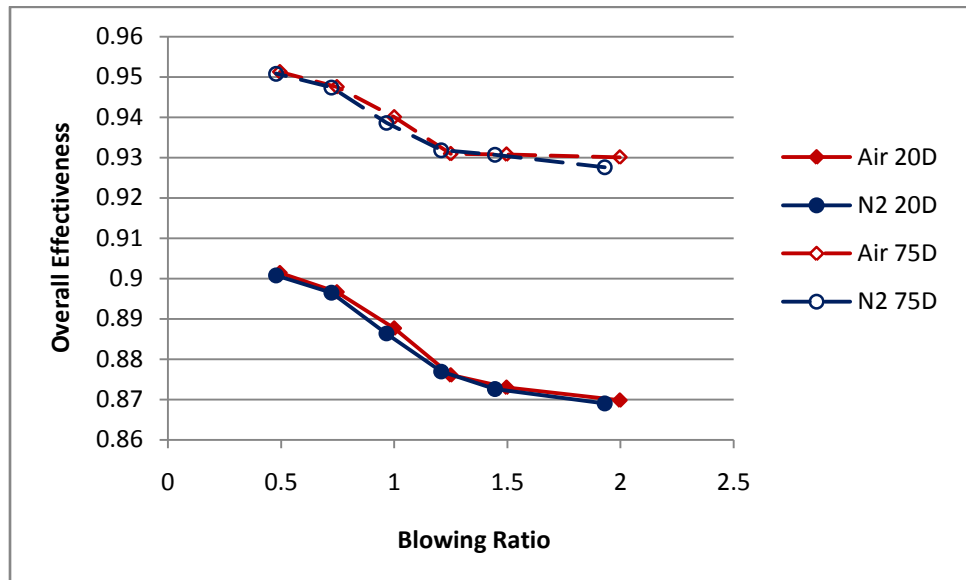


Figure 121. Dependence of φ on M , normal holes, $\Phi = 0.8$, $\dot{m}_{air} = 1020$ g/min

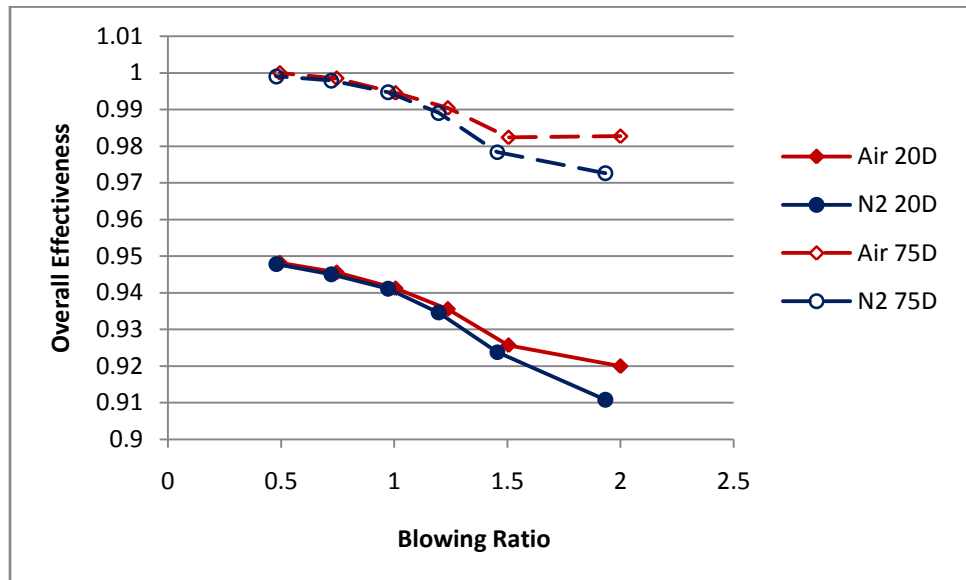


Figure 122. Dependence of φ on M , normal holes, $\Phi = 0.95$, $\dot{m}_{air} = 720$ g/min

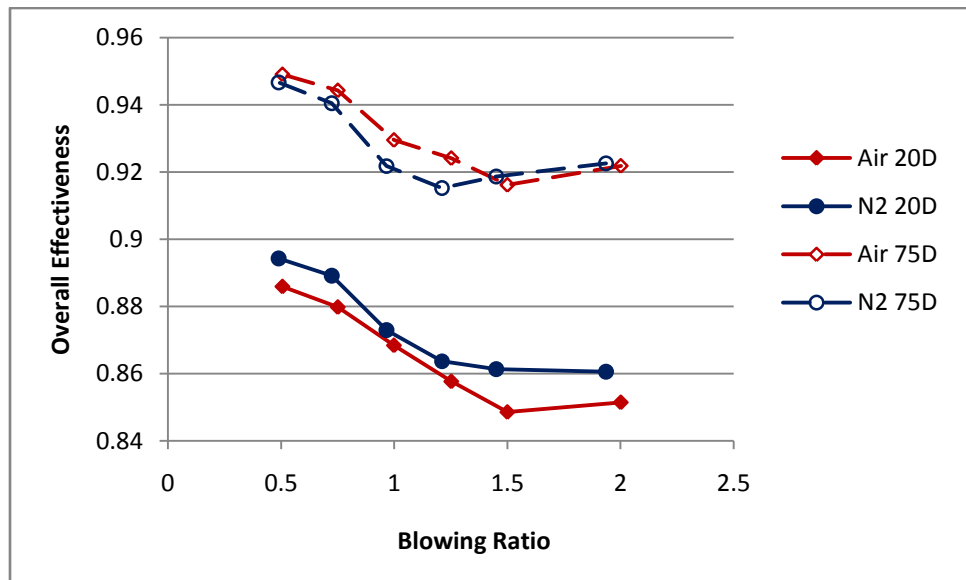


Figure 123. Dependence of φ on M , normal holes, $\Phi = 1.5$, $\dot{m}_{air} = 1020$ g/min

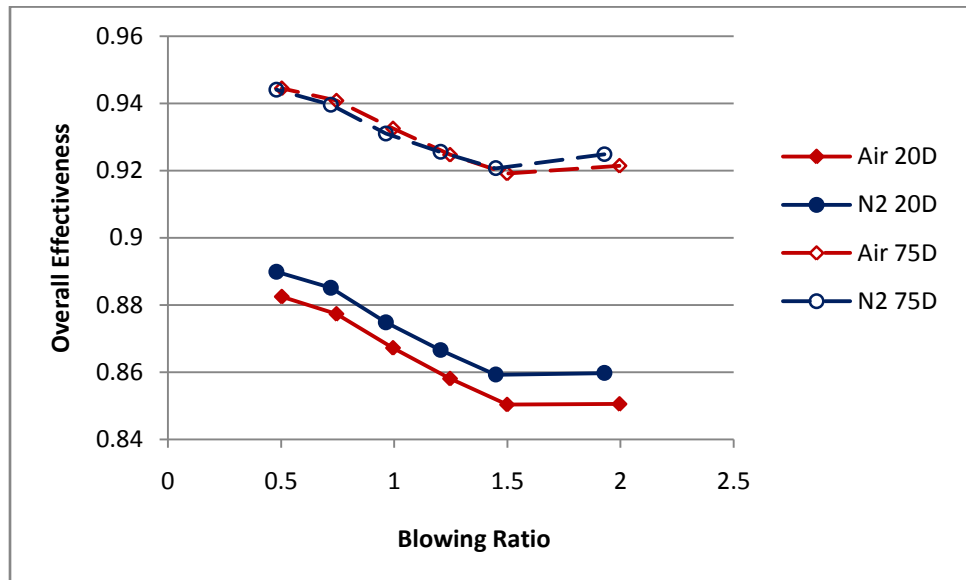


Figure 124. Dependence of φ on M , normal holes, $\Phi = 1.6$, $\dot{m}_{air} = 1020$ g/min

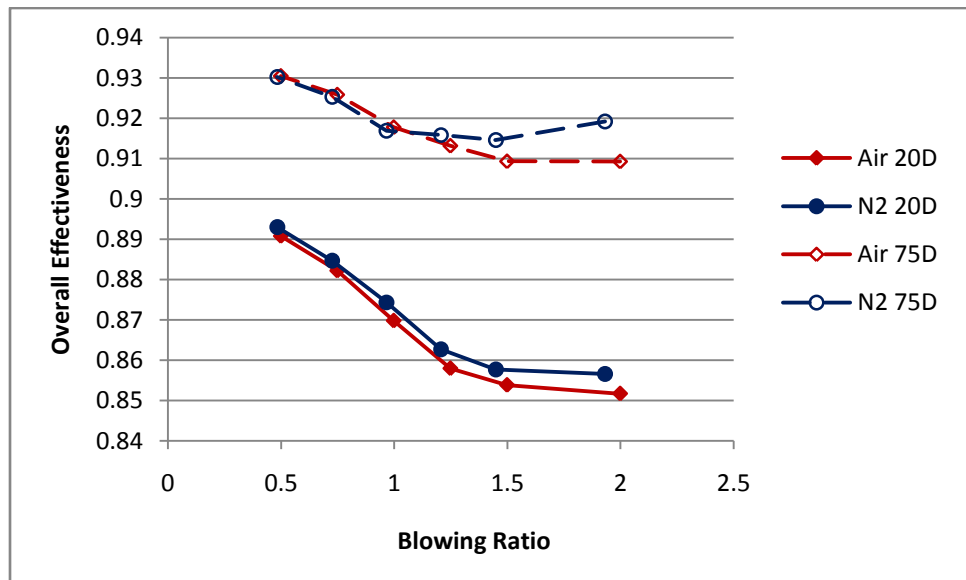


Figure 125. Dependence of φ on M , normal holes, $\Phi = 1.7$, $\dot{m}_{air} = 1020$ g/min

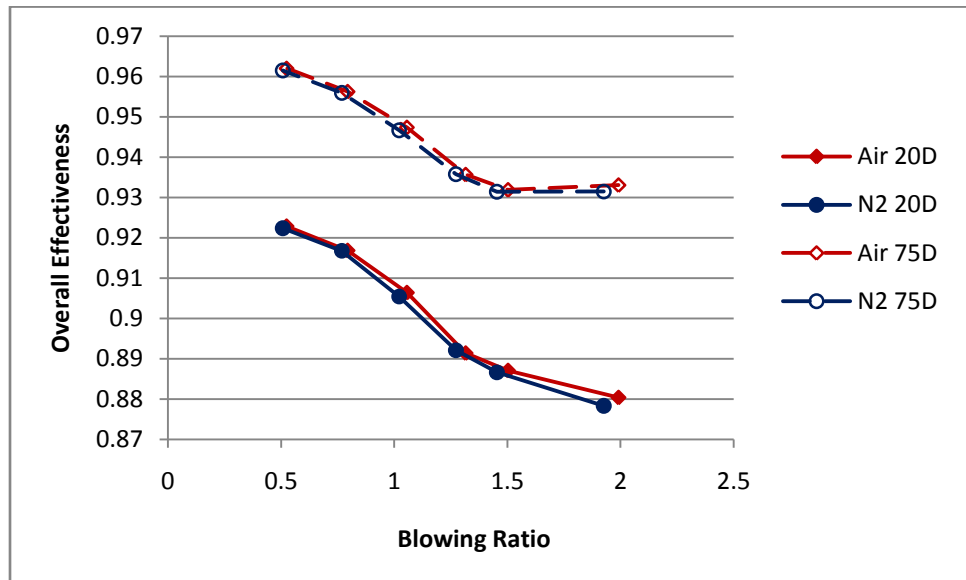


Figure 126. Dependence of ϕ on M , angled holes, $\Phi = 0.6$, $\dot{m}_{air} = 1020$ g/min

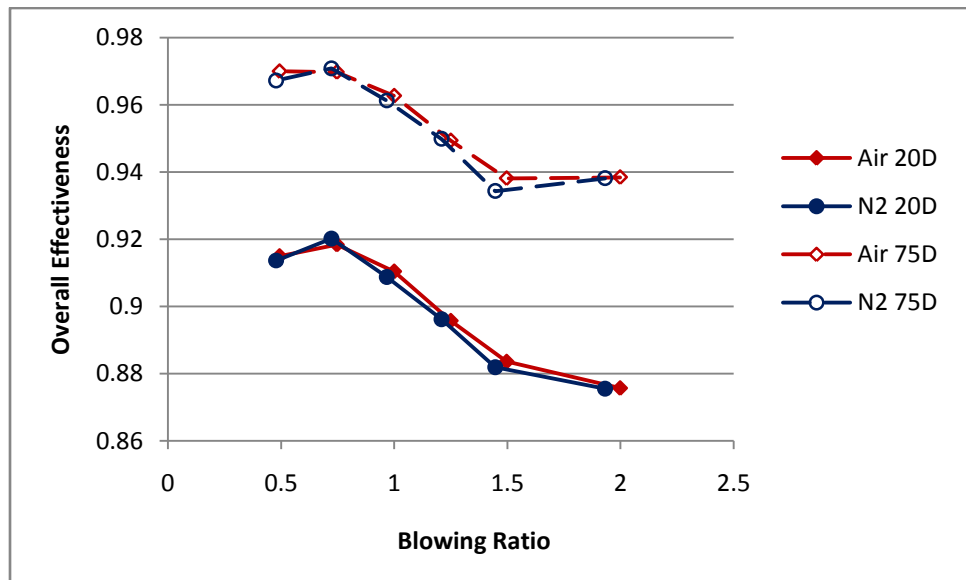


Figure 127. Dependence of ϕ on M , angled holes, $\Phi = 0.8$, $\dot{m}_{air} = 1020$ g/min

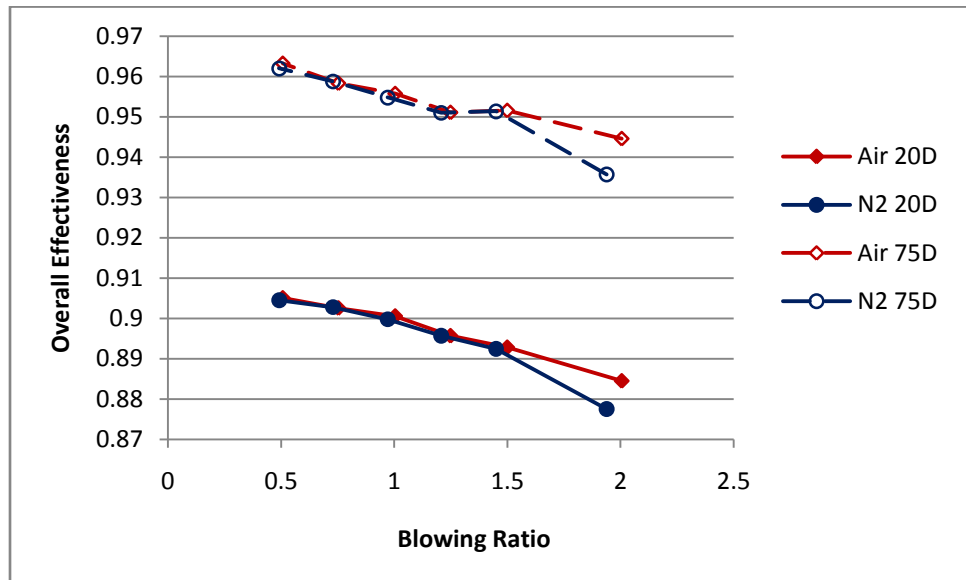


Figure 128. Dependence of ϕ on M , angled holes, $\Phi = 0.95$, $\dot{m}_{air} = 720$ g/min

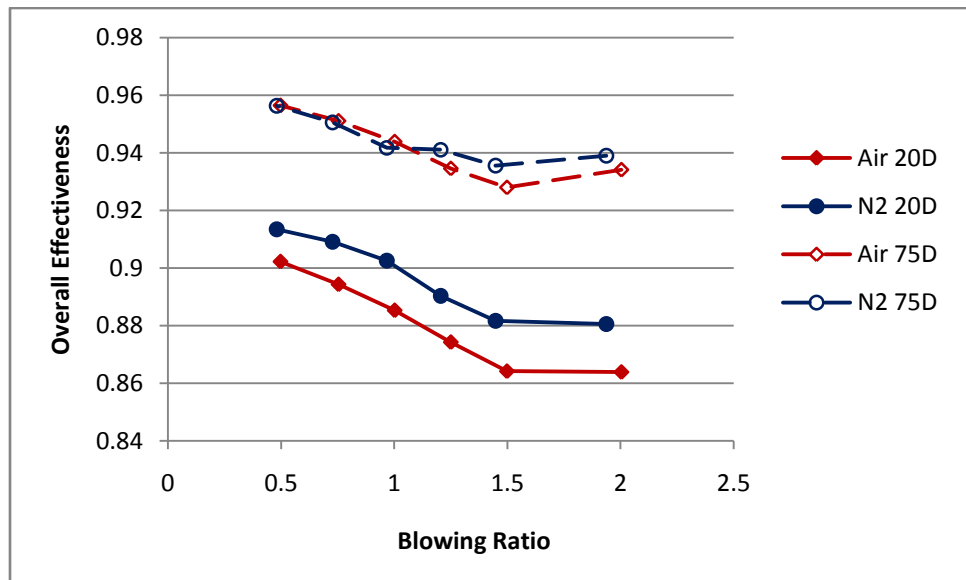


Figure 129. Dependence of ϕ on M , angled holes, $\Phi = 1.5$, $\dot{m}_{air} = 1020$ g/min

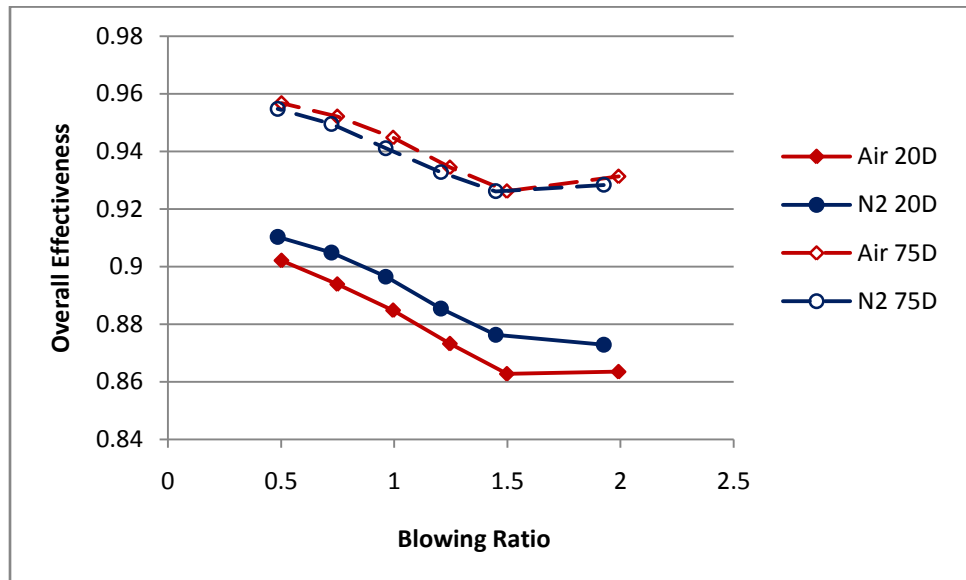


Figure 130. Dependence of ϕ on M , angled holes, $\Phi = 1.6$, $\dot{m}_{air} = 1020$ g/min

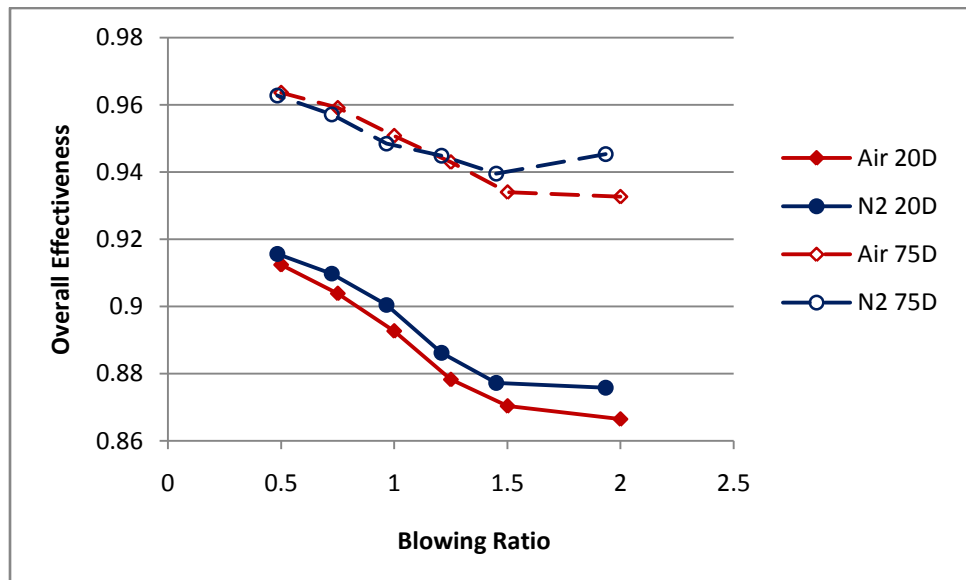


Figure 131. Dependence of ϕ on M , angled holes, $\Phi = 1.7$, $\dot{m}_{air} = 1020$ g/min

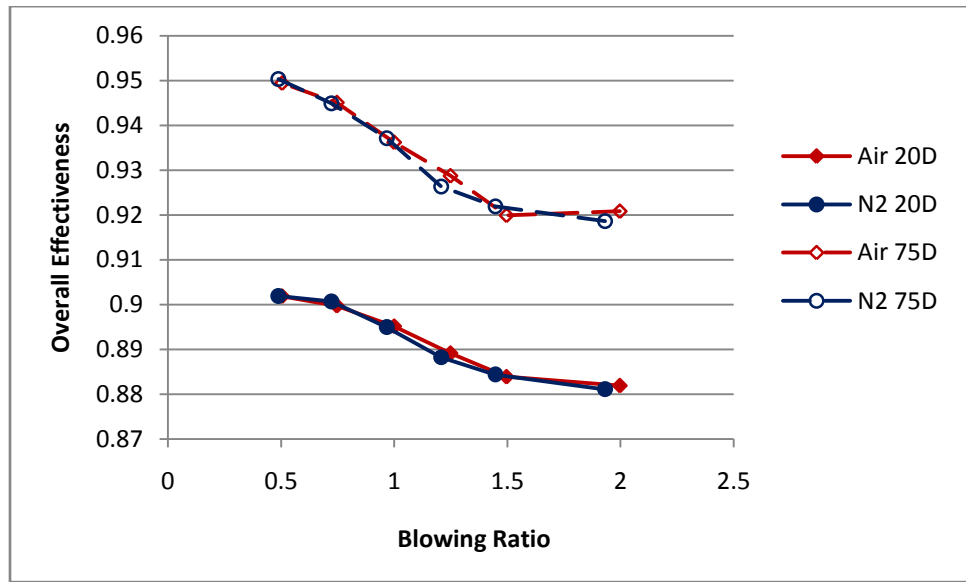


Figure 132. Dependence of ϕ on M , fan-shaped holes, $\Phi = 0.8$, $\dot{m}_{air} = 1020$ g/min

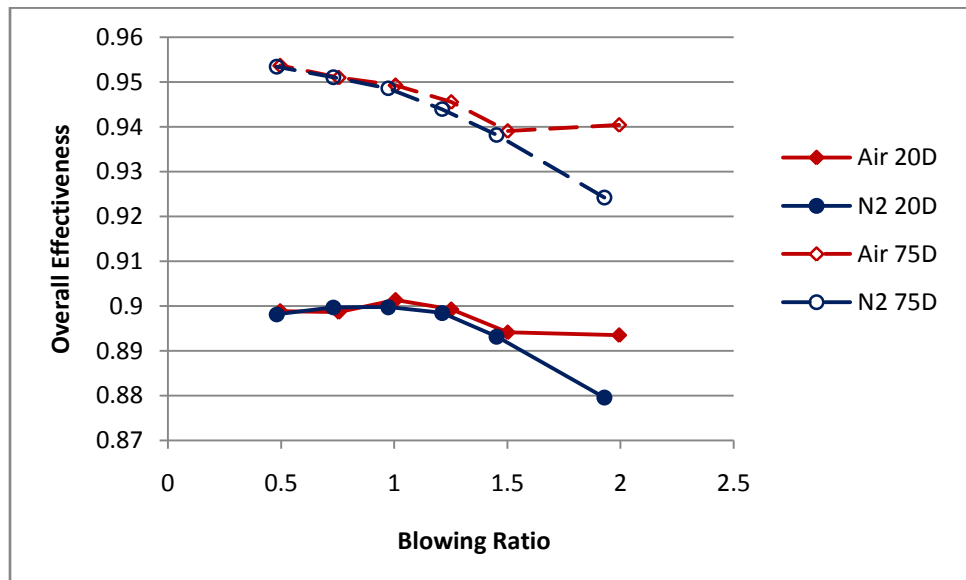


Figure 133. Dependence of ϕ on M , fan-shaped holes, $\Phi = 0.95$, $\dot{m}_{air} = 720$ g/min

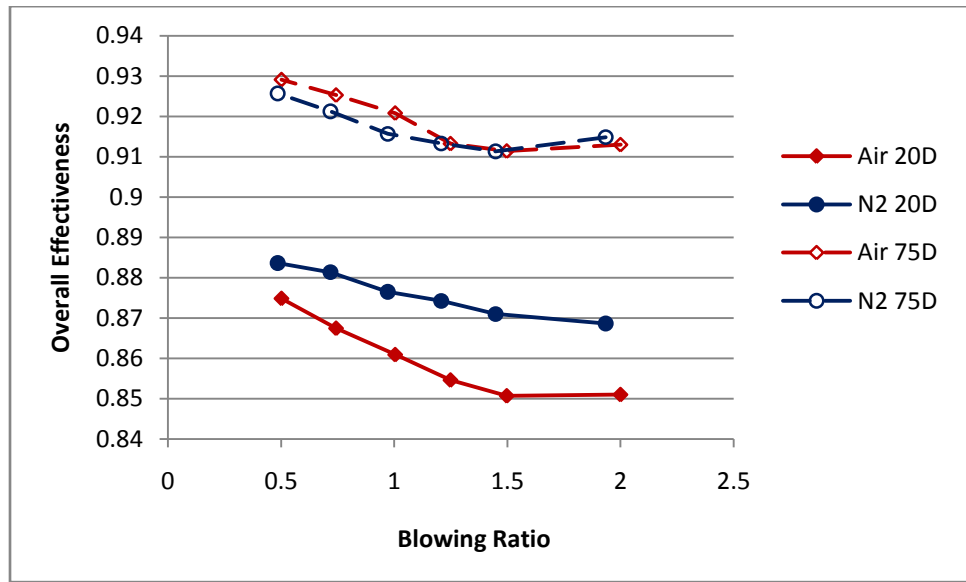


Figure 134. Dependence of ϕ on M , fanshaped holes, $\Phi = 1.6$, $\dot{m}_{air} = 1020$ g/min

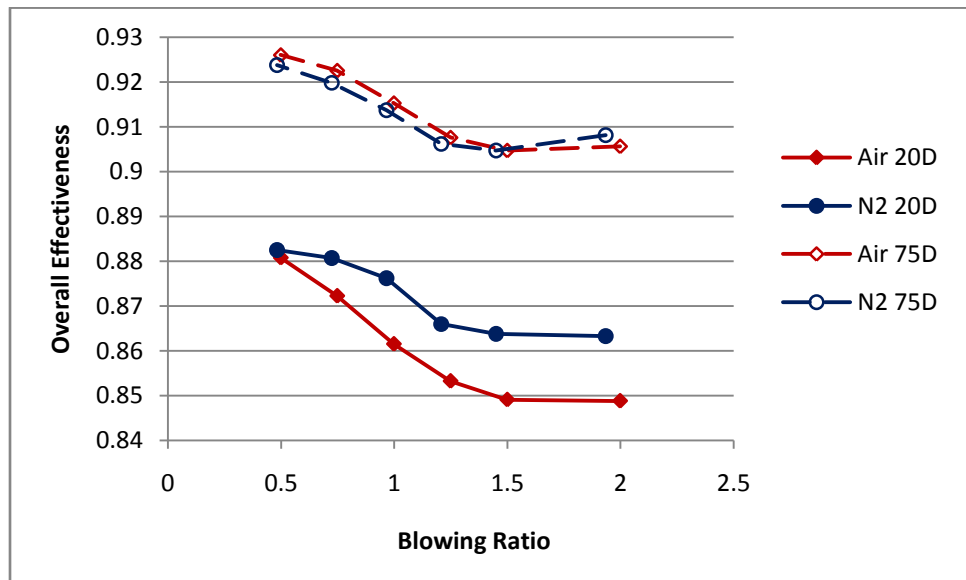


Figure 135. Dependence of ϕ on M , fanshaped holes, $\Phi = 1.7$, $\dot{m}_{air} = 1020$ g/min

Appendix C Heat Flux and Heat Transfer Coefficient Results

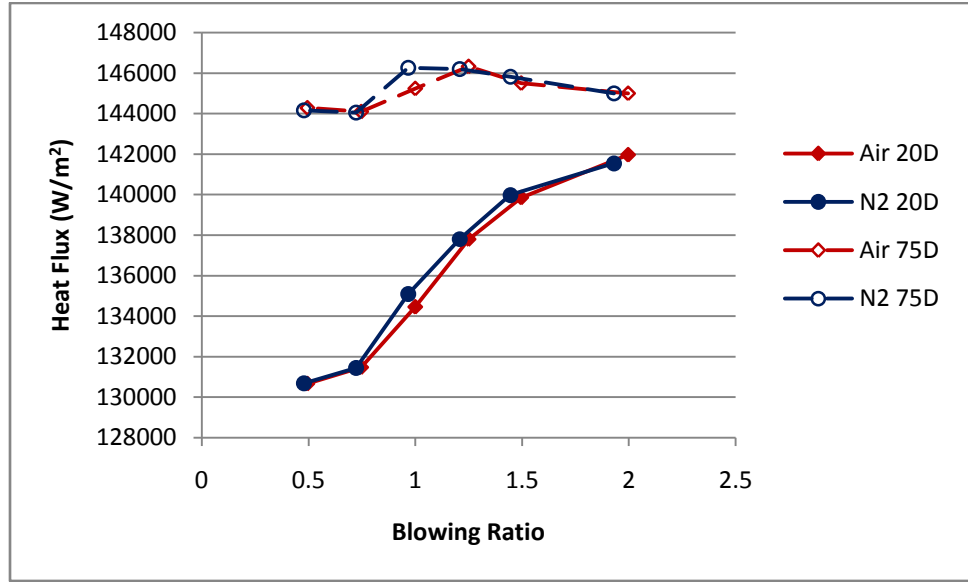


Figure 136. Dependence of q'' on M , normal holes, $\Phi = 0.8$, $\dot{m}_{air} = 1020$ g/min

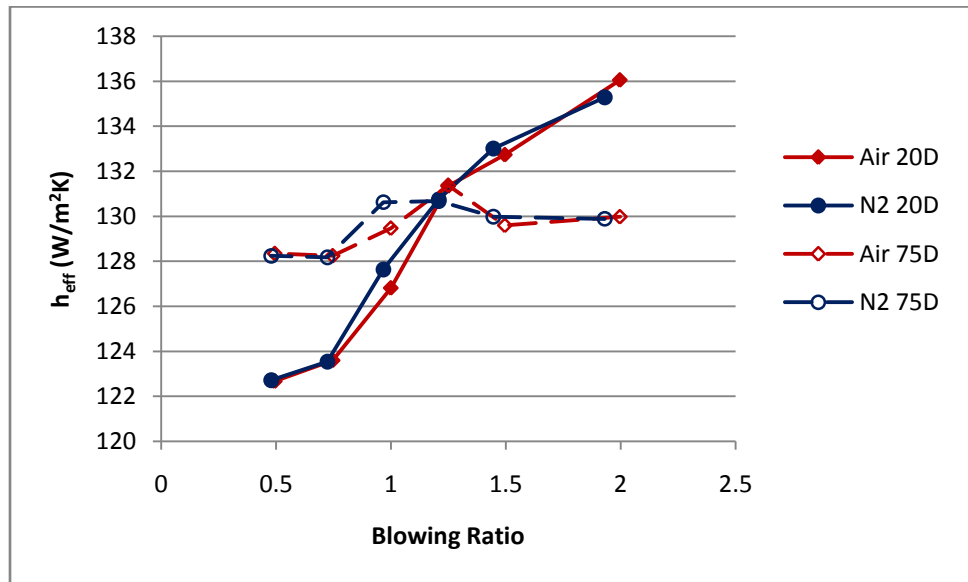


Figure 137. Dependence of h_{eff} on M , normal holes, $\Phi = 0.8$, $\dot{m}_{air} = 1020$ g/min

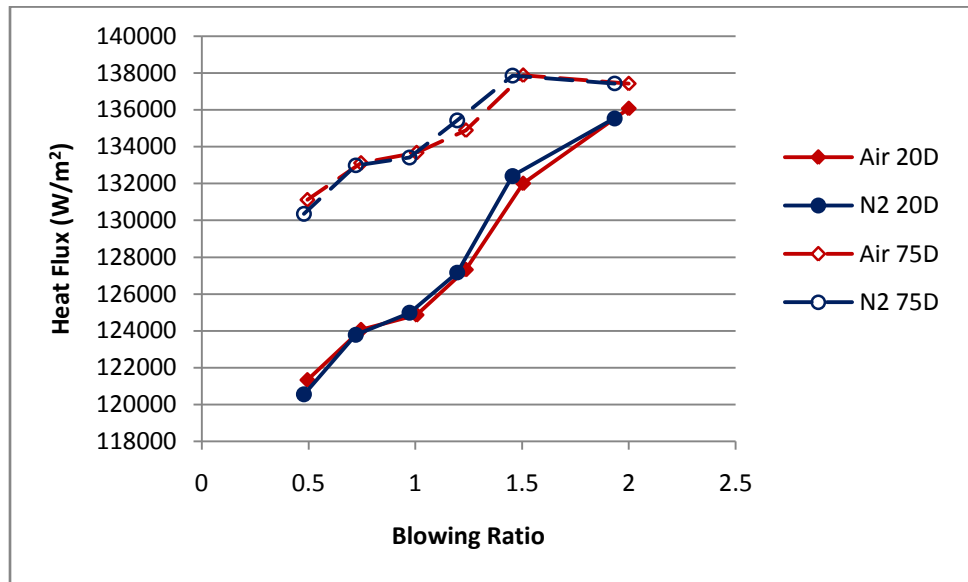


Figure 138. Dependence of q'' on M , normal holes, $\Phi = 0.95$, $\dot{m}_{air} = 720$ g/min

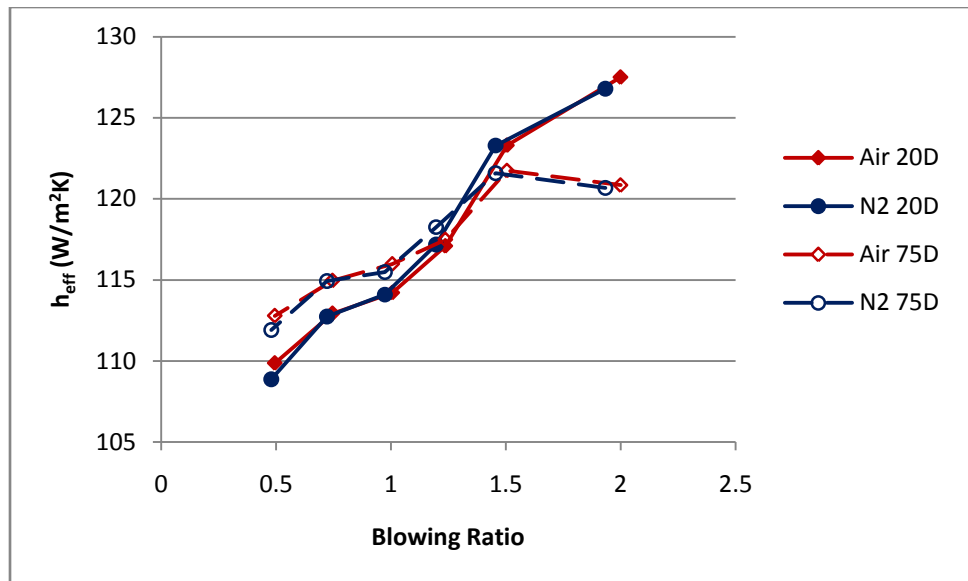


Figure 139. Dependence of h_{eff} on M , normal holes, $\Phi = 0.95$, $\dot{m}_{air} = 720$ g/min

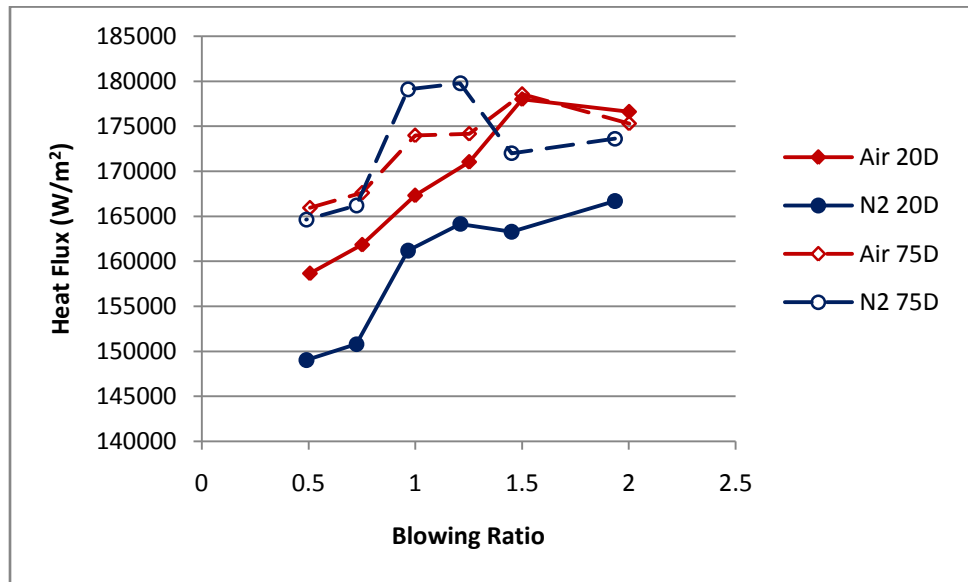


Figure 140. Dependence of q'' on M , normal holes, $\Phi = 1.5$, $\dot{m}_{air} = 1020$ g/min

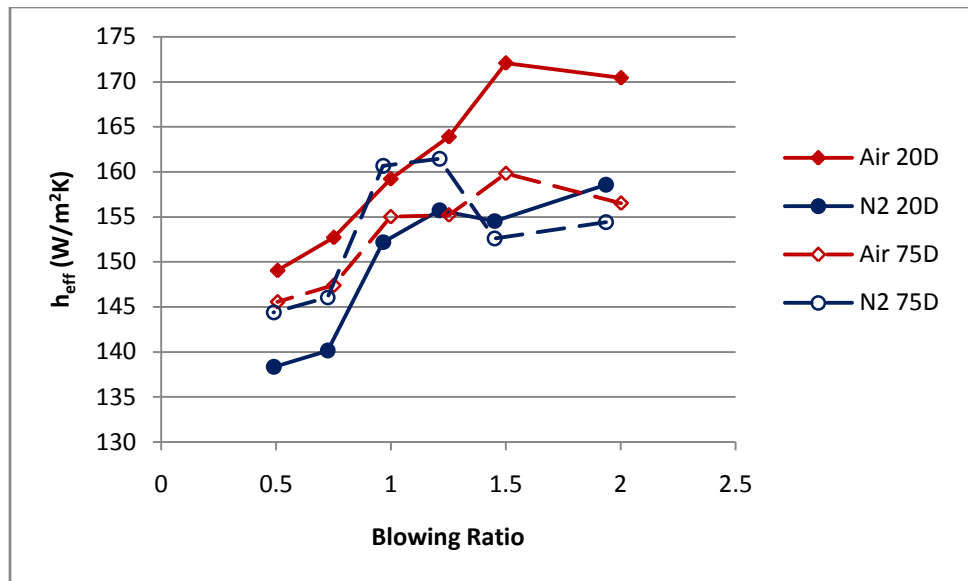


Figure 141. Dependence of h_{eff} on M , normal holes, $\Phi = 1.5$, $\dot{m}_{air} = 1020$ g/min

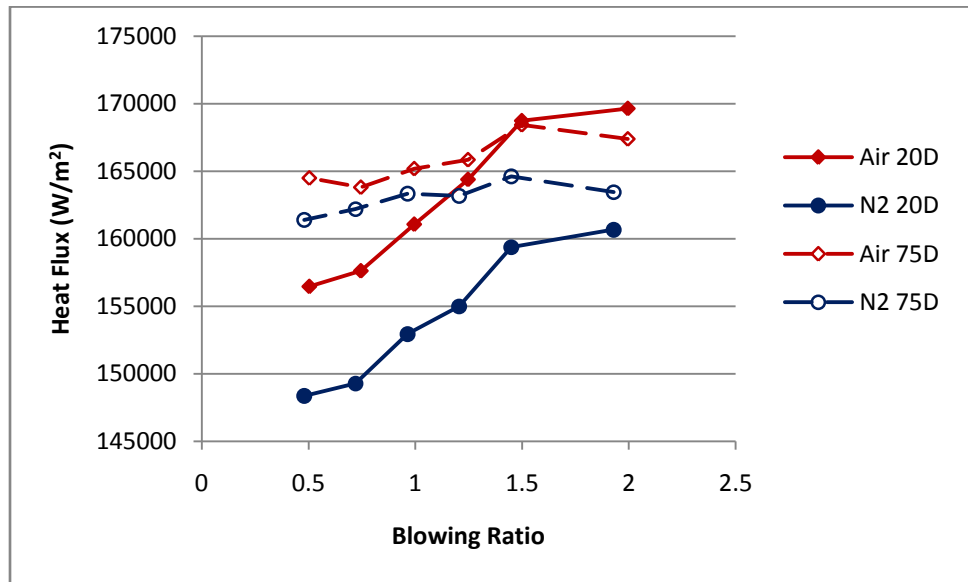


Figure 142. Dependence of q'' on M , normal holes, $\Phi = 1.6$, $\dot{m}_{air} = 1020$ g/min

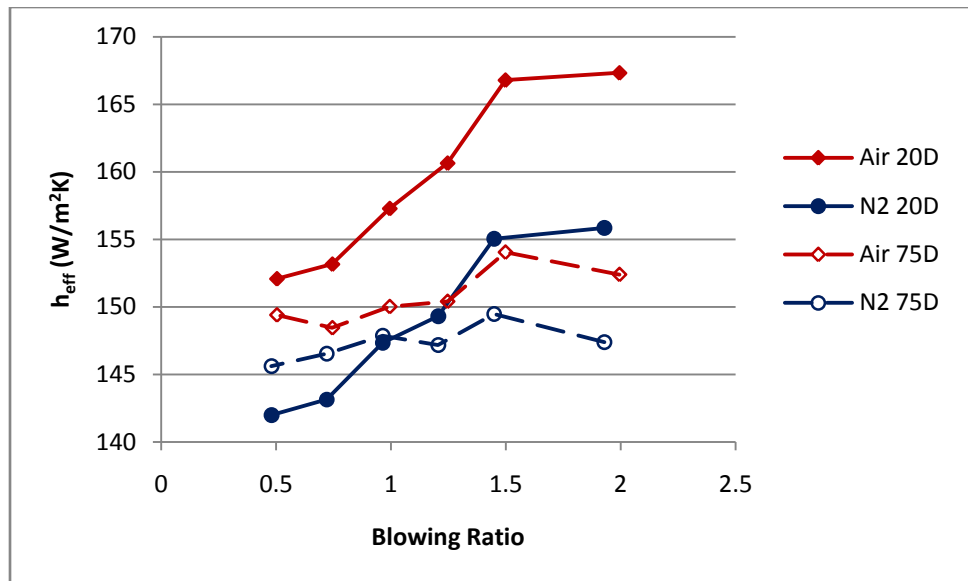


Figure 143. Dependence of h_{eff} on M , normal holes, $\Phi = 1.6$, $\dot{m}_{air} = 1020$ g/min

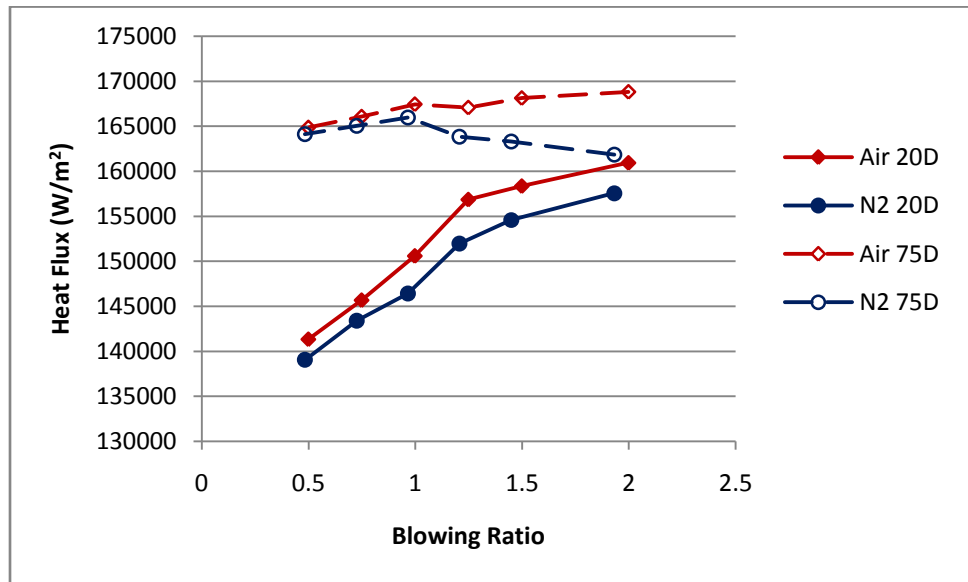


Figure 144. Dependence of q'' on M , normal holes, $\Phi = 1.7$, $\dot{m}_{air} = 1020$ g/min

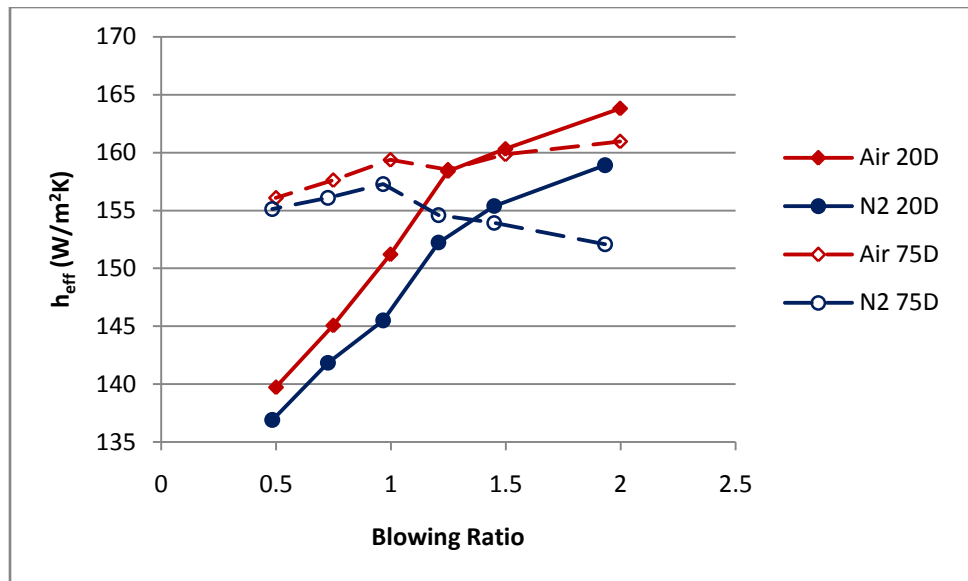


Figure 145. Dependence of h_{eff} on M , normal holes, $\Phi = 1.7$, $\dot{m}_{air} = 1020$ g/min

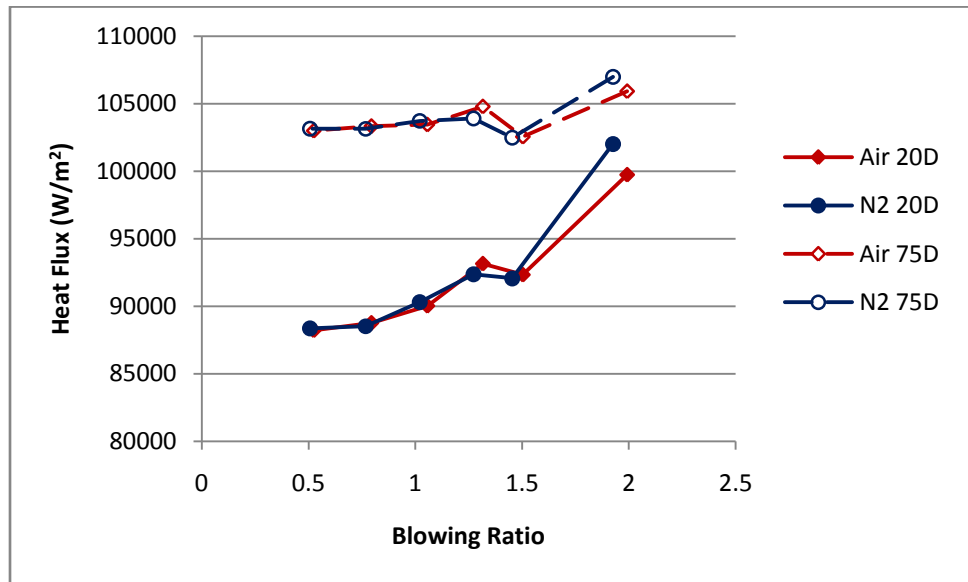


Figure 146. Dependence of q'' on M , angled holes, $\Phi = 0.6$, $\dot{m}_{air} = 1020$ g/min

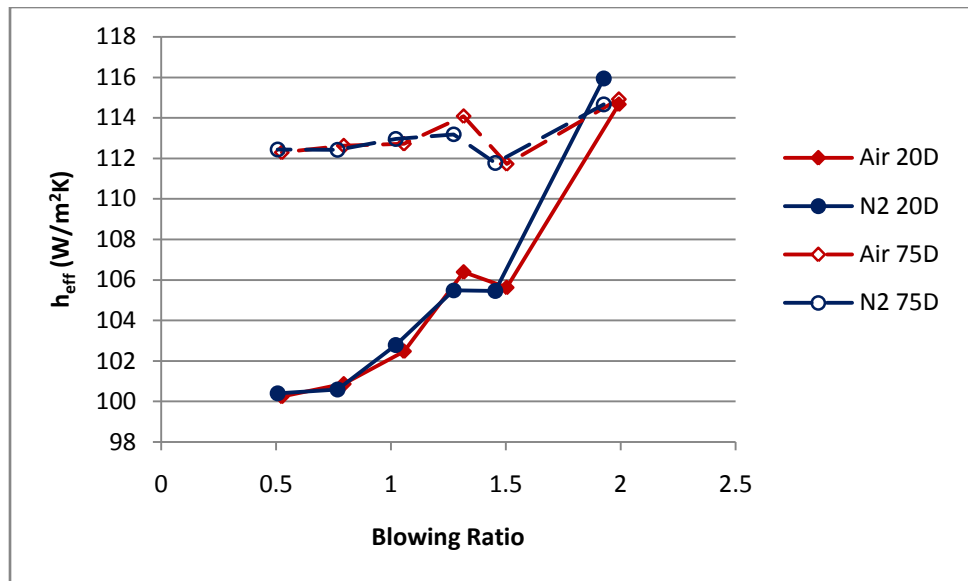


Figure 147. Dependence of h_{eff} on M , angled holes, $\Phi = 0.6$, $\dot{m}_{air} = 1020$ g/min

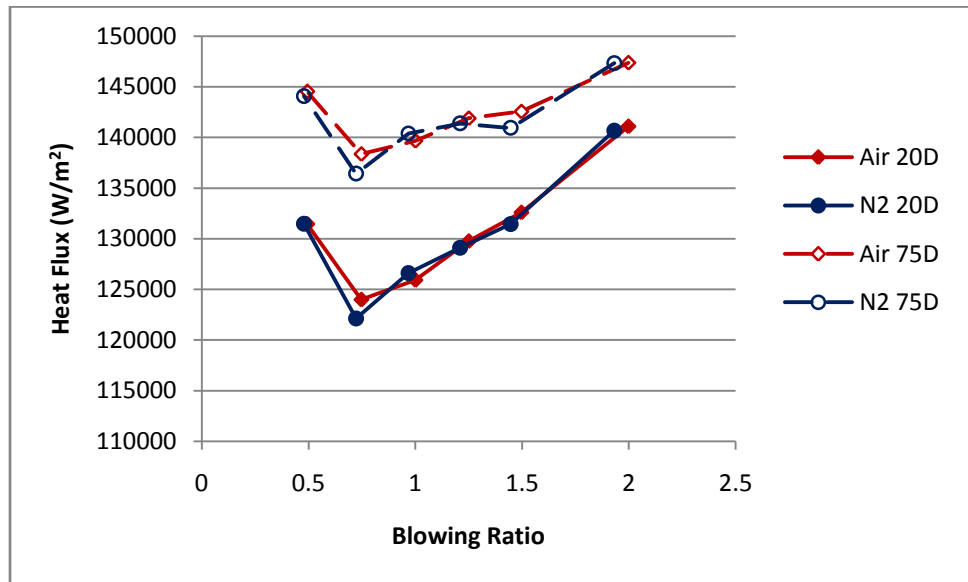


Figure 148. Dependence of q'' on M , angled holes, $\Phi = 0.8$, $\dot{m}_{air} = 1020$ g/min

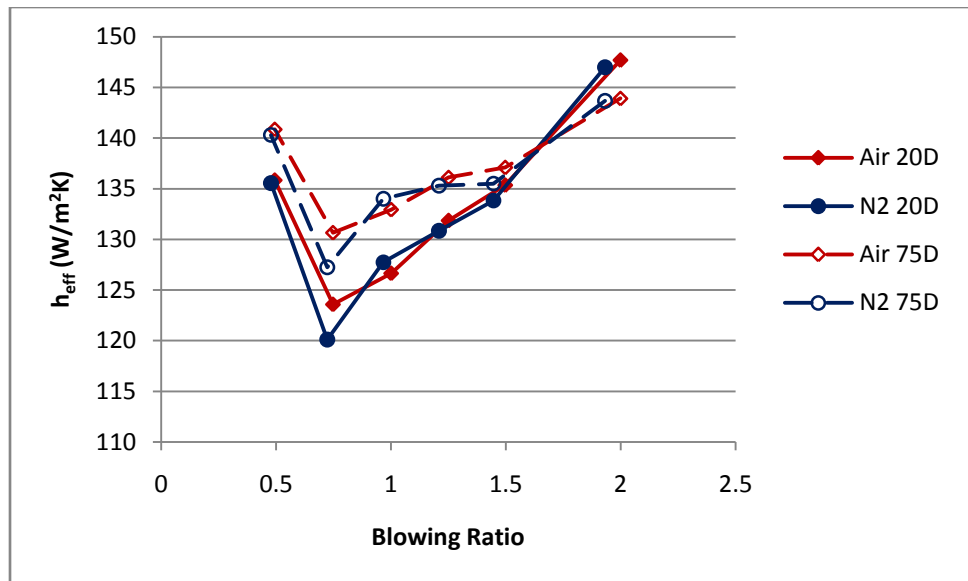


Figure 149. Dependence of h_{eff} on M , angled holes, $\Phi = 0.8$, $\dot{m}_{air} = 1020$ g/min

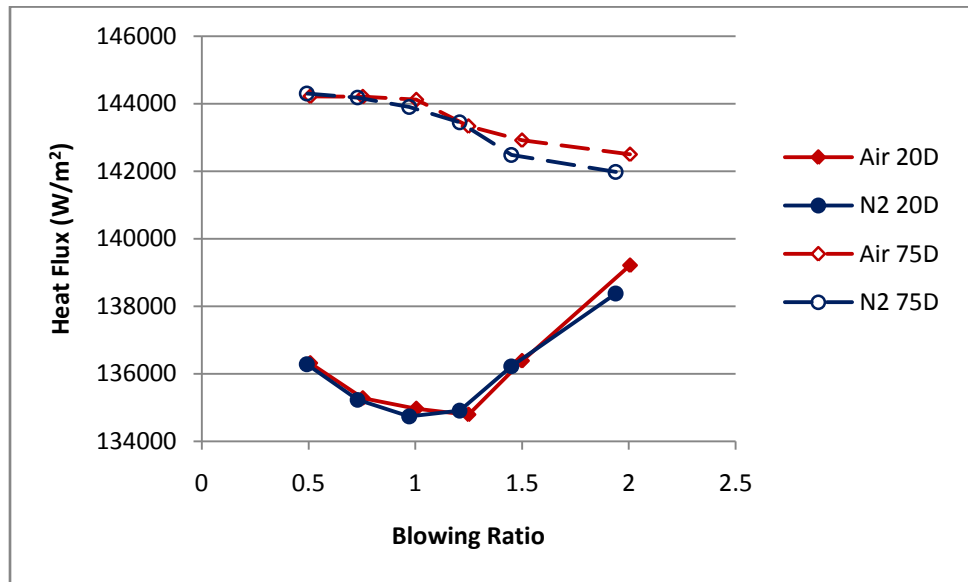


Figure 150. Dependence of q'' on M , angled holes, $\Phi = 0.95$, $\dot{m}_{air} = 720$ g/min

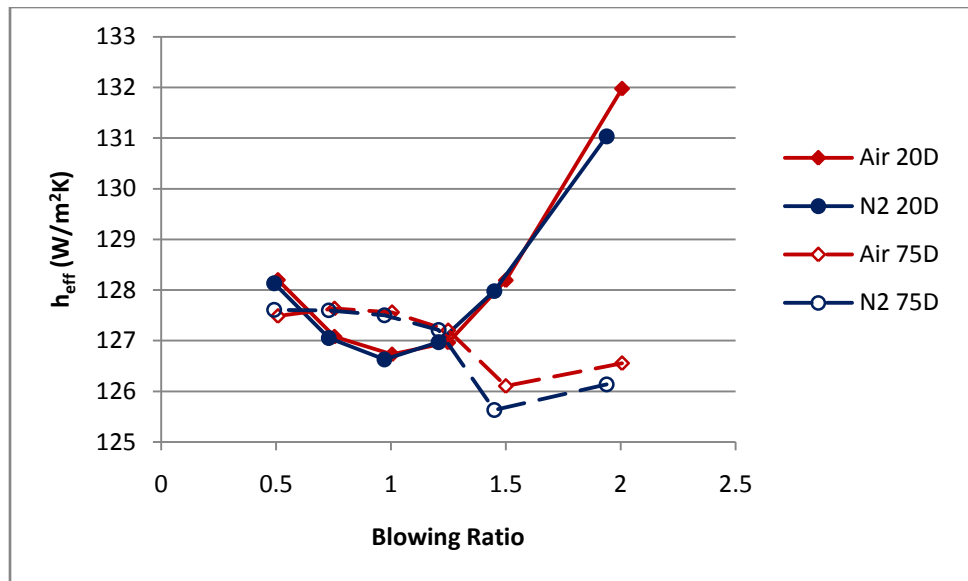


Figure 151. Dependence of h_{eff} on M , angled holes, $\Phi = 0.95$, $\dot{m}_{air} = 720$ g/min

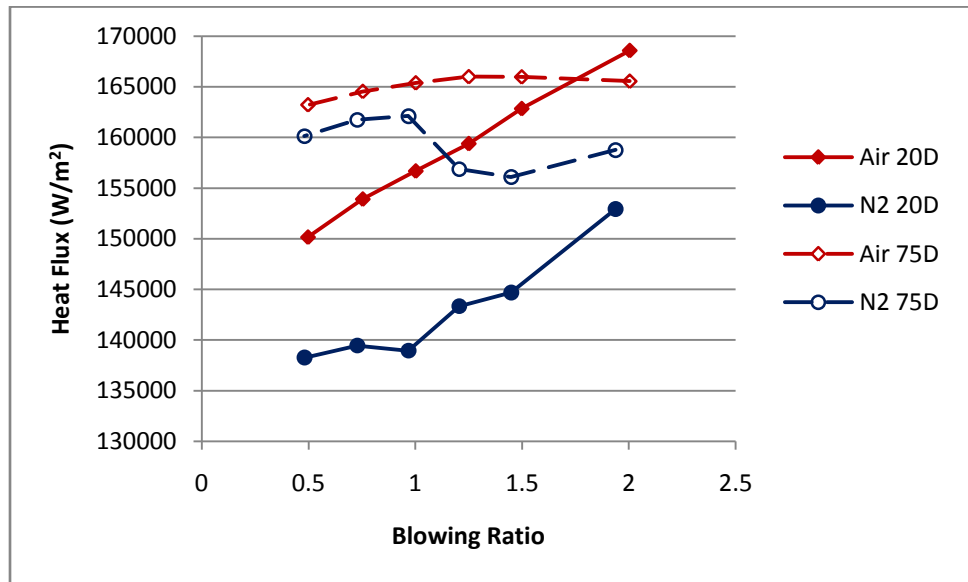


Figure 152. Dependence of q'' on M , angled holes, $\Phi = 1.5$, $\dot{m}_{air} = 1020$ g/min

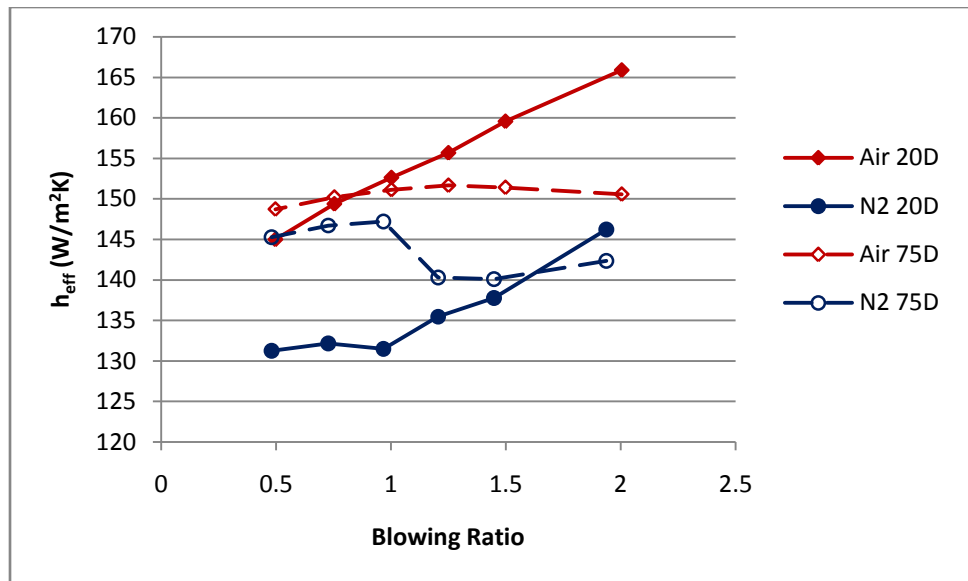


Figure 153. Dependence of h_{eff} on M , angled holes, $\Phi = 1.5$, $\dot{m}_{air} = 1020$ g/min

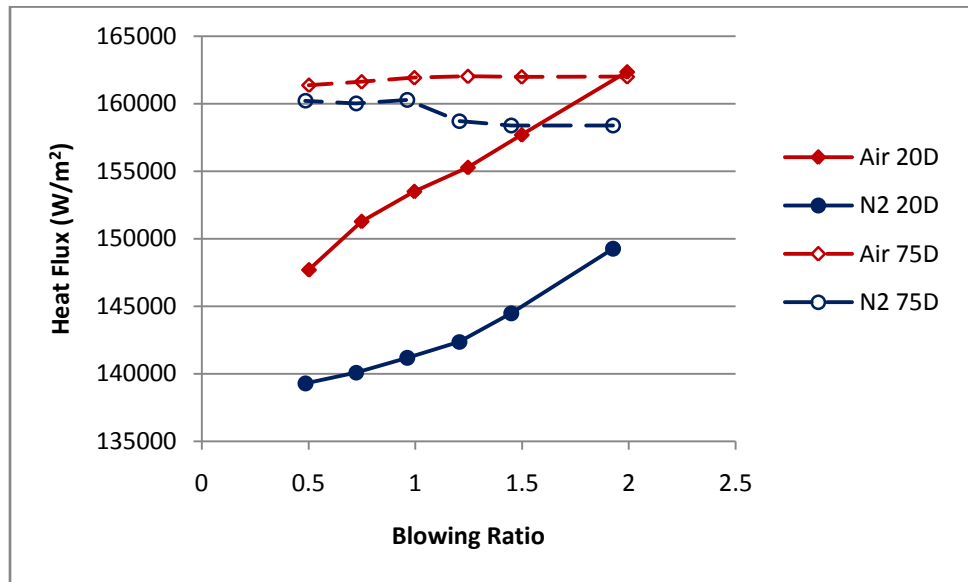


Figure 154. Dependence of q'' on M , angled holes, $\Phi = 1.6$, $\dot{m}_{air} = 1020$ g/min

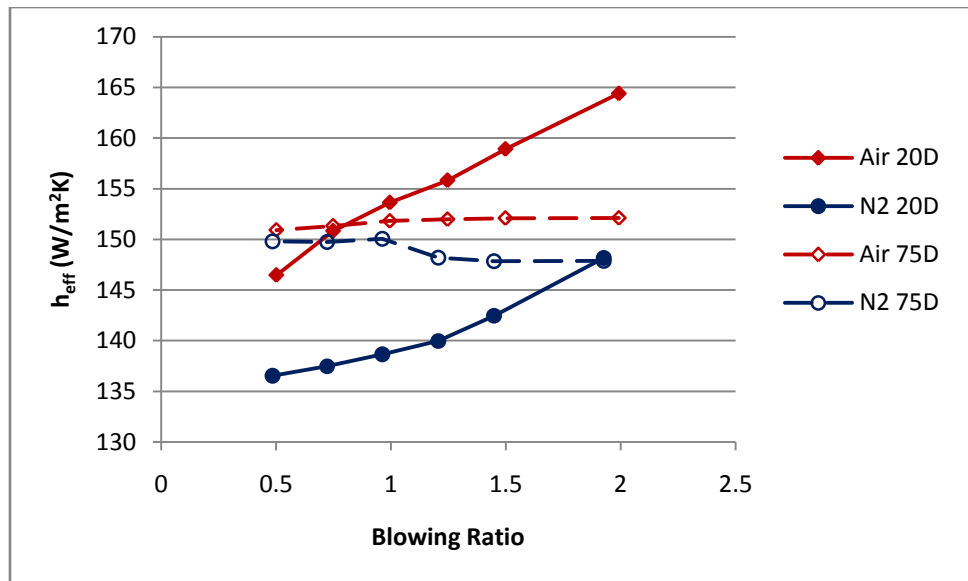


Figure 155. Dependence of h_{eff} on M , angled holes, $\Phi = 1.6$, $\dot{m}_{air} = 1020$ g/min

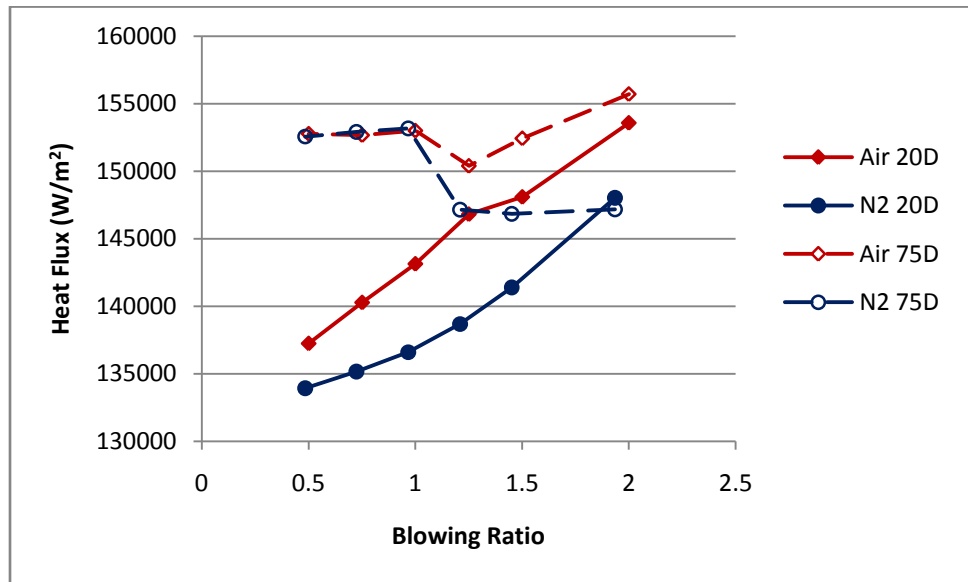


Figure 156. Dependence of q'' on M , angled holes, $\Phi = 1.7$, $\dot{m}_{air} = 1020$ g/min

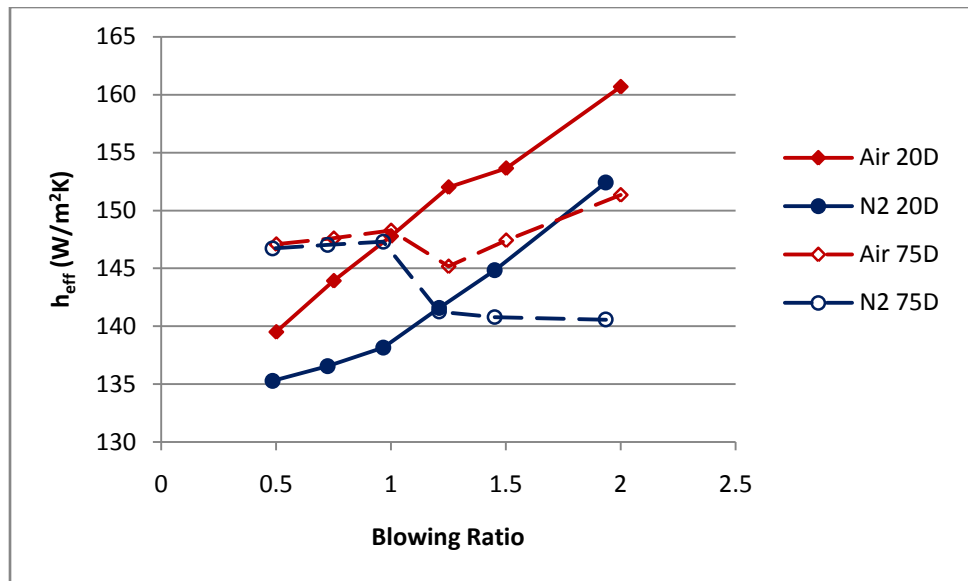


Figure 157. Dependence of h_{eff} on M , angled holes, $\Phi = 1.7$, $\dot{m}_{air} = 1020$ g/min

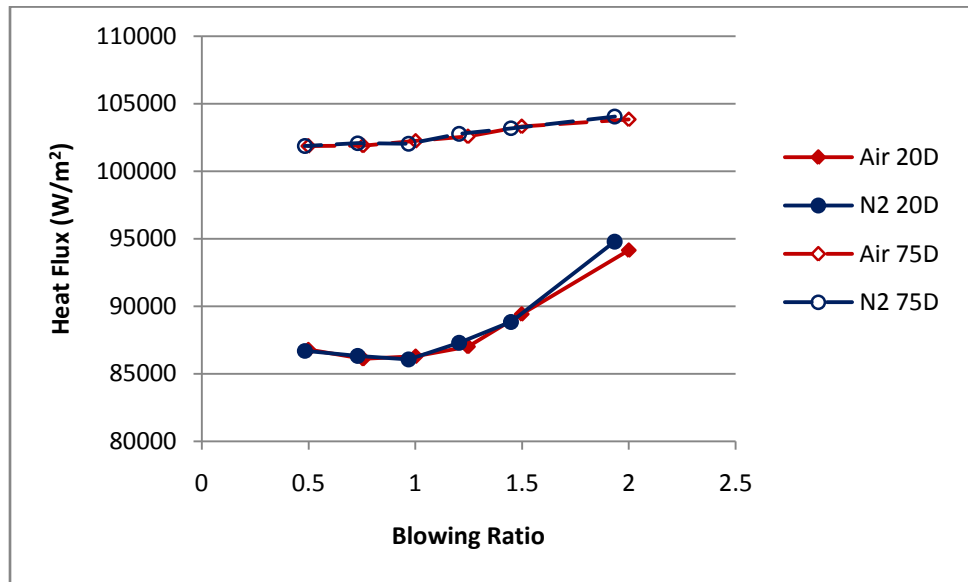


Figure 158. Dependence of q'' on M , fanshaped holes, $\Phi = 0.6$, $\dot{m}_{air} = 1020$ g/min

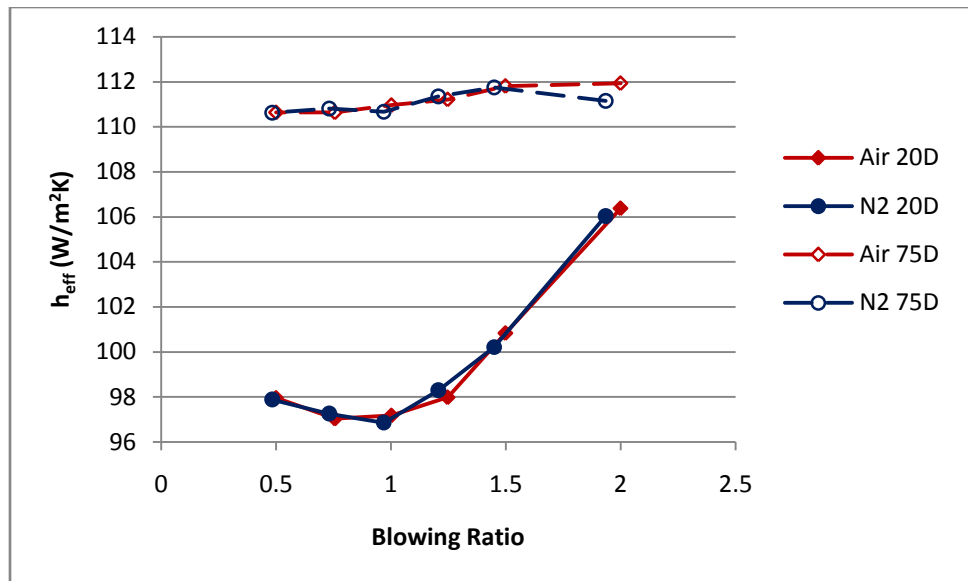


Figure 159. Dependence of h_{eff} on M , fanshaped holes, $\Phi = 0.6$, $\dot{m}_{air} = 1020$ g/min

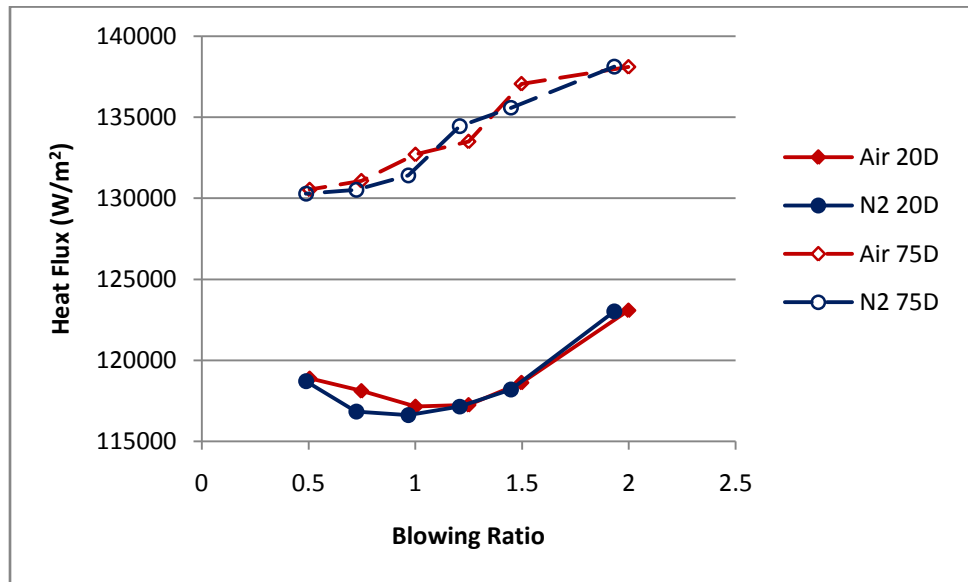


Figure 160. Dependence of q'' on M , fan-shaped holes, $\Phi = 0.8$, $\dot{m}_{air} = 1020$ g/min

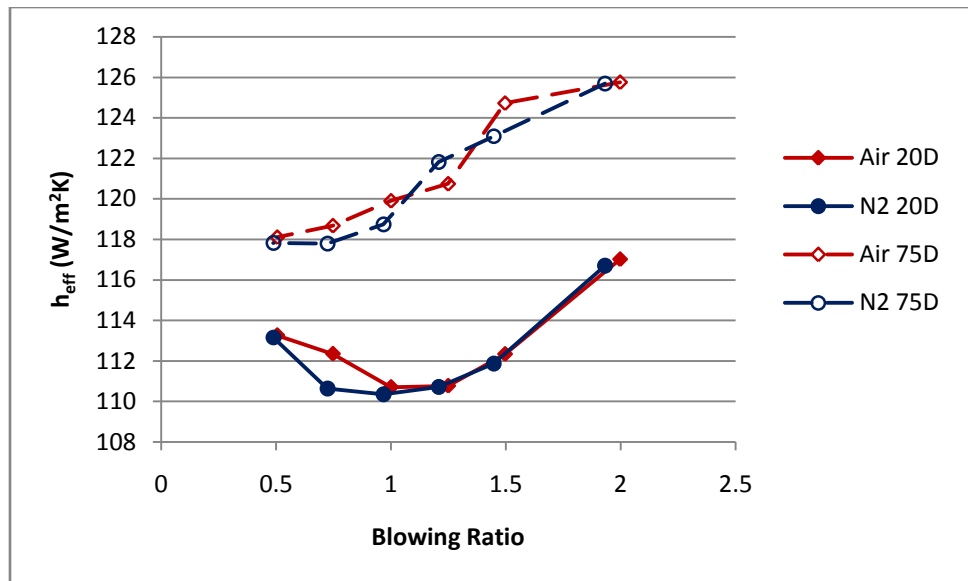


Figure 161. Dependence of h_{eff} on M , fan-shaped holes, $\Phi = 0.8$, $\dot{m}_{air} = 1020$ g/min

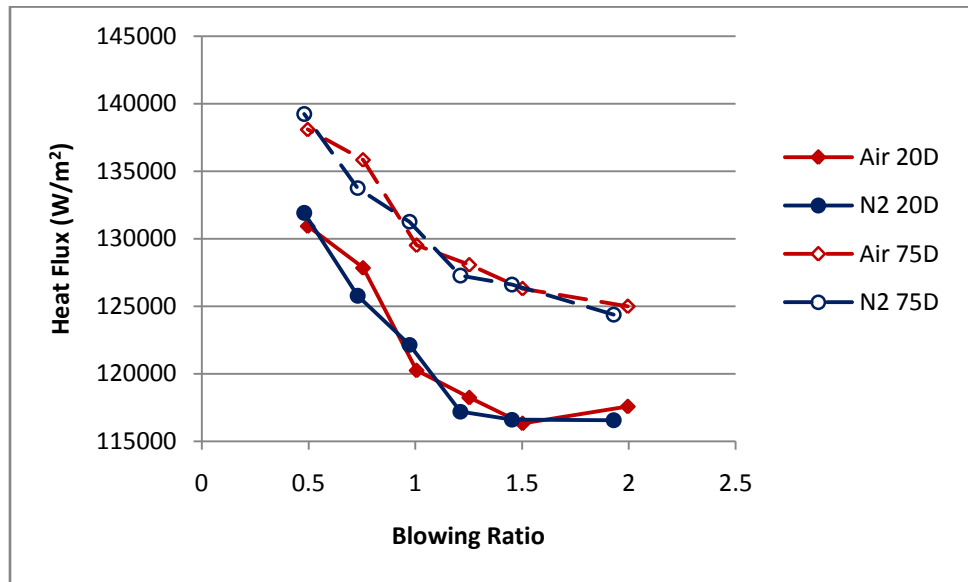


Figure 162. Dependence of q'' on M , fanshaped holes, $\Phi = 0.95$, $\dot{m}_{air} = 720$ g/min

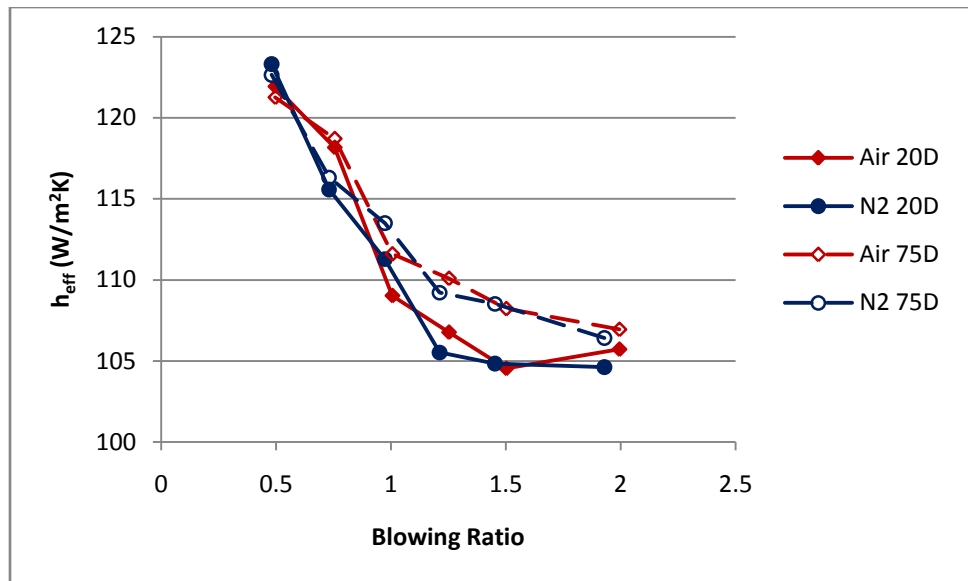


Figure 163. Dependence of h_{eff} on M , fanshaped holes, $\Phi = 0.95$, $\dot{m}_{air} = 720$ g/min

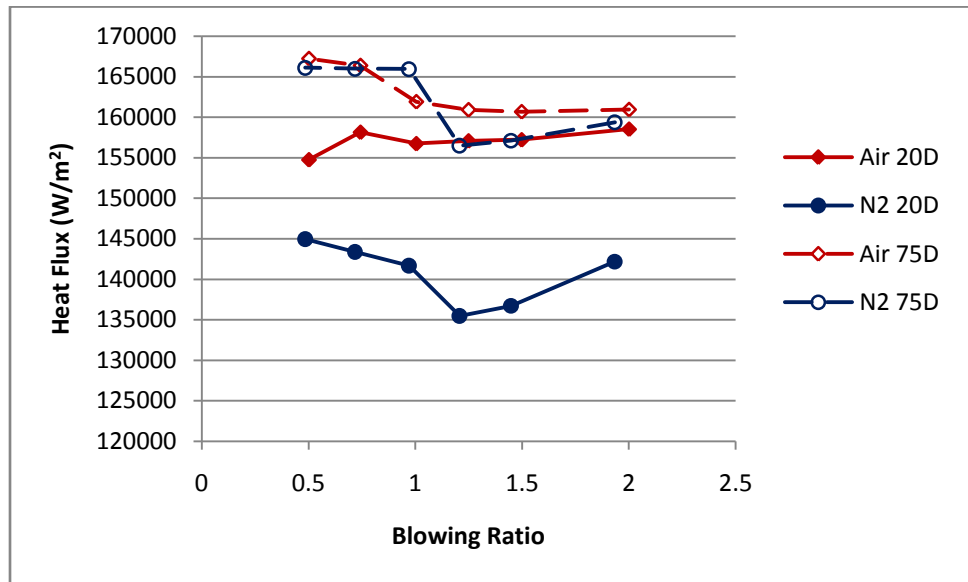


Figure 164. Dependence of q'' on M , fanshaped holes, $\Phi = 1.6$, $\dot{m}_{air} = 1020$ g/min

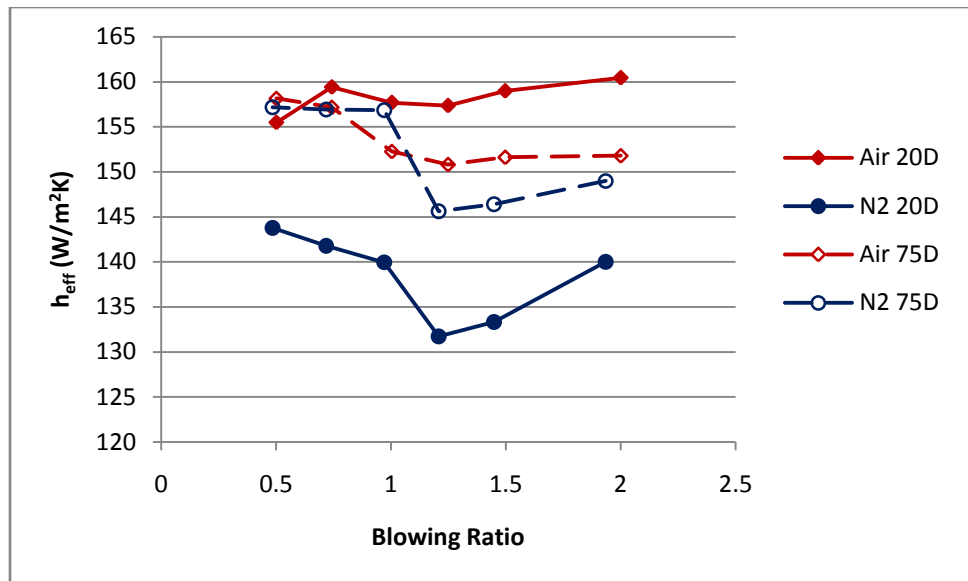


Figure 165. Dependence of h_{eff} on M , fanshaped holes, $\Phi = 1.6$, $\dot{m}_{air} = 1020$ g/min

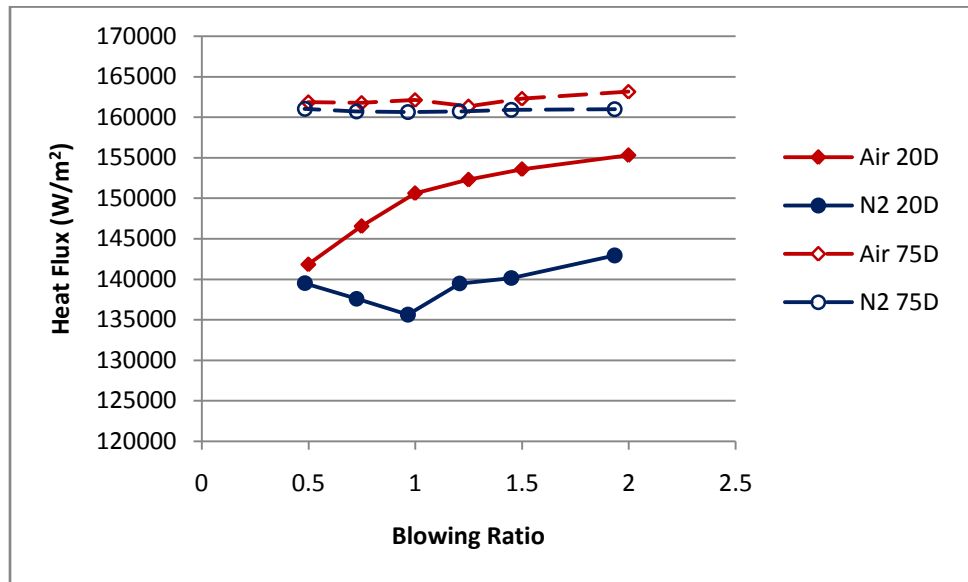


Figure 166. Dependence of q'' on M , fanshaped holes, $\Phi = 1.7$, $\dot{m}_{air} = 1020$ g/min

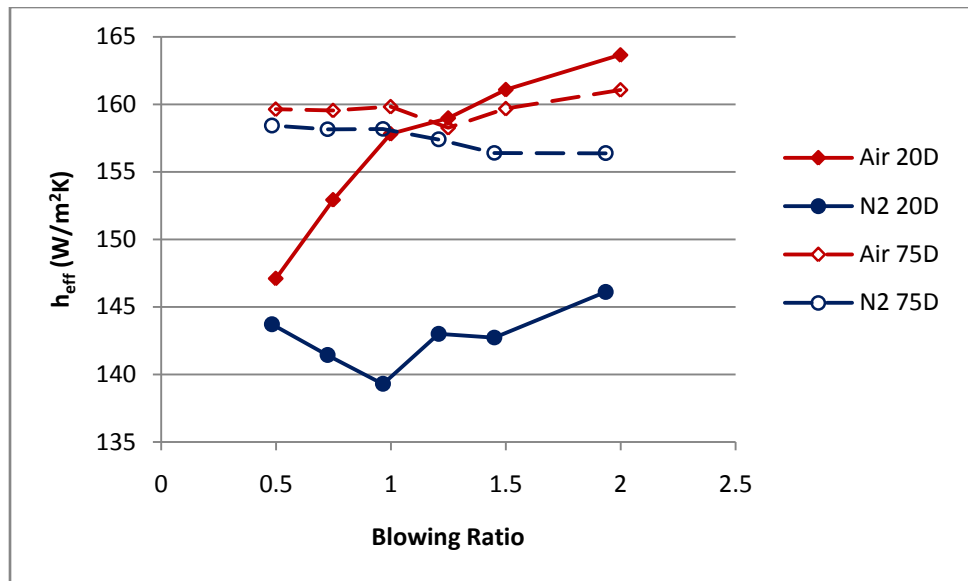


Figure 167. Dependence of h_{eff} on M , fanshaped holes, $\Phi = 1.7$, $\dot{m}_{air} = 1020$ g/min

Appendix D Thin Film Gauge Design and Operation

This study was designed for the inclusion of Thin Film Gauges (TFG) and High-Density Thin Film Gauge Arrays (HDTFG), which would provide high frequency and high spatial resolution surface temperature measurements. Unfortunately, manufacturing delays prevented their inclusion into the test program at the time of writing. Development is continuing, and the technology will be applied to future experiments.

TFGs and HDTFGs are manufactured using a photolithography technique in which a platinum film is sputtered onto a substrate, leaving a platinum only sensor and lead pattern²⁶. The resistance of the platinum film to current is dependent on temperature, so the surface temperature may be determined by monitoring the voltage drop across the film under a constant current (I_s), as given in Eq. (38)²⁷:

$$T_s = \frac{v_f}{\alpha_R V_0} \quad (38)$$

Where v_f is the voltage across the platinum film, α_R is the temperature coefficient of resistance (determined by calibration), and V_0 is the voltage across the film at the reference temperature. Figure 168 depicts a single platinum thin film gauge of the type used in the current study. A constant current enters from the top left, passes through the gauge (on the right), then exits through the bottom left. The voltage across the film, v_f , is measured between the traces marked with the red arrows.



Figure 168. Single serpentine-shaped Thin Film Gauge designed for the current study

High Density Thin Film Gauge arrays concentrate a number of TFGs into a small area. A simplified schematic of an array of five TFGs is shown in Figure 169. The current passes through the TFGs in series. The voltage is measured across each TFG, and the temperature of each gauge is determined separately. The six gauge HDTFGs designed for use in the current study are depicted in Figure 170. The current enters as indicated in the blue arrow, passing Voltage Lead #1. The current passes through the first TFG (1), where Voltage Lead #2 is located. The current then passes through each of the remaining TFGs in series, exiting as indicated by the blue arrow. To find the voltage across TFG #1, a measurement is taken between Lead #1 and Lead #2. Similarly, to measure the voltage across TFG #5, a measurement is taken between Lead #5 and Lead #6.

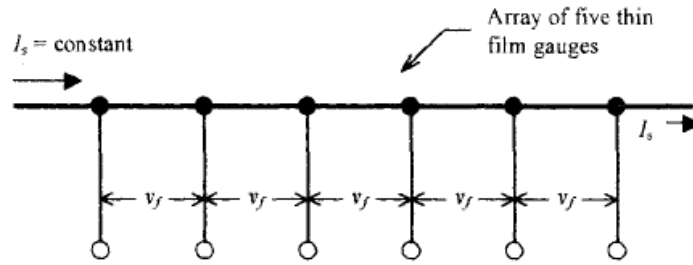


Figure 169. Schematic of High Density Thin Film Gauge array²⁶

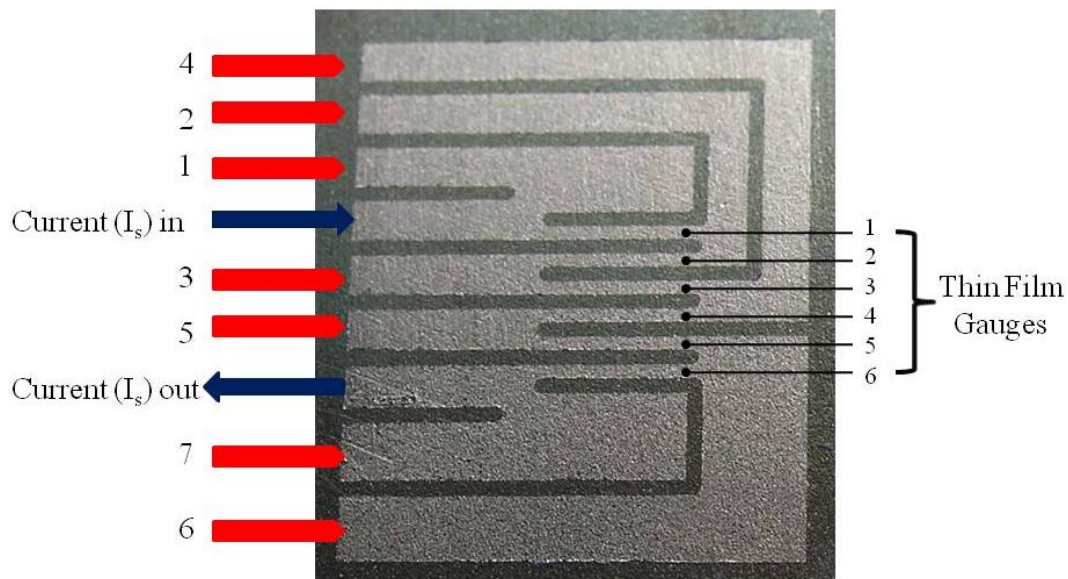


Figure 170. High Density Thin Film Gauge array

In previous studies^{26,27}, TFGs and HDTFGs were sputtered onto a flexible substrate that could then be bonded to the surface being measured. The use of this method would not allow the gauges to survive in the high temperature combustion environment of the current study. AFRL has developed a technique to allow HDTFGs to be used directly in combustion research. Instead of using a separate substrate, the surface to be measured

is coated completely with a dielectric material, and the gauges are sputtered onto this insulator. The voltage and current leads are sputtered onto a curved surface until far enough from the combustion environment to allow the soldering of wires, which are connected to the instrumentation.

The survivability of the HDTFGs in a combustion environment was unknown at the beginning of this study. The TFGs thin layer of platinum would be exposed to combustion products and particulates in addition to very high temperatures. Therefore, three different designs were proposed to determine surface temperature: Thermocouple-only gauge, single Thin Film Gauge, and High-Density Thin Film Gauge array. The HDTFG platinum traces are only 0.4 mm in width. The single TFG gauge has platinum traces twice that thickness, in an effort to increase resilience. The relative advantages and disadvantages of each design are shown in Table 12.

Table 12. Comparison of surface temperature measurement designs

Thermocouple Only	Single TFG	HDTFG Array
Steady State	High Frequency Response	High Frequency Response
Low Spatial Resolution	Low Spatial Resolution	High Spatial Resolution
Very Resilient	Less Resilient	Much Less Resilient

The heat transfer block design for use with the TFGs and HDTFGs are identical to each other, and is very similar to the thermocouple only design used in this study (Figure 171). The thin film gauge is printed onto the flat section on the surface of the block. The block has a curve machined into one side of the surface, with a channel cut all the way to the bottom. The curve has a large enough radius to allow the leads for the TFGs to be printed on the curve. At a point near the channel, the wires are soldered onto the leads,

and the wires are routed along the channel and out through the mount. The curve is then filled with a ceramic putty to protect the wires and solder joints from the heat and to preserve the smoothness of the test section. The TFG block mounts may be rotated 90° to allow the HDTFG array to measure temperature along the flow-wise and spanwise directions. These designs also incorporate a thermocouple at 19.1 mm from the surface, aligned with the center of the TFG or HDTFG array.

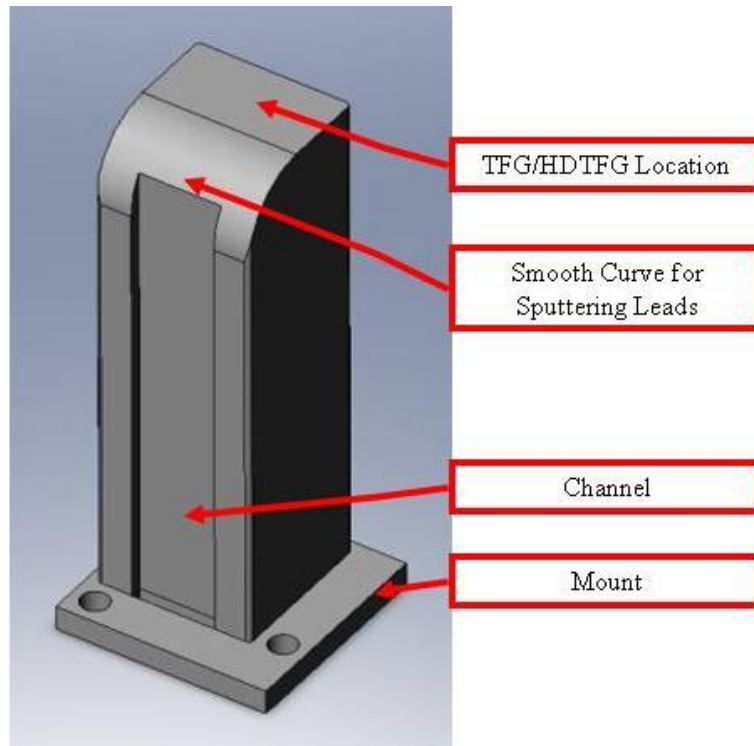


Figure 171. Design of TFG and HDTFG heat transfer gauge block

References

- ¹ Ballal, D.R., and Zelina, J., “Progress in Aero Engine Technology (1939-2003),” AIAA Paper No. 2003-4412, 2003.
- ² Bogard, D.G., and Thole, K.A., “Gas Turbine Film Cooling,” *Journal of Propulsion and Power*, Vol. 22, 2006, pp. 249-269.
- ³ Mattingly, J.D., Heiser, W.H., Daley, D.H., *Aircraft Engine Design*. Washington DC: AIAA, 1987.
- ⁴ Zelina, J., Sturgess, G.J., Shouse, D.T., “The Behavior of an Ultra-Compact Combustor (UCC) Based on Centrifugally Enhanced Turbulent Burning Rates,” AIAA Paper No. 2004-3541, 2004.
- ⁵ Lukachko, S.P., Kirk, D.R., Waitz, I.A., “Turbine Durability Impacts of High Fuel-Air Ratio Combustors, Part 1: Potential For Intra-Turbine Oxidation of Partially-Reacted Fuel,” GT-2002-30077. Presented at ASME Turbo Expo 2002: Land, Sea & Air, Amsterdam, The Netherlands.
- ⁶ Zelina, J., Shouse, D. T., and Hancock, R.D., “Ultra-Compact Combustors for Advanced Gas Turbine Engines,” ASME IGTI 2004-GT-53155.
- ⁷ Zelina, J., Ehret, J., Hancock, R.D., Shouse, D.T., Sturgess, G.J., and Roquemore, W.M., “Ultra-Compact Combustion Technology Using High Swirl to Enhance Burning Rate,” AIAA Paper No. 2002-3725, 2002.
- ⁸ Radke, J.T., “Efficiency and Pressure Loss Characteristics of an Ultra-Compact Combustor with Bulk Swirl,” MS Thesis, AFIT/GAE/ENY/07-J18, Graduate School of Engineering, Air Force Institute of Technology (AU), WPAFB OH, June, 2007.
- ⁹ Polanka, M.D., Anthony, R.J., Bogard, D. G., Reeder, M.F., “Determination of Cooling Parameters for a High Speed, True Scale, Metallic Turbine Vane Ring,” GT-2008-50281. To be presented at ASME Turbo Expo: Power for Land, Sea and Air, Berlin, Germany.
- ¹⁰ Baldauf, S., Schulz, A., and Wittig, S., “High-Resolution Measurements of Local Effectiveness From Discrete Hole Film Cooling,” *Journal of Turbomachinery*, Vol. 123, 2001, pp. 758-765.
- ¹¹ Foster, N.W., and Lampard, D., “The Flow and Film Cooling Effectiveness Following Injection Through a Row of Holes,” *Journal of Engineering for Power*, Vol. 102, 1980, pp. 584-588.

- ¹² Baldauf, S., Scheurlen, M., Schulz, A., and Wittig, S., "Correlation of Film-Cooling Effectiveness from Thermographic Measurements at Engine-like Conditions," *Journal of Turbomachinery*, Vol. 124, 2002, pp. 686-698.
- ¹³ Saumweber, C., Schulz, A., and Wittig, S., "Free-Stream Turbulence Effects on Film Cooling with Shaped Holes," *Journal of Turbomachinery*, Vol. 125, 2003, pp. 65-73.
- ¹⁴ Turns, S.R., *An Introduction to Combustion* (2nd Ed.). New York: McGraw-Hill, Inc., 1996.
- ¹⁵ White, Frank M., *Heat Transfer*, Reading, MA: Addison-Wesley Publishing Co., 1984.
- ¹⁶ Material Datasheet H-3009a, "Hastelloy® X Alloy", Kokomo IN: Haynes International Inc., 1997.
- ¹⁷ Kirk, D.R., Guenette, G.R., Lukachko, S.P., and Waitz, I.A., "Gas Turbine Engine Durability Impacts of High Fuel-Air Ratio Combustors Part 2: Near Wall Reaction Effects on Film-Cooled Heat Transfer," GT-2002-30182. Presented at ASME Turbo Expo 2002: Land, Sea & Air, Amsterdam, The Netherlands.
- ¹⁸ Kee, R.J., Rupley, F.M., and Miller, J.A., 1991, "CHEMKIN-II: A FORTRAN Chemical Kinetics Package for the Analysis of Gas-Phase Chemical Kinetics," SAND89-8009, Sandia National Laboratories, Livermore CA.
- ¹⁹ Nenniger, J.E., Kridiotis, A., Chomiak, J., Longwell, J. P., and Sarofim, A. F., "Characterization of a Toroidal Well Stirred Reactor," *Twentieth Symposium (International) on Combustion*, The Combustion Institute, pp. 473-479, 1984.
- ²⁰ Zelina, J., "Combustion Studies in a Well-Stirred Reactor," Ph.D. Thesis, University of Dayton, Dayton OH, 1995.
- ²¹ Stouffer, S.D., Striebich, R.C., Frayne, C. W., and Zelina, J., "Combustion Particulates Mitigation Investigation Using a Well-Stirred Reactor," AIAA Paper No. 2002-3723, 2002.
- ²² Stouffer, S., Pawlik, R., Justinger, G., Heyne, J., Zelina, J., and Ballal, D., "Combustion Performance and Emissions Characteristics for A Well-Stirred Reactor for Low Volatility Hydrocarbon Fuels", AIAA Paper No. 2007-5663, 2007.

²³ Wilson, D. G., *The Design of High-Efficiency Turbomachinery and Gas Turbines*. Cambridge, MA: The Massachusetts Institute of Technology, 1984.

²⁴ Kline, S.J., and McClintock, F.A., “Describing Uncertainties in Single-Sample Experiments”, *Mechanical Engineering*, Vol. 75, 1953, pp. 3-8.

²⁵ Beck, J., “Block Thermal Analysis”, Unpublished Report, Air Force Research Laboratories Turbine Engine Division, 2008.

²⁶ Anthony, R.J., Jones, T.V., and LaGraff, J.E., “Visualization of Transitional Boundary Layer Heat Flux Using High Density Thin Film Arrays”, AIAA Paper No. 2001-0553, 2001.

²⁷ Anthony, R.J., Jones, T.V., and LaGraff, J.E., “Unsteady Surface Heat Flux Under a Three-Dimensional Crossflow Boundary Layer”, AIAA Paper No. 2004-1344, 2004.

REPORT DOCUMENTATION PAGE				<i>Form Approved</i> OMB No. 0704-0188	
<small>The public reporting burden for this collection of information is estimated to average 1 hour per response, including the time for reviewing instructions, searching existing data sources, gathering and maintaining the data needed, and completing and reviewing the collection of information. Send comments regarding this burden estimate or any other aspect of this collection of information, including suggestions for reducing this burden to Department of Defense, Washington Headquarters Services, Directorate for Information Operations and Reports (0704-0188), 1215 Jefferson Davis Highway, Suite 1204, Arlington, VA 22202-4302. Respondents should be aware that notwithstanding any other provision of law, no person shall be subject to any penalty for failing to comply with a collection of information if it does not display a currently valid OMB control number. PLEASE DO NOT RETURN YOUR FORM TO THE ABOVE ADDRESS.</small>					
1. REPORT DATE (DD-MM-YYYY)		2. REPORT TYPE		3. DATES COVERED (From — To)	
19-06-2008		Master's Thesis		August 2006 — June 2008	
4. TITLE AND SUBTITLE The Impact of Heat Release in Turbine Film Cooling				5a. CONTRACT NUMBER	
				5b. GRANT NUMBER	
				5c. PROGRAM ELEMENT NUMBER	
6. AUTHOR(S) Evans, Dave S., LT, USN				5d. PROJECT NUMBER	
				5e. TASK NUMBER	
				5f. WORK UNIT NUMBER	
7. PERFORMING ORGANIZATION NAME(S) AND ADDRESS(ES) Air Force Institute of Technology Graduate School of Engineering and Management (AFIT/EN) 2950 Hobson Way WPAFB OH 45433-7765				8. PERFORMING ORGANIZATION REPORT NUMBER AFIT/GAE/ENY/08-J02	
9. SPONSORING / MONITORING AGENCY NAME(S) AND ADDRESS(ES) Dr. Marc Polanka 1950 Fifth Street Building 71B J Bay WPAFB, OH 45433-7251 DSN: 785-1922; Comm: (937) 255-1922				10. SPONSOR/MONITOR'S ACRONYM(S)	
				11. SPONSOR/MONITOR'S REPORT NUMBER(S)	
12. DISTRIBUTION / AVAILABILITY STATEMENT APPROVED FOR PUBLIC RELEASE; DISTRIBUTION UNLIMITED.					
13. SUPPLEMENTARY NOTES					
14. ABSTRACT The Ultra Compact Combustor is a design that integrates a turbine vane into the combustor flow path. Because of the high fuel-to-air ratio and short combustor flow path, a significant potential exists for unburned fuel to enter the turbine. Using contemporary turbine cooling vane designs, the injection of oxygen-rich turbine cooling air into a combustor flow containing unburned fuel could result in heat release in the turbine and a large decrease in cooling effectiveness. The current study explores the interaction of cooling flow from typical cooling holes with the exhaust of a fuel-rich well-stirred-reactor operating at high temperatures over a flat plate. Surface temperatures, heat flux, and heat transfer coefficients are calculated for a variety of reactor fuel-to-air ratios, cooling hole geometries, and blowing ratios. Results demonstrate that reactions in the turbine cooling film can result in increased heat transfer to the surface. The amount of this increase depends on hole geometry and blowing ratio and fuel content of the combustor flow. Failure to design for this effect could result in augmented heat transfer caused by the cooling scheme, and turbine life could be degraded substantially.					
15. SUBJECT TERMS Film Cooling, Gas Turbine Blades, Combustor, Combustion Heat, Fuel Air Ratio, Heat Transfer, Heat Transfer Coefficients, Cooling Hole Shape, Blowing Ratio, Ultra-Compact Combustor, Inter-Turbine Burner					
16. SECURITY CLASSIFICATION OF:			17. LIMITATION OF ABSTRACT	18. NUMBER OF PAGES	19a. NAME OF RESPONSIBLE PERSON
a. REPORT	b. ABSTRACT	c. THIS PAGE			Dr. Paul King (AFIT/ENY)
U	U	U	UU	165	19b. TELEPHONE NUMBER (Include Area Code) (937) 255-3636, ext 4628; e-mail: paul.king@afit.edu